

Lawrence Berkeley National Laboratory

Lawrence Berkeley National Laboratory

Title

Actinide Production in the Reaction of Heavy Ions with Curium-248

Permalink

<https://escholarship.org/uc/item/63j2n7kx>

Author

Moody, K.J.

Publication Date

1983-07-01



Lawrence Berkeley Laboratory

UNIVERSITY OF CALIFORNIA

RECEIVED
LAWRENCE
BERKELEY LABORATORY

AUG 29 1983

LIBRARY AND
DOCUMENTS SECTION

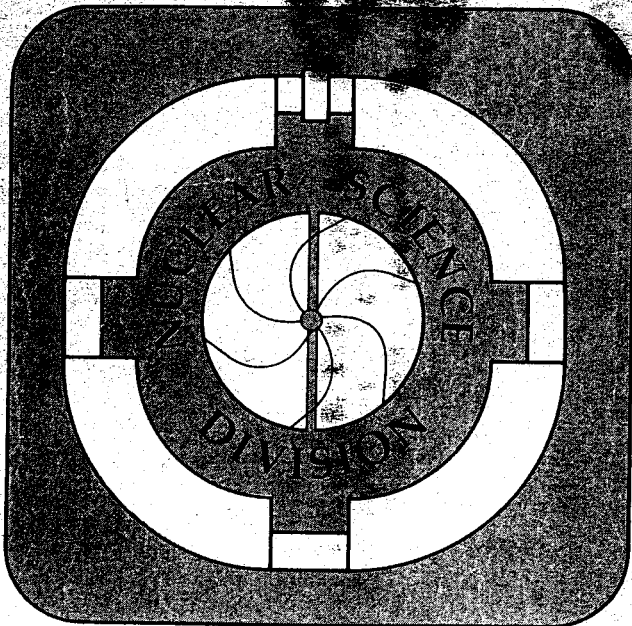
ACTINIDE PRODUCTION IN THE REACTION OF
HEAVY IONS WITH CURIUM-248

K. J. Moody
(Ph.D. Thesis)

July 1983

TWO-WEEK LOAN COPY

*This is a Library Circulating Copy
which may be borrowed for two weeks.
For a personal retention copy, call
Tech. Info. Division, Ext. 6782.*



LBL-16249

ACTINIDE PRODUCTION IN THE REACTION
OF HEAVY IONS WITH CURIUM-248

Kenton James Moody

Ph.D. Thesis

July 1983

Nuclear Science Division
Lawrence Berkeley Laboratory
University of California
Berkeley, CA 94720

This work was supported by the Director, Office of Energy Research,
Division of Nuclear Physics of the Office of High Energy and Nuclear Physics
of the U.S. Department of Energy under Contract DE-AC03-76SF00098.

Abstract

Chemical experiments were performed to examine the usefulness of heavy ion transfer reactions in producing new, neutron-rich actinide nuclides. A general quasi-elastic to deep-inelastic mechanism is proposed, and the utility of this method as opposed to other methods (e.g. complete fusion) is discussed.

The relative merits of various techniques of actinide target synthesis are discussed. A description is given of a target system designed to remove the large amounts of heat generated by the passage of a heavy ion beam through matter, thereby maximizing the beam intensity which can be safely used in an experiment. Also described is a general separation scheme for the actinide elements from protactinium ($Z=91$) to mendelevium ($Z=101$), and fast specific procedures for plutonium, americium and berkelium.

The cross sections for the production of several nuclides from the bombardment of ^{248}Cm with ^{18}O , ^{86}Kr and ^{136}Xe projectiles at several energies near and below the Coulomb barrier were determined. The results are compared with yields from ^{48}Ca and ^{238}U bombardments of ^{248}Cm . Simple extrapolation of the product yields into unknown regions of charge and mass indicates that the use of heavy ion transfer reactions to produce new, neutron-rich above-target species is limited. The substantial production of neutron-rich below-target species, however, indicates that with very heavy ions like ^{136}Xe and ^{238}U the new species ^{248}Am , ^{249}Am and ^{247}Pu should be produced with large cross sections from a ^{248}Cm target.

A preliminary, unsuccessful attempt to isolate ^{247}Pu is outlined. The failure is probably due to the half life of the decay, which is calculated to be less than 3 minutes. The absolute gamma ray intensities from ^{251}Bk decay, necessary for calculating the ^{251}Bk cross section, are also determined.

Acknowledgements

The work of many people is reflected in the pages that follow, and many other people worked to make my stay in graduate school enjoyable, though much too long. To any that I have forgotten, my apologies.

I wish to thank Glenn Seaborg for his support and his patience.

The skepticism of Albert Ghiorso was invaluable and, occasionally, deserved. (Yes, Al, I admit it.)

The tireless Diana Lee performed all the trans-berkelium element separations reported here. Without her assistance and expertise, none of us would ever finish our degrees.

Ken Thomas taught me most of my radiochemistry and showed me the ropes, at least enough to avoid catching my neck at the end of one. Yet.

Robert Welch assisted with most of the irradiations and developed the fast americium chemistry which resulted in the "heaviest" americium data.

Matti Nurmia provided both the original design and the philosophy of the target system used in bombardments with ^{86}Kr and ^{136}Xe ions. L. Archambault and A. Wydler helped fix things when they broke.

Ken Hulet and Ron Lougheed provided the targets used in SuperHILAC experiments.

Several people helped do chemistry or count samples at one point or another. Among them are K. Gregorich, Y. Morita, P. Wilmarth, R. McFarland, M. Perry, Y.-F. Liu and Luo Cheng.

People who have lent their support to this work or who have involved me in other interesting projects include D. C. Hoffman, J. M. Nitschke, J. J. Hogan, H. Groening, H. Kudo, S. Tanaka, L. Somerville, S. Yashita, P. Baisden, M. Schadel, H. Gaggeler and H. R. von Gunten. They are gratefully acknowledged.

I would like to express my deepest thanks to the Environmental Health and Safety Department at LBL, and particularly to E. Calhoon. Many times it would have been easier to cancel an experiment than to find a safe way to do it. This never happened.

I would like to thank the staff and crew of the 88-inch Cyclotron for routinely supplying excellent particle beams.

Special thanks go to all my friends at the SuperHILAC, who always seem to do the impossible with their eccentric accelerator. Besides the E.M.'s, M.M.'s and Acc.Tech.'s who keep things running (and brew coffee!), and Beam Development and the Scientific Staff who keep things exciting, I particularly want to thank the control room guys who tuned the beam and kept me awake: S. Boyle, G. Byer, N. Cash, R. Coates, T. Gimpel, R. Gisser, A. Guy, C. Hatch, R. Johnson, J. Smith, R. Stevenson, H. Syversrud, R. Thatcher, C. Timossi, and M. Wolfe. I had to promise to put them in my thesis to get the beam late one night. Are we square now?

My scientific enthusiasm was fostered by my teachers, though several may not want to take responsibility. My thanks to J. Hook, K. Robinson, T. Hughes and R. Martin. J. Rasmussen and S. Prussin read this manuscript and let me get away with it.

Last, but not least, I would like to thank my family, whose support kept me going when I faltered, and my wife, Zoe', who made me want to finish this and move on.

Table of Contents

Section 1 - Purpose and Introduction	1
1.1 Production of Neutron-rich Actinides and some Limitations	1
1.2 When Heavy Ions Collide	7
1.3 Actinide Yields from ^{248}Cm	11
Figures, Section 1	13
Section 2 - Experimental Methods	15
2.1 Targets	15
2.2 Target Systems	21
2.3 Chemical Separations	33
2.4 Detection of Characteristic Radiations	47
Figures, Section 2	51
Section 3 - Data Reduction	64
3.1 Determination of the Energy of the Beam Particles in the Target	64
3.2 Determination of Reaction Cross Sections	72
3.3 Collection Efficiency of Catcher Foils	83
Figures, Section 3	90
Section 4 - Results and Discussion	96
Figures, Section 4	115
Section 5 - Determination of the Properties of ^{251}Bk Decay	138
5.1 Background	138

5.2 The Difficulties Inherent in a Direct ^{251}Bk Determination	139
5.3 Experimental Details	141
5.4 The Half Life of ^{251}Bk	144
5.5 The Decay Scheme of ^{251}Bk	145
5.6 Summary	153
Figures, Section 5	153
Section 6 - The Search for ^{247}Pu	164
6.1 Predicted Properties of ^{247}Pu	164
6.2 Experimental	174
6.3 Summary	177
Figures, Section 6	178
Section 7 - Conclusion	187
References	188

Section 1 - Purpose and Introduction

The purpose of this work is to measure the yields of actinide products formed in heavy ion bombardments of ^{248}Cm , and to examine the possibility of picking optimum projectile, energy and target combinations for producing new, neutron-rich actinide nuclei. The characterization of these unknown species is important in furthering the understanding of mass and fission systematics in the heavy element region, where the limits of nuclear stability are being explored. These neutron-rich nuclides are inaccessible via the reaction mechanisms previously used in new actinide synthesis, so new methods must be studied.

1.1 Production of Neutron-rich Actinides and some Limitations

Nuclear reactions produce nuclides with an excess of energy over that of the ground state. A non-zero impact parameter in the reacting system can introduce an intrinsic angular momentum in the primary product nuclides considerably different than the spin of their ground states. Excess energy and angular momentum are removed via the emission of light particles and gamma photons, or by fission. In the heavy element region, where the energy released in the fission process is large and the barrier is low, fission becomes the predominant mode of de-excitation.

The statistical emission of light particles and gamma photons from equilibrium nuclei has been well-characterized [Rea65,Gil71, Bla80] since the potential barriers and the densities of receiving states as a function of energy and angular momentum [Lan66,Plo82] are well-defined. The high nuclear charge of actinide species severely inhibits de-excitation by proton and alpha particle emission relative to that by neutron emission due to the high Coulomb potentials against the processes. In the neutron-deficient actinides, apparent de-excitation by charged particle emission has been observed as a competing

process [Kuz67,Hah74,Wil78] due to the favorable energetics, but some contribution to the reaction products due to non-equilibrium processes is suspected. In the neutron-rich actinides, the emission of charged particles in evaporative de-excitation can be neglected in comparison to neutron emission and fission rates. Emission of "average" neutrons results in a loss of roughly 8 MeV of excitation energy and a few units of angular momentum. Several neutrons may have to be emitted to completely de-excite a primary reaction product down to the Yrast band of the final daughter [Gro67]. The one-shot fission process competes with the emission of each particle. Once the excitation energy of an evaporation residue is in the vicinity of the binding energy of the neutron above the Yrast line, photon emission becomes the primary competition to de-excitation by fission.

The fission probability is not nearly so well defined as the probability of particle emission [Van73]. Structure in the fission barrier as a function of the shape of the separating system can be inferred with the Strutinsky hybrid model [Str67,Str68] and is borne out by the existence of the fission isomers [Pol62,Mal67], but is difficult to quantify as a function of excitation energy [Nil68]. The presence of intrinsic angular momentum changes the height of the fission barrier [Coh74] and enhances the probability of fission relative to particle emission [Van73]. The mass- and charge-split in fission is non-discrete, so the density of receiving states is very complicated. The probability of fission relative to a given neutron emission, expressed as a ratio of decay widths, has been derived based on simple models of the fission process [Van73,Ign72,Sik67], but the results are highly dependent upon parameterization [Bec77].

Clearly, when looking for neutron-rich reaction products in the actinide region, two classes of synthesis methods are suggested: Either the reaction products must be directly formed with nearly the proper number of neutrons at

a low excitation energy that precludes particle emission, or the products must be made with an excess of neutrons at a high excitation energy and de-excite by evaporation. The minimal loss of reaction products to fission favors the first method for actinide synthesis.

As a result, reactions involving the complete fusion of heavy ions and heavy targets to form an evaporation residue are almost completely useless for formation of new, neutron-rich actinides. Due to the sharp bend of the valley of beta stability toward neutron excess, the fusion of a light projectile with a heavy target produces compound nuclei which are relatively neutron-deficient. Surmounting the Coulomb barrier requires a projectile kinetic energy which guarantees a fairly high primary product excitation energy. Complete fusion of more symmetric systems results in a much lower excitation energy due to the lower reaction Q-value, but the resulting reaction products are even more neutron-deficient than those resulting from asymmetric systems, the intrinsic angular momenta are higher [Bla80], resulting in a higher fission probability, and the geometrical problem of pushing the intermediate system into a more-or-less spherical configuration requires the addition of an excess of relative kinetic energy of the participants [Swi82,Bjo82]. Nevertheless, this technique has recently been used to synthesize neutron-deficient isotopes of elements 107 and 109 in the reactions of ^{209}Bi with ^{54}Cr and ^{58}Fe [Mun81,Mun82] with almost no excitation energy.

Figure 1a shows a section of the chart of the nuclides with reasonable neutron-rich target nuclides for use in heavy ion bombardments indicated; "reasonable" in this case means that the material is available in at least microgram quantities and the half life is on the order of a year or longer. Also designated on figure 1a is the neutron-rich limit of the known actinide nuclides [See81] and some compound nuclei formed from the heavy targets with com-

monly available projectiles. Even neglecting the necessary emission of neutrons in de-excitation, the lowest Z incursion into unknown territory is in the nobelium isotopes ($Z=102$) and the evaporation of particles puts the residues from even these reactions back into the known regions of charge and mass, since these are the very reactions which produced the most neutron-rich known isotopes of these elements [Sil73,Esk71,Ghi70].

The idea of producing neutron-rich short-lived species in primary projectile-target interactions which then interact in secondary reactions with the target to produce new species has been advanced, usually in the context of application to superheavy element synthesis [Kar69,Uni72,Fle73,Mar80]. In the more primitive experiments, a beam of high-energy protons or low-energy heavy ions was used to bombard a heavy element target, and the reaction products, produced with a high lab-frame kinetic energy, went on in turn to interact with the target material. Neutron-rich light nuclides are beginning to become available as actual "secondary beams" [Rav79,Duf80] and in coming years bombardments with species like ^{22}O at reasonable beam intensities may become possible. However, even the extension of the possible compound nuclei by several neutrons in excess of those designated in figure 1a will help little in neutron-rich actinide production, partly due to the absence of suitable target materials in the lead to radium region.

Many of the known neutron-rich actinide nuclides were produced through low-energy neutron irradiations of heavy targets, either in a nuclear reactor or in a nuclear explosion [Com66]. Indeed, the available heavy targets themselves are products of neutron irradiations of other products, all deriving ultimately from ^{238}U , ^{232}Th , and their natural decay daughters. In these reactions, the negligible energy of the fully or partially moderated neutron imparts an excitation energy to the primary capture product essentially equal to the binding

energy of the neutron, and imparts very little angular momentum. The probability of fission of the product directly displays the odd-even effect on this binding energy: The addition of a neutron to an actinide species with an even number of protons and an odd number of neutrons is more likely to result in fission than the addition of a neutron to an even-even nuclide, because the ground state of the even-even nucleus is stabilized by the pairing energy of the two neutrons, increasing the binding energy of the neutron in these species. The cross section for fission in the $n_{th} + {}^{235}\text{U}$ and $n_{th} + {}^{239}\text{Pu}$ reactions is considerably more than half of the reaction cross section, while the addition of still another neutron to each in the $n_{th} + {}^{238}\text{U}$ and $n_{th} + {}^{240}\text{Pu}$ reactions results in fission cross sections of less than a percent of the total [TOI78]. In experiments where heavy actinide yields were determined in nuclear explosions [Com66], the regularity of the mass yields of the actinide products, the odd-even excursions from that regularity, and the total absence of the formation of such shielded species as ${}^{250}\text{Cf}$ and ${}^{254}\text{Es}$ [Fie56], which can be made at lower flux in reactors, all was taken as evidence of the successive rapid capture of neutrons by uranium, followed by the beta decay of such exotic species as ${}^{257}\text{U}$. Calculations predict the significant probability of formation of ${}^{270}\text{U}$ [Mel76]. This, then, is one way of producing neutron-rich actinide species, and the existence of einsteinium and fermium isotopes in nuclear debris is evidence of the former presence of beta-minus unstable actinides of lower atomic numbers. However, it is not possible at present to isolate reaction products from these debris on any time scale remotely comparable to the half lives of the more exotic species, though beta-emitting 11-day ${}^{249}\text{Pu}$ [Eng55] and spontaneously fissioning 60-day ${}^{254}\text{Cf}$ [Hui57], among others, were first observed via this method.

Other neutron-rich actinides have been synthesized with direct reactions of neutrons, protons and bremsstrahlung photons with neutron-rich actinide

targets. These are non-equilibrium processes where the projectile (or photon) interacts with one or more nucleons in the target nucleus, transferring some or all of its momentum, leaving the rest of the nucleons as spectators [Seg77]. This can result in residual nuclei with very little excitation energy or angular momentum, depending upon the nucleons removed and the trajectories they take as they exit the nucleus. Transit of a substantial amount of nuclear matter results in a higher residual excitation. Examples of nuclides produced by this method are ^{232}Ac from the $^{232}\text{Th}(n,p)$ reaction [Cha73], ^{231}Ac from the $^{232}\text{Th}(\gamma,p)$ reaction [Tak60,Cha73], ^{235}Th from the $^{238}\text{U}(n,\alpha)$ reaction [Tra69], ^{236}Th from the $^{238}\text{U}(p,3p)$ reaction [Ort73], and ^{242}U (and the ^{242}Np daughter) from the $^{244}\text{Pu}(n,2pn)$ reaction [Hau79]. These methods are limited to the production of nuclides with no more than one neutron or proton more than the target nuclide, and are also limited by the number of particles that can be "knocked out" before the excitation energy of the residual nucleus becomes high enough to start the evaporation neutrons.

Neutron-rich actinides have also been produced with another class of direct reactions, called stripping. The most successfully used projectile is the tritium ion ($^3\text{H}^+$), for which beam intensities are sufficiently large to permit the use of exotic targets containing a limited number of target nuclides. The (t,p) reaction, where a pair of neutrons are transferred to the target nucleus while the proton proceeds on its way, has been used to produce ^{259}Fm from ^{257}Fm [Hof76a] and ^{256}Cf from a ^{254}Cf target [Hof77]. The (t,p) reaction is more favorable than the competing (t,n) reaction for actinide production due to the lower resulting excitation energy, and therefore lower fission probability. The (t, α) reaction, where the triton picks up a proton from the target, was used in determination of the level structure of ^{243}Np from the $^{244}\text{Pu}(t,\alpha)$ transfer reaction [Fly79] and was observed as a significant competition to the formation of ^{259}Fm

in $^{257}\text{Fm}(t,\alpha)^{258}\text{Es}$ reactions [Hof76a]. The (t,p) reactions and (t,α) reactions still show limited promise in the synthesis of new nuclides with the more exotic targets, but the product nuclides are still limited to within a few mass units of beta-stable nuclei. Other methods need to be employed to produce more neutron-rich species.

1.2 When Heavy Ions Collide

In the last few years considerable experimental and theoretical emphasis has been placed on the study of transfer reactions. The first problem encountered is always a matter of definition: What is meant by transfer? In the evolution of the understanding of the processes involved in the non-equilibrium partition of mass, charge, angular momentum and energy between two colliding nuclear species, the names applied have been deep-inelastic reactions, quasi-elastic transfer, quasifission, damped collisions, and incomplete fusion. All of these processes reflect different facets and extremes of the same process. Some excellent review articles are available [Sch77b, Lef78, Vol78].

When heavy ions collide, yet do not coalesce into an equilibrated compound nucleus, they can form a short-lived intermediate double-centered complex. While in contact with one another, on different time scales and to different degrees depending upon the depth of mutual interaction, several things can happen involving the collective properties of the system. One of the most dramatic results of such reactions is the "thermalization" of the relative kinetic energies of the participants into internal excitation energy. In the limit of a "fully damped" collision, the fragment kinetic energies in the center of mass are very little different from the mutual Coulomb repulsive energies of two charged, touching spheroids, much like the fission process. With the dissipation of relative kinetic energy into excitation energy, the conversion of orbital angular momentum of the rotary dinuclear complex into intrinsic angular

momentum of the products is also observed. In the early stages of energy damping, a rapid equilibration of the neutron-to-proton ratios of the participants occurs [Gat75,Sve78,Chi79,Kra80]. On a much slower time scale, the transfer of mass occurs. The equilibration of N/Z can be thought of as the motion of the individual nucleons, which are no longer in well-defined quantum-mechanical states, migrating inside the oddly-shaped, transient potential well of the colliding species, while the transfer of mass actually involves changing the shape of the whole potential, and therefore the orientations of all the nucleons.

The transfer of mass is generally tied to the degree of energy thermalization and the interaction time [Sve78,Mor76,Hui76]. In the reaction of nearly symmetric very heavy systems, the net flow of mass from one participant to the other favors symmetry due to the available level densities. With greatly asymmetric systems involving light heavy ions the net flow of mass is from the light particle to the heavy fragment, determined by the competing driving forces of both the reaction Q -value [Sie71], which is large compared with the relative energy of motion at the top of the potential barrier, and by the energetics of Coulomb separation, which favors an asymmetric mass split [Dia68], the N/Z being equilibrated between the fragments. Since N/Z equilibration can be related to motion of the nucleons in the two-centered potential, excitation energy can be thought of as being divided between the two fragments from a damped collision in proportion to the number of nucleons in each [Mor79]. This results in the light fragment from a multinucleon transfer reaction of a very asymmetric system being produced with very little excitation energy. The apparent addition of a piece of the projectile to the target in light heavy ion bombardments of actinides has led to the use of a no-intermediate model [McF82, Lee83], similar to the stripping reaction description above, which works

well for predicting projectile-like product yields with the very light heavy ion ^{18}O , but begins to fail with ^{22}Ne in bombardments of ^{232}Th targets [Art73a], and fails completely with ^{40}Ar projectiles [Jac75].

Quasi-elastic transfer reactions can be thought of as the very peripheral extremes of the process outlined above, occurring at large impact parameters where the interaction of nuclear matter and the consequent interaction of projectile and target collective degrees of freedom is minimal. Single particle effects dominate. The angular distributions of products in these reactions are typical of grazing. As the collision becomes more central, the interaction time increases, the thermalization of energy and angular momentum and the equilibration of N/Z becomes more complete, followed by the partial relaxation of the mass difference. This results in product mass distributions peaked around the entrance channel mass and charge values [Tho79,Bin77,Kra76,Kra74,Ott76,Sch78]. At the fully damped extreme lies the completely equilibrated system, which can be thought of as a quasi-compound nucleus. A fission-like process results in two fragments of similar mass and N/Z , emitted with a fission-like angular distribution [Mat79]. The kinematics of partially damped collisions is discussed in Section 3.

Like the fission process, the non-discrete character of the accessible final states of the interaction implies a statistical width for each degree of freedom [Nor74,Ayi78,Mor82]. While the average excitation energy splits proportionally with the masses of the products, fluctuations occur. The same is true of N/Z and the angular momentum partition. Therefore, while reactions which approach the quasi-elastic limit are those most likely to produce an actinide product with a low enough excitation energy and angular momentum to survive fission, the possibility exists for even a fairly "deep" process to result in a relatively cold actinide nucleus. And, while N/Z of the most probable products

approaches that of the composite system in these reactions, the width in the N/Z degree of freedom implies the possibility of synthesizing fairly neutron-rich species. Therefore, the use of incomplete fusion reactions offers some hope of producing neutron-rich species with low excitation energies.

The idea of producing new, neutron-rich nuclides in transfer reactions is not new. Before the reaction mechanism was well-characterized it was used to produce several new nuclides in the N,Z vicinity of the projectile in light heavy ion bombardments of ^{232}Th [Art71,Art70,Art72,Art71a]. The equilibration of N/Z between target and projectile favors a very neutron-rich projectile-like fragment. This has been employed more recently in isotope synthesis in the $^{40}\text{Ar} + ^{238}\text{U}$ reaction [Gue80]. Transfer reactions have also been used to synthesize new neutron-rich target-like species in the heavy lanthanides in reactions of ^{136}Xe with ^{nat}W [Kir82,Ryk83], but the absence of significant fission competition in this system makes extrapolation to the actinide region unreliable. Most of the work with transfer reactions to produce target-like species in the actinide region has concentrated on nuclides well above the target Z [Art74,Sch82a,Hul77,Sch78,Tho79,Vio80,Lee82,Lee83] or on the fission de-excitation products, hoping to be able to resolve the components due to complete fusion (or symmetric fully damped collisions [Mat79]) from those due to less-damped-to-quasi-elastic primary reaction products [Kra74,Kra76,Ott76,Kal77,Reu77,Kal77a,Ott78,Des78]. Quite a bit of work has been expended on the search for superheavy elements in these reactions [Sik67,Ott77,Vol78,Her79,Kra80a,Kra82,Hul81]. This is even more difficult than new actinide synthesis, because not only is a large N/Z drift from the products required to reach the postulated "island of stability," but the required mass drift is on the order of 40 units, with the attendant energy thermalization of the process.

Very little effort has been expended on the near- and below-target pro-

ducts in the heavy element region. Most of these studies have either emphasized products formed at the quasi-elastic limit or products so far below the target Z that particle evaporation is favorable relative to fission in the de-excitation process, so the product distributions no longer directly reflect the neutron-richness of the primary products [Luc79,Ott78a,Sch79,Oga74]. Work with ^{232}Th targets where excitation functions from ^{84}Kr [Bim72] and ^{22}Ne [Kum63] projectiles were measured concentrated on only neutron-deficient, near-target nuclides. Near- and below-target nuclides have been isolated in the reaction of ^{136}Xe with ^{238}U [Oga74a] and near- and below-target alpha-emitters have been seen in the reaction of ^{238}U with ^{238}U [Fre79].

1.3 Actinide Yields from ^{248}Cm

In this work, the production cross sections of the actinide products from the reactions of ^{18}O , ^{86}Kr and ^{136}Xe ions with ^{248}Cm are determined. Since the most neutron-rich products are desired, the bombarding energies are all in the neighborhood of the classical Coulomb barrier or lower; a substantial cross section for fission has been measured for ^{86}Kr - and ^{136}Xe -induced reactions with ^{248}Cm at substantially lower energies than the Coulomb barrier, so it is known that nuclear reactions can still occur [But77]. Each of the projectiles is the most neutron-rich isotope of its element, though far from the most abundant. The projectiles all have a magic number of neutrons or protons, but the effect of this upon the driving force of the reaction and the survival probabilities of the actinides is assumed to be negligible, though recent work indicates that there might be some shell effect on the driving force of the system [Sob79]. Above-, near- and below-target reaction products were chemically isolated. The ^{248}Cm nuclide is used as a target because it is the long-lived, neutron-rich actinide with the highest Z which is available in limited-but-sufficient quantities. ^{248}Cm can be handled safely and easily with minimal precautions. A wide variety

of product nuclides, both above and below the target Z , are easily observable.

The height and shape of the fission barrier is slowly changing in the actinide region [How80]. The reaction Q -value, if treated as a difference between entrance- and exit-channel mass defects, is also smoothly varying [Mye77]. The average excitation energy induced in the primary reaction products, and the distribution of that energy in their respective E - J spaces, should vary with the "depth" of the reaction and the amount of N/Z and mass drift. It can be postulated that the cross section for producing a particular actinide nuclide in a transfer reaction varies regularly as a function of neutron and proton numbers of the final products. The probability of producing an unobserved nuclide can be estimated from the cross sections of the neighboring nuclides with some accuracy, and that is the goal of this work.

A commonly asked question is: Why do a chemistry experiment? In this case it is easily justifiable. A physical technique is usually limited by solid angle and count rate, and in the experiments reported here both are important. Examination of the data in section 4 shows that some of the cross sections determined in this work are less than ten nanobarns. As a result, it was necessary to irradiate targets which were as thick as possible with high beam intensities and collect all of the reaction products (see section 3) to be able to detect even a few atoms of these species. Because of the reaction mechanism, the recoil angle of the products is poorly defined. Because of the target thickness, the recoil energies are poorly defined. Because of the beam intensity and high fission cross section, the beta, gamma and fission fragment count rate at all orientations to the target is very high. The necessary distance from the target due to the size of the apparatus used in a physics experiment limits the amount of solid angle subtended by a detector array. Also, with the high nuclear charge and mass of the actinide transfer products, purely physical techniques

do not give a unique identification of the Z and A [Gla77,Gou75], though progress is being made with on-line mass separation [Nit83]. The chemical technique, at least in the limited sense that it is applied in this work, is clearly the method of choice.

Figure Caption

Figure 1a - A section of the chart of the nuclides, showing (cross-hatched) the most neutron-rich target nuclides available in sufficient quantities to be useful in heavy ion irradiations. Also indicated are heavy ion reactions resulting in several compound nuclei in the actinides. The valley of beta stability follows the dashed line.

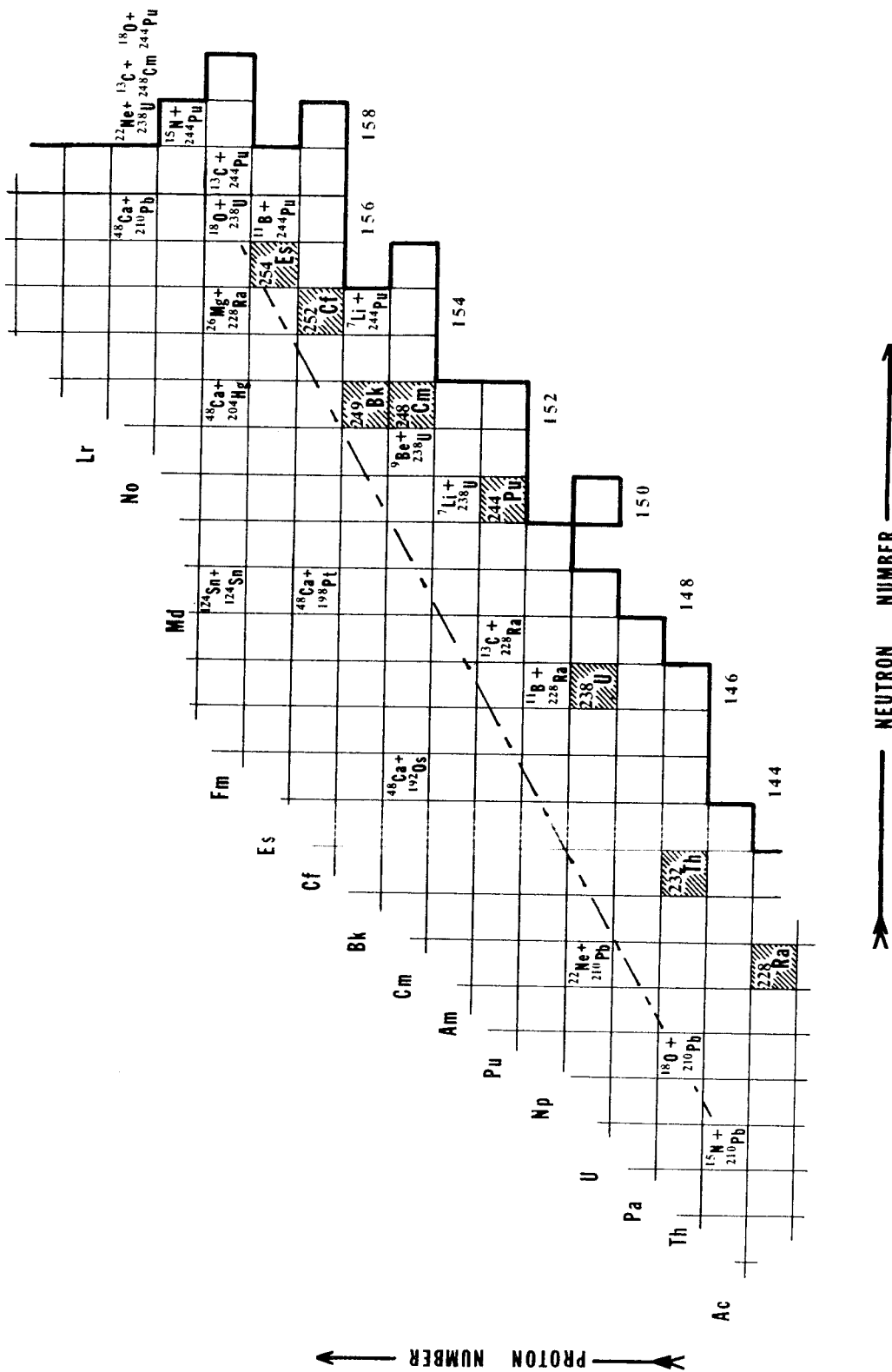


Figure 1a

Section 2 - Experimental Methods

Most of the experimental problems encountered in this work involve the severe loss of energy by very heavy ions in their passage through matter and the separation of the weak transfer product activities from a sea of interfering activities. The energy-loss problem is manifest not only in the calculation of the energy of the heavy ions when they get to the target material, but also in the heat which is evolved in the various components of the target system which limits the intensity which can be used in an irradiation. The chemical problem generated by a heavy ion bombardment of an actinide target is one of the worst imaginable: The interaction of the beam with the target backing, the catcher foil, the cooling medium, the other chemical components in the target, and with the actinide itself to make fission activities, each produces more activity than is present due to the projectile-target transfer reactions.

2.1 Targets

Targets used in heavy ion bombardments must meet several criteria: The component materials must be of uniform thickness to permit the accurate calculation of product cross sections and to degrade the beam energy to a uniform degree. The substrate, if any, should be as thin as possible to minimize the energy straggling of the beam. Target materials should be heat resistant and the finished target should be as mechanically durable as is needed. Finally, the chemical components of the targets should produce as few interfering activities as possible. The ultimate curium target would be a free-standing foil of curium metal, rolled to a uniform thickness; this has not proved feasible.

The target substrate used in all the experiments to be described was thin (approximately 13 micrometer) beryllium metal. Its mechanical properties can be compared to those of other materials in the form of a figure of merit [Nit76]. For all the ion beams used in this work, the beryllium figure of merit is

exceeded only by that of tungsten, which is not readily available in thin foils, and by certain alloys such as Havar [Hir75, Jar74]. The figure of merit does not express the damage caused by repeated heating and cooling due to the passage of beam through the material, to which alloys are more susceptible than pure materials; after long irradiations with xenon and lead ions at the fifty particle-nanoampere level, Havar beam windows (see Section 2.2) break down into a finely divided brown powder, while the beryllium-backed targets remain undamaged. Thin beryllium is rigid, which reduces flexing of the foil which tends to flake the target material from the backing. The low nuclear charge and mass of beryllium keeps the number of different beam-induced reaction products small, which is useful in subsequent chemical separations. The main disadvantage of beryllium is that the energy loss and straggling of the beam is more severe in beryllium than in any other metal [Nor70]. The heating effect of this energy loss is expressed in the figure of merit; it is the inaccuracy introduced into stopping power calculations to determine the energy of the beam in the target material which is the problem.

Several techniques have been employed in the past to make radioactive targets for accelerator experiments [Yaf62, Par60]. Methods involving the painting of the active materials in successive layers or evaporation of a solution to dryness on a backing are not suitable because the targets produced tend to be only locally uniform, and the formation of relatively large crystals of the solute is a problem. These methods have been used successfully in bombardments with light ions [Glo65, Wil78]. The most reliable techniques are those of electro spraying, vacuum sublimation, and molecular plating.

In the electro spray technique [Bru61], the material which is to be made into a target, usually in the nitrate form, is dissolved in an organic solvent with a low surface tension and boiling point. The solution is placed in a capillary

tube in which a thin platinum electrode has been suspended. The target backing is clamped to a heating element behind an insulating mask that defines the target spot, and the assembly is maintained at a temperature in excess of 300°C. A potential of 4500 V is applied across the gap between the capillary (+) and the target backing (ground). A spray of very fine droplets is produced which evaporate on their way to the backing or very shortly after reaching it. The distance between the capillary tip and the backing foil should be maintained at approximately 1.5 times the average diameter of the desired spot. A typical current across the gap is 0.2 to 0.4 microamperes. Periodically the foil must be dismantled and heated to complete the conversion of the target material to the oxide form. When remounted, the target should be placed in a different rotational orientation with respect to the axis of the spray to ensure a uniform deposit. Target thickness tends to be self-correcting; since the deposited material is usually less conductive than the backing, the spray "fills-in" areas which have less target material on them.

The electrospray technique has two drawbacks which make it unfeasible for the production of ^{248}Cm targets. The amount of ^{248}Cm available is limited, and this is a somewhat wasteful technique. It becomes more inefficient as the thickness of the target material builds up [Dak65]. While claims have been made of a 75% overall deposition efficiency for targets and thin sources [Glo65,Car57], others [Bru61] report values more on the order of 50%. In examining this technique for its applicability to ^{248}Cm , it was found that an overall deposition efficiency of 50% was routinely obtained with acetone solutions of the nitrates of ^{233}U , ^{232}Th and ^{242}Pu for targets up to 1 mg/cm² in thickness, but when natural gadolinium (the rare earth analogue of curium) or ^{154}Sm were electrosprayed, the efficiency was closer to 30%. The other drawback to the method is the quality of the targets themselves. When examined under a micro-

scope, uranium, thorium and plutonium targets looked very uniform, but gadolinium and samarium targets of over 0.5 mg/cm^2 average thickness seemed to be composed of closely-spaced "stalagmites" pointing upwards from the target backing. Experimenting with different solvents (isopropanol, ethanol) and capillary-backing geometries did not significantly affect these results.

The vacuum sublimation technique [Lou79] is very useful when an excess of target material is available. The material to be evaporated is placed in a crucible and heated in vacuum to the point where sublimation just begins (about 10^{-3} torr vapor pressure). The masked target substrate is placed in the vacuum chamber, and the amount of material deposited on it is determined by the configuration of the crucible, the solid angle subtended by the backing, and the amount of material evaporated [Glo65]. This technique offers many advantages: Impurities in the target can be reduced by preheating the target material before introduction of the target backing. The slow evaporation of the material produces very uniform targets. Virtually all of the target material which does not deposit on the target backing can be recovered from the components of the vacuum chamber and crucible. The targets produced by this technique can be made thicker than those produced by other techniques. The drawback to this method is that the chemical compounds most amenable to vacuum sublimation have low melting points, which makes them more susceptible to damage in heavy ion beams.

Most of the experiments involving ^{86}Kr and ^{136}Xe ions, described below, were performed with a target of 2.15 mg/cm^2 ^{248}Cm , vacuum evaporated as the fluoride in a 7 mm spot, on a 2.6 mg/cm^2 beryllium backing. In one ^{136}Xe irradiation a thinner (1.1 mg/cm^2) curium fluoride target was used. These targets were fabricated by R. W. Loughheed and E. K. Hulet of the Lawrence Livermore Laboratory.

Recently, vacuum sublimation techniques were used to produce curium metal targets on a variety of substrates [Lou82]. Possibly due to stresses generated by rapid heating and cooling between the metals along their strongly bonded interface, these targets failed during bombardments with uranium ions.

Molecular plating, or electrodeposition, has long been used for the preparation of thin sources for alpha- and beta-counting [Par64,Par64a,Get65,Get69]. Usually this is done via application of a high voltage across an organic solution of the material of interest. Metal ions migrate to the negative electrode. The addition of an electrolyte enhances the yield and shortens the necessary plating time. Quantitative plating can be accomplished in less than 30 minutes in most cases.

When making targets, however, other considerations predominate [Aum74, Mul75,Bar65]. With thin sources the build up of crystalline material and the loss of adhesion of the material to the substrate are not very important effects. When working with mass, the most uniform deposits are produced by plating the target material at a low current density (approximately 2 to 6 mA/cm²). Adhesion of the target material to the substrate is highest if layers of less than 100 $\mu\text{g}/\text{cm}^2$ thickness are plated, followed by heating to convert the material to the oxide before plating another layer. Layers plate more evenly if the solution is gently agitated to give it more uniformity.

The targets used in the following experiments with ¹⁸O ions were produced by molecular plating. Figure 2a shows a diagram of the apparatus. The target substrate is centered under the glass chimney and the assembly is fastened together with the clamping ring. Rubber pads under the screw heads insure that the glass chimney is not stressed. The base of the chimney defines the target spot. The plating solution is placed in the chimney and the platinum spiral is lowered into the solution. The spacing between the spiral and the substrate

should be about 5 to 8 mm, independent of the diameter of the target spot, and the spiral should cover the entire area of the chimney to give a uniform current density. The platinum spiral is suspended from a speaker assembly by which agitation of the solution is accomplished. It is given a positive potential relative to the substrate; the magnitude of the potential varies with the diameter of the target spot and the conductivity of the solution, but more than 150 V should be used. The potential is stepped up at 12 to 15 minute intervals for approximately three-quarters of an hour, after which the solution is decanted into a waste bottle and the target is rinsed with isopropanol before being placed in an oven at 300°C. A heating time of an hour is sufficient to convert the curium salt to the oxide, after which another layer can be plated. The plating efficiency for each layer is greater than 80%.

The curium used in these targets was obtained from the Oak Ridge National Laboratory where it was isolated as the decay product of mixed californium isotopes. As a result, it is 3% by weight ^{248}Cm . The curium used in the molecular plated targets came in the form of the dry chloride salt. The stock solution of curium nitrate is formed by repeatedly dissolving the dry curium material in 8M nitric acid and evaporating it to dryness at 90°C. After several such treatments, the residue is dissolved in water and evaporated to a damp deposit which is picked up in isopropanol. A convenient concentration is about 1 mg/ml. Small aliquots of this solution are added to the isopropanol in the chimney of the plating cell to make the plating solution. Curium obtained from Oak Ridge contains substantial amounts of iron [Fde81] and light transition metals, and these were present in the resulting targets, coloring the white curium oxide a medium brown color. For experiments with light ions like ^{18}O , involving a chemical separation scheme, these contaminants are not important. For other work [Ghi82], where interfering activities can obscure the activities of interest, the

curium was cleaned by precipitation of curium fluoride, dissolution of the precipitate in nitric acid/boric acid, precipitation of curium hydroxide, dissolution of the hydroxide in hydrochloric acid, running the solution through a saturated hydrochloric acid cation column, and running the resultant curium solution through an anion clean-up column. The curium chloride was converted to the isopropanol stock solution as above.

The targets produced by this method are very uniform, as can be seen from the alpha spectra taken at successive times during fabrication of a target, shown in figure 2b. The final material, curium oxide, is very refractory and will stand much higher beam intensities than will the fluoride, comparing the melting points of dysprosium oxide (2340°C) with dysprosium fluoride (1360°C) as surrogate compounds [Wea82]. Curium oxide also has a smaller stoichiometric amount of the anion than curium fluoride, reducing the energy loss in an equivalent amount of curium. Curium which does not plate out on the target can be recovered from waste to be used again, so effectively all of a small amount of curium can be plated out as a target, unlike the spraying and sublimation techniques. Unfortunately, plated targets always contain more contaminants than sublimated targets due to the indiscriminant nature of the plating process. Also, in the baking process the plated curium layer expands at a different rate than the target backing, causing a deformation of the beryllium substrate. This is the factor limiting target thickness in small diameter targets. For a 7 mm diameter target spot the backings begin to fail at a curium thickness of 1 mg/cm^2 . Going to a 9 mm spot it was possible to construct targets of as much as 1.7 mg/cm^2 thickness.

2.2 Target Systems

Many of the cross sections reported here for the production of actinide transfer products are very small, much less than a microbarn. The time

devoted to a particular experiment can be made shorter if the amount of beam delivered to the target can be maximized. Beam intensity is also important in the saturation level of short-lived species which are counted or processed off-line. When nuclides with half lives of a few minutes or less are studied, the speed with which a target or recoil catcher foil can be removed from the beam to the counting area or chemistry laboratory is critical.

The target system used in the irradiations with ^{18}O ions has been reported previously [Lee82,McF82]. Briefly, $^{18}\text{O}^{4+}$ ions were delivered by the Lawrence Berkeley Laboratory's 88-Inch Cyclotron. Five meters upstream from the target system in the High Level Cave, the beam is "wobbled" with the stator of an induction motor, operated at 60 Hz, which moves the beam profile in a small circle, smearing out local inhomogeneities in the heating of the foils. A 1 ampere current in the coils of the wobbler results in a loss of about 10% in beam intensity from the target to the collimator for the ^{18}O beam. A slammer valve [Gou76] at a position 9 meters upstream provides for the integrity of the accelerator: If either of two ion gauges near the target system detect a large increase in pressure, indicating a possible target failure, an explosive charge is ignited, driving a nylon wedge across the beam pipe aperture, making a vacuum seal protecting the cyclotron from contamination. Vacuum is maintained near 2×10^{-4} torr with a turbo pump.

A schematic of the target system itself is shown in figure 2c. The ion beam is collimated to a 6 mm diameter. Secondary electrons are suppressed with a magnet which surrounds the glass insulator. The beam current on the collimator is measured separately from the target-and-Faraday cup current for use in steering and focussing the beam. The beam next passes through a 1.8 mg/cm^2 Havar isolation foil, a volume of cooling nitrogen gas, the target substrate and, finally, the curium target material. The Havar foil and the target are both

clamped in the target holder, which is introduced as a unit into the target system. O-ring connections to the nitrogen supply are made upon proper insertion. Nitrogen gas is introduced in the 3 mm gap between the window and the target through a large orifice and is exhausted to the air, so the pressure of the coolant is a slight over-pressure on 1 atmosphere. The nitrogen comes from a liquid nitrogen dewar, but travels about 20 meters before entering the target system, and is therefore at ambient temperature. Reaction products recoiling from the target between 0° and 60° to the beam direction are caught on a 2 mg/cm^2 gold foil (which is also struck by the beam on its way to the Faraday cup) mounted on a frame, which is cooled by a quasi-stagnant volume of helium gas at a pressure of 90 torr; the energy loss of the beam is low enough in this thin gold and the thermal conductivity of it is high enough that this is the only cooling necessary. The distance between the foil and the target is approximately 5 mm, so no reaction products which escape the target should be lost by pre-stopping in the cooling medium. The Faraday cup and collimator are both water-cooled.

During the irradiation the sum of the Faraday cup and target/window beam currents is measured with a Brookhaven Instruments integrating electrometer. The integral is recorded by hand periodically for reconstructing the beam history. At the end of an irradiation, the chamber containing the catcher foil is vented to air, the top is removed and the catcher foil frame is unclamped, ready for transportation to the chemistry laboratory. It is not necessary to disturb the vacuum on the cyclotron side of the Havar isolation foil, so set-up time for the next irradiation can usually be kept to under five minutes.

The curium oxide target mounted in this system routinely withstood beam currents of a full particle-microampere of ^{18}O . This corresponds to a deposited heat of 25 watts/cm^2 in the 13 micrometer thick beryllium substrate [Hub80].

If the ^{136}Xe beam used in experiment $^{136}\text{Xe-I}$ (see Section 3) were available at this level, the beryllium would be heated at a rate of 400 watts/cm². Strictly speaking, this understates the problem, because the ^{136}Xe beam was produced by the SuperHILAC, which delivers pulses of beam at roughly a 10% duty cycle. To average 1 d.c. particle-microampere, the target would have to hold up under a series of equally-spaced pulses 10 microamperes in intensity for 3 milliseconds each. While the average effect is the same, it is hard to predict what peak temperatures would be reached [Lil73]. Even though SuperHILAC beams are not available in these intensities, it is clear that maximum care must be taken to deal with heat, particularly with the more volatile curium fluoride target used in those experiments.

There are several things about the 88-Inch Cyclotron target system which can be improved upon. The cooling gas is delivered from a large orifice into an atmosphere of pressure. The flow is turbulent rather than laminar, so the gas which has been warmed up in removing heat from the target is effectively used more than once, and spends more time in the path of the beam, which heats it further. The high pressure of the gas would severely degrade the energy of a very heavy ion beam. The target backing must maintain a pressure differential of almost a full atmosphere. The experiments which can be performed with this target system are limited to those which can be mounted on the lid of the recoil catcher chamber. Finally, the target system is exposed, providing no protection against airborne contamination.

These problems and others have been addressed in the construction of the Modular Fast Access Target System at the SuperHILAC [Moo81]. It is located in Cave S, at 0° with respect to the axis of the accelerator. Maximum beam intensity can be obtained in this orientation because all of the charge states produced by the accelerator can reach the target. This generates a problem in

performing an experiment with mono-energetic beams, however, because all tuning must be done with the driving RF gradients and phases in the accelerator.

Due to space limitations, the wobbler and slammer valve are located only 3 meters from the target. Though the average charge-to-mass ratios of the heavy SuperHILAC ions are comparable to that of $^{18}\text{O}^{4+}$, the shorter lever arm requires much higher currents for the wobbler to be effective; usually 3 to 4 amperes are required to smear 10% of the unwobbled beam onto the collimator. The proximity of the slammer valve to the target system requires an expansion volume to "hold-up" the pressure wave coming from a burst beam window to give the valve time to close. This is provided with a 60 centimeter diameter scattering chamber between the valve and the target system. The slammer valve at the SuperHILAC is of a similar design to that of the 88-Inch Cyclotron, except that two explosive charges are used to drive the larger nylon wedge required by the larger diameter beam pipes of the SuperHILAC. This slammer valve is triggered by a rate of pressure rise detected by either of two ion gauges near the target, and is not operational at pressures of more than 10^{-4} torr; at higher pressures the rate of rise is less sensitive. If a slow rise in pressure takes either ion gauge past 10^{-4} torr, a standard vacuum valve closes which disarms the slammer valve. An ion gauge closer to the accelerator also triggers the vacuum valve, protecting the target system from the vacuum accidents of other experimenters. The time from first detection of a sudden pressure rise to complete isolation of the SuperHILAC from the target with the slammer valve is 3 to 4 milliseconds. The slammer valve was tested by manually pushing a helium jet through a Havar isolation foil maintaining vacuum on one side. The slammer valve provided a complete seal of the beam pipe before any helium could migrate to the valve, because none was detected further upstream with a port-

able helium leak detector. The vacuum valve between the accelerator and the target system cannot be opened unless the slammer valve is operational, or unless a bypass key is turned in the SuperHILAC control room.

Vacuum is maintained in the beam line with a 15 centimeter diameter diffusion pump located between the scattering chamber and the target system. The usual operating pressure near the isolation foil is 1×10^{-5} torr. Also at this location is a beam stop/Faraday cup and a fluorescent paddle/video camera, both of which are inserted into or removed from the beam remotely and are used as steering aids in the control room. These devices must be thoroughly exercised before each run to remove trapped air from the Wilson seals, preventing accidental slammer valve firings. Just ahead of the target system is a final isolation valve which operates only manually.

Quite often it is necessary to perform more than one type of experiment during a given assignment of beam time. When incompatible targets have to be scheduled back-to-back, the speed with which one target system can be broken down and the next one put up determines the amount of accelerator time wasted in a change-over. The SuperHILAC target system is modular, and it can be dismantled, re-arranged, re-assembled and pumped down to operating pressure in well under an hour. Figure 2d [Tho79] shows the system for irradiating thick targets. The beam enters the target system from the left and is collimated to the required diameter with a graphite collimator which is clamped to the water-cooled collimator housing. Beam current striking the collimator can be measured separately from the target current for use as a steering and focussing aid. The collimator housing is bolted to a grounded flange between two teflon spacers. The bolts have an all-around clearance of 1.5 millimeters in the holes of the collimator housing, maintained by the two pins on the front and back of this piece, which mate with matching holes in the teflon spacers. This

maintains the electrical isolation of the collimator. The bolt-holes in the front teflon spacer are counter-bored so that the tops of the bolt heads are below the outer surface of the teflon. The arrangement shown in figure 2d is for the irradiation of targets which are too fragile or water-sensitive to be directly water cooled. Water is pumped through the small reservoir in the end piece at the rate of approximately ten liters per minute. An aluminum plate takes the brunt of the force of the water. The target is held firmly in place against this plate by a magnet for the suppression of secondary electrons, which in turn is held in place by the target clamp. The target clamp is screwed down to the end piece, holding the whole assembly rigid and supplying enough pressure to make an O-ring seal between the aluminum plate and the reservoir. For more durable targets, if the maximum cooling is desired, the aluminum plate can be left out and the target itself is then used to seal the reservoir. The end piece is lifted and pressed against the O-ring in the outer teflon spacer; a clockwise twist locks the wings in place under the restraining bolts, making a vacuum seal. The target system is rough-pumped with a rotary oil pump and then opened to the beam line via the manual isolation valve. During an irradiation the target beam current is measured independently due to the electrical isolation of the end piece. At the end of an irradiation, the manual valve is closed, the target system is vented to the air, and the end piece is twisted off the outer teflon spacer. The target is removed by unscrewing the target clamp.

A schematic of the system used in the experiments reported here with thin curium targets is shown in figure 2e. As before, the collimator system is electrically isolated between two teflon spacers. This unit of the system is bolted to the grounding flange with recessed bolts as before. The independent collimator current is used, once again, as a steering and focussing aid. The next large piece of the system is the gas cooling jacket. The gas which cools the target

must be isolated from the machine vacuum, so a thin window is introduced which must also be cooled. Nitrogen gas is delivered to the cooling jacket at the rate of about half a liter at STP per second from a liquid nitrogen dewar on the roof of the cave. The nitrogen travels through about 10 meters of copper tubing between the dewar and the target system. This is approximately the minimum length with 7 mm diameter tubing to prevent pressure surges in the delivery line. The gas is approximately equally divided between two jets, one of which cools the target and the other which cools the window. The gas is maintained at a pressure of approximately 150 torr between the window and the target with a constantly operating high volume rotary oil pump. The target must stand up to only the mechanical pressure of the jet, because the pressure on both sides is equilibrated by a large communicating passage. The jets are designed with a tapered nozzle to allow for the supersonic expansion of the gas into the partially evacuated volume, giving a cold, low turbulence flow.

For the experiments reported here, the beam window/isolation foil used was 1.8 mg/cm² Havar (2.1 micrometer). Windows are constructed by applying a thin, uniform layer of quick-drying epoxy to a frame, which is pressed down on a sheet of the alloy which has been checked for pinholes. The Havar is cut around the edge of the frame, and the frame is screwed to the window holder, making an O-ring seal. The window diameter is 1 centimeter, and the thin Havar can maintain a pressure of less than 10⁻⁵ torr against a full atmosphere of pressure at this diameter. The window holder bolts to the back of the gas cooling jacket, again sealing against O-rings (not shown). A magnet for secondary electron suppression is fastened around the window opening. The back of the window holder seals to the O-ring in the second teflon spacer. The target is set in a depression in the target clamp, which limits the outer edge of the substrate to a 1.3 centimeter diameter. The target clamp is bolted to the target holder

from the downstream side using recessed bolts, and the target holder bolts to the gas cooling jacket as shown.

The cooling jacket is fastened on top of the second teflon spacer with bolts originating in a third, outer one. This outer spacer holds the restraining bolts that clamp the end piece. As before, there is an all-around clearance of 1.5 millimeters between the bolt shafts and the gas cooling jacket and collimator housing, the rotational orientation being maintained with pins. The cooling jacket is electrically isolated from both the collimator housing and the grounding flange. The charge deposited in the window and target is combined with that deposited in the beam stop to give the beam intensity. The target can be mounted or dismounted without dis-assembling the rest of the target system.

The choice of nitrogen as a cooling gas is a compromise between the best cooling and the cheapest cooling. It has been shown [Nit76] that cold helium and hydrogen are the "best" cooling gases, but their cost requires the implementation of a gas recirculating, purifying and cooling system. Nitrogen is inexpensive and, when taken from the liquid in a dewar, it is cold and reasonably clean. It is used once and then exhausted to air. The liquid in a standard 160 liter dewar is sufficient for a 20 to 30 hour irradiation.

Figure 2f shows a close up of the end piece used in the experiments reported here. As before, this assembly hangs on the end of the target system against an O-ring when in use. Recoiling reaction products at wide angles to the beam direction are caught on a truncated conical catcher foil of 50 mg/cm² gold which is not struck by the majority of the beam particles. This eliminates cooling problems and simplifies the chemistry. The beam is deposited in the thin nickel or tantalum beam stop, which is water cooled. The catcher foil is stuck to the foil holder with a small piece of double-sided tape. For an analysis of the laboratory angles covered by the catcher foil, see Section 3. Both sides

of the window are rough-pumped, the accelerator side is valved off then opened to the beam line vacuum with the manual isolation valve, then the roughing pump is used to draw the nitrogen cooling gas through the rest of the system. Beam current is measured during the experiment with a Brookhaven Instruments integrating electrometer, with the scaler integral being recorded by hand periodically. At the end of an irradiation the target system is manually isolated with the vacuum valve, the gas flow and pumping are interrupted, and the system is vented to air. The end piece is removed and the catcher foil is immediately available. The time necessary to remove a catcher foil after the end of an irradiation is typically under one minute.

For beam energy measurements, to be discussed in section 3, the end piece was replaced with the one depicted in figure 2g. The surface barrier detectors are made by ORTEC and have a 100 mm^2 active area. The amount of beam which these "crystals" can tolerate is measured in particles per second, so the SuperHILAC beam has to be attenuated before an energy measurement can be performed; this is accomplished by inserting a series of wire mesh screens into the beam path before the ions are accelerated by the Alvarez tanks. The surface barrier detectors are operated at +75 V. The signal from the detector is picked up by a preamplifier which hangs from the end piece, minimizing the noise in the signal by minimizing the distance it has to travel. The preamplifier output is picked up by a linear amplifier, which outputs to an analog-to-digital converter. The energy spectra were obtained from a pulse height analysis stored in a 1024 channel multichannel analyzer. To take the measurements, the target system is built up piece by piece, starting with nothing between the accelerator and the surface barrier detector. The detected pulse height, corrected for the pulse height defect (see Section 3), is calibrated against a dual pulser to give a measure of the energy of the beam particles.

The Modular Fast Access Target System can be used in other ways than those outlined above. All forward-recoiling reaction products, including those at 0° to the beam direction, can be caught on a gas cooled catcher foil as shown in figure 2h. With ions like ^{136}Xe , stopping the recoils requires too great a thickness of catcher foil to be adequately cooled by the gas jet at high beam intensities, but this configuration was recently used successfully in a search for superheavy elements with ^{48}Ca ions [Gag83]. If a different gas than the one between the window and the target is used to cool the catcher foil, the area which allows the gas to reach both sides of the target can be plugged, which makes the independent pumping of both sides of the target a necessity. In another configuration, as yet untried, forward-peaking recoil ranges can be determined using up to ten thin foils, each of which has its own cooling jet. The whole arrangement fits in a rectangular rack which clamps against the beam stop.

Since both SuperHILAC time and ^{248}Cm targets are valuable commodities, several devices have been installed to continuously monitor parameters vital to the safety of the target. The beam stop water supply is a closed system containing only three liters of distilled water; the pressure of the water leaving the cooling/circulating system closes a pressure switch which opens if the pump shuts off. The temperature difference between the incoming and outgoing beam stop fluid is monitored with a thermocouple which registers on a chart recorder with a trip level contact built in. The light emission from the recoil chamber is similarly monitored with a photodiode which sees both target emission and fluorescence of the cooling gas through a window in the end piece; if some part of the lateral beam profile becomes too intense, even if the average intensity over the target as a whole remains unchanged, the light emission jumps, actuating a trip level. The current in the coils of the wobbler is sampled to make sure

the wobbler is running with more than one ampere of current. Finally, the pressure of the cooling gas is monitored relative to the beam line vacuum with a differential pressure meter. The signals from each of these devices are sent to a central relaying point. If any of them shows a value outside of the permissible bounds, a signal is sent to the SuperHILAC control room which turns off the magnet which bends the beam from the injector into the Alvarez tanks. This interrupt condition is maintained until the situation is remedied and the alarm system is reset by hand. Each device in this system is checked out before each experiment involving an actinide target.

The grounding flange to which the target system is bolted is incorporated in the back wall of a glove box which encloses the target system. The extra time needed to enter the gloves and then do a careful pass-out of the irradiated foil is usually under 30 seconds. Any airborne contaminants are contained in the negative pressure atmosphere of the box, which exhausts through a filter system.

The Modular Fast Access Target System has been thoroughly tested in the configuration shown in figure 2e. The typical running conditions are outlined above. The collimator diameter was always 6 mm in these experiments. Preliminary tests were performed using dummy targets of 13 micrometer thick beryllium and 5 micrometer thick titanium. The first test was with 36 pulses per second of 3.5 milliseconds duration of $144 \text{ MeV } ^{20}\text{Ne}^{7+}$. No problems occurred up to the maximum available beam current, which was an average 5 electrical microamperes. Even though thermal equilibrium is generally reached in less than 200 milliseconds [Lil73] both targets were irradiated for 30 minutes. In the second test, an intense beam of 2 pulses per second of 2.5 millisecond duration of $100 \text{ MeV } ^{12}\text{C}^{6+}$ was used. With the beryllium target in place, the system withstood instantaneous intensities of 80 electrical microamperes for approxi-

mately 10 minutes. The window and target were intact, but the 0.25 mm thick gold beam stop had been drilled through. The test ended when the water introduced into the cooling gas cavity tripped the differential pressure meter. The third test was performed with 36 pulses per second of 1150 MeV $^{136}\text{Xe}^{29+}$, probably at a 3 to 4 millisecond pulse width. No problems occurred in 30 minutes of running with an average beam current of 1.5 electrical microamperes with the beryllium target in place. With the titanium foil, however, combustion of the target in the cooling gas was initiated at a beam current of 1.2 microamperes; at this point the peak temperatures reached the ignition point of titanium in nitrogen with a small amount of oxygen contaminant.

In the experiments performed for this work, the $^{136}\text{Xe}^{29+}$ and $^{86}\text{Kr}^{22+}$ beam intensities were limited to 1 electrical microampere on the thick $^{248}\text{CmF}_3$ target.

2.3 Chemical Separations (Cerium Wars)

Five different chemical separations were performed in the experiments reported here. The chemistry for ^{136}Xe and ^{86}Kr runs was designed to generate the maximum number of transfer cross sections from a single irradiation. The chemistry used in ^{18}O irradiations was an abbreviated chemistry aimed at isolating only near- and below-target gamma ray emitting nuclides, since the above-target alpha emitters have been studied previously [Lee82, Lee83]. The other three chemistries were designed to quickly isolate the single elements berkelium, americium and plutonium, free from contaminants. Except where otherwise noted, the procedures are modifications of those found in compilations of standard radiochemical methods [Gri62, Pen60, Hig60, Bur74, Col65].

The chemistry used in SuperHILAC runs is outlined in figure 2i. As with most chemistries which are aimed at the separation of a large variety of products of various half lives, a compromise must be made between the speed with which a sample can be prepared and the purity and yield obtained with a given

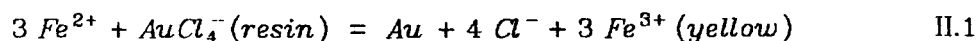
procedure. The catcher foil used in SuperHILAC experiments is gold, with a mass of about 150 mg. After irradiation, the foil is placed in a warm 15 ml centrifuge cone containing 0.25 ml of fuming nitric acid and roughly 10^3 alpha disintegrations per minute each of ^{241}Am , ^{237}Np , ^{238}Pu and ^{236}U , for determination of chemical yields. To this mixture is added approximately 0.4 ml of concentrated hydrochloric acid to dissolve the gold foil containing the recoil products. When the reaction begins to slow, additional hydrochloric acid is added to give a total volume of 1.0 ml. This results in a gold solution of minimum volume in which the effective acidity is approximately 6 molar. This solution is loaded on a 3 mm diameter column packed with 12 cm of Dowex 1x8 -400 mesh anion resin in 9M hydrochloric acid. The eluant is forced from the column with dry nitrogen and collected in a 15 ml centrifuge cone. The original sample cone is washed with small portions of 9M hydrochloric acid, which are added to the top of the column and forced through, then the column is washed directly with 9M hydrochloric acid. The total volume of combined eluant collected from this column is roughly 3 ml.

This step in the chemistry separates the transplutonium actinides from some of the lighter actinides. The tripositive transplutonium elements elute from the column, which binds the gold and uranium, neptunium and plutonium. In the $^{136}\text{Xe-0}$, $^{136}\text{Xe-I}$ and $^{86}\text{Kr-I}$ experiments, concentrated hydrochloric acid was used as an eluant and protactinium isotopes also bonded to the anion resin in the column, but this increased the contamination of the final samples so protactinium yields were sacrificed in the later experiments. It would have been more convenient to have developed a chemistry in which the mass of gold was removed before the anion column with an ether or ethyl acetate solvent extraction followed by boiling to remove the solvent from the aqueous phase. Then only a small anion column and small eluant volumes would have been required.

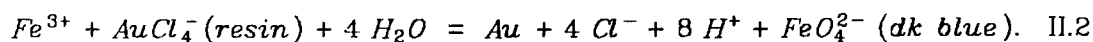
The purpose of running the large column procedure is to reproducibly collect more than 95% of the transplutonium elements, determined from more than fifty runs with ^{241}Am tracer. Since tracer nuclides are not readily available for the higher actinides, a chemistry consisting of steps which are absolutely reproducible must be used. The precolumn step of extraction with ether does not consistently leave 100% of the activity in the aqueous phase due to difficulties in separating the phases in the presence of high gold concentrations, and ethyl acetate is worse due to the hydrolysis of the ester. The distribution coefficients of uranium, neptunium and plutonium on anion resin in 9M hydrochloric acid are between 10 and 10^8 and the column sites are roughly 80% occupied by the mass of gold, so a significant fraction of each of these elements is sacrificed at this point since they slowly dribble off the column with the tail of the higher actinides.

At this point the chemistry branches and requires a second person to isolate and prepare alpha sources of the trans-berkelium elements while the first person prepares uranium, neptunium and plutonium for gamma ray detection. The large anion column presents an interesting problem: The gold is permanently attached to the anion resin, so the activities of interest must be eluted from the column in the presence of gold. The usual ways of removing these light actinide elements from anion resin involve either complexation with fluoride ions or reduction to a lower oxidation state with a lower distribution coefficient. Unfortunately, in this case if fluoride ions are added they are immediately consumed by complexation with gold, and if a reducing agent is added, the gold tends to reduce to an impenetrable plug of gold metal. Reducing the acidity of the column allows some of the lower actinides to leach off, but yields are very poor. The reagent which solves the problem is ferrous chloride. Gold is reduced only very slowly to the metal [Eme61] so it is possible to main-

tain the column solvent flow. After conversion of the gold is mostly complete, fluoride complexation can be used to strip the remaining actinides from the column. So, after the 9M hydrochloric acid step, activity is eluted with 1.5 ml of 3M hydrochloric acid, followed by 1.5 ml of water, added in small amounts, to minimize the acidity in the column. A 2 ml aliquot of freshly prepared ferrous chloride solution is run through the column, followed by 1 ml of water to remove the iron. It is important to run all the ferrous solution through the column at one time, because the resin bed has a tendency to crack if the pressure is released before the bulk of the gold has been reduced. The light green ferrous solution leaves the column as a dark green to black solution which is effervescent. From this evidence it can be deduced that the reactions occurring are



and



Reaction II.2 does not occur in the absence of the strongly basic anion resin or at acid concentrations far above neutral. In acidic solution ferrate ions are unstable, reacting with water to evolve oxygen [Cot80]. If allowed to sit for several hours the eluant converts entirely to the yellow ferric form.

To the combined eluant from this column is added an aliquot of lanthanum chloride carrier containing 1.5 mg of lanthanum. After thorough mixing of the eluant, the centrifuge cone is once again placed under the column to collect 2.5 ml of a solution 0.1M in hydrochloric acid and 1.0M in hydrofluoric acid. This completes the strip of the large anion column. To the eluant is added 0.2 ml of concentrated hydrofluoric acid. After mixing, the solution is heated in boiling water for several minutes, cooled in ice for several minutes, then centrifuged. A precipitate of lanthanum fluoride forms, carrying neptunium and plutonium.

The bulk of the uranium stays in solution as UO_2^{2+} , which is transferred to a 40 ml plastic centrifuge cone. The precipitate is washed once with an aliquot of 2M hydrochloric acid/2M hydrofluoric acid, and the wash solution is added to the uranium solution in the plastic cone.

The lanthanum fluoride precipitate is dissolved in minimum equal volumes of saturated boric acid and fuming nitric acid. Heat is usually necessary. This solution is loaded onto a 2 mm diameter column packed with 7 cm of Dowex 1 anion resin in 8M nitric acid. The column is run at more than atmospheric pressure with nitrogen. The column is washed with five column volumes of 8M nitric acid, followed by two column volumes of 9M hydrochloric acid to remove the nitric acid. Plutonium is eluted from the column with a freshly prepared solution of 1 part hydriodic acid to 10 parts concentrated hydrochloric acid. This reduces plutonium to the 3+ oxidation state which is not sorbed onto the anion exchange resin. A small portion of 9M hydrochloric acid is used to rid the column of iodide ion, then neptunium is eluted with a solution 4M in hydrochloric acid and 0.1M in hydrofluoric acid. If concentrated (12M) hydrochloric acid is used in this procedure routinely in place of 9M hydrochloric acid, protactinium elutes from the column with neptunium.

The solution in the centrifuge cone containing uranium is boiled after the addition of excess boric acid to complex the fluoride. Enough 10M sodium hydroxide is added to precipitate ferric hydroxide, which carries uranium, though poorly. The precipitate is first washed with sodium hydroxide, and then dissolved in nitric acid. This solution is saturated with ammonium nitrate, and uranium is extracted into diethyl ether.

All sources for counting are prepared by evaporating to dryness the solutions containing the activities on hot platinum disks which are then flamed.

While the light actinides are being isolated, the first eluant solution

containing the tripositive transplutonium elements is evaporated to dryness and the activity taken up in a few drops of 0.5M hydrochloric acid and loaded onto a 2 mm diameter, 5 cm long column of Benson BC-x12, 7-10 micron cation resin. The following procedure is not complicated, but the conditions under which it is performed must be carefully controlled. The column must be uniformly heated to 80°C. After the column is loaded with the activity, it is rinsed with water, then buffered with ammonium chloride, then rinsed with water again. The actinides (and lanthanides) are differentially eluted in reverse order (highest Z first) with a 0.5M solution of alpha-hydroxyisobutyric acid, buffered with ammonia to a pH of 3.71. The pH is selected to give the best separation of mendelevium, fermium, einsteinium and californium. If the pH is increased, these elements come off more quickly with little or no resolution. The alpha-hydroxyisobutyrate makes a complex with the 3+ actinides (and lanthanides) of varying strength depending on the size of the ion, the degree of protonation of the ligand, the degree of hydration of the ion and the kinetics (temperature). The best separation of the elution peaks of activity is obtained with a low flow rate, on the order of 3 drops per minute from a 0.7 millimeter outer-diameter platinum tip. The drops are collected on platinum disks, two drops per disk, and heated to dryness. The disks are quickly surveyed for alpha activity with an open window gas proportional counter. The position of the peak of activity from each element is very nearly the same from experiment to experiment, so in runs where little activity was observable the positions of the heaviest elements were extrapolated from the position of the californium peak, which is the last element eluted from the column, generally with peak activity near drop 35. Activity from the neighboring platinum disks is quantitatively transferred to the disk with the greatest activity for that element. The four final disks are flamed to make good alpha sources of californium, einsteinium, fermium and men-

delevium.

In principle, continued elution of activity from the column at pH 3.71 with alpha-hydroxyisobutyric acid will result in a berkelium fraction, but the width of the peak in the elution curve makes it difficult to reproducibly obtain the same chemical yield. The only losses in the chemistry are due to transfers of the activity from one place to the next for fractions from californium through mendelevium. Berkelium, curium and americium are stripped from the column with pH 4.2 alpha-hydroxyisobutyrate, which provides very little separation of these elements. The eluant is reduced in volume by heating the sample cone in oil under a nitrogen stream, then the alpha-hydroxyisobutyrate is broken down with addition of concentrated nitric and hydrochloric acids. The resultant nearly-weightless residue is picked up in two drops of 3M hydrochloric acid and loaded on a 2 mm diameter, 6 cm long AG MP50 cation column in saturated (13M) hydrochloric acid. The empty sample cone is washed with two drops of 13M hydrochloric acid which are then also loaded onto the column. The actinides are eluted from the cation column before the lanthanides with saturated hydrochloric acid. This is a particularly important step in ^{136}Xe irradiations because of the huge amounts of cerium and lanthanum arising from compound nuclear reactions with the beryllium target substrate. Once again, the sample is evaporated to dryness on hot platinum and flamed. The chemical yield for americium determined from the tracer is assumed to be the same as for curium and berkelium, though the existence of the accessible 4+ oxidation state for berkelium may make this estimate a few percent too high for the Bk isotopes.

Typical chemical yields for this procedure are: 75% to 80% for californium, einsteinium, fermium and mendelevium; 50% to 70% for americium, curium and berkelium; 25% to 35% for plutonium; 30% to 40% for neptunium; 15% to 20% for

protactinium (under the modifications noted above); 10% for uranium. Yields are determined by direct comparison against a standard aliquot, except in the case of the heavy actinides where the yield is assumed based on numerous trials with californium and einsteinium tracer activities. Americium yields are determined from the 60 keV gamma ray of ^{241}Am , neptunium yields from the 86 keV gamma ray of ^{237}Np , and protactinium yields from the 312 keV gamma ray of 27-day ^{233}Pa , which is in equilibrium with the ^{237}Np tracer. Plutonium and uranium yields are determined from the alpha activity of ^{238}Pu and ^{236}U respectively. In each of these cases enough of the tracer activity was added to make the amount produced in the reaction a negligible perturbation.

In most cases contaminating activities are not a severe problem. The californium, einsteinium, fermium and mendelevium fractions contain rare earth gamma ray emitters which do not affect the alpha particle and spontaneous fission counting which is performed on these samples. The terbium and dysprosium alpha emitters elute from the alpha-hydroxyisobutyrate column with californium and einsteinium respectively, but the alpha particle energies are so low that they do not interfere with the pulse-height analysed data; they do, however, tend to lead to some confusion during the chemistry when the drops of eluant are assayed to define the activity elution positions. The mendelevium fraction always contains small amounts of thorium (less than 10 counts per day), which could be removed with an 8M nitric acid anion column, but the added time makes it an inadvisable step when looking for the short-lived mendelevium isotopes. No mendelevium activity was positively identified in these experiments. The americium/curium/berkelium sample sometimes contains cerium and sodium activities. The uranium fraction frequently contains a small amount of hafnium. The contamination of the plutonium sample with cerium isotopes, particularly in irradiations with ^{136}Xe , is severe; the critical step is the

nitric acid wash of the small anion column. The neptunium fraction, besides containing protactinium, is prone to zirconium contamination; this is acute in ^{86}Kr irradiations where zirconium is the compound nucleus in reactions with the target backing.

Typical time intervals between the end of an irradiation to the start of data acquisition for the chemical fractions are: 2 hours for plutonium and neptunium, 2.5 hours for californium, einsteinium, fermium and mendelevium, 4 hours for americium/curium/berkelium, and 5 hours for uranium. Figure 2j shows some typical pulse height spectra from experiment $^{86}\text{Kr-I}$.

The chemistry for ^{18}O experiments is diagrammed in figure 2k. It is simpler than that for ^{136}Xe and ^{86}Kr experiments for two reasons: The heavy actinides were not determined, so the procedure could start with a solvent extraction and use much smaller columns; and the amount of interfering activities produced by ^{18}O is much less than that produced by heavier ions.

The catcher foil used in these experiments is gold, 2 mg/cm^2 thick, with a mass of about 8 to 10 mg total. After irradiation the foil is placed in a 15 ml centrifuge cone containing about 10^3 disintegrations per minute each of ^{241}Am , ^{238}Pu and ^{237}Np , and 20 microliters of fuming nitric acid. The cone is placed in hot water and an aliquot of 50 microliters of concentrated hydrochloric acid is added to dissolve the gold foil. After dissolution, water is added to dilute the volume to roughly 0.2 ml and the cone is cooled in ice. Gold is extracted from the aqueous phase with 1 ml of diethyl ether, after which the aqueous solution is heated in a hot water bath under a nitrogen jet for five minutes to drive off residual ether. The solution is then loaded on a 2 mm diameter column, 6 cm long of Dowex 1x8 anion resin in 8M nitric acid. Plutonium, neptunium, uranium and protactinium adhere to the resin and the tripositive transplutonium elements do not. The sample cone is washed onto the column in 8M

nitric acid and three column volumes of 8M nitric acid are used to complete the elution. The sample cone containing eluant is placed in hot oil under a nitrogen stream and heated until dry.

The anion resin in the column is converted to the chloride form with 9M hydrochloric acid, then plutonium is eluted with a freshly prepared solution of 1 part concentrated hydriodic acid to 10 parts concentrated hydrochloric acid. Once again, the column is washed with 9M hydrochloric acid, then neptunium and protactinium are eluted with a solution 4M in hydrochloric acid and 0.1M in hydrofluoric acid. The plutonium fraction is evaporated to dryness on a hot platinum disk, then flamed. To the neptunium/protactinium fraction is added 1.5 mg of lanthanum carrier and 5 drops of concentrated hydrofluoric acid. The mixture is agitated, then heated for five minutes, then cooled in ice. The lanthanum fluoride precipitate carrying neptunium and protactinium is filtered out on a 3 micron thick nitrocellulose filter, which is then washed with a solution 2M in hydrochloric acid and 2M in hydrofluoric acid.

The transplutonium elements are picked up in one drop of 3M hydrochloric acid, then loaded on a 2 mm diameter, 5 cm long AG MP50 cation column in 13M hydrochloric acid. The sample cone is washed onto the column with one drop of 13M hydrochloric acid, then the actinides are eluted with 13M hydrochloric acid before the lanthanides, which remain on the column. The eluant is diluted with water by a factor of four, then 1.5 mg of lanthanum carrier is added. The addition of hydrofluoric acid, followed by mixing, heating and cooling as before, forms a precipitate of lanthanum fluoride which carries the actinides. The precipitate is filtered on a 3 micron thick nitrocellulose filter and washed with 2M hydrochloric acid/2M hydrofluoric acid. Due to their similar chemistries, the yield of all the transplutonium actinides is assumed to be the same as that of americium.

Typical chemical yields for this chemistry are: 80% to 90% for transplutonium elements; 80% to 90% for plutonium; 60% to 80% for neptunium; and 30% to 50% for protactinium. The determination of chemical yields is the same as for the longer chemistry described above. The transplutonium fraction and the neptunium/protactinium fraction are essentially without contamination. The plutonium fraction, however, tends to contain significant levels of ruthenium. Typical time intervals from the end of bombardment to the start of data acquisition are 30 to 60 minutes for the plutonium and neptunium/protactinium fractions and 60 to 90 minutes for the transplutonium sample.

In attempts to observe ^{247}Pu , discussed in Section 6, it was necessary to isolate plutonium in the minimum possible time in the maximum state of decontamination from other activities, particularly americium and cerium. The best way to purify plutonium on a tracer scale involves oxidation-reduction cycles utilizing the 6+ and 4+ states, but the conversion of 4+ plutonium to plutonyl ions is very slow, taking on the order of half an hour to come to completion; this step was not incorporated in the chemistry.

Catcher foils used in fast plutonium chemistry experiments are nickel, of varying thicknesses depending on the projectile. The foil is placed in a 15 ml centrifuge cone containing 10^8 dpm each of ^{238}Pu , ^{241}Am and ^{144}Ce tracers, 1.5 mg of lanthanum carrier, and 0.8 ml of 14M nitric acid. Ice is necessary to moderate the violent reaction. After completion of the dissolution, the cone is placed in boiling water and approximately 3 ml of water and 0.3 ml of concentrated hydrofluoric acid are added. When the lanthanum fluoride precipitate has formed, the cone is quickly cooled in ice made by freezing water in liquid nitrogen. The cone is centrifuged, the supernate is discarded, and the precipitate is washed with a cold solution 2M in hydrochloric acid and 2M in hydrofluoric acid. The lanthanum fluoride, which contains the plutonium (and

americium), is dissolved in 75 microliters of hot saturated boric acid and 75 microliters of fuming nitric acid. The resultant solution is loaded on a short 2 mm diameter column of Dowex 1x8 anion resin in 8M nitric acid. The sample cone is washed onto the column with 8M nitric acid, then the column is washed with a large volume of 8M nitric acid, followed by two column volumes of 9M hydrochloric acid to convert the resin in the column to the chloride form before plutonium is eluted with a solution of 1 part concentrated hydriodic acid to 10 parts concentrated hydrochloric acid. The eluant is evaporated on a hot platinum disk and flamed to produce the final sample.

The typical chemical yield from this procedure is 40% to 60% for plutonium. The yield of 3+ actinides is always less than 0.1%, so the decontamination of plutonium from its americium beta-decay daughters is very good. No other contaminants are observed except cerium, which seems to come through the procedure with a variable yield between 0.1% and 1%. In experiments with 180 ions this was not a problem, since the cerium isotopes are not important reaction products. In experiments with ^{86}Kr and ^{136}Xe ions, it was impossible to routinely get rid of all cerium activity on this time scale. The total time from the end of irradiation to the start of data acquisition, including transportation time from the accelerator to the chemistry laboratory, is between 22 and 30 minutes, based on more than twenty experiments. The chemistry could probably be performed five minutes faster if done by more than one person. The time when plutonium is completely free from its americium daughters is at the end of the 9M hydrochloric acid wash of the anion column.

The chemical procedure used to isolate the most neutron-rich known americium isotopes, whose cross sections are reported here [Wei82], is based on the oxidation of americium to the hexavalent state [Moo63, Hol64]. This oxidation is more difficult than the plutonium oxidation mentioned above, and chemi-

cal yield is limited by the amount of time available. However, alternate methods of separating americium from the other 3+ lanthanides and actinides are very time consuming, involving the use of finicky differential elution methods.

The catcher foil in experiments involving hexavalent americium is aluminum, which is dissolved in a 15 ml centrifuge cone containing 10^3 dpm of ^{241}Am tracer and several milliliters of 10M sodium hydroxide. The addition of lanthanum carrier precipitates lanthanum hydroxide which carries americium. The supernate, containing the aluminum, is discarded and the precipitate is washed in dilute base. The precipitate is then dissolved in nitric acid and americium is oxidized to americyl ion with hot peroxydisulfate catalyzed by silver ion. The addition of ammonium fluoride causes the precipitation of lanthanum fluoride, carrying all lanthanides and 3+ actinides, including any americium which is unoxidized. If performed with care, this step can be quantitative. The supernatant solution, containing americyl ions, is removed from the precipitate, and manganous nitrate is used to reduce the americium to the 3+ state. Addition of more lanthanum carrier causes the precipitation of lanthanum fluoride once more, this time carrying the americium. The precipitate is filtered and washed on a 3 micron thick nitrocellulose filter, as before.

The chemical yield from this procedure is dependent upon the digestion time in the oxidation to americyl ion. In the usual compromise, the entire chemistry takes about 40 minutes, with the oxidation occupying about 10 minutes of that time. Yields tend to be unpredictable, but can approach 50%. Plutonium follows the americium through this procedure with a higher yield, but since the production rate for plutonium isotopes is lower than that for the short-lived americium isotopes from a ^{248}Cm target, further purification is not performed. The usual contaminants are scandium, yttrium and, of course, cerium, which are incompletely coprecipitated in the first lanthanum fluoride

step, and silver, presumably due to the presence of the small mass of silver catalyst.

The chemistry used for the rapid isolation of a very pure berkelium fraction for the spectroscopic study of the decay of ^{251}Bk , discussed in Section 5, is described in detail elsewhere [Liu83]. It is an adaptation of the procedure used in the first isolation of 7-minute ^{242}Bk [Wil79], but contains additional steps to remove the substantial amounts of cerium, molybdenum and technetium contamination to which that procedure is prone.

The catcher foil used in these experiments, all performed with ^{18}O ions, is 2 mg/cm² gold. The foil is dissolved in a 15 ml centrifuge cone in a minimum volume of hot, concentrated hydrochloric acid and nitric acid. The solution is diluted to approximately 0.5 ml with 7M hydrochloric acid. Several solvent extractions are performed in rapid succession: The mass of gold is extracted with diethyl ether, which also removes several of the reaction products from interactions of the beam with the gold catcher foil, like thallium and mercury, and fission products, like molybdenum and zirconium. A methylisobutyl ketone extraction removes technetium and polonium. A 5% triisooctylamine in xylene solution is used to extract lead, bismuth, palladium and silver contaminants. The aqueous phase, still containing berkelium, is heated to dryness under a nitrogen stream, then taken up in freshly-made hot 0.5M sodium bromate in 4M nitric acid, which oxidizes berkelium to the 4+ state, which is extracted into a 0.15M HDEHP (di-2-ethylhexylorthophosphoric acid) solution in heptane. This step leaves behind the 3+ lanthanides and actinides. The HDEHP solution is scrubbed with 4M nitric acid, then berkelium is reduced back to the 3+ state and back-extracted with a 5% H_2O_2 solution in 4M nitric acid, which leaves niobium and tantalum in the organic phase. The aqueous phase contains only berkelium and the ever-present cerium. The solution is evaporated to dryness

in a hot oil bath, taken up in a minimum volume of 0.5M hydrochloric acid, and loaded on a 2 mm diameter, 4 cm long cation exchange column at 80°C packed with Benson BC-x12, 7-10 micron resin. The column is buffered with ammonium chloride, then berkelium is preferentially eluted from the column with a pH 4.0 0.5M alpha-hydroxyisobutyrate solution. The sample is prepared by evaporation of this solution to dryness on a platinum plate which is then flamed.

Since no adequate berkelium tracer is available, the chemical yield is estimated from the ^{250}Bk activities, the beam histories and the published cross section for the production of ^{250}Bk [Lee82] to average roughly 20%. This procedure was not used in cross section determinations. Most of the yield is lost due to incomplete phase separations in the solvent extraction steps and incomplete oxidation of the berkelium. The berkelium fraction is free from contaminating activities, and the time required for separation is only 30 to 40 minutes.

2.4 Detection of Characteristic Radiations

The determination of how much of a particular nuclide is present at a particular time can be made from its decay rate, the fractional probability of its producing a particular radiation, and the amount of that radiation. Depending upon the nuclide studied, the cross sections reported in this work were determined from the detection of alpha particles, gamma rays and spontaneous fissions. The detection of beta particles, used only in connection with the spectroscopy of ^{251}Bk , is discussed in Section 5.

All gamma ray detection is performed with one of several ORTEC coaxial, lithium-drifted germanium detectors ($\text{Ge}(\text{Li})$), biased at roughly 3500 V. The samples with the lowest high energy gamma activity are measured with detectors with a high active volume, as much as 90 cm^3 . The samples with the most contaminants (usually plutonium) are counted with detectors with the greatest resolution, as high as 1.9 keV FWHM for the 1332.5 keV line of ^{60}Co . Each

detector is shielded with 5 to 10 centimeters of lead to minimize background radioactivity. In most cases, the inside of this lead "cave" is lined with 3 millimeters of steel and 3 millimeters of aluminum to reduce the induced fluorescence of lead, which interferes with measurements below 80 keV. Events which produce ion pairs in the semiconductor result in a pulse of electrons which are collected at the input stage of the preamplifier and output as voltage signals to a linear amplifier. The amplifier output is taken by an ADC (analog-to-digital converter) and subjected to pulse height analysis, which determines the energy of the event supplied to make ion pairs. This value is summed with previous events in an MCA (multichannel analyzer) which periodically stores the 4096 channels of data on floppy disks or magnetic tapes, along with start times, counting intervals and TAG words.

The detector is calibrated with a standard mixed radionuclide source, formerly available from the National Bureau of Standards but now produced by Amersham (source QCD.1). This source contains several long-lived radionuclides which emit one or two gamma rays whose absolute intensities are known. The nuclides are: ^{109}Cd (88 keV), ^{57}Co (122 and 136 keV), ^{139}Ce (166 keV), ^{203}Hg (279 keV), ^{113}Sn (392 keV), ^{85}Sr (514 keV), ^{137}Cs (662 keV), ^{60}Co (1173 and 1332 keV), and ^{88}Y (898 and 1836 keV). The source is assayed and the disintegration rate for each gamma ray is known at a reference time to within roughly $\pm 3\%$. With the known half life of each nuclide, the gamma ray intensity at the time of a measurement can be determined. The source is mounted in the same orientation as an experimental sample and counted for a fixed period of time. Any counting system dead time is compensated for by the ADC. The peaks in the pulse height spectrum are analyzed with the program SAMPO [Rou69], which fits a functional form to the data and integrates the peak over the detector background. Detector efficiency is obtained by calculating the ratio of detector

count rate to source photon rate at each energy and fitting the resultant efficiency-energy points to the function [Rou69]

$$EFFICIENCY = P_1 * (E^{P_2} + P_3 \exp (P_4 E)) \quad II.3$$

where the energy E is in keV and the parameters P are determined. The relative error, determined from the fit, the error on the photon intensities of the source, and the statistical error of the peak integration, is about 3%. Typical detector efficiencies for the detectors used in this work are 8% to 15% for 150 keV photons, decreasing to 0.7% to 1.1% at 1 MeV. The same mixed standard source is used to determine the energy calibration of the detector, which is adjusted so that 1 MCA channel is 0.5 keV. A lower level discriminator is set to reject events below 40 keV.

Samples for gamma counting are prepared either as a small spot on a 2.5 cm diameter 50 mg/cm² platinum plate by evaporation, or as a 1.7 cm diameter spot of precipitate on a 3 micron thick nitrocellulose filter. These samples are covered with Parafilm and taped to a standard aluminum counting card which fits in a slotted rack in front of the end window of the Ge(Li) diode. The activity in all samples is so low that dead time is not a problem, so the samples are placed at a distance of approximately one centimeter from the end window. This minimizes effects from finite source size [Wie76] but maximizes detector efficiency. Scatter of photons by the sample mount has a negligible effect on the source intensity.

Alpha particles and spontaneous fissions are detected with a set of four ORTEC gold-plated silicon surface barrier detectors. The active area of these detectors is 100 mm². The energy resolution of the detection system is approximately 20 keV FWHM for the 5.48 MeV alpha particle of ²⁴¹Am. The bias voltage of 50 to 75 V is provided through each preamplifier from four individual power supplies. Alpha particles and spontaneous fission events in each detector

produce electron pulses which are picked up by the detector's preamplifier, whose output goes in turn to two linear amplifiers. One amplifier from each detector outputs through a linear gate stretcher. The other amplifier discriminates against low energy (alpha) events, sending a signal for events of more than 15 MeV to a single channel analyzer which counts spontaneous fission events. All eight signals enter a router/biased amplifier. The alpha particle events from each detector, tagged by the router are run into an ADC and stored in one of four different groups of 1024 channels in an MCA. Fission events from each detector are stored using the first channel of each group as a scaler. Only alpha events from 5 to 10 MeV are stored. Since only one ADC/MCA/clock combination is used, data acquisition in all four detectors is simultaneous. At the end of preset times, all four groups of 1024 channels of the MCA, each with its own TAG word, are stored on magnetic tape, along with the start time of the count and the time interval. The efficiency of the detector depends only on the geometry of the sample with respect to the active area of the detector. Samples are mounted face downwards on the rim of the vertically placed detectors. For sources with a spot size of less than 5 millimeters diameter, the efficiency is $23 \pm 1 \%$, determined with standard sources. Efficiency for detection of spontaneous fissions is exactly twice as high, since twice as many detectable particles can strike the detector per decay. The energy calibration is accomplished with a source of ^{241}Am , which is used to calibrate a dual pulser input to the detector preamplifier. Count rates are low enough that summing is not a problem; no two alpha particle events sum to 15 MeV, so "accidental" fissions are extremely unlikely.

Alpha particle sources prepared in the experiment are formed from the evaporation of several drops of column eluant to dryness on a 2.5 cm diameter, 50 mg/cm² platinum disk, followed by heating in a Bunsen burner flame to red

heat. Samples are "weightless" to prevent loss of energy resolution due to degradation of the alpha particles in the source, and are less than 5 millimeters in diameter so that the detector efficiency can be accurately applied.

Figure Captions

Figure 2a - Assembly of the cell for electroplating ^{248}Cm targets. The plating solution is held in the glass chimney, whose base defines the diameter of the target spot.

Figure 2b - Successive alpha particle energy spectra measured from a ^{248}Cm target at three different thicknesses. The "square" tops of the energy peaks in the spectrum taken at $340\ \mu\text{g}/\text{cm}^2$ show the uniformity of the target material. At $920\ \mu\text{g}/\text{cm}^2$ the overlap of one peak into the next distorts the effect.

Figure 2c - A cut-away view of the Actinide Recoil System used in ^{18}O irradiations of ^{248}Cm .

Figure 2d - An exploded view of the Modular Fast Access Target System, as used in thick target irradiations.

Figure 2e - An exploded view of the Modular Fast Access Target System, as used for recoil experiments. This was the configuration used in the ^{86}Kr and ^{136}Xe irradiations reported here.

Figure 2f - A close-up of the end piece used to collect actinide recoils in the experiments reported here.

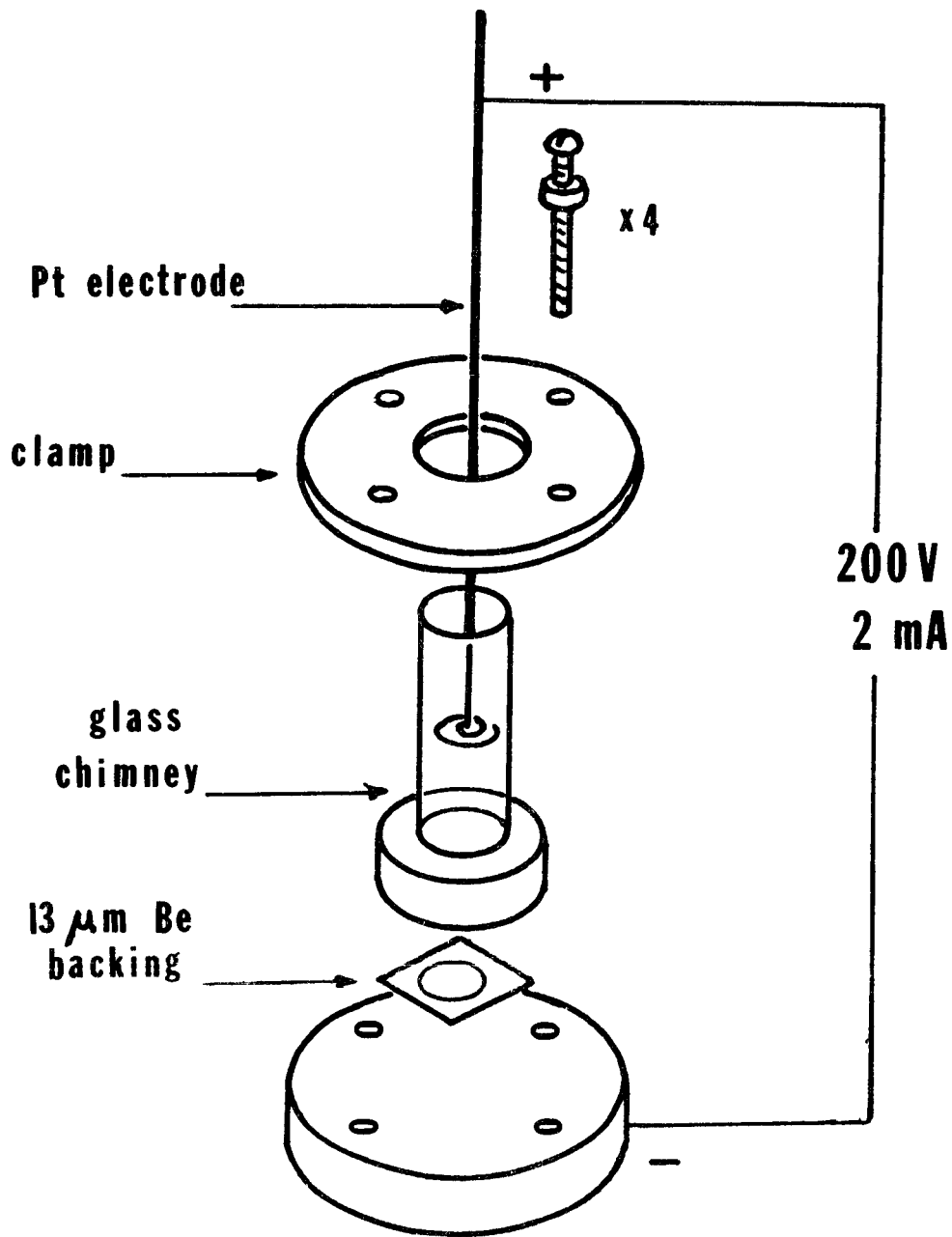
Figure 2g - The endpiece used in determinations of the energy of the beam projectiles after passing through successive media.

Figure 2h - A modification of the target system end piece for catching complete fusion recoils. The catcher foil is gas cooled.

Figure 2i - An outline of the chemistry used to separate the actinide products from the reaction of ^{86}Kr and ^{136}Xe with ^{248}Cm , starting with a gold recoil foil.

Figure 2j - Typical gamma ray and alpha particle energy spectra from the reaction of approximately 520 MeV ^{86}Kr with ^{248}Cm .

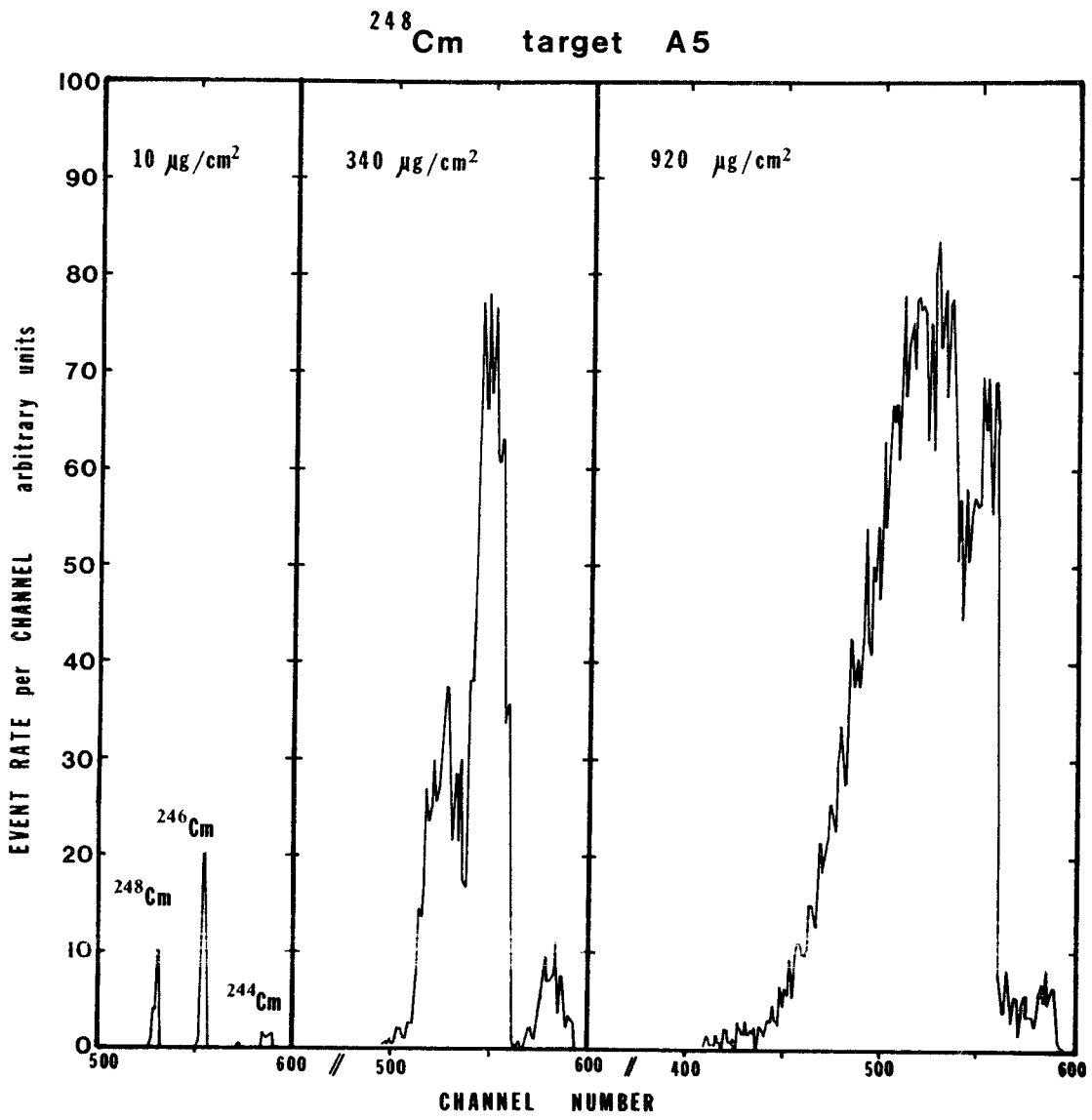
Figure 2k - An outline of the chemistry used to separate the actinide products from the reaction of 96 MeV ^{18}O with ^{248}Cm .



Target Fabrication

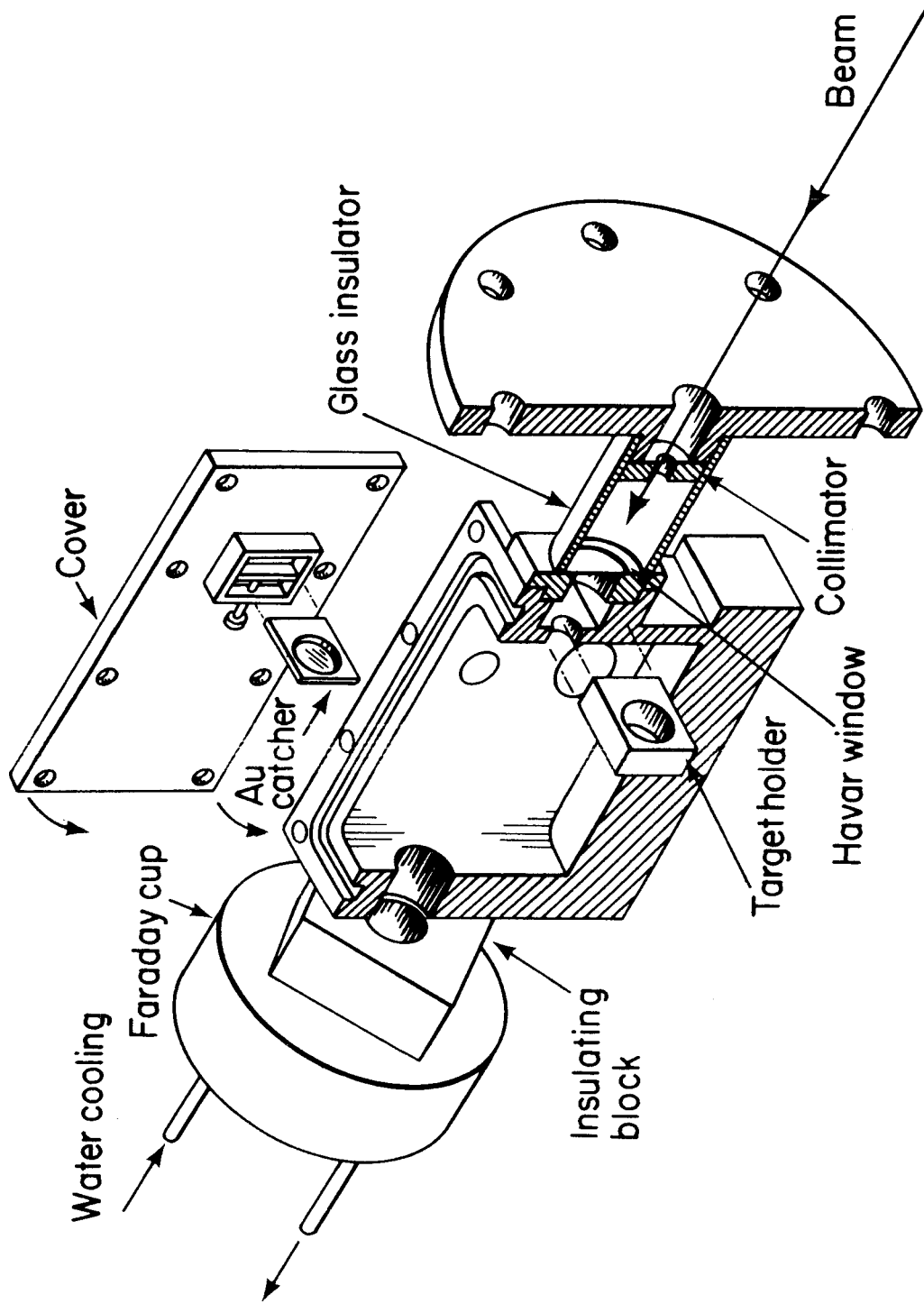
XBL 836-10246

Figure 2a



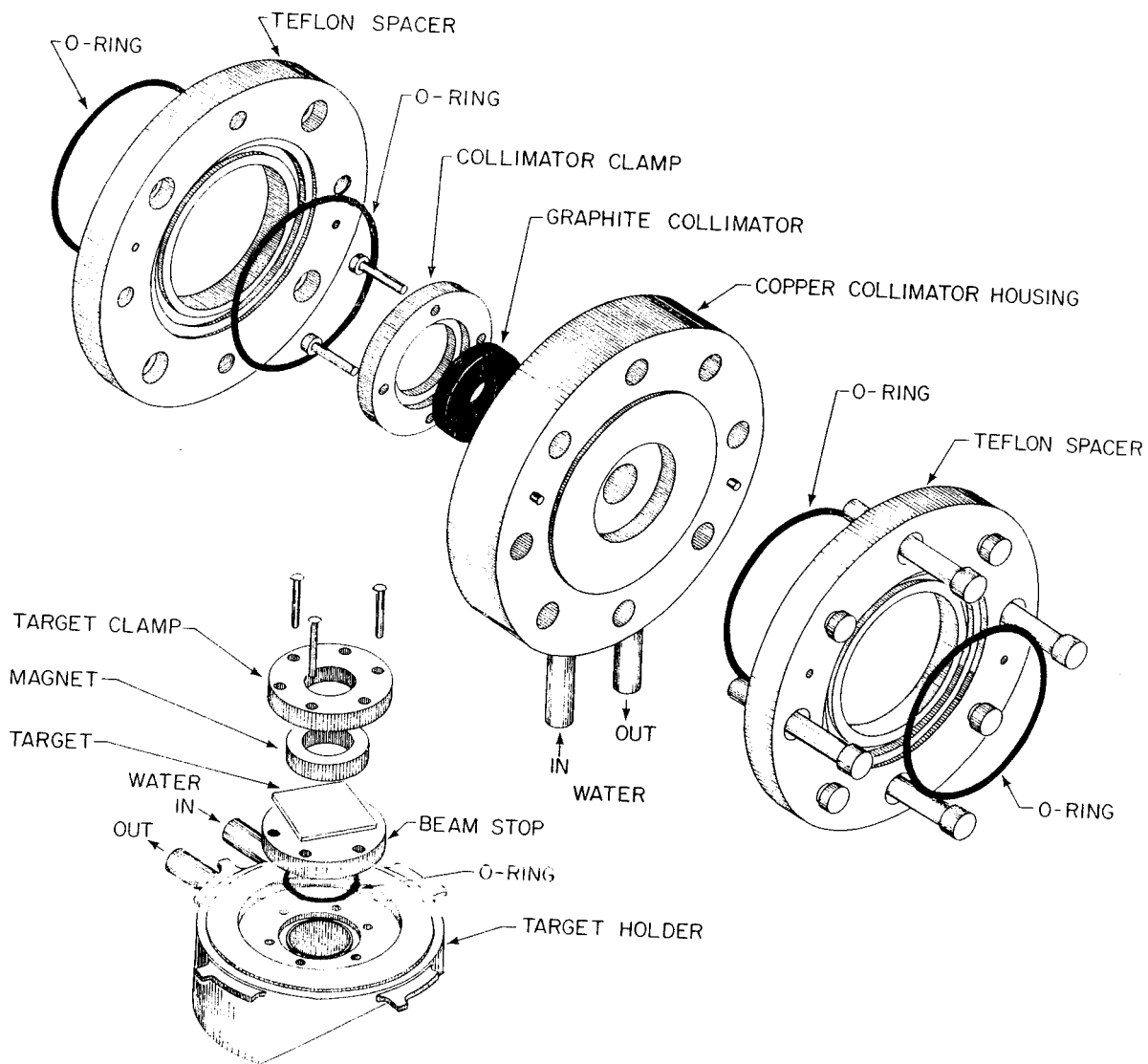
XBL 836-10245

Figure 2b



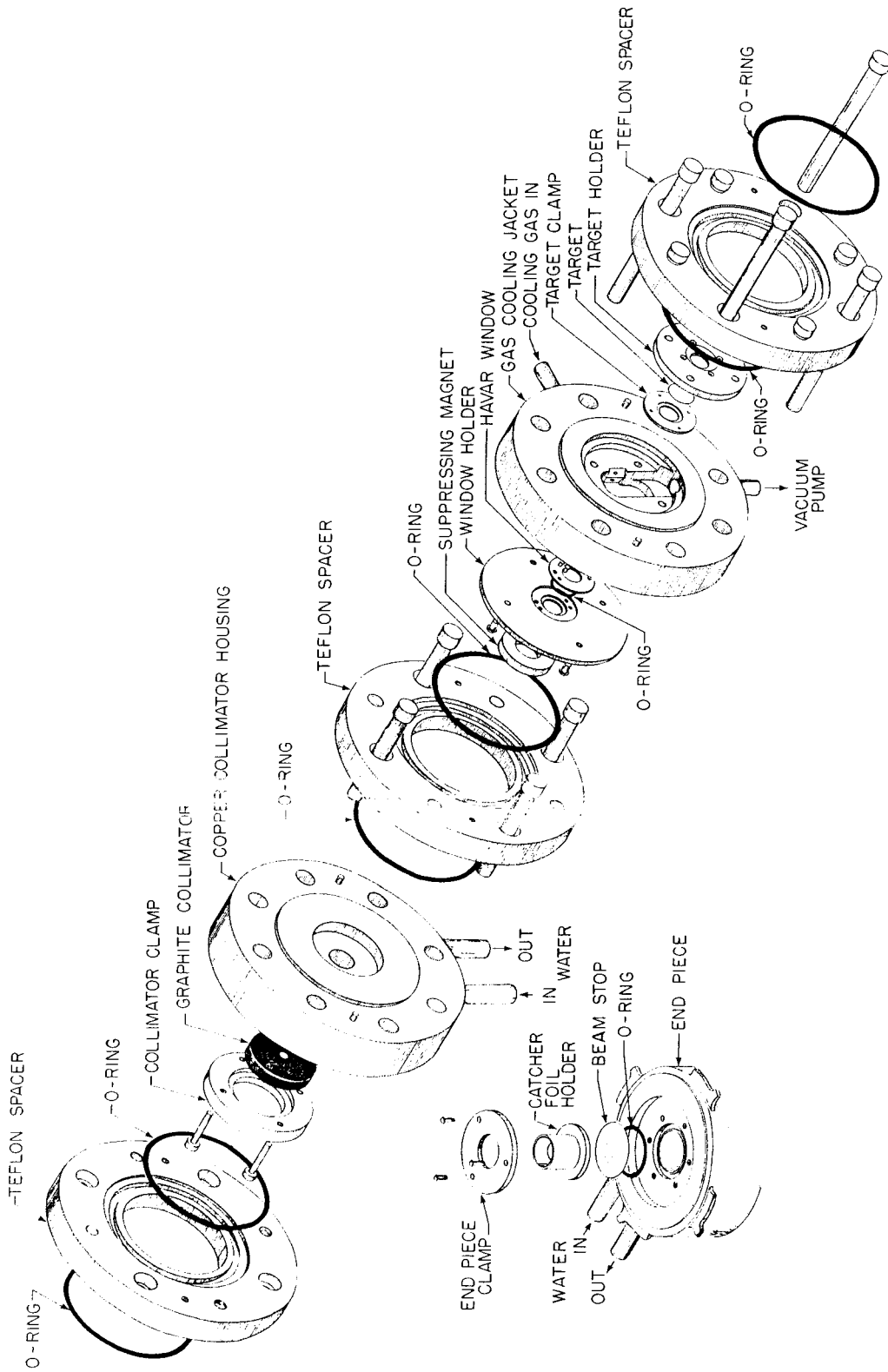
XBL 814-645

Figure 2c



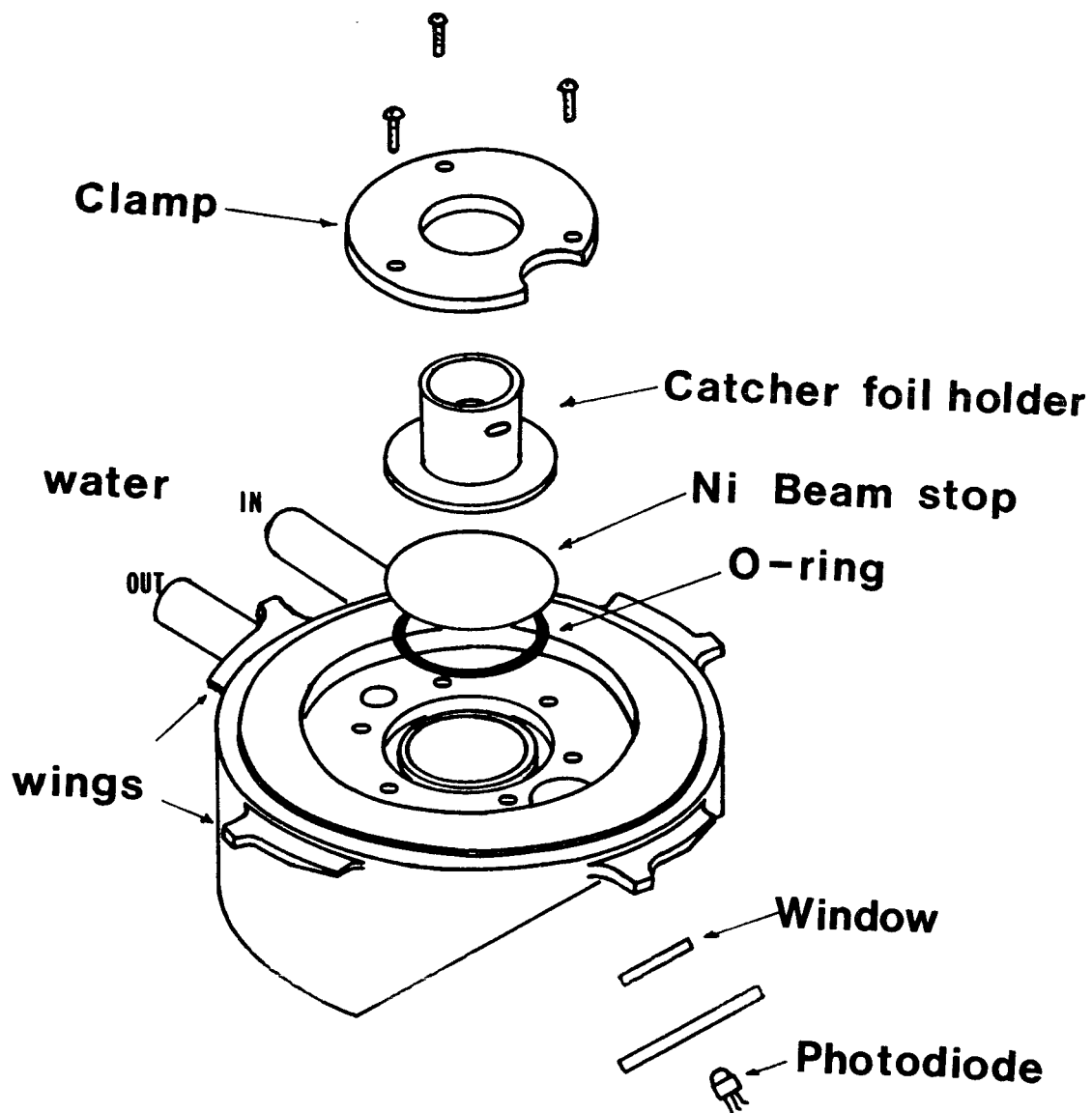
XBL 7910-4518

Figure 2d



XBL 803-503

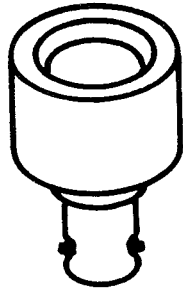
Figure 2e



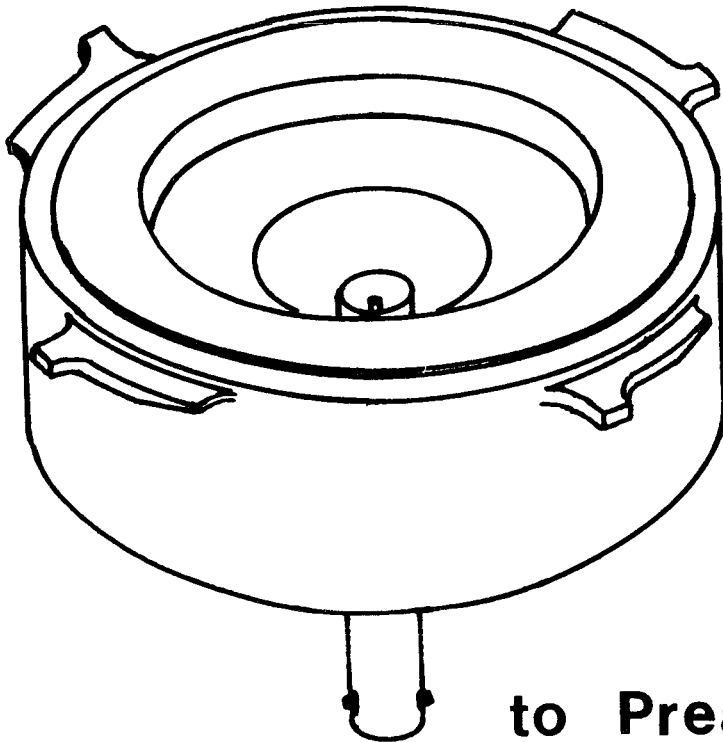
**END PIECE
ACTINIDE RECOILS**

XBL 836-10251

Figure 2f



**ORTEC
surface barrier
detector**

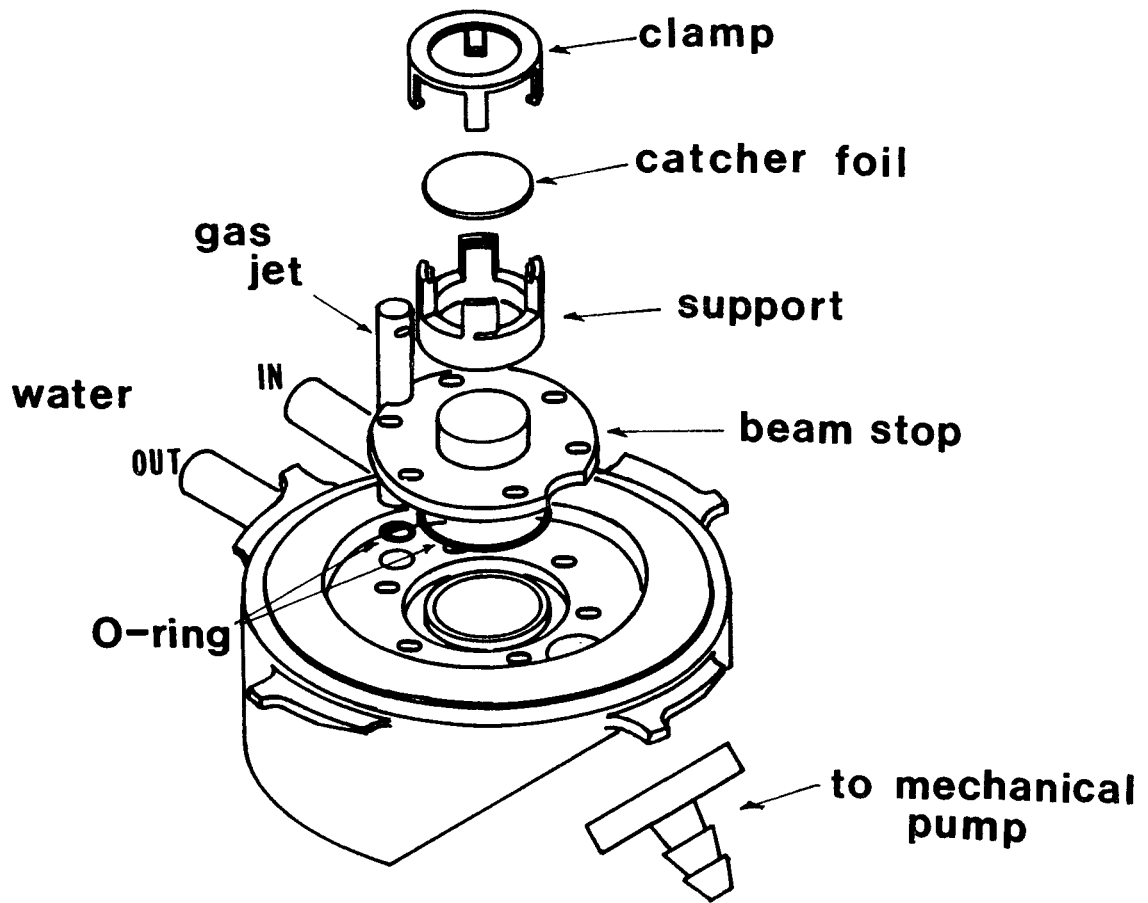


to Preamplifier

END PIECE

ENERGY MEASUREMENTS

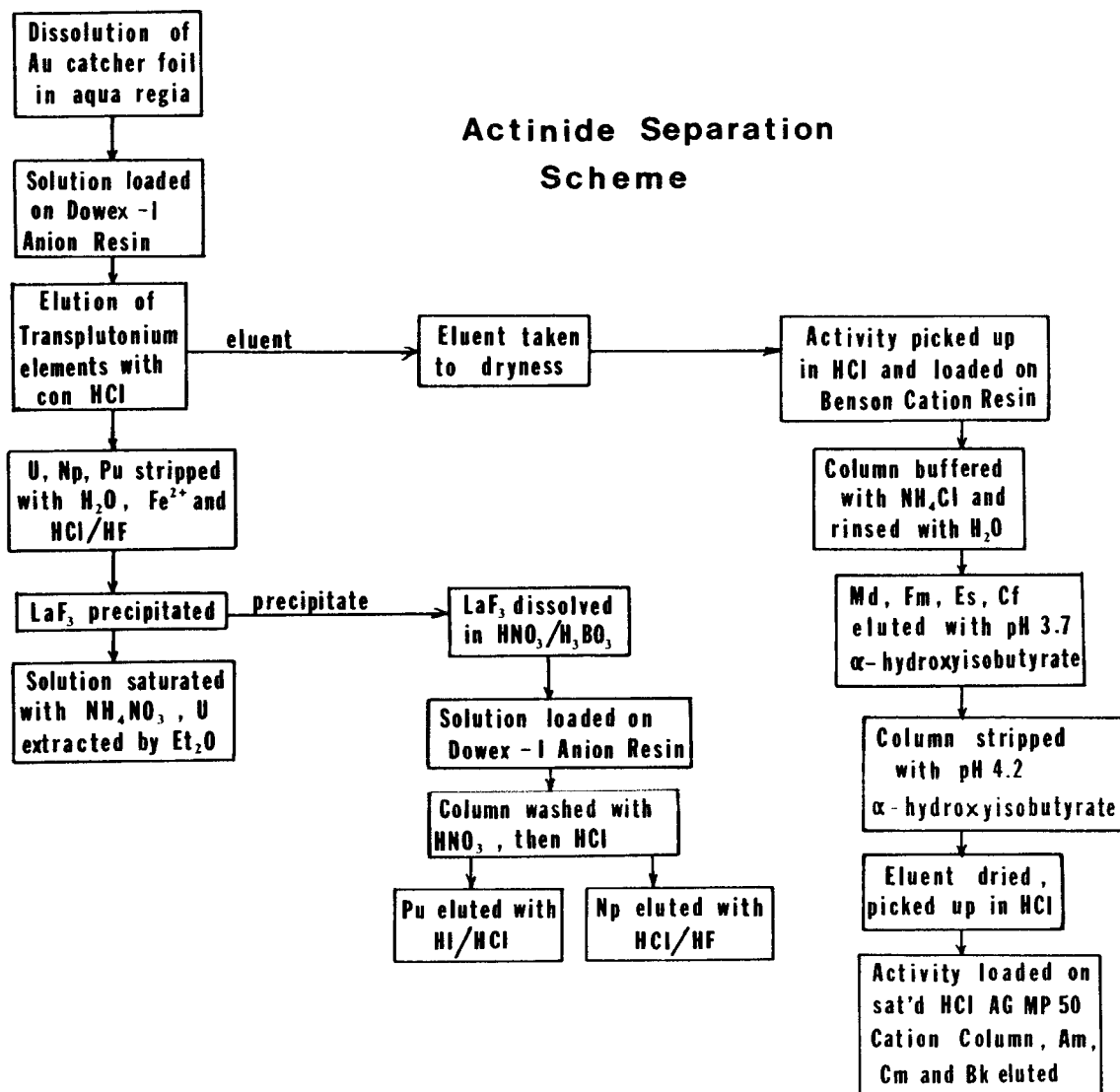
XBL 836-10242



**END PIECE
COMPLETE FUSION RECOILS**

XBL 836-10248

Figure 2h



XBL 836-10391

Figure 2i

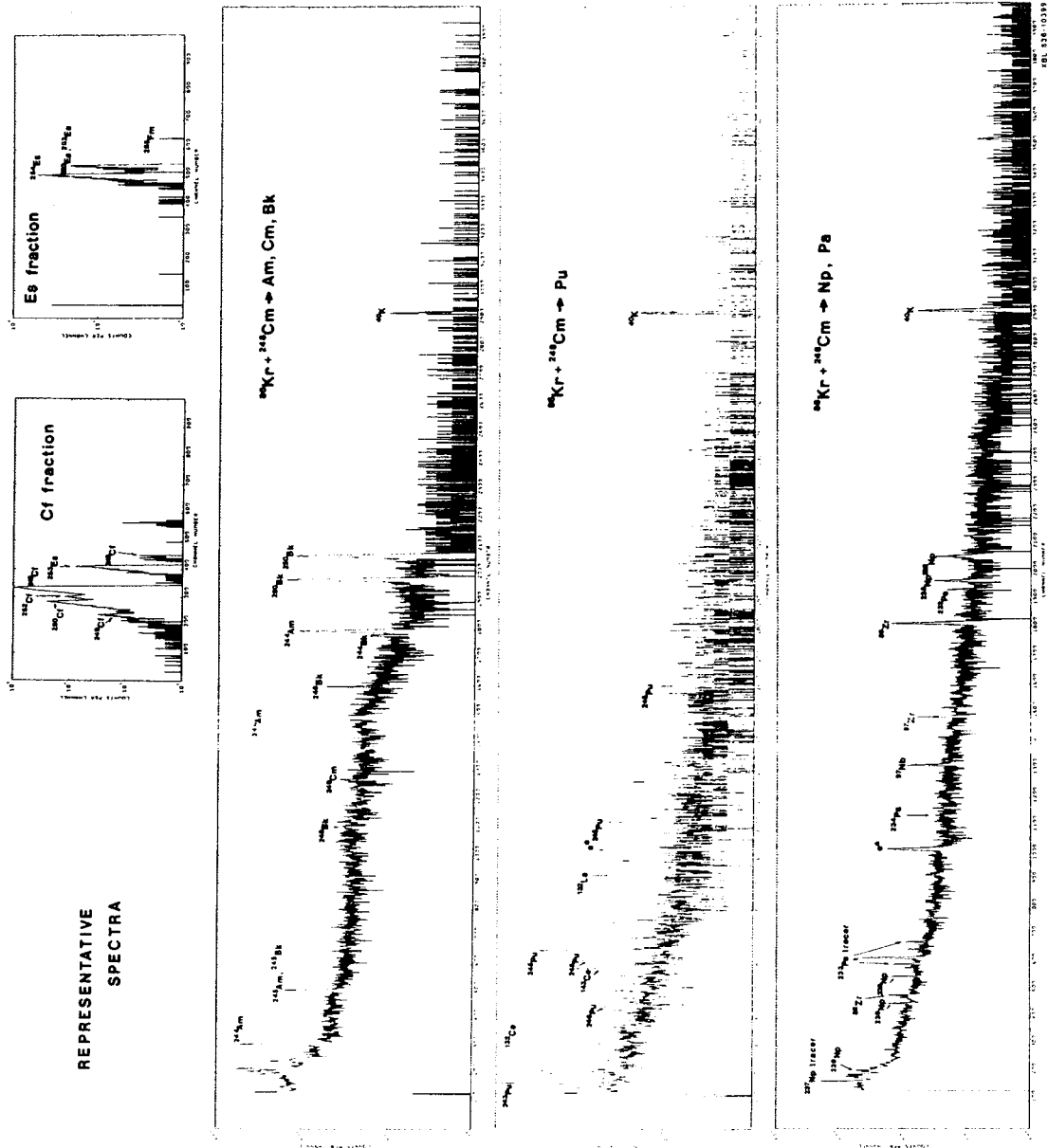
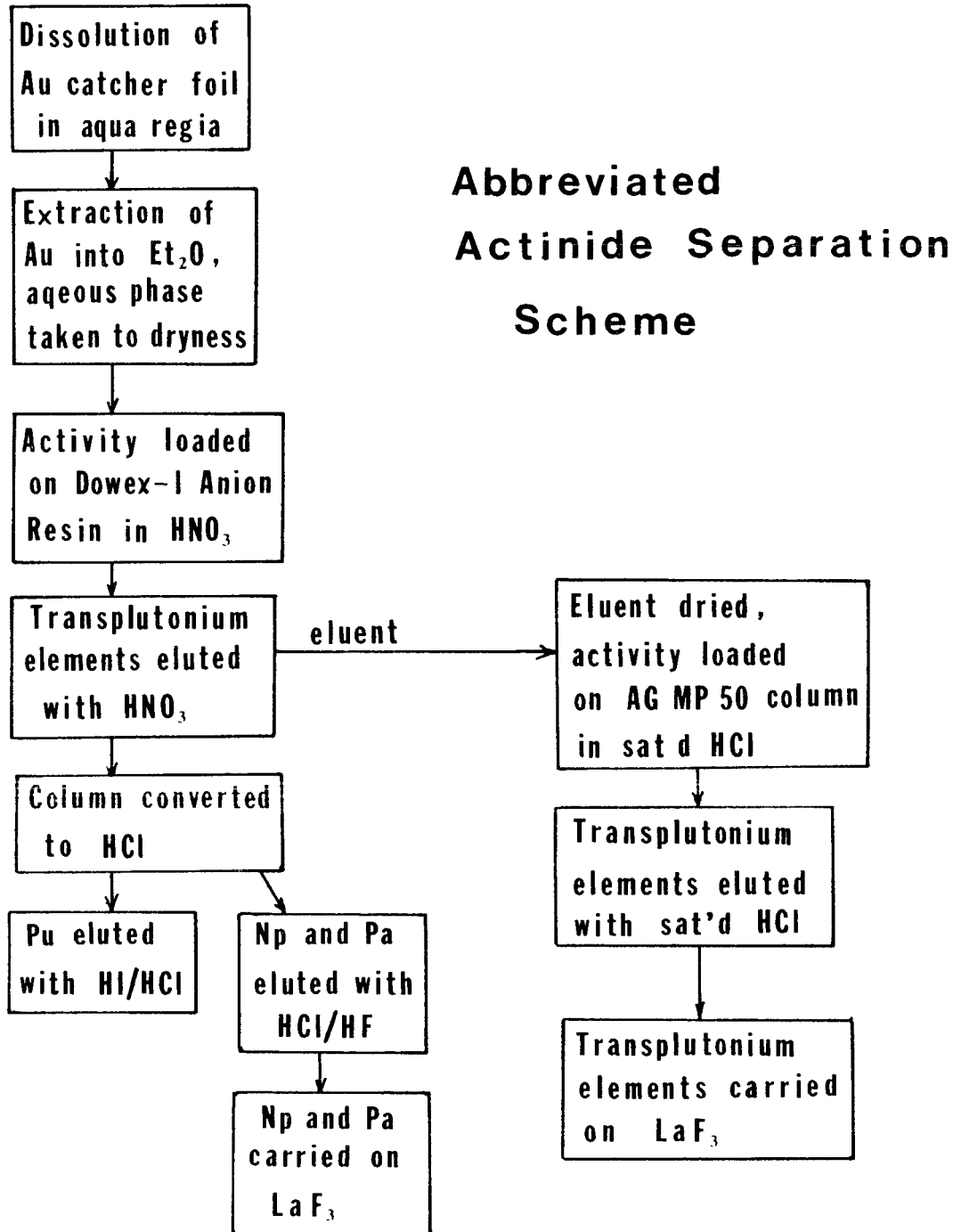


Figure 2j



XBL 836-10393

Figure 2k

Section 3 - Data Reduction

Alpha particle, spontaneous fission and gamma ray data are stored in terms of multichannel analyzer spectra on magnetic tape or floppy disks. Gamma ray data are accumulated for one month and alpha particle and spontaneous fission data for half a year. The problem of how to convert this large volume of data into cross sections as a function of the relative kinetic energy of the reactants is now addressed. The problem reduces to three parts: the determination of projectile energies, the determination of cross sections, and the determination of the efficiency for collecting reaction products.

3.1 Determination of the Energy of the Beam Particles in the Target

In experiments where it is important to know the energy of the ion reacting with the target material, the loss of energy of the ions as they pass through windows, target substrates, etc. must be determined. With very heavy ions, where energy loss is severe, this is particularly important.

In the past, typically, energy loss was calculated using the Northcliffe and Schilling range tables [Nor70]. The tables are based on an extrapolation of the experimental data available in 1970 to unknown regions of ion energy and nuclear charge based on some simple theoretical considerations. For each Z, a representative ion mass is selected and the electronic and nuclear stopping powers over a wide range of energies are converted into a range in various media from the relationship

$$Range = \int_E^0 (dE/dx)^{-1} dE \quad \text{III.1}$$

where dE/dx is the stopping power for the ion in a given medium. Ranges and stopping powers of ions in elemental media not tabulated can be determined by simple extrapolation. If one is fortunate, all the media which degrade the beam

energy in a given experiment are pure elements and the ions are the same mass as those selected in the tables. Energy loss can then be calculated by the method of residual ranges. In the case of this work, however, the stopping media include Havar, which is a complicated mixture (see Table 3-1) and the curium itself, which is present as a salt. Also, ^{18}O , ^{86}Kr and ^{136}Xe are all the most neutron-rich stable isotopes of each element, but not the most abundant, so other masses are tabulated.

Table 3-1 The major components of Havar [Ham76]

component	weight %
cobalt	42.5%
chromium	20.0%
iron	17.9%
nickel	13.0%
tungsten	2.8%
molybdenum	2.0%
manganese	1.6%
carbon	0.2%
beryllium	0.04%

The stopping power tables for a given Z are valid for all isotopes of that element at a given velocity or energy per nucleon. Therefore the stopping power of ^{18}O , ^{86}Kr and ^{136}Xe in various elemental media can be calculated from the tables for ^{16}O , ^{84}Kr and ^{132}Xe . The stopping power in a mixed medium can be calculated from the Bragg additivity rule, which holds for heavy ions though not for protons or helium ions [Sau65], by summing the stopping powers of the various constituents, weighted by their mass fraction in the medium. Then using equation III.1 and the residual range technique the energy loss in a series of

media can be computed. For the work presented here, this is done with the program RANGY [Wel80], which takes as input the tabular stopping power data for the ion of interest as a function of velocity in several elemental media, extrapolates the stopping power for any necessary untabulated elemental components via a high order polynomial, constructs stopping power tables for each experimental medium, fits these data with another set of high order polynomials and numerically integrates to determine the successive energy loss in each medium.

In the last eight years discrepancies between energy losses calculated with the Northcliffe and Schilling tables and experimentally determined energy losses have begun to be noticed [Var76], particularly for the heaviest ions in the lightest media [Bim78], reaching 30% or more with ^{84}Kr ions in carbon foils. In some of the experiments performed for this work ^{136}Xe ions passed through beryllium ($Z=4$) target substrates! The more recent compilation of range tables by Hubert et.al. [Hub80], using a more sophisticated model and drawing on a larger volume of experimental data for parameterization, gives more reasonable results [Bim80,lai82].

In order to calculate the energy of the beam in the target material, it is necessary to know the energy of the beam entering the target system. For the 88-Inch Cyclotron experiments with ^{18}O ions this problem is trivial, because for a beam of ions of mass 18, with the cyclotron operating at 5.568 MHz, the beam energy is determined from the cyclotron equation. With constants substituted in for the 88-Inch Cyclotron, this equation is [Gou79]

$$E = mc^2 \{ [1 - (\omega / 48.616)^2]^{-1/2} - 1 \} \quad \text{III.2}$$

where ω is the cyclotron frequency in megahertz, E is the beam energy in MeV, and mc^2 is the ion mass in MeV. The first harmonic of the cyclotron frequency was used.

For the SuperHILAC experiments with beams of ^{86}Kr and ^{136}Xe , the beam energy is dependent upon the complicated interplay of the various gradients and phases of the accelerating sections and on the charge states of the ions. Two methods of measuring the SuperHILAC beam energy are used. One involves the use of a phase probe system which directly measures the velocity of the beam. The phase probes do not give a measure of low level beam "contaminants" coming through the accelerator at different energies than the primary beam. The other method of measuring the beam energy involves the use of surface barrier detectors which are inserted into the beam. These detectors, similar to those described in Section 2, are calibrated with alpha particles of a known energy from a radionuclide standard and with a pulser. The energy of heavy ions determined with these detectors is always too low due to the pulse height defect [Wil71] which arises from three contributing factors: energy loss in the gold "window" of the detector, nuclear stopping power (not important for alpha particles and light heavy ions), and the recombination of electron-hole pairs in the semiconductor due to their high density along the heavy ion's path. All surface barrier detectors of this type with active layers deep enough to stop the ion of interest display almost identical behavior [Ste72], varying slightly with the thickness of the gold layer on the entrance side of the detector and the effect of high resistivities on the recombination term. The magnitude of the pulse height defect has been determined from experimental data [Mou78] and is applied to the measured energy to give the "true" energy. Surface barrier detectors are highly prone to damage from heavy ion beams. All measurements are taken from beams which have been attenuated before the Alvarez tanks of the SuperHILAC to the rate of 50 particles per second in the detector. Even so, the detectors slowly go bad, indicated by a rise in the leakage current across the semiconductor, produced by the detector bias.

Table 3-II gives the energies of the ions used in the various experiments, as measured both with phase probes and with surface barrier detectors. Correction for pulse height defect has been made.

Table 3-II Beam energy delivered to the target system for various experiments.

Experiment	Energy (MeV) from Surface Barrier Detector	Energy (MeV) from Phase Probes
$^{136}\text{Xe-0}$	1150	--- °
$^{136}\text{Xe-I}$	~1100 *	1133 ± 14
$^{136}\text{Xe-II}$	1064	1060 ± 10
$^{86}\text{Kr-I}$	730	--- °
$^{86}\text{Kr-II}$	680	682 ± 4
$^{86}\text{Kr-III}$	650	--- °
$^{86}\text{Kr-IV}$	~600 *	630 ± 4
$^{18}\text{O-I}$		111 +
$^{18}\text{O-II}$		111 +

* High leakage current makes these measurements unreliable.

° Phase probes unavailable (or broken).

+ Cyclotron energy, not measured.

Surface barrier measurements are taken periodically throughout Super-HILAC experiments. Beam energies are quite unstable, changing by several MeV even when the machine is not being actively tuned, due to heating and cooling in the accelerating sections. Quite often "satellite" energy peaks appear, approaching the magnitude of the primary peak. Even though the transport optics of the beam after it exits the last accelerating section discriminates against these extraneous beams finding their way through the 6 mm collimator ahead of the target, if the satellite intensities reach more than 10% of the total beam measured in the surface barrier detector, or if the primary beam shifts

by more than 10 MeV in energy, the catcher foil is discarded. This, in part, explains the absence of runs $^{136}\text{Xe-III}$ and $^{86}\text{Kr-0}$ from the lists of reported experiments. When there is a discrepancy between a phase probe measurement and a surface barrier detector measurement, the phase probe measurement is used; the surface barrier detector spectrum is still a sensitive measure of the existence of energy satellites and the width of the peak. In all experiments, the FWHM of the energy spectrum was less than 20 MeV.

Table 3-III gives the energy of the beam in the target material, calculated by use of the tables of both Northcliffe and Schilling, and Hubert et.al. The uncertainty on the number in the incident energy column is probably less than 10 MeV.

Table 3-III Calculated energies in the curium target material for several experiments, from the tables in [Nor70] and [Hub80].

Experiment	Incident E (MeV)	E entering curium		E exiting curium	
		[Nor70]	[Hub80]	[Nor70]	[Hub80]
$^{136}\text{Xe-0}^*$	1150	931	808	896	761
$^{136}\text{Xe-I}^\circ$	1133	914	790	844	699
$^{136}\text{Xe-II}^\circ$	1064	839	716	768	624
$^{86}\text{Kr-I}^\circ$	730	603	546	562	493
$^{86}\text{Kr-II}^\circ$	680	549	490	507	436
$^{86}\text{Kr-III}^\circ$	650	516	457	473	402
$^{86}\text{Kr-IV}^\circ$	630	494	435	450	379
$^{18}\text{O-I}^+$	111	96.5	96.5	95.5	95.5
$^{18}\text{O-II}^+$	111	96.5	96.5	95.5	95.5

* Target used was 1.10 mg/cm² curium, as the fluoride, on 2.63 mg/cm² Be

° Target used was 2.15 mg/cm² curium, as the fluoride, on 2.63 mg/cm² Be

+ Target used was 0.52 mg/cm² curium, as the oxide, on 2.23 mg/cm² Be

The discrepancy between the Northcliffe and Schilling energies and the Hubert et.al. energies is insignificant for the ^{18}O experiments, but is so large for ^{136}Xe and ^{86}Kr that one must worry about the validity of all such calculations. Therefore, using the energy measuring device described in Section 2 and shown in figure 2g, the energy of the beam through successive media was measured during experiments $^{136}\text{Xe-II}$ and $^{86}\text{Kr-IV}$. These two experiments are those using the lowest energy of each beam, so the energy loss and energy straggling are the most extreme of those in any of the experiments. Table 3-IV gives the results from the measurements, compared with the energy loss calculated with the tables of Hubert et.al.

Table 3-IV Measured energy (corrected for pulse height defect) and calculated energy (from Hubert et.al. [Hub80]) for two experiments. Energy given in MeV.

	$^{136}\text{Xe-II}$		$^{86}\text{Kr-IV}$	
	measured	calculated	measured	calculated
Incident	1064		630	
Energy through 1.8 mg/cm ² Havar window	981	979	581	581
Energy through Havar and 0.55 mg/cm ² nitrogen	939	937	552	552
Energy through Havar, 0.20 mg/cm ² nitrogen, 2.63 mg/cm ² beryllium, 2.64 mg/cm ² $^{248}\text{CmF}_3$ and 0.35 mg/cm ² nitrogen	621	624	362	361

Figure 3a shows the successive beam energy spectra from experiment $^{136}\text{Xe-II}$. The range table calculations yield the centroid of the beam energy spectrum [Nor63] rather than the most probable energy, which is what was read off with

the pulser, but in most cases the spectrum is fairly close to symmetric. The data in the table indicate that the energies calculated from the tables of Hubert et.al. can be used with confidence. The discrepancy is only a few MeV in the worst case, and this could be due to the pressure of the nitrogen cooling gas being only poorly reproducible. The calculated energy values in Table 3-III will be used to characterize the reactions.

The spectra in figure 3a also show the degree of energy straggling through the various media. This is not readily calculable because much of the straggling comes from inhomogeneities in the stopping materials, particularly the target, rather than from the statistical straggling phenomenon itself. In the ^{136}Xe -II experiment, the width of the energy distribution of the beam after passing through all the media (including an extra amount of nitrogen between the target and the detector) is $(655 - 578) = 77$ MeV, which is less than the energy loss in the target (~ 90 MeV). For ^{86}Kr -IV, the measured straggling width is $(378 - 346) = 32$ MeV, again less than the loss in the target (~ 55 MeV). Some of the apparent width of the energy spectrum is due to "puddling" of the curium fluoride target material, since these were the last two experiments performed with the target. This affects only the low energy (exiting) portion of the energy distribution in the target. Another source of spectrum width is due to the proximity of the surface barrier detector to the target (~ 1 cm); the high event rate in the detector from target alpha particles and spontaneous fission fragments tends to broaden the energy spectrum.

In other words, the effect of energy straggling on the energy distribution of the beam particles in the target is only poorly known. Energies reported for the experiments performed for this work are determined only from the entering and exiting values calculated with the Hubert et.al. range tables [Hub80]; no estimate of the effect of energy straggling is made. However, even in the "worst

cases" detailed above, the straggling effect is smaller than the primary energy loss effect, though how much smaller is uncertain. This is an important concern, because most of the reaction cross section for experiments near or below the nominal Coulomb barrier comes from the high energy part of the distribution of projectile energies in the target material.

3.2 Determination of Reaction Cross Sections

Each cross section reported here was determined from the characteristic radiation of the decaying nuclide. In the case of gamma emitters, the initial activity of the nuclide was determined from more than one gamma ray, if possible, particularly in the case of protactinium and neptunium isotopes, where the activity levels were very low. For alpha emitting nuclides, the daughter activity was also determined, if possible, particularly in the case of the fermium isotopes. The detected radiations of the tracer activities were discussed in the previous section. Observed nuclides, their half lives and detected radiations, taken from data in reference [TOI78], are:

^{232}Pa - half life 1.31 day, observed gamma rays at 894 keV (24 ± 2)% and 969 keV (53 ± 5)%.

^{234}Pa - half life (6.75 ± 0.03) hours, observed gamma ray at 131 keV (20%).

^{237}U - half life (6.752 ± 0.002) days, observed gamma ray at 60 keV (36.0 ± 3.6)%.

^{240}U - half life (14.1 ± 0.2) hours, observed gamma rays at 554 keV (21.2 ± 1.4)% and 597 keV (13%) arising from 7.5 minute $^{240\text{m}}\text{Np}$ daughter.

^{238}Np - half life (2.117 ± 0.002) days, observed gamma rays at 984 keV (27.8 ± 0.8)% and 1028 keV (20.3 ± 1.4)%, the latter usually being integrated with the lower intensity 1026 keV line (9.7 ± 0.9)%.

^{239}Np - half life (2.346 ± 0.004) days, observed gamma rays at 106 keV (27.8

$\pm 0.9\%$, 228 keV ($11.4 \pm 0.3\%$) and 278 keV ($14.5 \pm 0.4\%$). The gamma ray at 106 keV is difficult to use due to neighboring Pu X-rays.

^{240}Np - half life (67 ± 1) minutes, observed gamma rays at 566 keV ($29 \pm 7\%$) and 974 keV ($30 \pm 7\%$).

^{243}Pu - half life (4.955 ± 0.003) hours, observed gamma ray at 84 keV ($23 \pm 2\%$).

^{245}Pu - half life (10.48 ± 0.05) hours, observed gamma rays at 308 keV ($5.0 \pm 1.0\%$) and 327 keV ($26 \pm 3\%$). Occasionally the ^{245}Am daughter can be observed.

^{246}Pu - half life (10.85 ± 0.02) days, observed gamma ray at 224 keV ($24 \pm 2\%$). Also observed via 25 minute ^{246}Am daughter gamma rays at 799, 1062 and 1079 keV. See $^{246}\text{Am}(1)$.

^{244}Am - half life (10.1 ± 0.1) hours, observed gamma rays at 744 keV ($66 \pm 3\%$) and 898 keV ($28 \pm 2\%$).

^{245}Am - half life (2.05 ± 0.01) hours, observed gamma ray at 253 keV ($6.1 \pm 0.6\%$). See ^{245}Bk .

$^{246}\text{Am}(1)$ - half life (25.0 ± 0.2) minutes, observed gamma rays at 799 keV ($26 \pm 1\%$), 1062 keV ($18 \pm 1\%$) and 1079 keV ($29 \pm 2\%$).

$^{246}\text{Am}(2)$ - half life (39 ± 3) minutes, observed gamma rays at 154 keV ($25 \pm 5\%$) and 679 keV ($52 \pm 5\%$).

^{247}Am - half life (24 ± 3) minutes, observed gamma rays at 226 keV ($5.8 \pm 1.6\%$) and 285 keV ($23 \pm 5\%$).

^{241}Cm - half life (32.8 ± 0.2) days, observed gamma ray at 472 keV ($71 \pm 3\%$).

^{249}Cm - half life (65.3 ± 0.6) minutes, observed gamma ray at 634 keV ($1.5 \pm 0.1\%$).

^{245}Bk - half life (4.90 ± 0.03) days, observed gamma ray at 253 keV ($31.3 \pm 2.0\%$). ^{245}Am is usually in the same chemical fraction and has the same gamma

ray arising from a transition in ^{245}Cm ; decay curve analysis is performed to separate the two.

^{246}Bk - half life (1.80 ± 0.02) days, observed gamma ray at 799 keV (61.4 ± 3.7)%.

^{248}Bk - half life (23.5 ± 0.2) hours, observed gamma ray at 551 keV (4.6 ± 0.3)%.

^{250}Bk - half life (3.222 ± 0.005) hours, observed gamma rays at 989 keV (45.2 ± 0.8)% and 1032 keV (35.2 ± 0.4)%, the latter integrated with the lower intensity 1029 keV line (4.4 ± 0.2). Occasionally lines at 890 keV (1.65 ± 0.06)% and 929 keV (1.37 ± 0.06)% are observed.

^{251}Bk - half life (55.6 ± 1.1) minutes. See Section 5 for gamma rays.

^{246}Cf - half life (35.7 ± 0.5) hours, alpha particle energy 6.76 MeV.

^{248}Cf - half life (333.5 ± 2.8) days, alpha particle energy 6.26 MeV.

^{250}Cf - half life (13.08 ± 0.09) years, alpha particle energy 6.03 MeV.

^{252}Cf - half life (2.646 ± 0.004) years, alpha particle energy 6.12 MeV, (96.908 ± 0.008)% alpha decay, also observed by (3.092 ± 0.008)% spontaneous fission branch.

^{253}Cf - half life (17.82 ± 0.09) days, observed via growth and decay of ^{253}Es daughter in (99.69 ± 0.04)% of decays.

^{254}Cf - half life (60.5 ± 0.2) days, observed via (99.69 ± 0.02)% spontaneous fission branch.

^{249}Es - half life (1.70 ± 0.01) hours, observed gamma ray at 380 keV (40.4 ± 2.5)%.

^{250}Es - half life (8.6 ± 0.1) hours, observed from ^{250}Cf daughter with alpha particle energy 6.03 MeV.

^{251}Es - half life (33 ± 1) hours, observed via 6.49 MeV alpha particle with $(0.49 \pm 0.12)\%$ abundance.

^{252}Es - half life (471.7 ± 1.9) days, observed directly from $(78 \pm 2)\%$ alpha particle branch of 6.63 MeV, and via growth of ^{252}Cf $(22 \pm 2)\%$. Daughter fissions are observable. See ^{253}Es .

^{253}Es - half life (20.47 ± 0.02) days, observed from alpha particle decay with 6.63 MeV energy. Decay curve analysis is necessary to separate ^{253}Es from ^{252}Es alphas.

^{254m}Es - half life (39.3 ± 0.2) hours, observed from growth and decay of ^{254}Fm daughter 7.19 MeV alpha particles in $(99.59 \pm 0.01)\%$ of decays.

^{255}Es - half life (38.3 ± 0.3) days, observed directly from 6.30 MeV alpha particle in $(8.0 \pm 0.4)\%$ of decays and indirectly from growth and decay of ^{255}Fm daughter alphas at 7.02 MeV in $(92.0 \pm 0.4)\%$ of decays.

^{256}Es - half life 7.6 hours, observed from growth and decay of ^{256}Fm spontaneous fissions in $(91.9 \pm 0.3)\%$ of decays.

^{252}Fm - half life (25.39 ± 0.05) hours, alpha particle energy 7.04 MeV. Also seen from daughter ^{248}Cf alpha activity. See ^{255}Fm .

^{253}Fm - half life (3.00 ± 0.13) days. Observed directly from $(12 \pm 1)\%$ alpha branch at ~ 6.9 MeV (broad), and indirectly from growth and decay of ^{253}Es daughter alphas in $(88 \pm 1)\%$ of decays.

^{254}Fm - half life (3.240 ± 0.002) hours, observed 7.19 MeV alpha particle.

^{255}Fm - half life (20.07 ± 0.07) hours, observed 7.02 MeV alpha particle. Resolving ^{255}Fm from ^{252}Fm can only be accomplished via calculation of the intensity of the ^{252}Fm activity from that of the ^{248}Cf daughter.

^{256}Fm - half life (2.627 ± 0.021) hours, observed via $(91.9 \pm 0.3)\%$ spontaneous fission branch.

It should be noted that for ^{234}Pa , ^{240}Np , ^{244}Am , ^{248}Bk and ^{254}Es only one member of known isomeric pairs was observed. In growth and decay determinations of ^{250}Es and ^{256}Es , only the longest lived isomer is assumed to contribute to the daughter activity due to the saturation level of the activities produced by the long bombardment. In several experiments ^{249}Cf (main alpha energy 5.81 MeV) and ^{254}Es (alpha energy 6.43 MeV) were observed, but since these nuclides are used to calibrate the alpha-hydroxyisobutyrate column prior to each experiment, no guarantee can be made that all of the activity comes from the reaction. The ^{244}Bk nuclide (4.35 hour half life, 218 keV and 892 keV gamma rays) was observed in ^{86}Kr bombardments, but the gamma ray intensities are not known, so no cross section could be determined.

Areas of full energy peaks in the gamma ray spectra were integrated by hand. In most cases the statistics of the data determining the peak areas were too low to make the fitting of a functional form a valid technique [Phi78]. The peak was determined by establishing high- and low-energy limits on the peak and defining areas representative of background. The area over background is determined with the expression

$$AREA = \sum_p C_p - \left[\frac{\sum_L C_L}{N_L} + \frac{\sum_R C_R}{N_R} \right] \cdot \frac{N_p}{2} \quad \text{III.3}$$

where p, R and L are the indices for the channels in the peak, right background and left background respectively, N refers to the number of channels of each type and C refers to the number of events stored in each channel. The error on this value is given by the expression

$$ERROR = \left\{ \frac{N_p^2}{4} \left[\frac{\sum_L C_L}{N_L^2} + \frac{\sum_R C_R}{N_R^2} \right] + \sum_p C_p \right\}^{\frac{1}{2}} \quad \text{III.4}$$

taking the statistical error on $\sum_L C_L$, $\sum_R C_R$ and $\sum_p C_p$ to be the square root of

the number of counts in the sum in each case. Once the high and low channel limits are established for a given peak they are not moved from one spectrum to the next unless some shift in the stability of the detector warrants it. This helps remove any "optimism" from the data which can be introduced by trying to minimize the background by moving it from place to place. Generally, if two peaks are close enough together that a two channel background cannot be established between them, they are integrated as one peak. If possible, as many as five channels were included in both the right and left backgrounds.

Alpha analysis offers both advantages and disadvantages relative to gamma counting. In a clean system, each single alpha event is significant, so very low cross sections can be determined. For a single peak the area is merely the sum of all counts in those channels over which the peak is spread and, if the area is large enough, the statistical error is equal to the square root of the area. Unfortunately, peaks in the alpha particle spectra tend to tail to the low-energy side due to source thickness and to satellite peaks from alpha decay to higher members of rotational bands in the daughter. In the fermium fractions measured in this work this is not a problem, because the alpha particle peaks are either widely separated in energy or decay at different rates, except for the ^{252}Fm - ^{255}Fm peak which is deconvoluted as described above. The same is true in the einsteinium fractions, except for ^{255}Es , where the main alpha particle group is found on the low-energy tail of the ^{254}Es peak. In the californium fraction, the small differences between alpha particle energies combined with the long half lives of most of the californium nuclides creates a real problem. If it is assumed that most of the tailing of the alpha peaks is due to source thickness, then each peak should have roughly the same shape, barring small changes with the alpha particle energy. When the californium fraction is counted after ^{248}Cf has decayed to an undetectable level, the ^{253}Es peak from ^{253}Cf decay

stands alone at 6.63 MeV, well above the nearest peak at 6.26 MeV. Several spectra are summed together to maximize the statistics, then the peak is cut into energy bins referenced to the channel with the peak maximum in it. Using the fractional peak area in each bin, and starting with the peak at highest energy, the contribution of each peak to those below it in energy can be calculated and subtracted out. Similarly, the ^{254}Fm peak from $^{254\text{m}}\text{Es}$ decay is used to deconvolute the ^{255}Es peak in the einsteinium fraction.

In experiments with beam energies well below the classical Coulomb barrier, the activity levels in the final alpha samples are very low. In cases where the number of alpha events in a single spectrum for a single nuclide is less than nine, several spectra are added together to effectively make a much longer count. This way the square root of the number of counts as an error bar is still justified. The choice of the number nine is arbitrary.

Each peak area is divided by the length of the accumulation. This rate is associated with the time at the midpoint of the counting interval, if the counting interval is less than the half life of the nuclide of interest. If not, the time associated with the peak is given by

$$\delta_1 = \frac{1}{\lambda} \ln \frac{\lambda \Delta t}{1 - \exp(-\lambda \Delta t)} \quad \text{III.5}$$

where δ_1 is the time after the start time of the count which is to be assigned to the peak area, λ is the decay constant of the nuclide, and Δt is the counting interval. This equation is only valid for single component decay.

The activity present at the end of bombardment due to each nuclide is determined from the activity data as a function of time after bombardment with the iterative non-linear least-squares decay curve code FUTILE. The best fit of a function f to a set of data points (x_i, y_i) is determined by picking parameters for the function which give a minimum χ^2 [Bev69].

$$\chi^2 = \sum_i \frac{1}{\sigma_i^2} [y_i - f(a_1, a_2, \dots, a_n, x_i)]^2 \quad \text{III.6}$$

where i is the data point index, σ_i is the error associated with y_i , and a_1, a_2, \dots, a_n are the parameters of function f to be determined. Minimization of the χ^2 with respect to each parameter a_j ($j = 1, n$) gives a system of n equations in n unknowns

$$\frac{\partial \chi^2}{\partial a_j} = 0 = -2 \sum_i \left\{ \frac{1}{\sigma_i^2} [y_i - f(a_1, a_2, \dots, a_n, x_i)] \frac{\partial f(a_1, a_2, \dots, a_n, x_i)}{\partial a_j} \right\}. \quad \text{III.7}$$

For a non-linear function f this is a difficult system of equations to solve. To bypass this, a set of trial parameters $\{a_1^0, a_2^0, \dots, a_n^0\}$ is selected. Defining $y_i^0 = f(a_1^0, a_2^0, \dots, a_n^0, x_i)$ and expanding about y_i^0 gives:

$$0 = -2 \sum_i \sum_k \left\{ \frac{1}{\sigma_i^2} \left[y_i - \left(y_i^0 + \frac{\partial f_o}{\partial a_k} (a_k - a_k^0) + \frac{1}{2} \frac{\partial^2 f_o}{\partial a_k^2} (a_k - a_k^0)^2 + \dots \right) \right] \frac{\partial f_o}{\partial a_j} \right\} \quad \text{III.8}$$

where $\frac{\partial f_o}{\partial a_k}$, $\frac{\partial f_o}{\partial a_j}$ and $\frac{\partial^2 f_o}{\partial a_k^2}$ are "true" derivatives of function f , evaluated at $\{a_1^0, a_2^0, \dots, a_n^0, x_i\}$. If all a_k^0 values are close to a_k , the best value, then

higher order terms in $(a_k - a_k^0)$ can be neglected. Rearranging the result gives

$$\sum_k \sum_i \left\{ \frac{1}{\sigma_i^2} \frac{\partial f_o}{\partial a_k} \Delta a_k \frac{\partial f_o}{\partial a_j} \right\} = \sum_i \left\{ \frac{1}{\sigma_i^2} (y_i - y_i^0) \frac{\partial f_o}{\partial a_j} \right\} \quad \text{III.9}$$

for each j , where $\Delta a_k = a_k - a_k^0$. This describes the system of simultaneous equations

$$\vec{A} \cdot \vec{\Delta a} = \vec{h} \quad \text{III.10}$$

where the elements of the matrices are

$$A_{jk} = \sum_{i=1}^n \frac{\partial f_o}{\partial a_j} \frac{\partial f_o}{\partial a_k} \frac{1}{\sigma_i^2} \quad \text{III.11a}$$

$$\Delta a_k = \Delta \alpha_k \quad \text{III.11b}$$

$$h_j = \sum_{i=1}^n \frac{\partial f_o}{\partial a_j} (y_i - y_i^o) \frac{1}{\sigma_i^2} \quad \text{III.11c}$$

The Δa_k values, which are the deviations between the real, minimum a_k values and the guessed a_k^o values (to first order) are determined from this expression. Defining a new set of "guesses" where $a_k^{(1)} = a_k^o + \Delta a_k$, and a new $y_i^{(1)} = f(a_1^{(1)}, a_2^{(1)}, \dots, a_n^{(1)})$, and going back to equation III.10, leads to a new, better set of a_k values. In the limit where all the "guessed" parameters are very close to the real minima, all Δa_k values become zero. The error values for the parameters are difficult to determine analytically, but to a good approximation the error on parameter a_j is ϵ_{jj} , the diagonal element of array $\left[\vec{A} \right]^{-1}$ [Bev69].

In using the FUTILE code on the experimental decay curve data, all half lives were held fixed. In the case of growth and decay data where it was certain that the daughter activity was entirely removed by the chemistry, an initial daughter activity of zero was enforced. By holding these parameters fixed, the effect of uncertainties in their values was removed, giving smaller error bars for the initial activity parameters. Since the half lives of the nuclides are known to a high degree of accuracy in most cases, this method for "firming up" the initial activity data is justified. It is assumed that in all cases the feeding of daughter activities from parent activities after the end of bombardment but before the chemical separation is negligible. Examining the resulting cross sections, it can be seen that this is true in every case except the $^{250}\text{Bk} - ^{250}\text{Cf}$ pair, but even so, feeding during the bombardments, which all exceeded 12 hours in length, was certainly more important than feeding during a few hours of chemistry. Figure 3b shows some typical decay curves.

In all the calculations which follow, the uncertainty of a particular result is determined from the standard propagation of error formulae, derived from

$$\lambda^2(F) = \left(\frac{\partial F}{\partial x} \right)^2 \lambda^2(x) + \left(\frac{\partial F}{\partial y} \right)^2 \lambda^2(y) + \dots \quad \text{III.12}$$

for non-systematic errors and from

$$\lambda(F) = \frac{\partial F}{\partial x} \lambda(x) + \frac{\partial F}{\partial y} \lambda(y) + \dots \quad \text{III.13}$$

for systematic errors [Sho74]. In these equations $\lambda(F)$ is the error on the derived quantity F , which is a function of x, y, \dots , each of which has its associated error $\lambda(x), \lambda(y), \dots$. The initial activities calculated by the use of the FUTILE code are corrected for detector efficiency and branching ratio for the particular type of radiation emitted by the nuclide in question, both with their associated non-systematic errors. If more than one radiation is observed for a particular nuclide, a weighted average of the resultant disintegration rate is taken:

$$\bar{y} = \frac{\sum_i \frac{y_i}{\sigma_i^2}}{\sum_i \frac{1}{\sigma_i^2}} \quad \text{III.14}$$

The error bar on \bar{y} is given by

$$\bar{\sigma} = \left[\sum_i \frac{1}{\sigma_i^2} \right]^{-1/2} \quad \text{III.15}$$

If it is assumed that no feeding takes place during the bombardment, the cross sections of the nuclides of interest can be determined from the expression

$$\text{cross section} = \frac{A_0}{YN^0 \sum_{i=1}^n \varphi_i \left[1 - e^{-\lambda \Delta t_i} \right] e^{-\lambda(t-t_i)}} \quad \text{III.16}$$

where A_0 is the initial activity of the nuclide, whose decay constant is λ . N^0 is the number of target atoms per square centimeter. Y is the chemical yield. φ_i is the flux of the beam in particles per unit time during the i^{th} interval of the bombardment, the length of the interval being Δt_i . The term $(t - t_i)$ is the time from the end of the i^{th} interval to the end of the bombardment. Breaking the bombardment into a series of short intervals and using the average beam current for each interval permits a more accurate calculation of the cross sections of nuclides whose half lives are on the order of the bombardment length or less. During the experiment the integrated beam flux is recorded periodically throughout the bombardment, becoming more frequent toward the end. Conversion of the integrated beam flux from Coulombs to particles requires that the charge state of the ion be known. Errors on the quantities in equation III.16 are treated as systematic errors in calculating the error on the cross section. They are the uncertainties on the initial activity, chemical yield, the charge state on the ion, and the half life of the nuclide. Uncertainty in the target thickness is assumed to be zero, though this is certainly not correct; it is to be hoped that this is a small error relative to the others. The error on the charge state of ^{18}O ions ($4+$) was taken to be zero, since no other charge states could be in resonance in the cyclotron. The accuracy of this depends on how successfully electrons are suppressed in the target system. The charge states of beams from the SuperHILAC are not as easy to predict. Nominally, anything which leaves the accelerator can find its way to the target system, since it is located at 0° to the machine axis. Tuning for maximum intensity and energy resolution tends to discriminate in favor of the few most intense charge states leaving the mid-machine stripper foil. The average charge states used for ^{86}Kr and ^{136}Xe in these calculations are $22+$ and $29+$ respectively [Sup79], with a probable uncertainty of ± 1 .

3.3 Collection Efficiency of Catcher Foils

When catcher foil collection efficiency is to be determined, three problems must be addressed: are the products emerging from the target at an angle which is subtended by the catcher foil; do the products have sufficient energy to escape the target and pass through any intervening material to reach the catcher foil; are the products moving slowly enough that the catcher foil is of sufficient thickness to stop them?

Postulate a circular catcher foil of radius a , at a distance of b from and parallel to a circular target spot of radius R . See figure 3c. A perpendicular to the target at its center is co-linear with a perpendicular to the catcher foil passing through its center, both of which are parallel to the beam direction. The radius of the target is less than the radius of the foil. In an experiment, it can be assumed that the distribution of the beam across the target spot is uniform due to the wobbler and its distance from the collimator. Consider a point on the target at a distance r from the axis. Reaction products are emitted at a variety of angles ϑ to the beam direction from point r . There is an angle ϑ_{\min} below which all products are collected from point r regardless of their orientation to the target axis. There is an angle ϑ_{\max} above which all products miss the catcher foil, regardless of their orientation to the target axis. Between ϑ_{\min} and ϑ_{\max} , some fraction of the emitted products miss the foil. The probability of a product emitted from point r at an angle ϑ of missing the foil is proportional to the arc length of the circle that the angle ϑ traces out when spun about an axis through r at a distance of b which is outside the boundary of the catcher foil. In Cartesian coordinates, defined with the target axis at the origin and the x-axis through point r , the equation for this circle is

$$(x + r)^2 + y^2 = b^2 \tan^2 \vartheta \quad . \quad \text{III.17}$$

The boundary of the catcher foil is described by

$$x^2 + y^2 = a^2 \quad \text{III.18}$$

The problem is symmetrical about the x-axis. The two points of intersection of the two circles occur when

$$x = (b^2 \tan^2 \vartheta - a^2 - r^2) / 2r \quad \text{III.19}$$

The probability of missing the catcher foil is proportional to twice the arc length s of equation III.17 from the point where $y = 0$ to the intersection point.

$$s = \int_{x_1}^{x_2} \left[1 + \left(\frac{dy}{dx} \right)^2 \right]^{\frac{1}{2}} dx =$$

$$\int_{-b \tan \vartheta - r}^{(b^2 \tan^2 \vartheta - a^2 - r^2) / 2r} \left\{ 1 + \frac{(x+r)^2}{[b^2 \tan^2 \vartheta - (x+r)^2]} \right\}^{\frac{1}{2}} dx =$$

$$b \tan \vartheta \left[\sin^{-1} \left(\frac{b^2 \tan^2 \vartheta - a^2 + r^2}{2r b \tan \vartheta} \right) + \frac{\pi}{2} \right] \quad \text{III.20}$$

The probability of missing the foil is

$$P_{\vartheta,r} = \frac{2s}{2\pi b \tan \vartheta} = \frac{1}{\pi} \left[\sin^{-1} \left(\frac{b^2 \tan^2 \vartheta - a^2 + r^2}{2r b \tan \vartheta} \right) + \frac{\pi}{2} \right] \quad \text{III.21}$$

To obtain the total collection efficiency of the foil, this equation must be integrated over the total target area. Since the function is only piecewise continuous this is most easily done numerically. Figure 3d shows the result for the catcher foil used in ^{18}O experiments. All recoils between 0° and 50° to the beam axis which have sufficient energy to reach the foil are caught. The truncated cone used in ^{86}Kr and ^{136}Xe experiments can be treated as two separate

problems like that outlined above; the result is given in figure 3e. All recoils between 25° and 50° to the beam direction are caught, decreasing in probability until no recoils at 0° or above 70° are caught.

Without making any assumptions about the type of reaction which produces the actinide products other than the fact that it is a binary process, upper and lower limits can be set on their recoil energies. With ⁸⁶Kr and ¹³⁶Xe bombardments, where the kinetic energies of the projectiles are hundreds of MeV and the amount of mass exchanged in the reaction is small compared to the mass of either of the participants, the reaction Q-value and the change of nuclear charge are small effects. The maximum possible recoil energy, induced by approximately 800 MeV ¹³⁶Xe, comes from completely elastic collisions at zero impact parameter. Classical kinematics gives this recoil energy as being 730 MeV. The minimum recoil energy possible is for a "fully damped" collision, where all the energy of relative motion is converted into internal excitation energy of the products. In the center of mass the products recede at their mutual Coulomb repulsive energy [Tho74], assuming an intermediate of two touching charged spheres. The distance of centers for these two spheres can be stated as

$$R = R_p + R_t + a + d \quad \text{III.22}$$

where R_p and R_t are the "hard sphere" radii of the projectile and target respectively, a is the range of the Yukawa force and d is an overlap parameter determined from heavy ion complete fusion data [Kra73]. The equation can be parameterized [Lef76] as

$$R \text{ (in fm)} = 1.16 (A_p^{1/3} + A_t^{1/3}) + 2.6 \quad \text{III.23}$$

The height of the Coulomb barrier due to the mutual repulsion of the positive nuclei is given by $V_C = Z_p Z_t e^2 / R$, which equals 85.5 MeV for the ¹⁶O + ²⁴⁸Cm

system, 332 MeV for the $^{86}\text{Kr} + ^{248}\text{Cm}$ system and 471 MeV for the $^{136}\text{Xe} + ^{248}\text{Cm}$ system, all in the center of mass. With 400 MeV (lab frame) ^{86}Kr ions, the lowest momentum projectile used in experiments with the conical catcher foil, conservation of momentum and energy gives a curium-like recoil energy of 150 MeV at 45° to the beam direction. The range of 730 MeV curium in gold is about 28 mg/cm² [Hub80], much less than the 50 mg/cm² catcher foils. Experiments which were aimed at observing ^{247}Pu and measuring heavy americium nuclide cross sections used foils of 45 mg/cm² nickel and 14 mg/cm² aluminum, respectively, and the ranges of full momentum recoils are 14 mg/cm² and 10 mg/cm², respectively [Hub80]. The conical catcher foils are thick enough to stop all recoils which reach them. Similarly, the range of minimum energy recoils is on the order of 10 mg/cm² curium fluoride [Nor70], so the amount of activity lost in the 2.15 mg/cm² curium target (2.6 mg/cm² curium fluoride) is negligible, even at wide angles. The presence of approximately 0.3 mg/cm² of quasi-stagnant nitrogen between the target and the catcher foil is also negligible.

The angular distributions of reactions with heavy ions have been classified according to the modified Coulomb (Sommerfeld) parameter [Gal76]:

$$\eta' = Z_p Z_t e^2 / \hbar v' \quad \text{III.24}$$

where v' is the relative velocity of the reactants at the interaction radius. These values can be calculated easily if the projectile energy is over the hard-sphere Coulomb potential V_C by assuming that $v' = [2(E - V_C)/\mu]^{1/2}$. For ^{86}Kr and ^{136}Xe systems at the highest energies used in this work, the η' values are approximately 500 and 1000 respectively. At lower energies η' becomes larger. These values can also be extrapolated from a tabulation in the literature [Wil80]. For values of η' larger than 300, the reaction cross section as a function of product angle peaks close to the grazing angle, independent of product kinetic energy, and the peaking becomes more pronounced as η' increases

[Gal76]. Classically, there is an impact parameter for each projectile energy of more than the mutual Coulomb energy at which two charged spheres just touch. The angle at infinite distance at which the projectile recedes, defined by the Coulomb trajectory, is the grazing angle [Sco77]. By definition, then, the grazing angle can be calculated only at energies above the Coulomb barrier. For near- and below-barrier reactions, where the Coulomb potential dominates the interaction, the quarter-point angle from the Fresnel scattering model is more appropriate. At the highest energies of ^{86}Kr and ^{136}Xe used in this work, the calculated grazing angles [Sco77], translated to the laboratory frame for target-like products [Mar69], and the quarter-point angles extrapolated from literature values [Wil80] are, approximately, 43 and 33 degrees to the beam direction, respectively. The angular distribution of target-like fragments has been measured for the $^{84}\text{Kr} + ^{238}\text{U}$ system [Luc79] and agrees well with this prescription at the energy studied. As the beam energy decreases, increasing the importance of more central collisions to the reaction process, the target-like fragment grazing angle approaches zero. In this simple model, then, most of the reaction products which are somehow formed below the reaction barrier are lost through the hole in the center of the catcher foil. The nuclei are not, however, properly described as hard spheres. The diffuseness of the nuclear surfaces and the deformation of the target nucleus [Mye77] both serve to extend nuclear matter out past the hard sphere radius. This effectively lowers the Coulomb barrier for otherwise sub-barrier reactions, which increases the scattering angle for target-like recoils. Another way of saying this is that the reaction itself requires a certain amount of juxtaposition of nuclear matter in the two participants. Since mass and charge flow take time [Mor76], a certain amount of sticking and rotation about the combined nuclear centers is required, even at "sub-barrier" energies, which throws the otherwise forward-

moving recoils somewhat to the side.

With ^{18}O -induced reactions, the kinematics of the reaction is not so straight-forward. The difference between the incoming and outgoing partition of charge and mass between the target and projectile produces a serious discontinuity in the Coulomb trajectory of the collision. The reaction Q-value is significant in the presence of the low projectile energy. Experimental data on the interaction of ^{18}O with ^{245}Cm and ^{249}Cf are available [McF82] which directly give the beam direction component of the range of trans-target reaction products, stopped in thin aluminum foils. The catcher foils used in the work presented here are 2 mg/cm^2 gold, which translates to 0.7 mg/cm^2 aluminum for curium-like recoil ions. While the range of products was found to tail to larger values than 0.7 mg/cm^2 in aluminum, the bulk of the products (more than 90%) stopped in that distance at the energy over the Coulomb barrier that was used in this work. Some of the observed long-range tailing may have been due to pin-holes in the thin aluminum foils. As expected for two body interactions, an increase in the projectile energy causes the target-like products to move to larger angles with respect to the beam direction, corresponding to lower parallel ranges at higher bombarding energies. Examination of the structure of the range data indicates that the activity in the first foils in the experiments at the same fraction of the beam energy over the reaction barrier as was used in this work is substantial. The possibility exists that some few percent of the reaction products stopped in the 0.52 mg/cm^2 ^{249}Cf and 0.24 mg/cm^2 ^{245}Cm targets. In other work on the $^{18}\text{O} + ^{248}\text{Cm}$ system [Lee82, Lee83], the target used was 0.9 mg/cm^2 ^{248}Cm as the fluoride. In the work presented here, the target was 0.5 mg/cm^2 ^{248}Cm as the oxide. The discrepancies between the berkelium cross sections reported for the experiments at the same energies in the two studies, otherwise identical, are probably partly due to recoil losses in the

thicker target. Furthermore, at the higher energies used in the previous work [Lee83], the wider recoil angles made the target even thicker to the recoiling reaction products. The structure in the reported excitation functions is not due entirely to the physics of the reaction, but has a contribution from target thickness as well.

The angular distributions of products for 96 MeV ^{18}O reactions with ^{248}Cm can be approximated by extrapolation of data from the $^{18}\text{O} + ^{249}\text{Cf}$ reaction [McF82], with the aid of quarter angle calculations [Wil80], or by conversion of projectile data from similar systems [Art73,Ale75]. All indicate a peak in the lab frame angular distributions near 30° to 50° for trans-target species. The subject of the formation of target-like reaction products at a Z below that of the target in these light heavy ion reactions has been avoided since no experimental data are available. The more equal partition of charge and mass should increase the recoil energy of the heavy fragment as well as decrease its nuclear charge, both of which effectively increase the particle range. No large effect on the range of the products was seen over four charge units in reactions of ^{18}O with ^{245}Cm [McF82], so it can be hoped that the trend will continue to product species below the target, unless the reaction mechanism changes. There is no evidence for this (see Section 4).

In summary, there is some possibility that at bombarding energies far below the Coulomb barrier with ^{86}Kr and ^{136}Xe ions, some of the reaction products may be lost by passing through the center of the truncated conical catcher foil. In ^{18}O bombardments, a few percent of the trans-target products may pass all the way through the catcher foil, and what may be a larger fraction of the sub-target species also. Only minimal numbers of products miss the catcher foil in ^{18}O bombardments. In the data presented in the next section, no correction for catcher foil geometry has been made on the magnitude of the

reaction cross sections.

Figure Captions

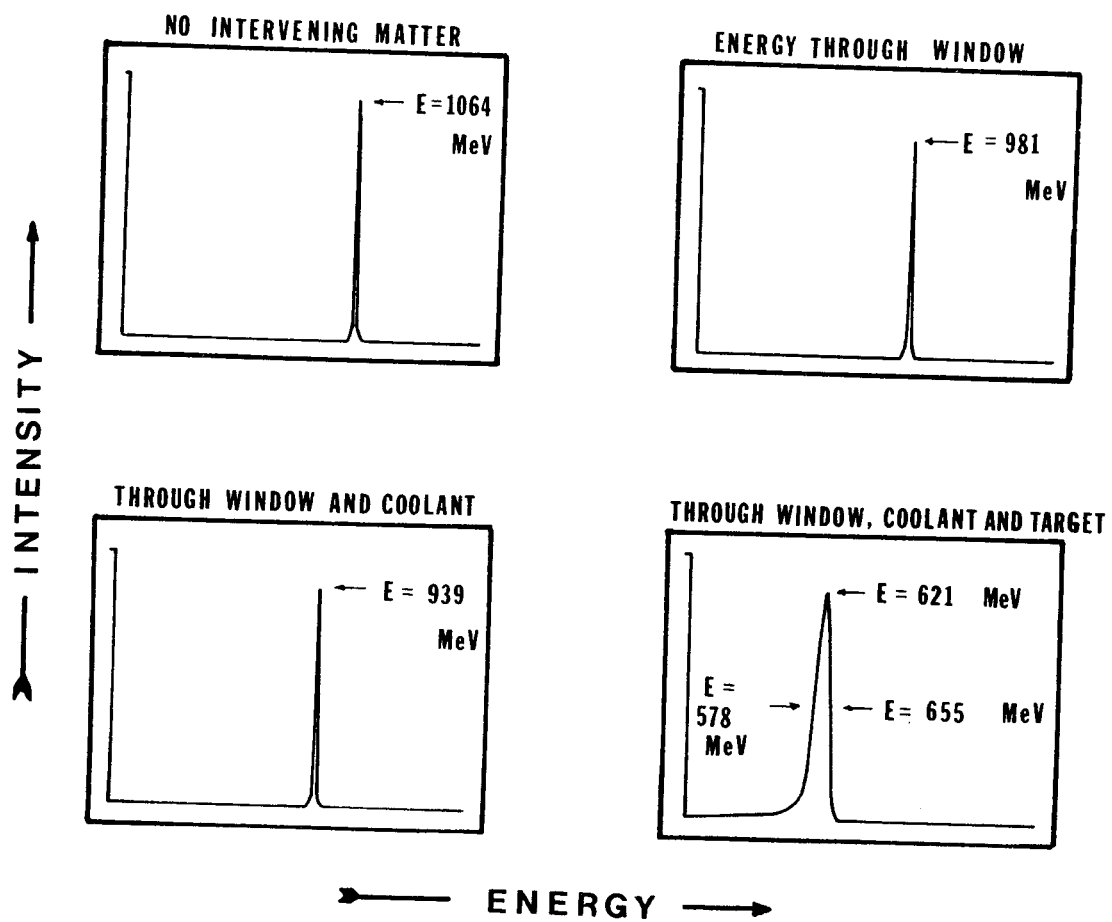
Figure 3a - Successive energy spectra of beam particles passing through the components of the Modular Fast Access Target System for 1064 MeV incident ^{136}Xe ions. The energy of the peak, as determined with a pulser and corrected for pulse height defect, is indicated.

Figure 3b - Typical decay curves of actinide products from the bombardment of ^{248}Cm with ^{136}Xe ions.

Figure 3c - A diagram of the calculation to determine the collection efficiency of the recoil catcher foils as a function of laboratory angle.

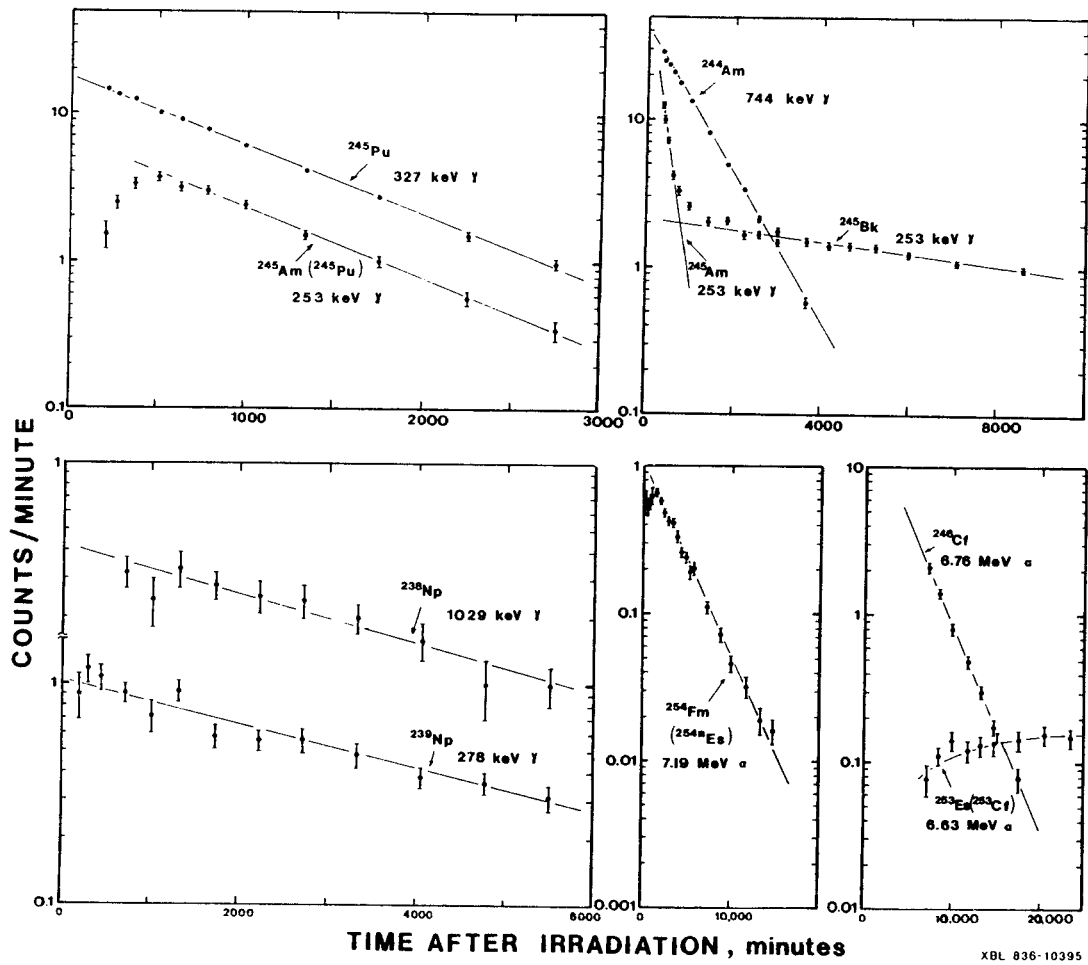
Figure 3d - Recoil collection efficiency as a function of laboratory angle for ^{180}O irradiations.

Figure 3e - Recoil collection efficiency as a function of laboratory angle for ^{86}Kr and ^{136}Xe irradiations (truncated conical foil).



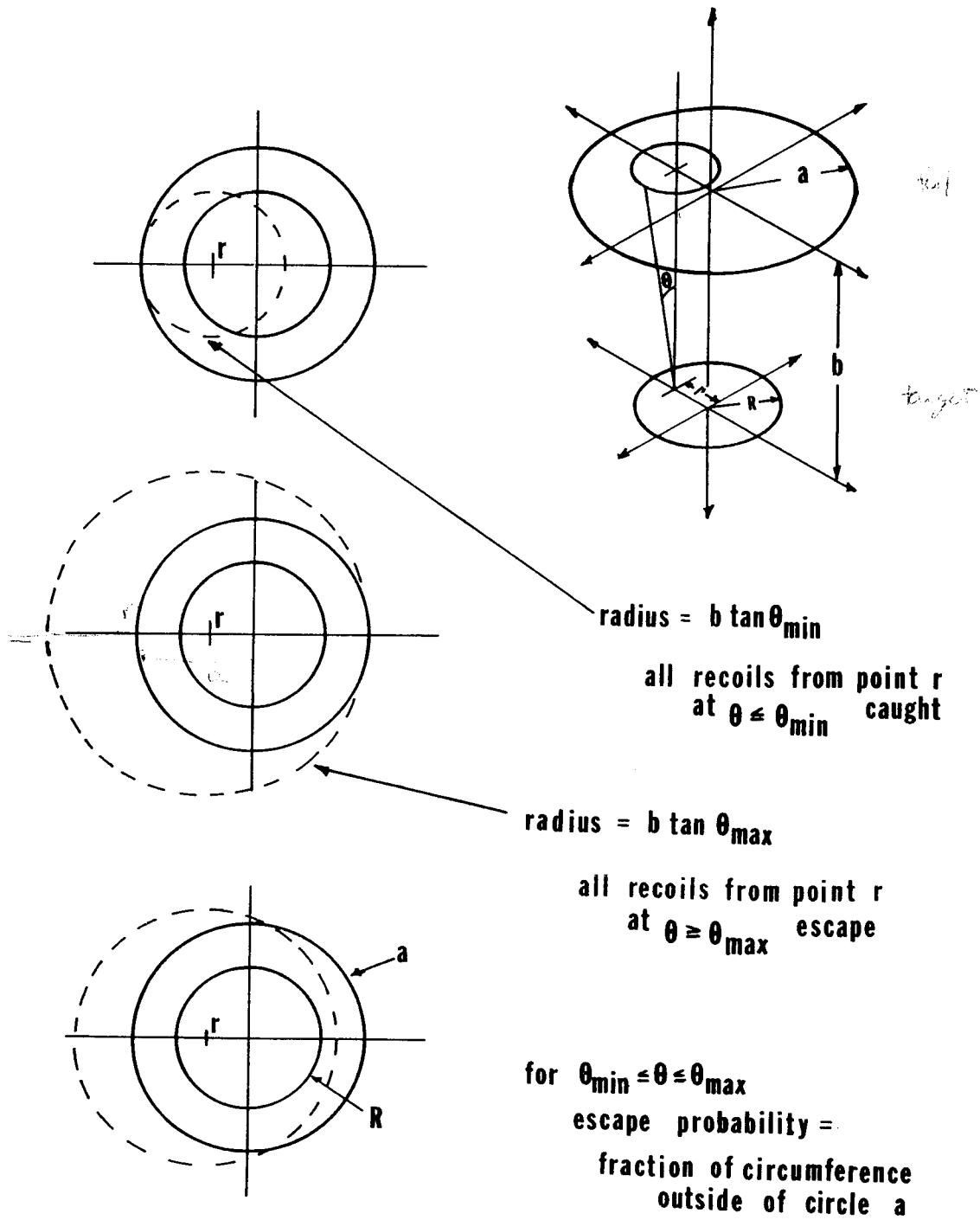
XBL 836-10253

Figure 3a



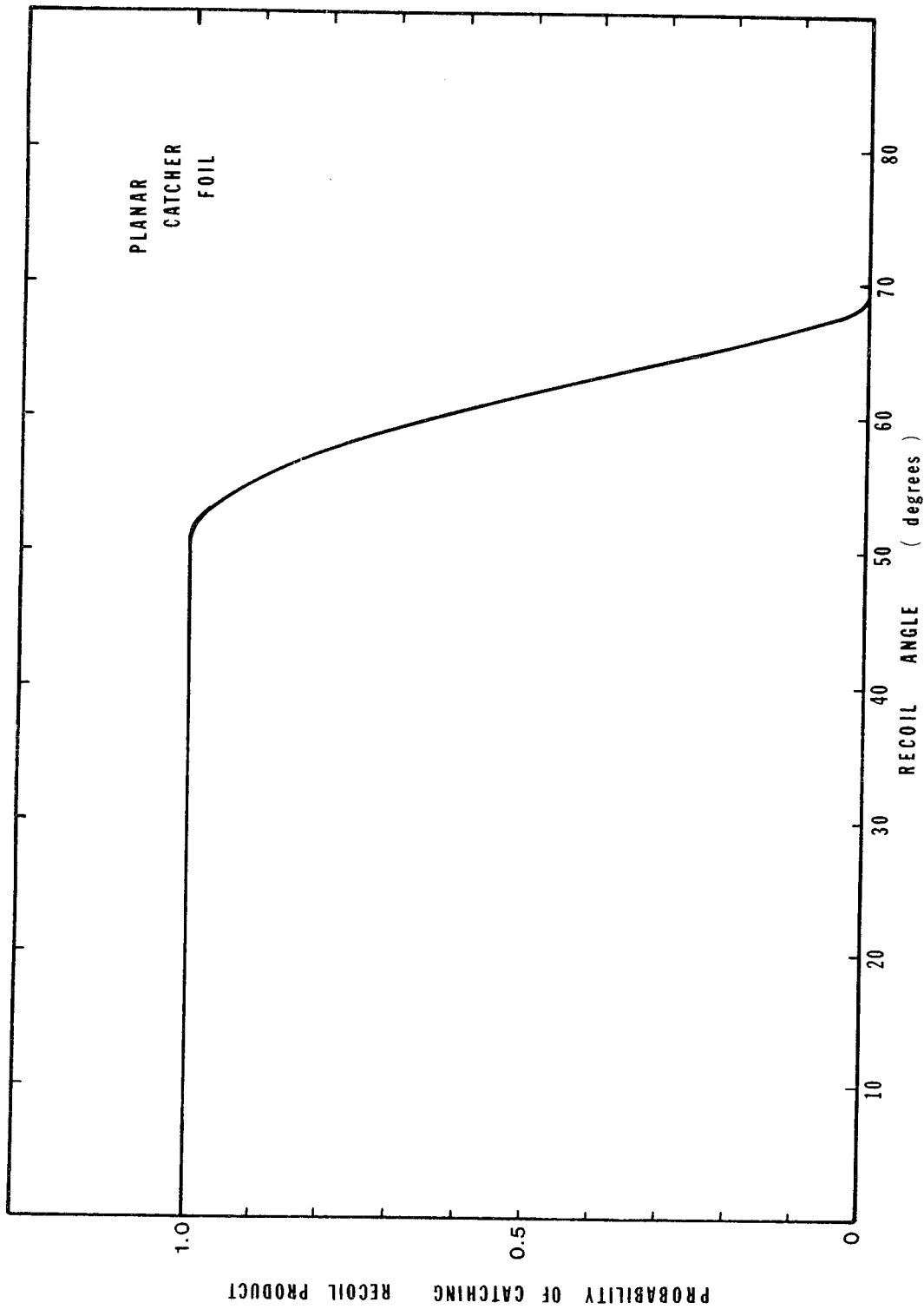
XBL 836-10395

Figure 3b



XBL 836-10249

Figure 3c



XBL 836-10235

Figure 3d

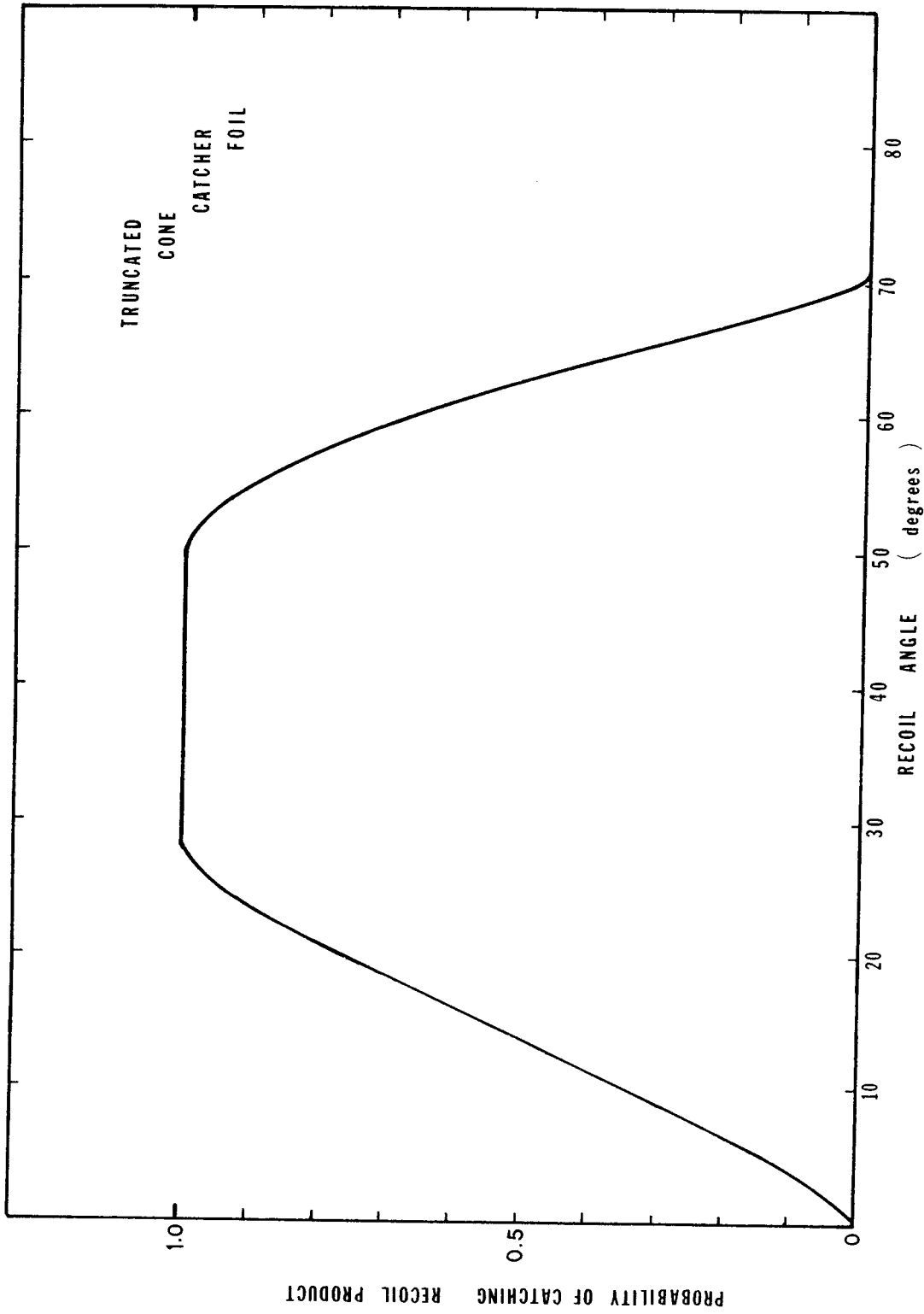


Figure 3e

XBL 836-10234

Section 4 - Results and Discussion

The following tables give the results from the irradiations of ^{248}Cm with ^{136}Xe , ^{86}Kr and ^{18}O ions. A discussion of the determination of beam energies and catcher foil efficiencies is given in Section 3, as is a discussion of the propagation of errors.

Table 4-I Cross sections from the irradiation of a 1.1 mg/cm^2 ^{248}Cm target with 761 to 808 MeV* ^{136}Xe ions. Experiment $^{136}\text{Xe-0}$ (trial run).

Nuclide	Cross section (μb)	Nuclide	Cross section (μb)
^{234}Pa	75 ± 30	^{243}Pu	1100 ± 300
^{238}Np	112 ± 45	^{245}Pu	1430 ± 130
^{239}Np	332 ± 56	^{246}Pu	1100 ± 150
^{240}Np	153 ± 73		

* corresponds to 1.04 to 1.11 times the Coulomb barrier

Table 4-II Cross sections from the irradiation of a 2.15 mg/cm² ²⁴⁸Cm target
with 699 to 790 MeV* ¹³⁶Xe ions. Experiment ¹³⁶Xe-I.

Nuclide	Cross section (μb)	Nuclide	Cross section (μb)
²³² Pa	50 ± 27	²⁴⁸ Bk	450 ± 130
²³⁴ Pa	72 ± 12	²⁵⁰ Bk	1130 ± 80
²³⁷ U	120 ± 50	²⁴⁸ Cf	1.1 ± 0.1
²⁴⁰ U	260 ± 160	²⁴⁸ Cf	93 ± 9
²³⁸ Np	116 ± 16	²⁵⁰ Cf	980 ± 110
²³⁹ Np	227 ± 29	²⁵² Cf	138 ± 17
²⁴⁰ Np	125 ± 48	²⁵³ Cf	11.6 ± 1.0
²⁴³ Pu	850 ± 180	²⁵⁴ Cf	1.53 ± 0.17
²⁴⁵ Pu	1190 ± 220	²⁵² Es	8.7 ± 1.5
²⁴⁶ Pu	930 ± 150	²⁵³ Es	4.4 ± 0.7
²⁴⁴ Am	490 ± 40	^{254m} Es	1.25 ± 0.14
²⁴⁵ Am	2290 ± 440	²⁵⁵ Es	0.51 ± 0.11
²⁴⁶ Am (39 m)	1940 ± 550	²⁵⁶ Es	0.039 ± 0.009
²⁴⁶ Am (25 m)	1640 ± 510	²⁵² Fm	0.084 ± 0.054
²⁴⁷ Am	9960 ± 4180	²⁵³ Fm	0.33 ± 0.12
²⁴⁹ Cm	48000 ± 14000	²⁵⁴ Fm	0.360 ± 0.075
²⁴⁵ Bk	22.1 ± 5.1	²⁵⁵ Fm	0.205 ± 0.074
²⁴⁶ Bk	102 ± 14	²⁵⁶ Fm	0.069 ± 0.021

* corresponds to 0.95 to 1.08 times the Coulomb barrier

Table 4-III Cross sections from the irradiation of a 2.15 mg/cm² ²⁴⁸Cm target with 624 to 716 MeV* ¹³⁶Xe ions. Experiment ¹³⁶Xe-II.

Nuclide	Cross section (μb)	Nuclide	Cross section (μb)
²³⁸ Np	13 ± 11	²⁴⁶ Cf	0.036 ± 0.008
²³⁹ Np	< 22	²⁴⁸ Cf	6.1 ± 1.0
²⁴³ Pu	84 ± 31	²⁵⁰ Cf	94 ± 14
²⁴⁵ Pu	92 ± 34	²⁵² Cf	4.7 ± 0.8
²⁴⁶ Pu	79 ± 29	²⁵³ Cf	0.51 ± 0.09
²⁴⁴ Am	35.0 ± 5.8	²⁵⁴ Cf	0.026 ± 0.018
²⁴⁵ Am	246 ± 70	²⁵⁰ Es	< 1
²⁴⁶ Am (39 m)	180 ± 45	²⁵² Es	0.212 ± 0.081
²⁴⁷ Am	800 ± 330	²⁵³ Es	0.135 ± 0.026
²⁴⁹ Cm	10300 ± 2800	^{254m} Es	0.016 ± 0.005
²⁴⁵ Bk	1.8 ± 1.6	²⁵⁵ Es	0.015 ± 0.005
²⁴⁶ Bk	6.4 ± 2.3	²⁵⁴ Fm	0.018 ± 0.009
²⁴⁸ Bk	71 ± 28	²⁵⁸ Fm	0.004 ± 0.003
²⁵⁰ Bk	91 ± 12	²⁵² Fm + ²⁵⁵ Fm	0.012 ± 0.003

* corresponds to 0.85 to 0.98 times the Coulomb barrier

Table 4-IV Cross sections from the irradiation of a 2.15 mg/cm² ²⁴⁸Cm target
with 493 to 546 MeV* ⁸⁶Kr ions. Experiment ⁸⁶Kr-I.

Nuclide	Cross section (μb)	Nuclide	Cross section (μb)
²³² Pa	75 ± 45	²⁵⁰ Bk	2020 ± 200
²³⁴ Pa	30 ± 23	²⁴⁶ Cf	28.4 ± 5.3
²³⁷ U	240 ± 80	²⁴⁸ Cf	790 ± 130
²³⁸ Np	92 ± 12	²⁵⁰ Cf	2620 ± 490
²³⁹ Np	103 ± 12	²⁵² Cf	142 ± 27
²⁴³ Pu	680 ± 140	²⁵³ Cf	7.8 ± 1.3
²⁴⁵ Pu	460 ± 80	²⁵⁴ Cf	0.34 ± 0.07
²⁴⁶ Pu	290 ± 40	²⁵⁰ Es	104 ± 20
²⁴⁴ Am	1160 ± 130	²⁵¹ Es	82 ± 36
²⁴⁵ Am	3280 ± 680	²⁵² Es	53 ± 27
²⁴⁶ Am (39 m)	2660 ± 750	²⁵³ Es	11.8 ± 1.9
²⁴⁶ Am (25 m)	2520 ± 810	^{254m} Es	1.25 ± 0.20
²⁴⁷ Am	8710 ± 4220	²⁵⁶ Es	0.009 ± 0.004
²⁴⁹ Cm	22500 ± 6400	²⁵² Fm	5.58 ± 0.80
²⁴⁵ Bk	410 ± 63	²⁵³ Fm	4.93 ± 1.06
²⁴⁶ Bk	1400 ± 200	²⁵⁴ Fm	1.80 ± 0.31
²⁴⁸ Bk	3240 ± 500	²⁵⁶ Fm	0.186 ± 0.047

* corresponds to 1.10 to 1.21 times the Coulomb barrier

Table 4-V Cross sections from the irradiation of a 2.15 mg/cm² ²⁴⁸Cm target with 436 to 490 MeV* ⁸⁶Kr ions. Experiment ⁸⁶Kr-II.

Trans-berkelium nuclides lost in chemistry.

Nuclide	Cross section (μb)	Nuclide	Cross section
²³⁸ Np	56 ± 36	²⁴⁶ Am (39 m)	650 ± 110
²³⁹ Np	76 ± 30	²⁴⁶ Am (25 m)	620 ± 160
²⁴³ Pu	116 ± 33	²⁴⁷ Am	2960 ± 690
²⁴⁵ Pu	96 ± 32	²⁴⁹ Cm	6000 ± 5500
²⁴⁶ Pu	38 ± 34	²⁴⁵ Bk	41 ± 17
²⁴⁴ Am	167 ± 33	²⁴⁶ Bk	186 ± 41
²⁴⁵ Am	760 ± 280	²⁴⁸ Bk	600 ± 250
		²⁵⁰ Bk	278 ± 35

* corresponds to 0.97 to 1.09 times the Coulomb barrier

Table 4-VI Cross sections from the irradiation of a 2.15 mg/cm² ²⁴⁸Cm target with 402 to 457 MeV* ⁸⁶Kr ions. Experiment ⁸⁶Kr-III.

Nuclide	Cross section (μb)	Nuclide	Cross section (μb)
²³⁹ Np	9.3 \pm 8.0	²⁴⁸ Cf	86 \pm 14
²⁴³ Pu	36 \pm 15	²⁵⁰ Cf	560 \pm 90
²⁴⁵ Pu	26 \pm 14	²⁵² Cf	29 \pm 13
²⁴⁶ Pu	23 \pm 16	²⁵³ Cf	1.25 \pm 0.20
²⁴⁴ Am	58 \pm 11	²⁵⁴ Cf	0.030 \pm 0.025
²⁴⁵ Am	300 \pm 260	²⁵⁰ Es	20 \pm 14
²⁴⁶ Am (39 m)	72 \pm 25	²⁵² Es	4.0 \pm 1.1
²⁴⁷ Am	590 \pm 110	²⁵³ Es	1.6 \pm 0.3
²⁴⁵ Bk	29 \pm 9	^{254m} Es	0.049 \pm 0.011
²⁴⁶ Bk	63 \pm 12	²⁵⁵ Es	0.018 \pm 0.006
²⁴⁸ Bk	220 \pm 70	²⁵² Fm	0.34 \pm 0.06
²⁵⁰ Bk	107 \pm 24	²⁵³ Fm	0.52 \pm 0.12
²⁴⁶ Cf	1.97 \pm 0.32	²⁵⁴ Fm	0.15 \pm 0.04

* corresponds to 0.89 to 1.02 times the Coulomb barrier

Table 4-VII Cross sections from the irradiation of a 2.15 mg/cm² ²⁴⁸Cm target
with 379 to 435 MeV* ⁸⁶Kr ions. Experiment ⁸⁶Kr-IV.

Nuclide	Cross section (μb)	Nuclide	Cross section (μb)
²³⁸ Np	9.5 ± 4.4	²⁴⁸ Cf	20.6 ± 3.4
²³⁹ Np	< 20	²⁵⁰ Cf	96 ± 48
²⁴³ Pu	15 ± 8	²⁵² Cf	3.8 ± 0.8
²⁴⁵ Pu	54 ± 31	²⁵³ Cf	0.078 ± 0.017
²⁴⁶ Pu	17 ± 10	²⁵⁰ Es	< 3
²⁴⁴ Am	21 ± 4	²⁵² Es	0.32 ± 0.08
²⁴⁵ Am	140 ± 47	²⁵³ Es	0.11 ± 0.02
²⁴⁹ Cm	1430 ± 870	^{254^m} Es	0.0088 ± 0.0031
²⁴⁵ Bk	3.8 ± 1.5	²⁵² Fm	0.082 ± 0.015
²⁴⁶ Bk	22.5 ± 4.3	²⁵³ Fm	0.081 ± 0.020
²⁴⁸ Bk	92 ± 32	²⁵⁴ Fm	0.029 ± 0.008
²⁵⁰ Bk	37 ± 6	²⁵⁶ Fm	< 0.0025
²⁴⁶ Cf	0.48 ± 0.09		

* corresponds to 0.84 to 0.97 times the Coulomb barrier

Table 4-VIII Cross sections from the irradiation of a 0.52 mg/cm² ²⁴⁸Cm target with 95.5 to 96.5 MeV* ¹⁸O ions. Experiment ¹⁸O-I.

Nuclide	Cross section (μb)	Nuclide	Cross section (μb)
²³² Pa	11.4 \pm 3.8	²⁴¹ Cm	20 \pm 10
²³⁸ Np	< 4	²⁴⁹ Cm	11000 \pm 1000
²³⁹ Np	6.7 \pm 3.0	²⁴⁵ Bk	< 8
²⁴³ Pu	13.6 \pm 3.3	²⁴⁶ Bk	5.1 \pm 1.7
²⁴⁵ Pu	5.3 \pm 2.3	²⁴⁸ Bk	188 \pm 33
²⁴⁶ Pu	7.2 \pm 3.9	²⁵⁰ Bk	2880 \pm 90
²⁴⁴ Am	16.0 \pm 8.5	²⁵¹ Bk	650 \pm 120
²⁴⁵ Am	65.6 \pm 15.2	²⁴⁹ Es	8 \pm 5

* corresponds to 1.04 to 1.05 times the Coulomb barrier

Table 4-IX Cross sections from the irradiation of a 0.52 mg/cm² ²⁴⁸Cm target with 95.5 to 96.5 MeV* ¹⁸O ions. Experiment ¹⁸O-II.

Nuclide	Cross section (μb)	Nuclide	Cross section (μb)
²⁴⁰ Np	< 7	²⁴⁷ Am	72 \pm 26
²⁴⁵ Am	67 \pm 31	²⁴⁹ Cm	9000 \pm 900
²⁴⁶ Am (39 m)	15 \pm 10	²⁵⁰ Bk	2820 \pm 140
²⁴⁶ Am (25 m)	21 \pm 9	²⁵¹ Bk	550 \pm 110

* corresponds to 1.04 to 1.05 times the Coulomb barrier

Figure 4a is a plot of the data in Table 4-I for experiment $^{136}\text{Xe-0}$.

Figure 4b is a plot of the data in Table 4-II for experiment $^{136}\text{Xe-I}$.

Figure 4c is a plot of the data in Table 4-III for experiment $^{136}\text{Xe-II}$.

Figure 4d is a plot of the data in Table 4-IV for experiment $^{86}\text{Kr-I}$.

Figure 4e is a plot of the data in Table 4-V for experiment $^{86}\text{Kr-II}$.

Figure 4f is a plot of the data in Table 4-VI for experiment $^{86}\text{Kr-III}$.

Figure 4g is a plot of the data in Table 4-VII for experiment $^{86}\text{Kr-IV}$.

Figure 4h is a plot of the data in Tables 4-VIII and 4-IX, and the data in reference [Lee83] for the same reaction, of 96 MeV ^{18}O with ^{248}Cm .

As mentioned in Section 3, the data in the above tables are not corrected for growth and decay during the bombardment or before the chemical separation, because the parent activities are either produced with a much smaller cross section than the daughter, or the half life of the parent is long compared with the bombardment length. However, ^{239}Np yields are anomalously high due to feeding from ^{239}U , and ^{250}Cf yields are too high due to feeding from ^{250}Bk . In the case of the ^{250}Cf - ^{250}Bk pair, the size of the cross sections provides a check on the relative chemical yields of the californium and berkelium fractions, neither of which is directly measured. The measured ^{250}Cf cross section should be the same size or slightly larger than the ^{250}Bk cross section due to the short half life of ^{250}Bk relative to the bombardment length. In experiment $^{136}\text{Xe-I}$, the assumption of an 80% chemical yield for californium is evidently slightly too high. In experiment $^{86}\text{Kr-III}$, the application of the americium yield to the berkeliums is evidently incorrect, possibly due to some of the berkelium being eluted from the alpha-hydroxyisobutyrate column before the stripping step. In figure 4h, where the data from experiments $^{18}\text{O-I}$ and $^{18}\text{O-II}$, as well as data from the literature are plotted, the ^{250}Cf cross section has been corrected for feed-

ing. In Section 3, the possibility that the target used in [Lee82] and [Lee83] was too thick for all the recoils to escape was discussed. Figure 4i shows the comparison of the berkelium cross sections from that work and from this one. The ^{251}Bk cross sections do not directly compare due to the use of a different gamma ray abundance in the two cross section calculations. In reactions taking place at the quasi-elastic limit, the previous experiments clearly suffered from a loss of a substantial amount of the recoiling products. For the lighter mass berkeliums, the cross section values from the two different targets become equal, so the ^{245}Bk and ^{246}Bk data from the older experiments are plotted in figure 4h.

Figure 4j shows several excitation functions from ^{86}Kr and ^{136}Xe reactions with ^{248}Cm . In the neighborhood of the Coulomb barrier and below, a change in projectile energy does very little to change the relative neutron-richness of the products. Compare, for instance, ^{246}Cf and ^{254}Cf in the ^{136}Xe data and ^{246}Cf and ^{253}Cf in the ^{86}Kr data. In the $^{86}\text{Kr} + ^{248}\text{Cm}$ system, however, where a bombardment was performed at 10% to 20% in excess of the nominal Coulomb barrier, the neutron-rich products become slightly depleted relative to the neutron-deficient products. At the higher bombarding energy, more excitation energy is thermalized in the reaction, resulting in fractionally more particle emission. The depletion of highly excited products due to fission competition makes the shift away from neutron-richness less important than it might otherwise be. This has also been seen in the $^{18}\text{O} + ^{248}\text{Cm}$ system [Lee83] where most of the excitation energy is deposited in the massive component of the reaction. At the energy excess explored in this work, the cross sections for all surviving evaporation residues are still increasing with energy. This reflects the increase in the total reaction cross section in the vicinity of the Coulomb barrier. At still higher energies, where the mean excitation energy and angular momentum in

the primary products is still increasing, the fraction of products which are cool enough to survive fission will decrease more quickly than the slowly-changing reaction cross section is increasing, so the evaporation residue cross sections should "turn over," starting with those products with the highest Z difference where the mass flow and excitation energies are highest. This has been seen in $^{48}\text{Ca} + ^{248}\text{Cm}$ bombardments at several energies up to 20% in excess of the Coulomb barrier [Gag83] and in $^{18}\text{O} + ^{248}\text{Cm}$ bombardments [Lee83].

A measure of angular momentum in products surviving fission can be obtained from isomer ratios [Gro83]. In ^{246}Am , the two isomers have roughly the same energy, the spin of the 25 minute isomer is 2- and the spin of the 39 minute isomer is 7- [TOI78]. If the mean intrinsic angular momentum of the primary products surviving fission to result in ^{246}Am were significantly greater than $7\hbar$, production of the 39 minute isomer would dominate. Instead, the two isomers are produced in roughly equal amounts, though in the case of the ^{18}O -II results (Table 4-IX) the data are poor. In bombardments where ^{250}Es was formed from ^{249}Cf with ^{18}O [Lee82a], the 1- isomer is greatly favored over the 6+ isomer, with the ratio of 6+ to 1- increasing at higher bombarding energy. The light ^{18}O projectile does not transfer as much angular momentum into intrinsic modes in a peripheral reaction as do ^{86}Kr and ^{136}Xe , though the amount increases at higher bombarding energies. No direct information was determined for isomer ratios in deeper collisions in these systems, though the downward deviation of the ^{254m}Es (spin=2+) point relative to the other einsteinium isotopes in figures 4b, 4c and 4f indicates that the cross section of the ground state ^{254}Es (spin=7+) is of a similar magnitude as that of the isomer. The primary products which could produce ^{254}Es evaporation residues must have higher intrinsic angular momenta than those which produce ^{246}Am , since the collision is more damped. Yet the observed ^{254}Es seems to result from the de-

excitation of primary products with little more angular momentum. Therefore, very high angular momentum components in the primary distributions are all more severely depleted by fission than are the low angular momentum components. The low barrier to fission in the actinides acts as an angular momentum filter.

A striking difference between the reaction of very heavy ions like ^{86}Kr and ^{136}Xe and the reaction of light heavy ions like ^{18}O with ^{248}Cm is the apparent augmentation of above-target products and the depletion of the below-target products in the light heavy ion reactions. This is due to the combination of two effects: the reaction Q-values and the Coulomb separation energies. If one is used to thinking in chemical terms, these can be compared with the evolved heat and the activation energy of the reaction, respectively. The Coulomb energy of two touching spheres can be calculated using the radius defined in equation III.23. In figure 4k, the Coulomb potentials of touching spheres arising from the binary reactions indicated, assuming N/Z equilibration, are plotted as a function of the Z of the heavy product. The Coulomb potential of the initial system is subtracted. From a purely Coulomb standpoint, the removal of charge from the target to the projectile is unfavorable, and in the case of ^{18}O reactions, where the exchange of one charge is a large fraction of the whole projectile, it is particularly unfavorable. Furthermore, an energy excess of 5% over the potential barrier is only 4 MeV with ^{18}O , while with the heavier ions it is considerably more. Thus, with ^{18}O induced reactions the amount of "free" energy is small relative to the driving force of the Coulomb potentials. In the intermediate colliding system, the tendency will be for charge to flow toward the large fragment. Since N/Z is equilibrated, this pushes the mass flow in that direction. This effect is very strong in the $^{18}\text{O} + ^{248}\text{Cm}$ system, driving toward the compound nucleus. With heavier ions, this transient driving potential is less

important, especially in comparison with the size of the Coulomb potential and the projectile energy necessary to overcome it.

Figure 4l shows the Q-values for forming particular species from ^{248}Cm in binary reactions with various heavy ions. Once again, the most extreme results are for the lightest ions. In this case, however, the driving force is in the other direction. The production of fermium isotopes in the reaction of ^{18}O with ^{248}Cm is favored by the push of the Coulomb potentials at contact, but is "endothermic" by 30 to 50 MeV. This negative Q-value acts to decrease the excitation energy of the primary fermium products, making them more likely to survive fission. Not only are below-target species unfavorable from the Coulomb argument, but those which are produced are depleted by fission due to the "exothermic" nature of the reaction. One thing which helps the below-target species to survive is the mass of the complementary fragment, which carries away considerably more of the excitation energy and angular momentum than that of the more asymmetric reaction resulting in the fermium isotopes. It is therefore hardly surprising that the above-target yields are very high in the $^{18}\text{O} + ^{248}\text{Cm}$ reaction compared to those arising from reactions with heavier ions. Figure 4j shows that with very heavy ions the cross sections of both above- and below-target species increase with energy. No similar data exists for the $^{18}\text{O} + ^{248}\text{Cm}$ system, but in $^{18}\text{O} + ^{249}\text{Cf}$ reactions, the cross sections of the berkelium reaction products drop off with energy well before the above-target cross sections [Moo82], indicating that even in reactions near the Coulomb barrier the excitation energies of these products are well into the region where fission is predominant.

The regular behavior of Q-values and Coulomb potentials from one projectile-target combination to the next, as well as the expected regularity of the thermalized energy and angular momentum and the partition of these

quantities between the participants, indicates that the ratio of the production cross sections of a below-target species to an above-target species should be more-or-less regular. Figure 4m shows the plot of the ratio of $\sigma(^{246}\text{Pu})$ to $\sigma(^{253}\text{Es})$ as a function of projectile identity. The ^{18}O point is a combination of the ^{246}Pu point determined in this work with the ^{253}Es point at the same energy of bombardment in the literature [Lee83]. The ^{48}Ca data, taken from a reaction at 10% over the barrier, was derived from other work [Hof83,Gag83]. The ^{86}Kr and ^{136}Xe data points are from the highest energy bombardments reported here. The ^{208}Pb point is from some preliminary data taken at roughly 20% over the reaction barrier [Wel83]. The two nuclides were picked because they are independent yields and they are both on the neutron-rich side of the maximum of the distributions for their respective elements. The downward deviation of the ^{86}Kr point is due, in part, to its N/Z and to the energy excess of the bombardment. The ^{208}Pb point may also be low due to the very high bombarding energy, which would deplete the neutron-rich ^{246}Pu more than the ^{253}Es , which is very close to the maximum of the einsteinium distribution.

The small, but non-zero, cross section for below-target nuclides in light heavy ion bombardments is interesting from another standpoint. The population of shape isomers in heavy ion bombardments has been observed, both in complete fusion reactions [Spe73], where the isomer ratio of shape isomer to ground state in the light americium isotopes is in the range of 10^{-3} to 10^{-4} , and in quasi-elastic reactions [Gan67], where the isomer ratio is closer to 10^{-5} . Presumably, with an intermediate reaction mechanism, an intermediate isomer ratio would arise. Below-target actinide cross sections in the reaction of ^{18}O ions with ^{248}Cm are on the order of tens of microbarns, meaning that spontaneous fission isomers in americium and curium might be expected to be formed with nanobarn cross sections. This directly affects the use of short-lived spon-

taneous fission activities to characterize new isotopes and elements

[Som82,Oga70] since the production cross sections are on this order.

As shown above, the neutron-richness of the reaction products is only weakly dependent upon the projectile energy near the Coulomb barrier. It is determined by a combination of the height of the fission barrier and the lower edge of the low angular momentum energy distributions of the primary reaction products. An upward shift in the energy distributions of, say, a fermium nuclide will not directly increase the number of neutrons that have to be emitted to de-excite the primary product; rather, it decreases the fractional number of primary products which survive the fission process. Figure 4n shows a plot of fermium isotope cross sections from several experiments, all in the neighborhood of, or slightly over, the nominal Coulomb barrier, plotted against the difference between the isotope mass and the mass of a $Z=100$ species with the N/Z of the composite intermediate of the reaction. The formation of fermium isotopes is a large enough exchange that it can be thought of as being due purely to a damped reaction, and not to have any peripheral, quasi-elastic components. The distribution in the fermium isotopes in ^{18}O induced reactions [Lee83] peaks roughly two mass numbers below that predicted for N/Z equilibration. The peaks from ^{48}Ca [Hof83] and ^{86}Kr reactions are only about one mass number below the prediction. Even though the reaction to produce fermium isotopes in the $^{18}\text{O} + ^{248}\text{Cm}$ system is very endothermic, the partition of energy and angular momentum between the projectile and target produces a higher intrinsic excitation of the target due to the extremely small mass of the other reaction component. Also, the small amount of angular momentum induced by the ^{18}O projectile in the actinide products effectively raises the "average" fission barriers relative to those of the heavier systems, making particle emission more favorable in comparison with fission. For a while, at least, an

increase in the mass of the projectile and the corresponding introduction of more angular momentum into the primary reaction products decreases the average number of neutrons emitted in forming evaporation residues by decreasing the survival probability of the more highly excited species. The average number of neutrons emitted by the primary products which survive fission to produce fermium is lower in ^{48}Ca and ^{86}Kr reactions with ^{248}Cm than it is in the $^{18}\text{O} + ^{248}\text{Cm}$ system. As the mass of the projectile increases still further, however, the number of emitted neutrons increases. In bombardments with ^{136}Xe , the peak in the fermium cross section distribution is two mass units below the equilibrated N/Z value, and in bombardments with ^{238}U ions [Sch82], the peak is four mass units low. This latter number is in rough agreement with the results obtained from calculations involving relative neutron and fission decay widths. The greater energy evolved in the reaction and the loss of any endothermic enhancement of the cross section for survival decreases the number of primary products formed at a low enough excitation to produce fermium isotopes by the emission of only a couple of neutrons to the point that, even with their increased probability of survival, they are not an important contribution to the evaporation residue cross sections.

In spite of the fact that surviving actinide products from damped collisions of the heaviest ions with ^{248}Cm are those which have lost the most neutrons in their de-excitation, the relative neutron-richness of these products is as high as those resulting from any of the other systems due to the neutron-richness of the projectiles. The ^{254}Fm nuclide is designated in each distribution in figure 4n. This shows that the position of the peak in the fermiums relative to the absolute neutron numbers of the products is in roughly the same place for each reaction except for the $^{86}\text{Kr} + ^{248}\text{Cm}$ system which has a lower N/Z (1.530) than any of the other reactions (from 1.552 for $^{48}\text{Ca} + ^{248}\text{Cm}$ to 1.585 for $^{238}\text{U} +$

^{248}Cm). The best projectile for producing new, neutron-rich isotopes above the target is, then, the one which produces the broadest cross section distribution in the element of interest. This is expected to be the largest projectile, not only due to the enhanced statistical fluctuation of neutrons and protons in the separating system, but also due to low level contributions of products formed in de-excitation channels involving the emission of significantly fewer neutrons than that resulting in the peaks of the isotopic distributions. Figure 4o demonstrates this with the cross sections of the heaviest californium isotopes resulting from the same bombardments that produced the data in figure 4n. Clearly, ^{136}Xe and ^{238}U projectiles are superior to the lighter ions for production of californium isotopes heavier than mass 255, even taking into account the fact that beam intensities of the heavier ions are limited by target heating (see Section 2). Another aspect of this is demonstrated in figures 4p and 4q, which show the excitation functions of ^{253}Es and ^{253}Cf , respectively. Production of ^{253}Es is better accomplished with the light projectile ^{16}O [Lee83]. A single curve can be drawn through the points arising from ^{86}Kr , ^{136}Xe and ^{238}U bombardments. With the more neutron-rich ^{253}Cf , the cross sections from ^{40}Ca and ^{86}Kr bombardments move well below those from ^{136}Xe and ^{238}U bombardments, and the data from ^{16}O bombardments look relatively less favorable.

The examination of figure 1a shows that with neutron-rich actinide targets, considerable transfer of mass has to take place to reach unknown nuclides at a higher Z than the target. Most of these targets, however, are perched right on the edge of unknown territory at Z -values below that of the target. Therefore, while a deep-inelastic mechanism must be assumed for the formation of new above-target nuclides in these transfer reactions, below-target nuclides can be produced in quasi-elastic reactions. The advantage here is not only that the intrinsic energy and angular momentum of the primary products is lower, but

that the neutron-richness of the actinide product is more determined by the neutron number of the target than by the N/Z of the composite system. This is shown in figure 4r, where the plutonium cross sections arising from various heavy ion bombardments are plotted against the difference between the isotope mass and the value expected at $Z=94$ from N/Z equilibration. The peaks of the distributions are all much more neutron-rich than those expected from a damped mechanism. Unfortunately, there are no "observable" plutonium isotopes in the region of the equilibrium A whose cross sections can be compared with the magnitude of the quasi-elastic peak, but deep-inelastic products are observed in the neptunium, uranium and protactinium isotopes.

Since ^{136}Xe has a higher N/Z than either ^{48}Ca or ^{86}Kr , the probability of a neutron-rich transfer to the target is statistically more probable. This is shown by comparison of figures 4s and 4t, where plutonium cross sections from the reactions of heavy ions with ^{248}Cm are plotted as a function of the beam energy, stated as a fraction of the Coulomb barrier. The augmentation of ^{246}Pu yields is seen relative to ^{243}Pu yields in the $^{136}\text{Xe} + ^{248}\text{Cm}$ reactions. Presumably the reaction of larger, more neutron-rich projectiles would produce an even greater augmentation of neutron-rich plutonium yields.

Simple extrapolations of cross section distributions for a given element from the reaction of heavy ions with ^{248}Cm paint a pretty grim picture for above-target neutron-rich new isotope synthesis. Cross sections on the order of 10 nanobarns can be expected for the production of ^{257}Cf and ^{257}Es from the reaction of ^{238}U with ^{248}Cm at an energy in excess of the nominal Coulomb barrier by approximately 10%. Since both of these nuclides are known to be largely beta-minus emitters [Com66], they are produced below the limit of detection by normal chemical methods, though in combination with an on-line mass separator the presence and decay of these species might be observable. The cross

section for ^{260}Fm , whose decay mode is uncertain, should be on the order of 100 picobarns or less in this same reaction. There is some hope for the production of beta-minus decaying ^{252}Bk , which is near enough to the target mass and charge to make ^{18}O the best projectile. The production cross section should be on the order of 50 microbarns. The situation below the target is considerably different. With heavy projectiles, like ^{136}Xe or ^{238}U , in bombardments at energies over the nominal Coulomb barrier, the production of unknown species like ^{248}Am , ^{249}Am and ^{247}Pu from ^{248}Cm targets should take place on the 100 microbarn to 1 millibarn level. Section 6 describes an unsuccessful chemical search for ^{247}Pu .

Extension of this work to other targets suggests that the best ways to make new neutron-rich isotopes of uranium and neptunium is with a ^{244}Pu target, and the best way to produce new heavy berkelium isotopes is with a ^{252}Cf target. Both of these materials are available in quantities to make heavy ion bombardments feasible, though the difficulty of handling the ^{252}Cf material requires the use of elaborate safety precautions. The use of heavy ion transfer reactions with actinide targets to make trans-target species is limited. The usable beam intensities are low due to the energy loss of the beam, and this necessitates the use of large amounts of target material to produce an observable amount of product activity. Only ^{254}Es , currently producible in the tens of micrograms, is located in a position on the chart of the nuclides to be useful in making new neutron-rich activities above the target Z in measurable amounts in these reactions [Sch82a]. A nuclide which is currently unavailable in microgram quantities, but is potentially the most useful for both above- and below-target new actinide synthesis, is ^{250}Cm . It is by far the most neutron-rich actinide with a long half life ($\sim 10^4$ years) [TOI78]. At present it is producible in useful quantities only in nuclear explosions, and the expense of recovering it is prohibitive.

Figure Captions

Figure 4a - Actinide yields from the reaction of 761 to 808 MeV ^{136}Xe ions with ^{248}Cm . Experiment ^{136}Xe -0.

Figure 4b - Actinide yields from the reaction of 699 to 790 MeV ^{136}Xe ions with ^{248}Cm . Experiment ^{136}Xe -I.

Figure 4c - Actinide yields from the reaction of 624 to 716 MeV ^{136}Xe ions with ^{248}Cm . Experiment ^{136}Xe -II.

Figure 4d - Actinide yields from the reaction of 493 to 546 MeV ^{86}Kr ions with ^{248}Cm . Experiment ^{86}Kr -I.

Figure 4e - Actinide yields from the reaction of 436 to 490 MeV ^{86}Kr ions with ^{248}Cm . Experiment ^{86}Kr -II.

Figure 4f - Actinide yields from the reaction of 402 to 457 MeV ^{86}Kr ions with ^{248}Cm . Experiment ^{86}Kr -III.

Figure 4g - Actinide yields from the reaction of 379 to 435 MeV ^{86}Kr ions with ^{248}Cm . Experiment ^{86}Kr -IV.

Figure 4h - Actinide yields from the reaction of 95.5 to 96.5 MeV ^{18}O ions with ^{248}Cm . Experiments ^{18}O -I and ^{18}O -II, plotted with trans-berkelium yields from [Lee83].

Figure 4i - A comparison of the berkelium isotope yields from the reaction of 96 MeV ^{18}O with ^{248}Cm from this work and from the work of Lee et.al. [Lee83]. Depletion of the heaviest berkelium nuclides is attributed to losses in the thick target used by Lee et.al.

Figure 4j - Some excitation functions from the reactions of ^{86}Kr and ^{136}Xe with ^{248}Cm . The energy is given in terms of a fraction of the nominal Coulomb barrier. Energy error bars describe the difference between the energy of the ions entering and leaving the target material. It should be realized that most of

the reaction cross section is coming from projectiles at the highest energy extremes of the error bars.

Figure 4k - The difference between the Coulomb repulsive energy of two touching spherical reaction products and the Coulomb energy of the reactants at contact. The equilibration of N/Z is assumed in the mass numbers used in calculating the hard sphere radii of the products. The Coulomb driving force of the reactions is toward asymmetry.

Figure 4l - Q_{gg} values for the isotopes of even-Z actinide reaction products arising from several heavy ion reactions with ^{248}Cm targets. Production of below-target products is exothermic. The mass excess data used in the calculations was taken from [How80].

Figure 4m - The ratio of the cross section for the formation of ^{246}Pu to that for ^{253}Es for several heavy ion reactions with ^{248}Cm at energies near or above the nominal reaction barrier.

Figure 4n - Production of fermium isotopes from several heavy ion reactions with ^{248}Cm at energies near or above the nominal Coulomb barrier. The data are plotted against the difference of the nuclide mass number and the mass expected for a Z=100 primary species arising from N/Z equilibration. The ^{254}Fm data points are filled in.

Figure 4o - Neutron-rich californium yields arising from the reaction of various heavy ions with ^{248}Cm .

Figure 4p - The production of ^{269}Es from the reaction of heavy ions with ^{248}Cm as a function of energy relative to the nominal Coulomb barrier.

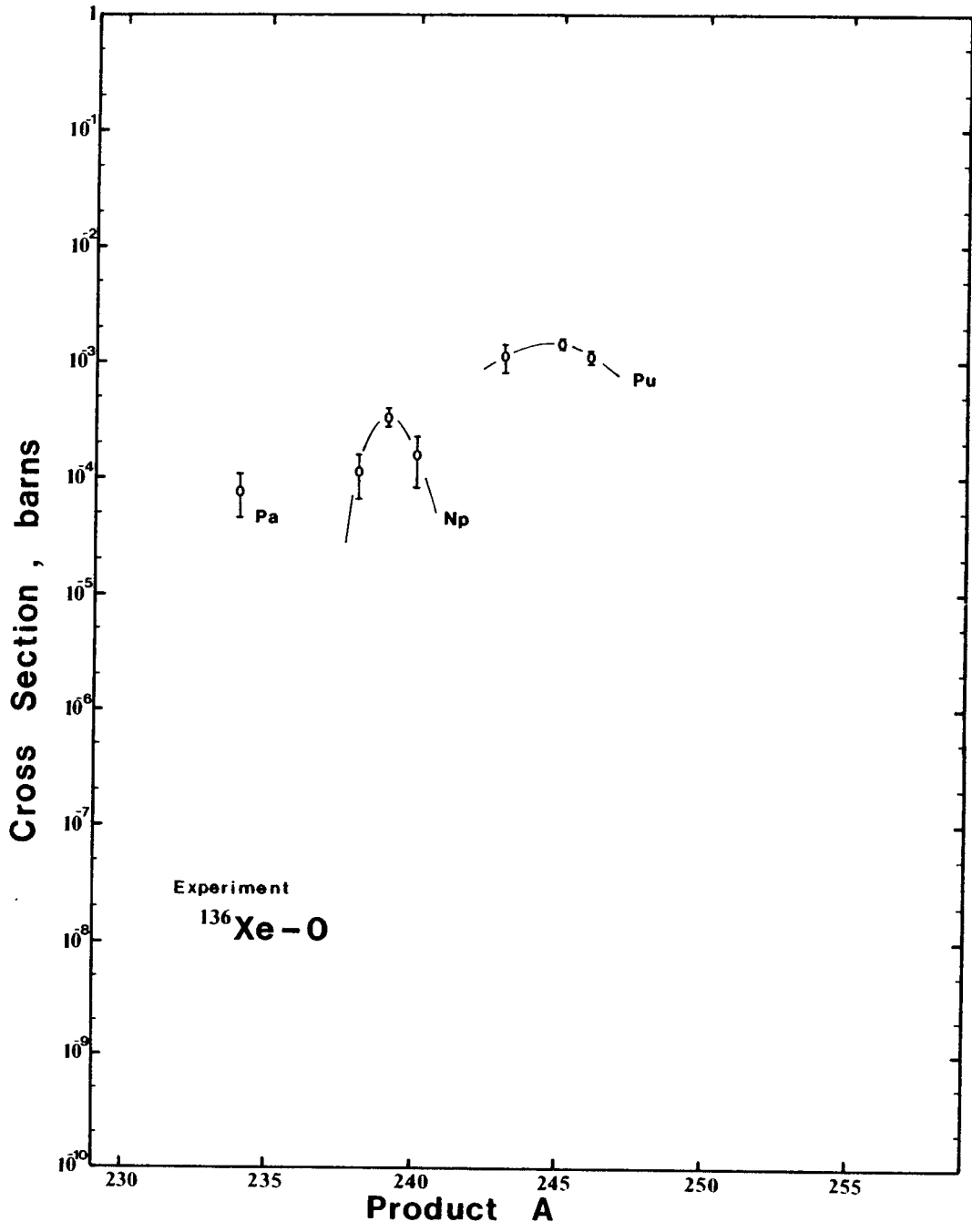
Figure 4q - The production of ^{253}Cf from the reaction of heavy ions with ^{248}Cm as a function of energy relative to the nominal Coulomb barrier.

Figure 4r - Production of plutonium isotopes from several heavy ion reac-

tions with ^{248}Cm at energies near or above the nominal Coulomb barrier. The data are plotted against the difference of the nuclide mass number and the mass expected for a $Z=94$ species arising from N/Z equilibration. The highest mass point on each distribution is ^{246}Pu .

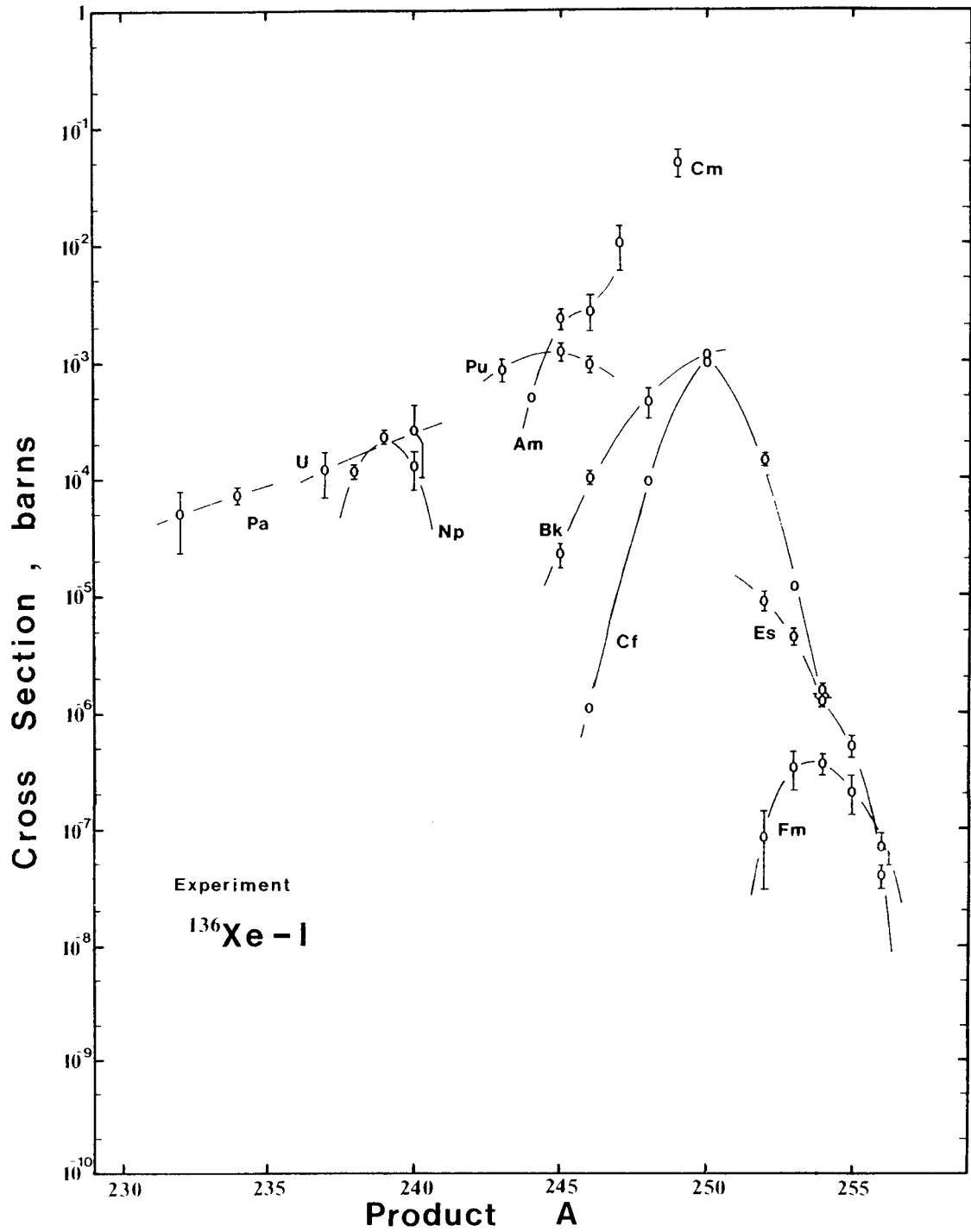
Figure 4s - The production of ^{243}Pu from the reaction of heavy ions with ^{248}Cm as a function of energy relative to the nominal Coulomb barrier.

Figure 4t - The production of ^{246}Pu from the reaction of heavy ions with ^{248}Cm as a function of energy relative to the nominal Coulomb barrier.



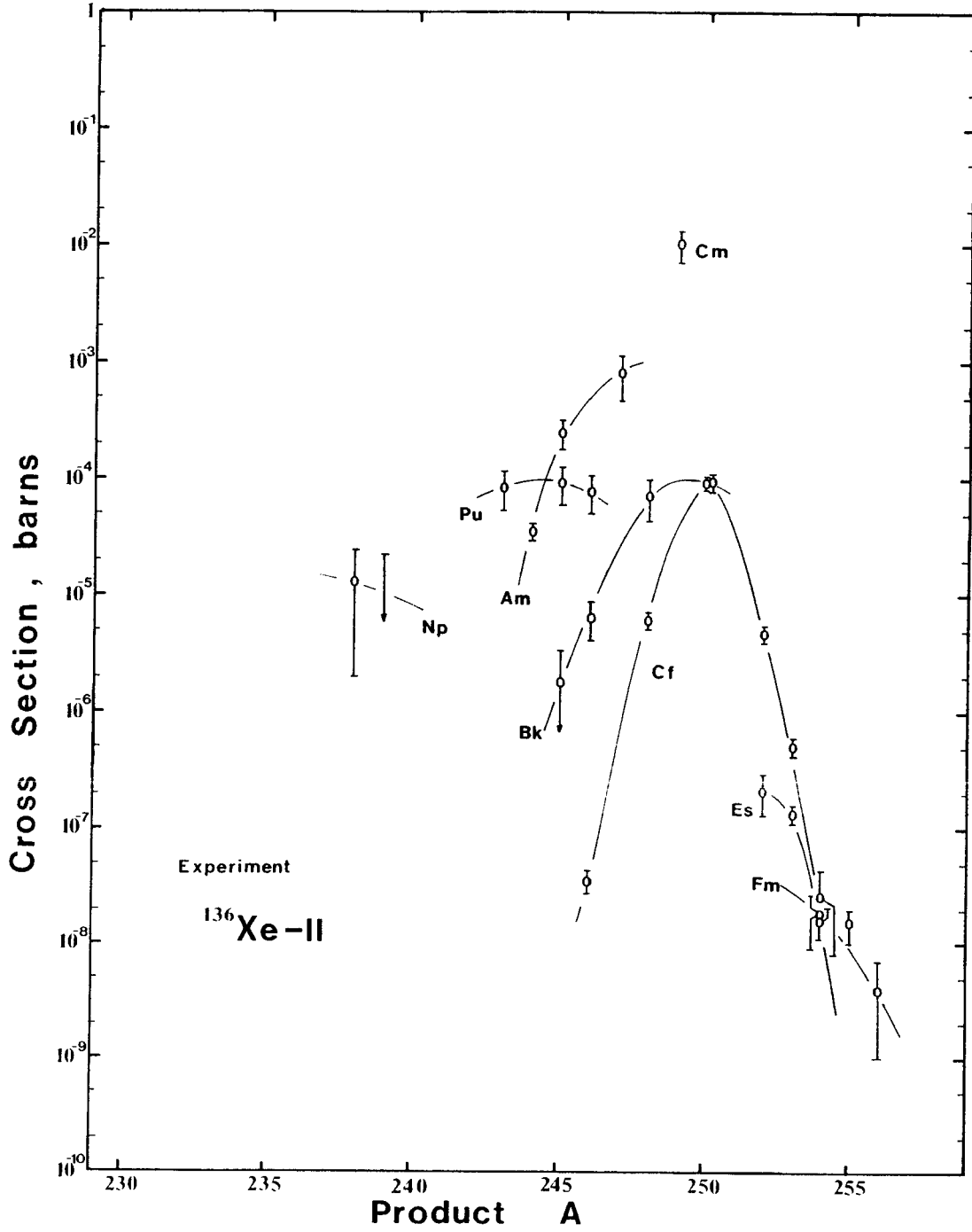
XBL 836-10236

Figure 4a



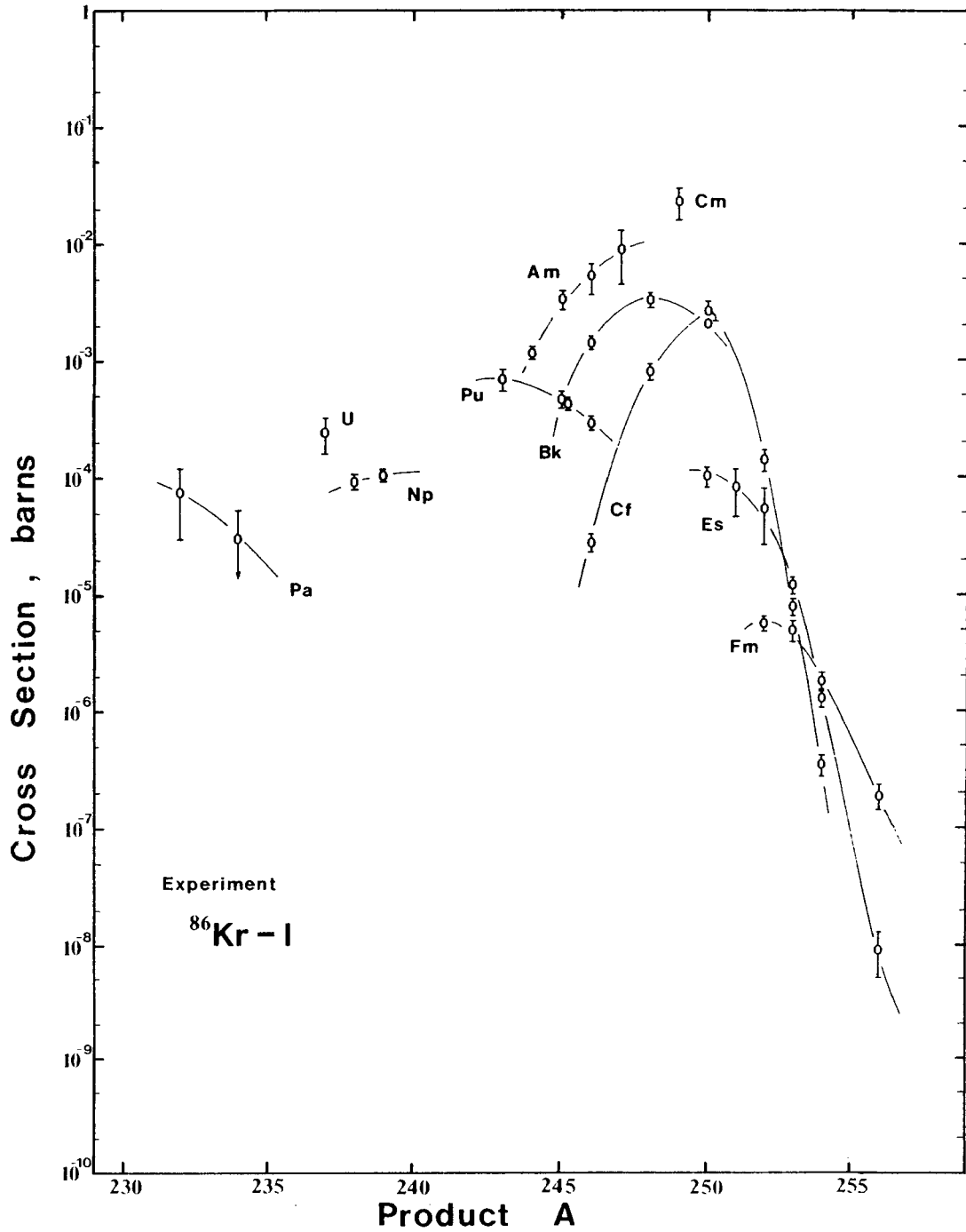
XBL 836-10237

Figure 4b



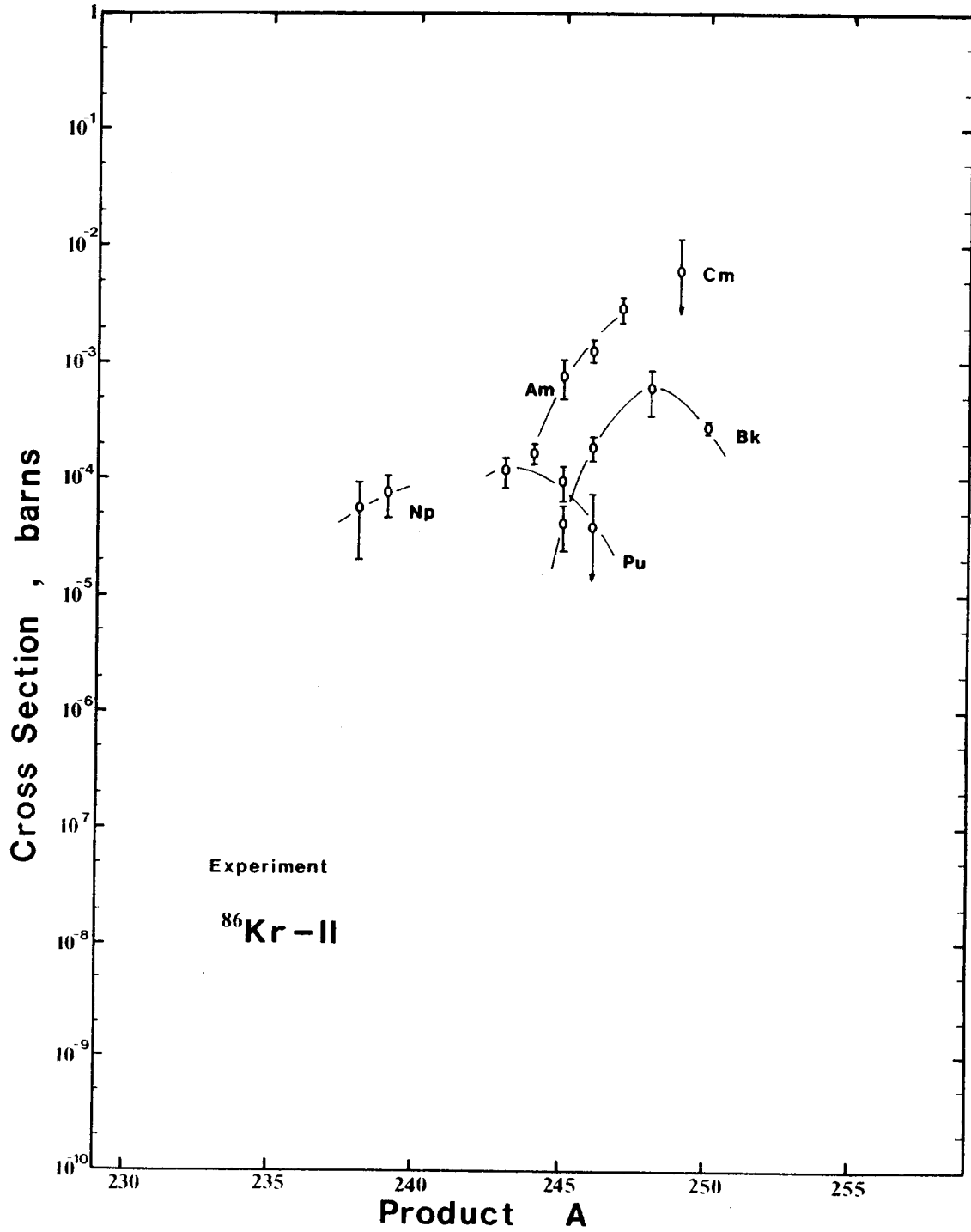
XBL 836-10238

Figure 4c



XBL 836-10227

Figure 4d



XBL 836-10292

Figure 4e

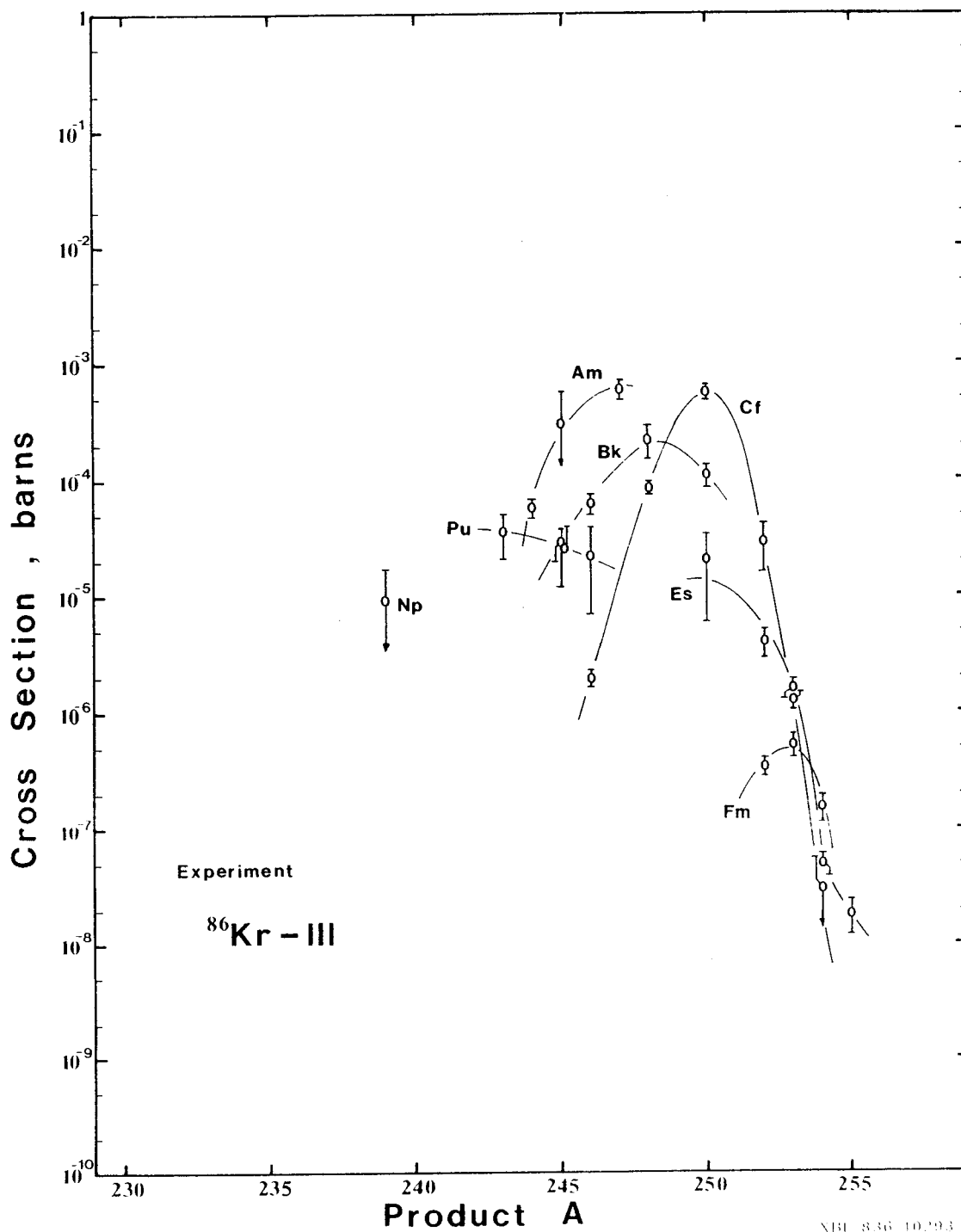


Figure 4f

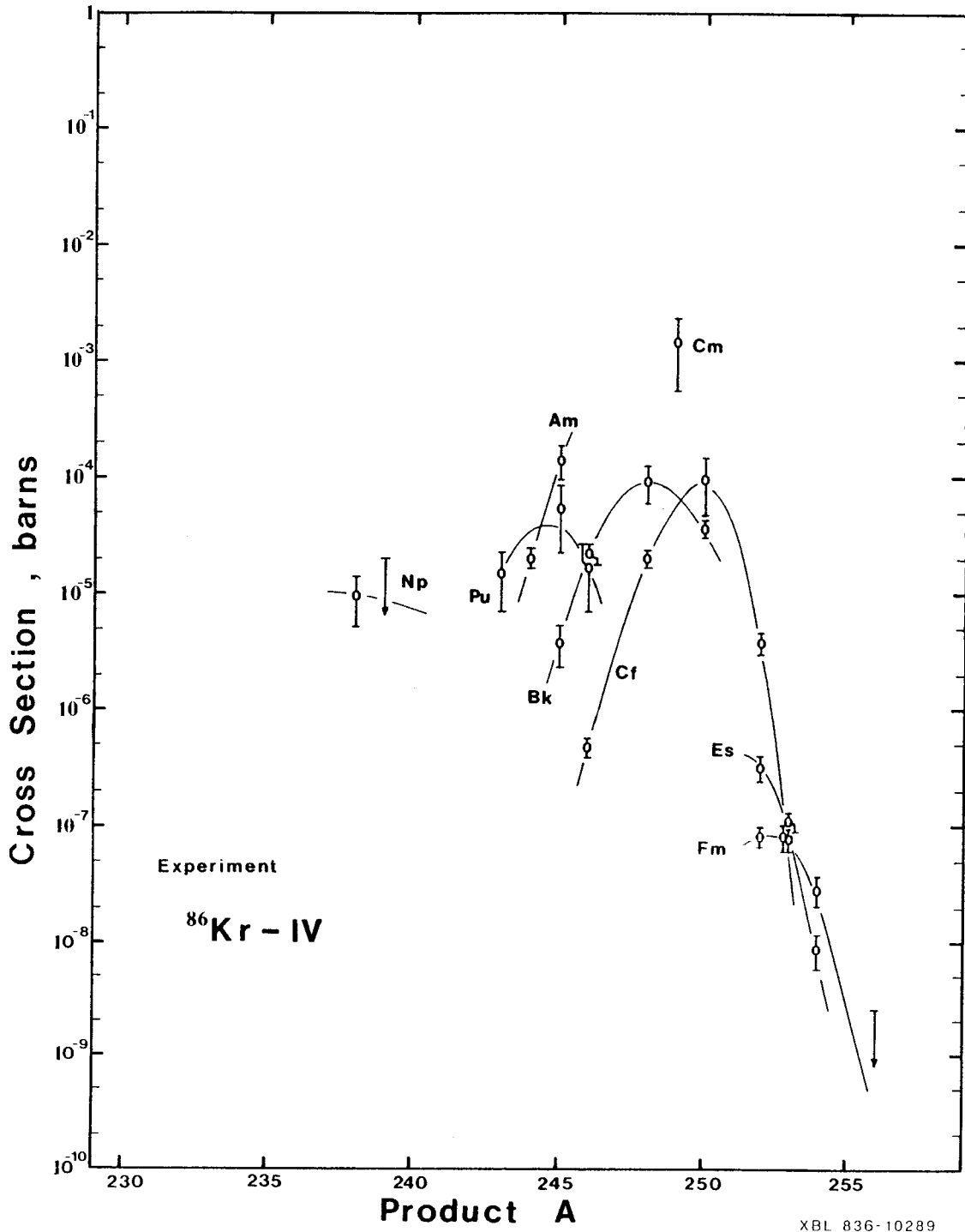


Figure 4g

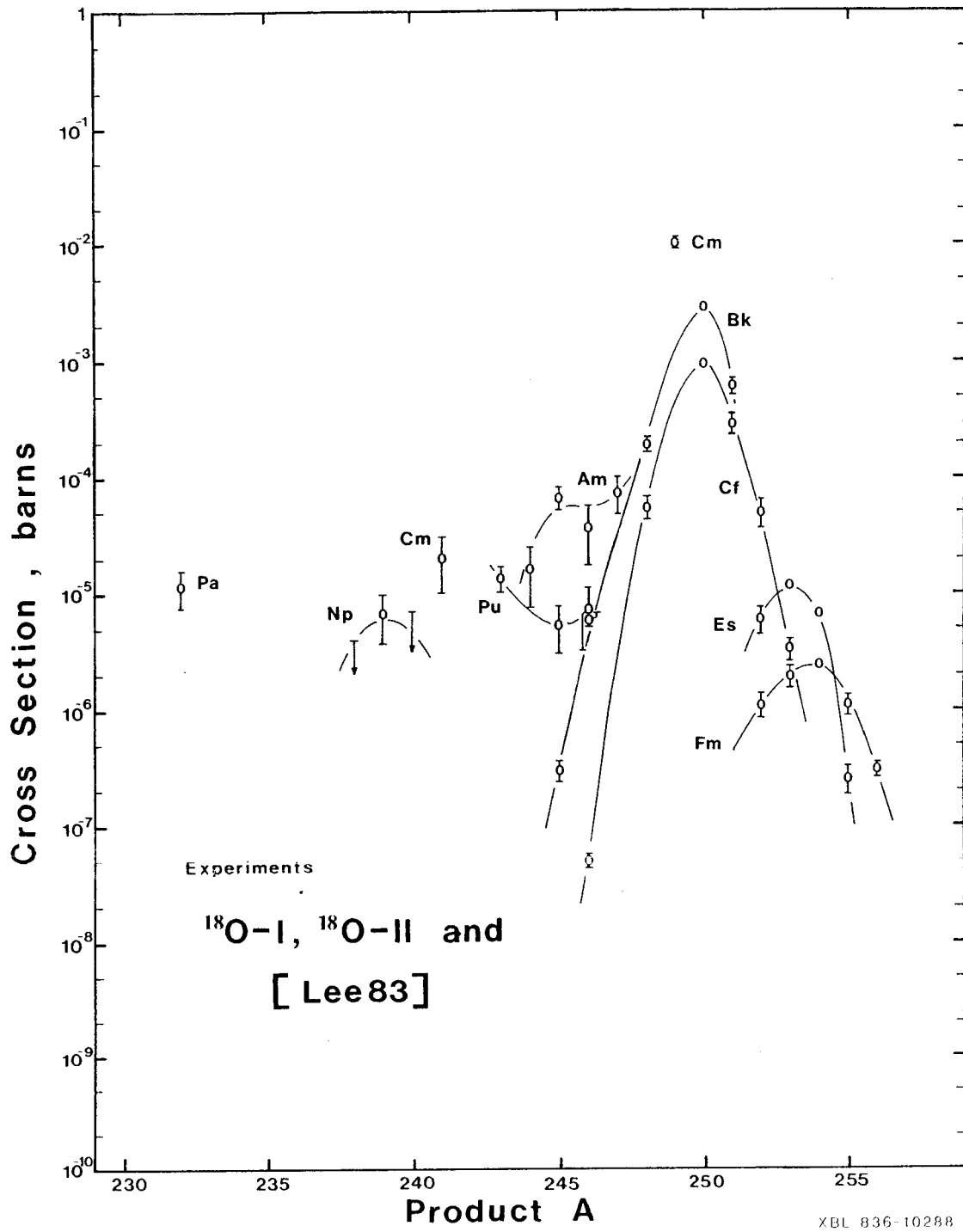
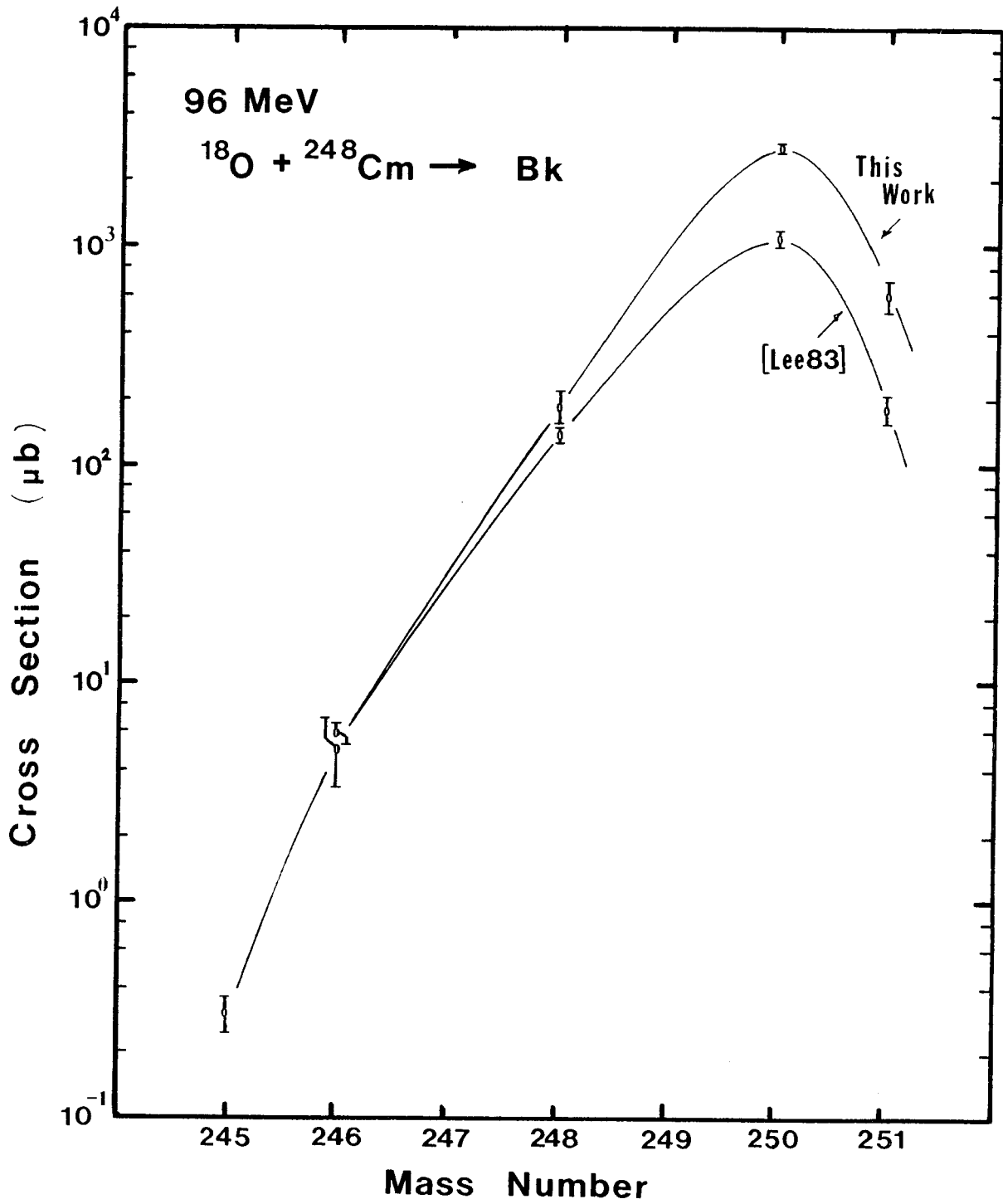
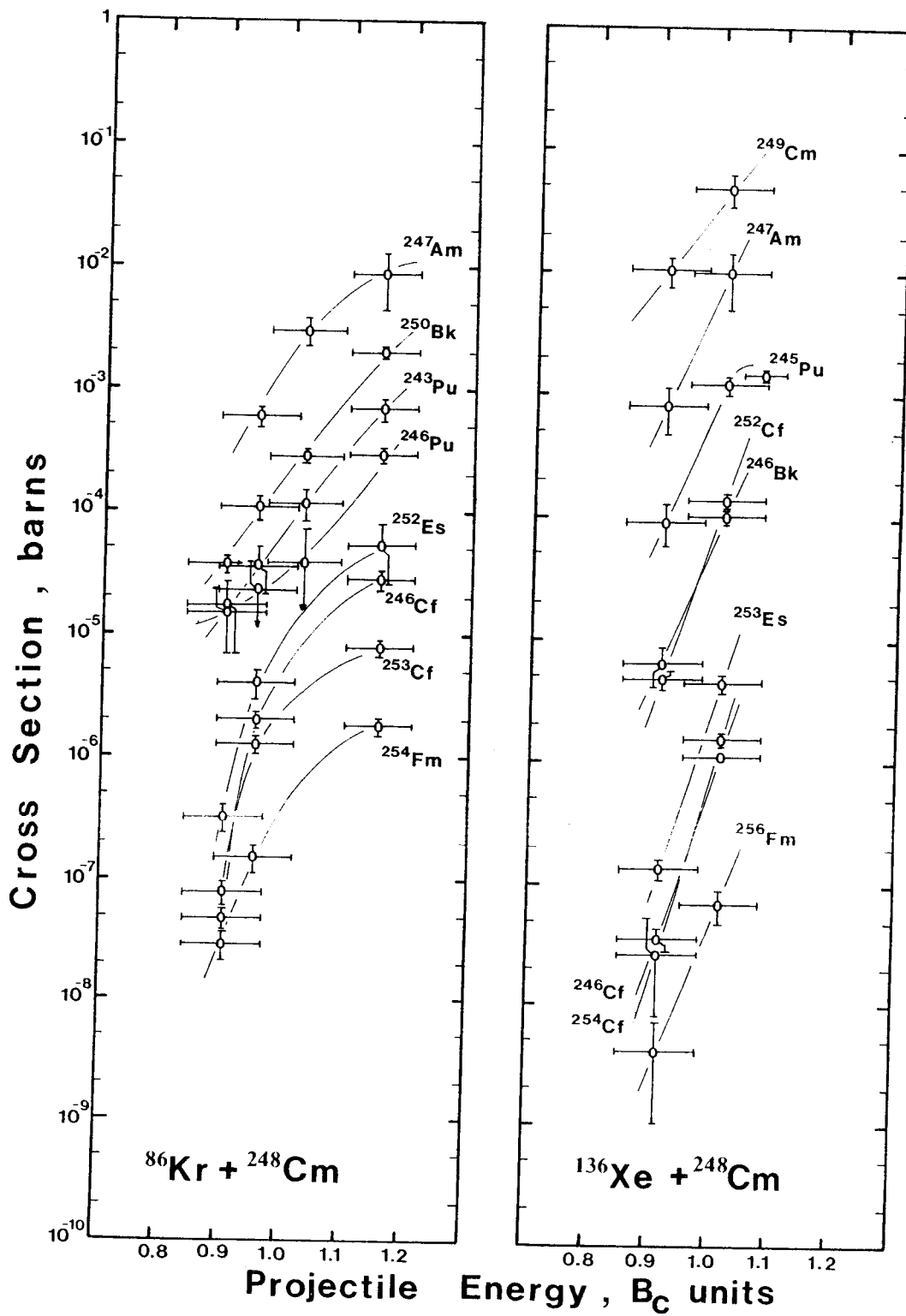


Figure 4h



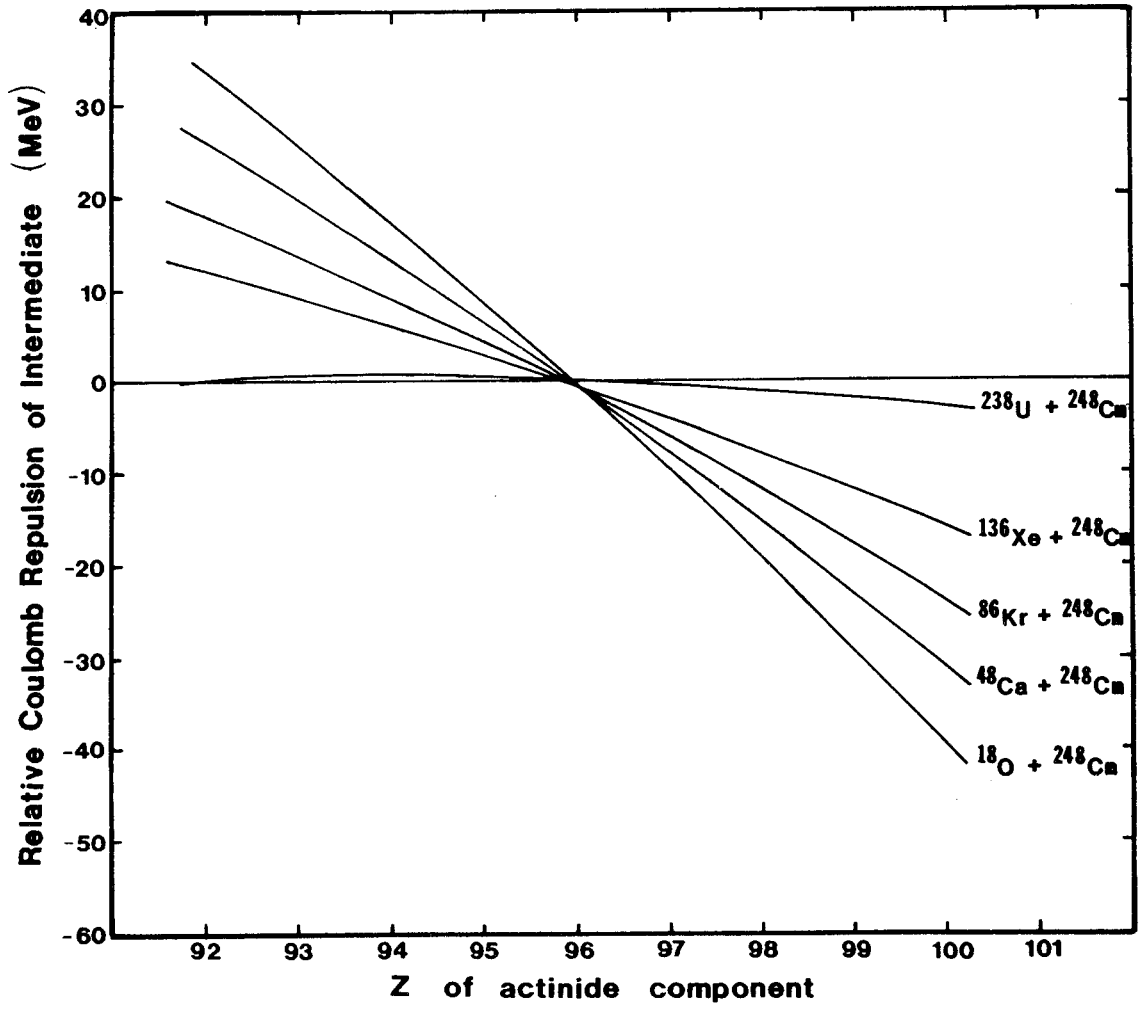
XBL 836-10250

Figure 4i



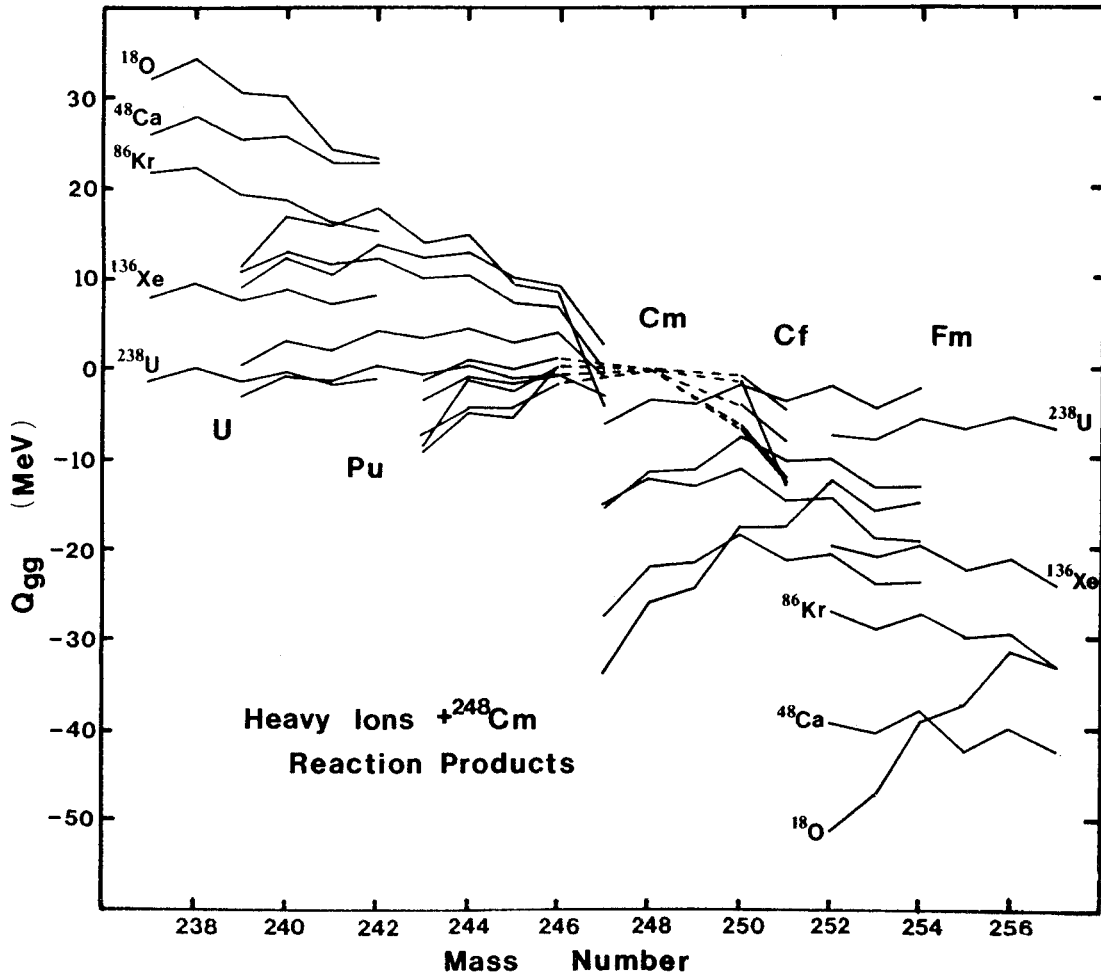
XBL 836-10287

Figure 4j



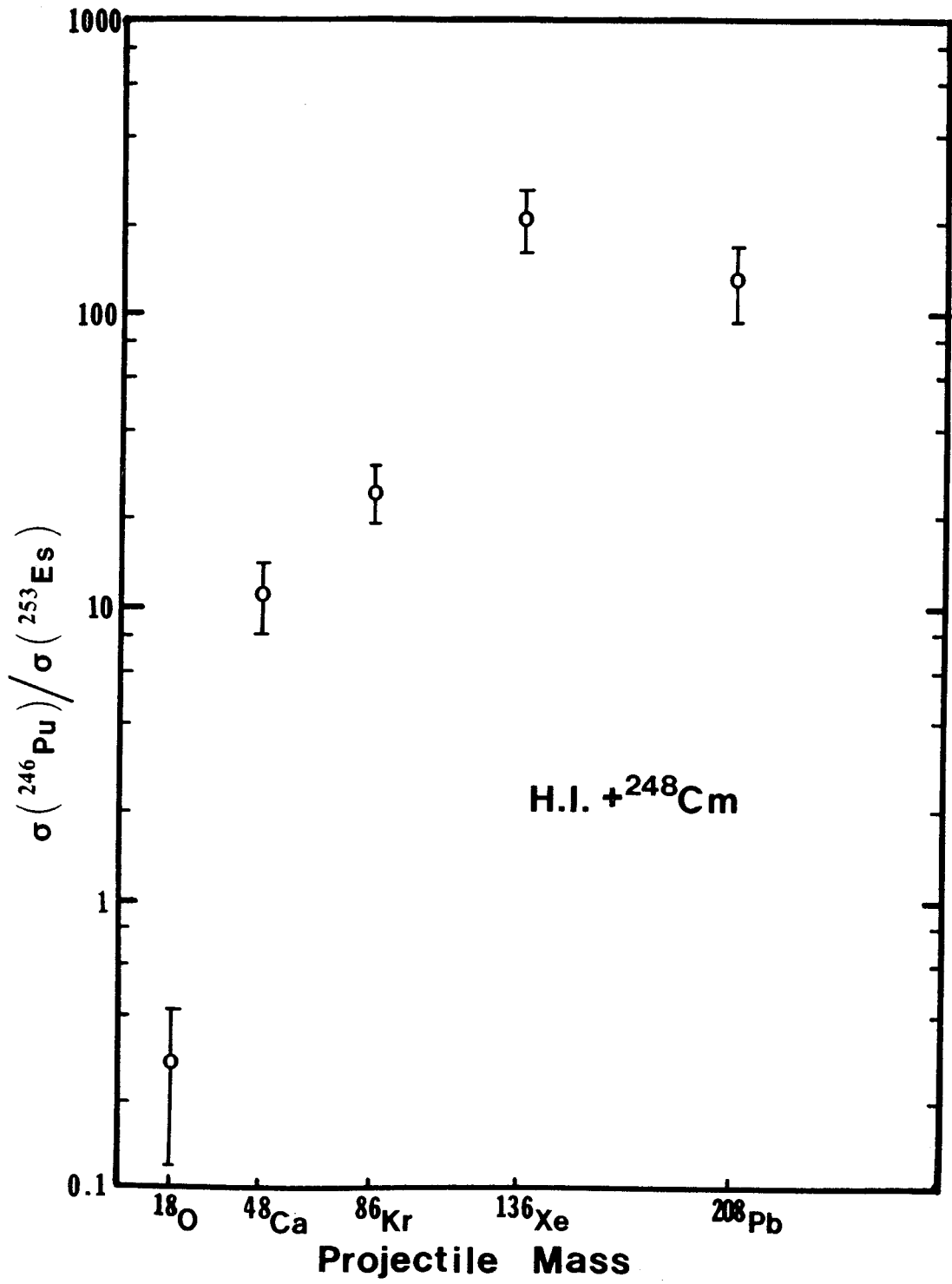
XBL XBL 836-10239

Figure 4k



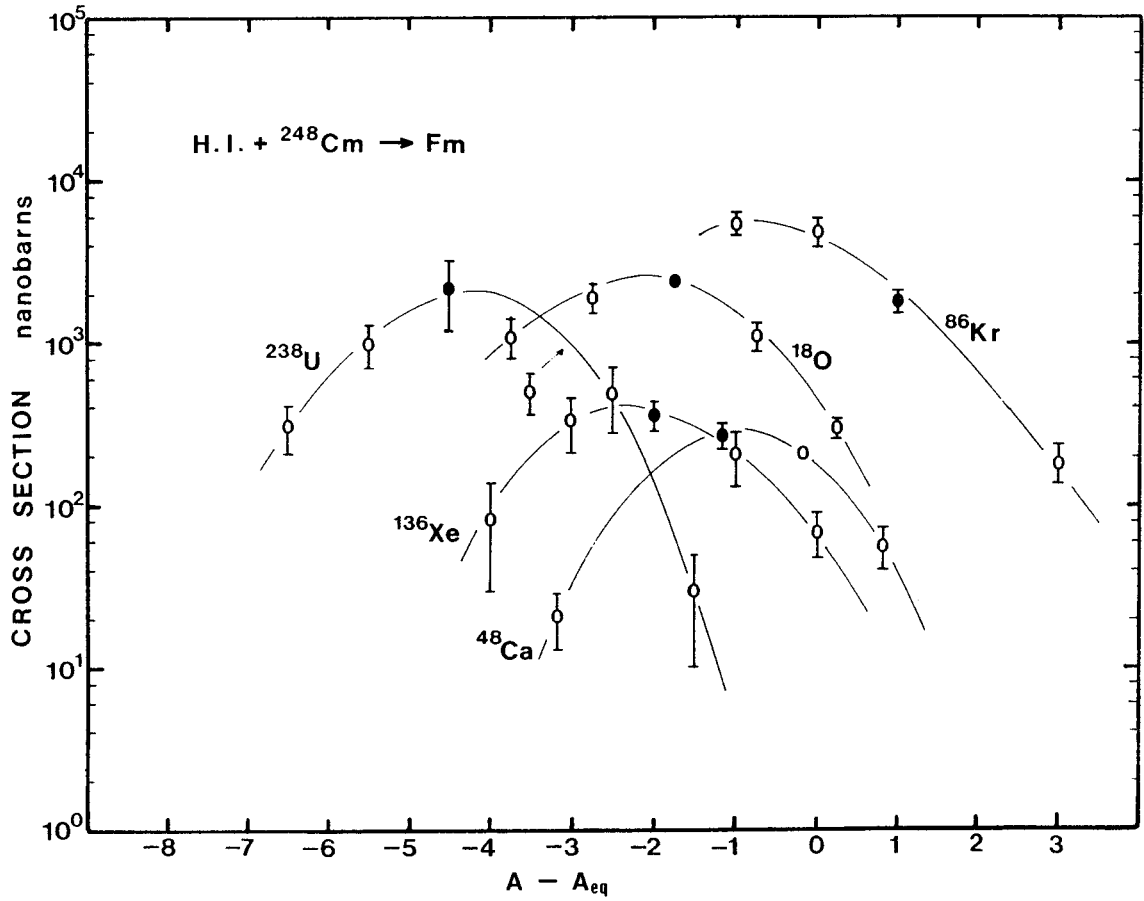
XBL 836-10243

Figure 41



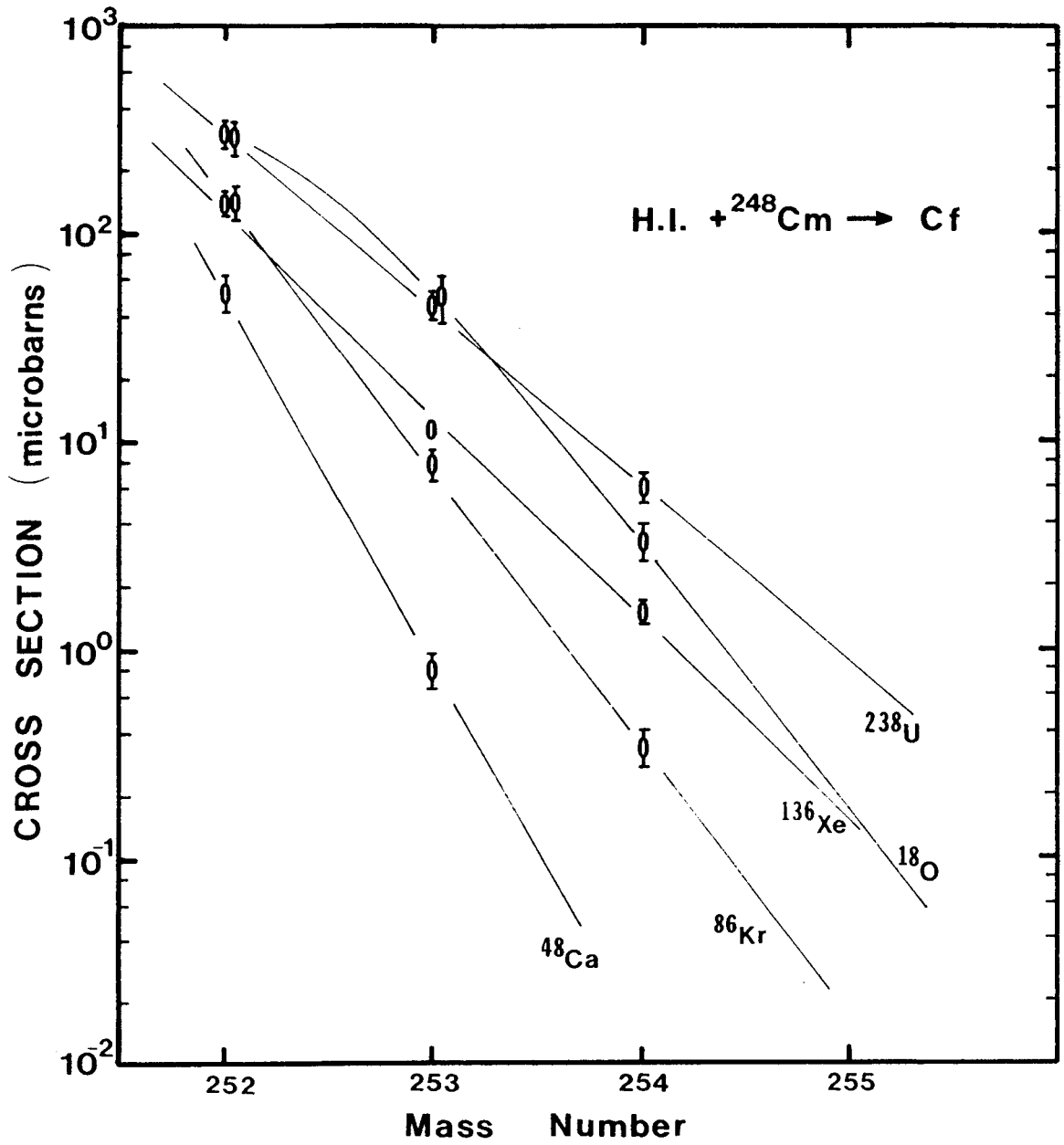
XBL 836-10247

Figure 4m



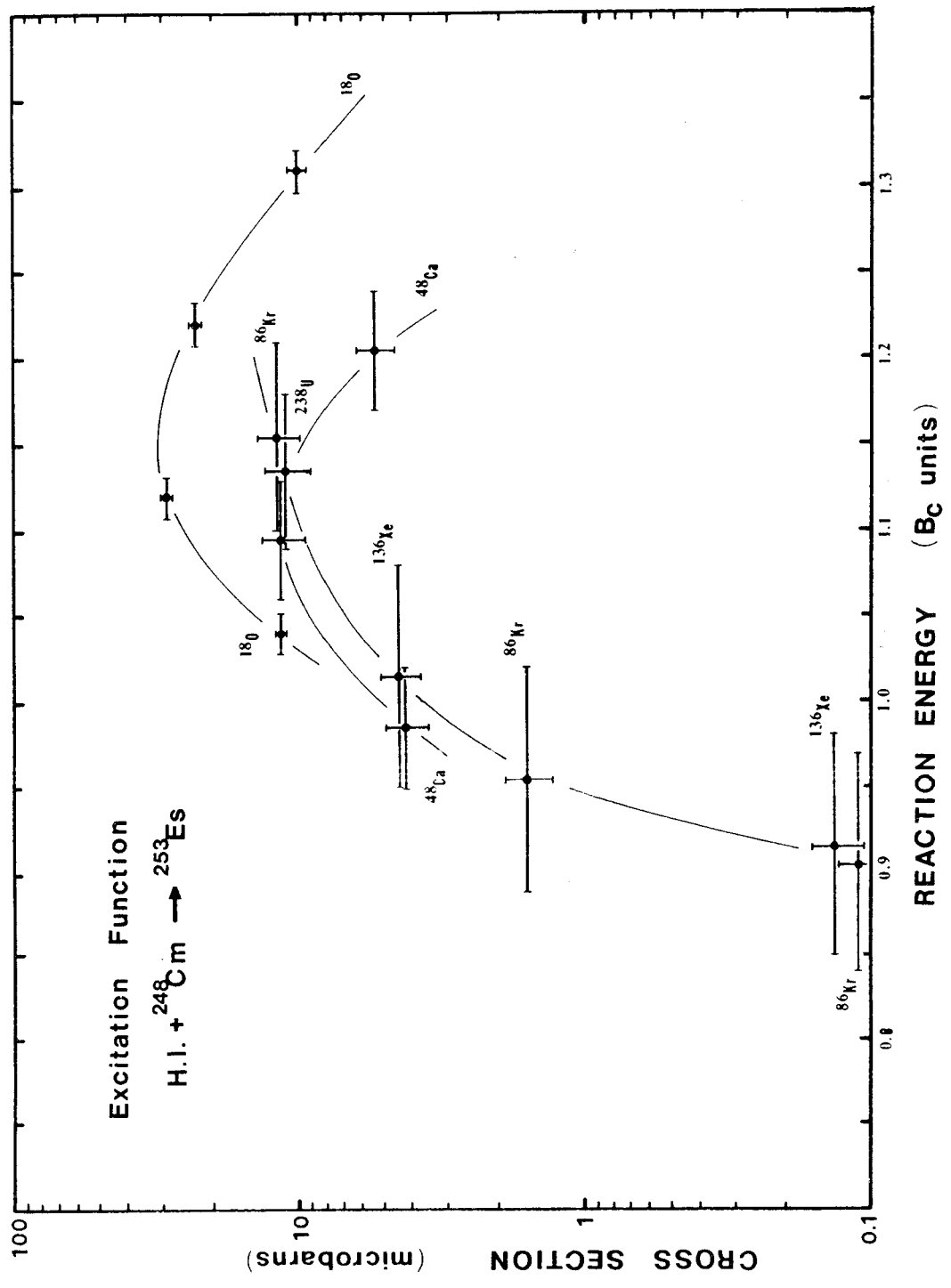
XBL 836-10228

Figure 4n



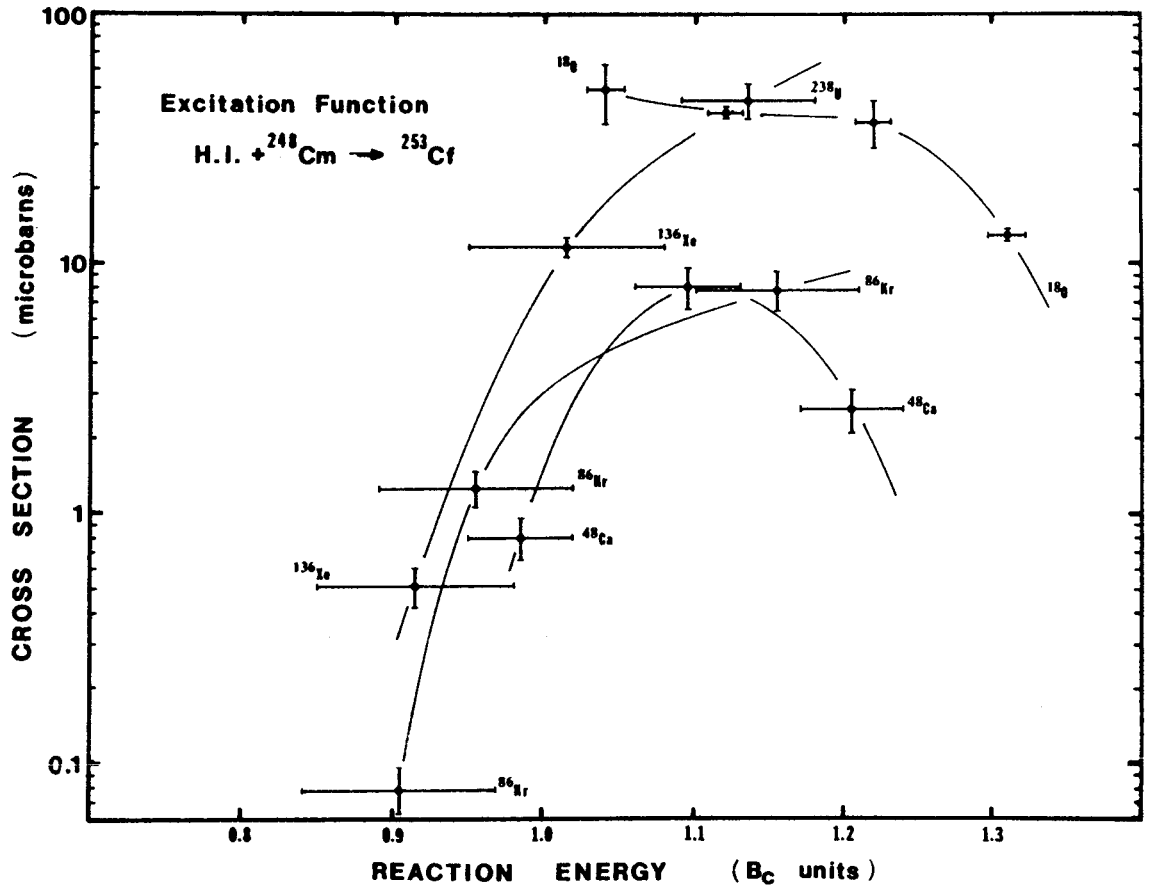
XBL 836-10240

Figure 4o



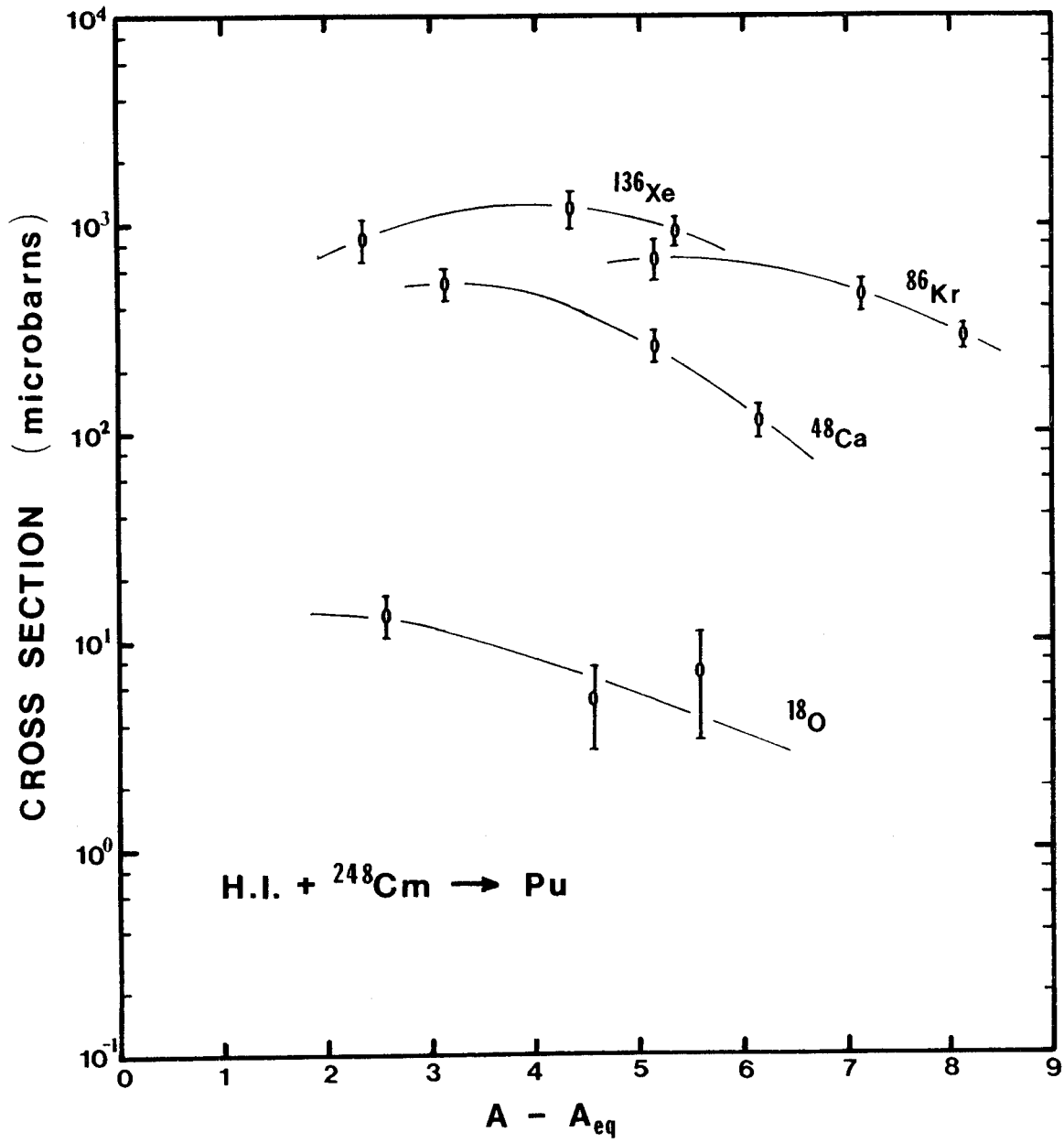
XBL 836-10233

Figure 4p



XBL 836-10229

Figure 4q



XBL 836-10241

Figure 4r

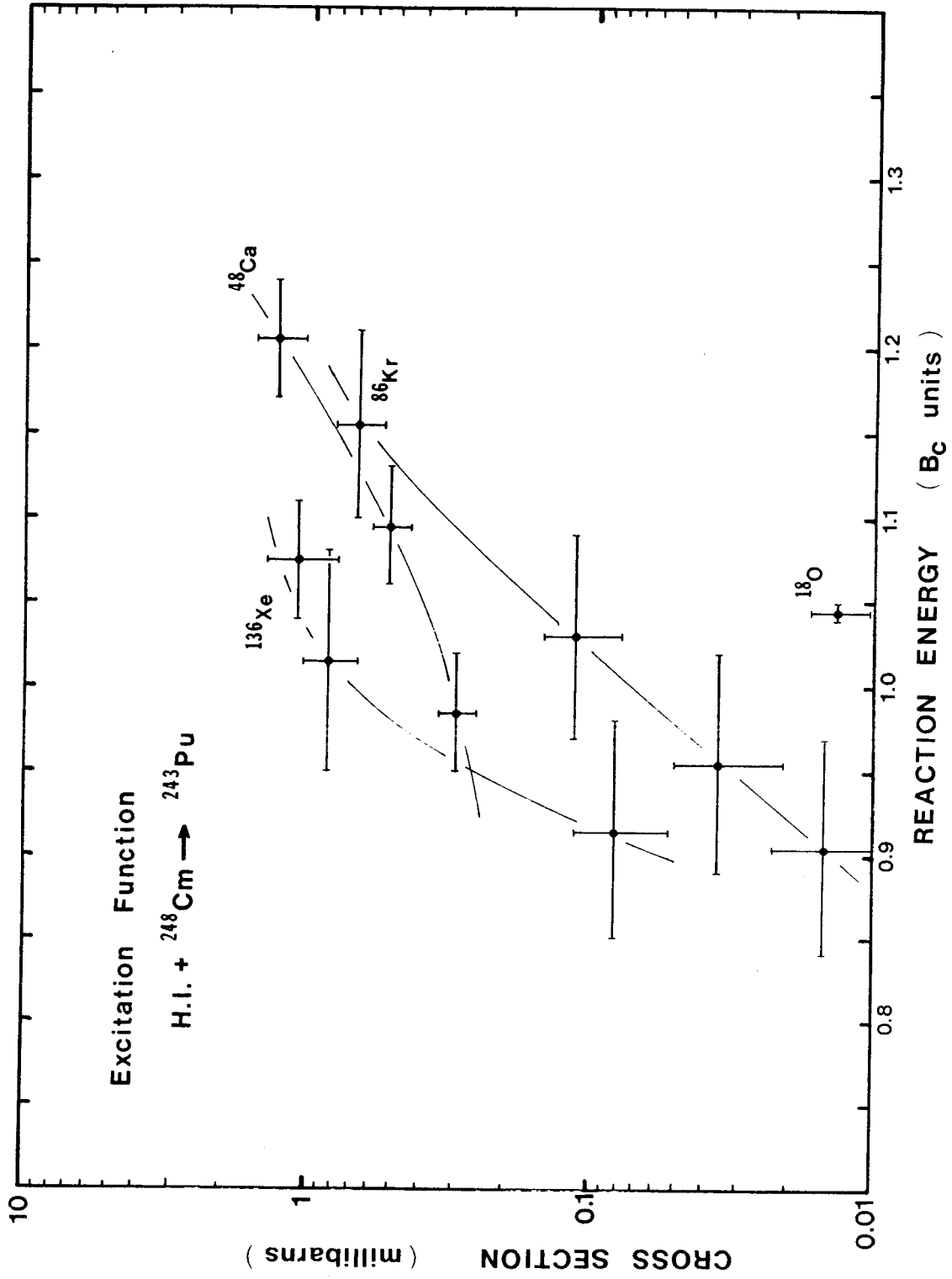


Figure 4s

XBL 836-10232

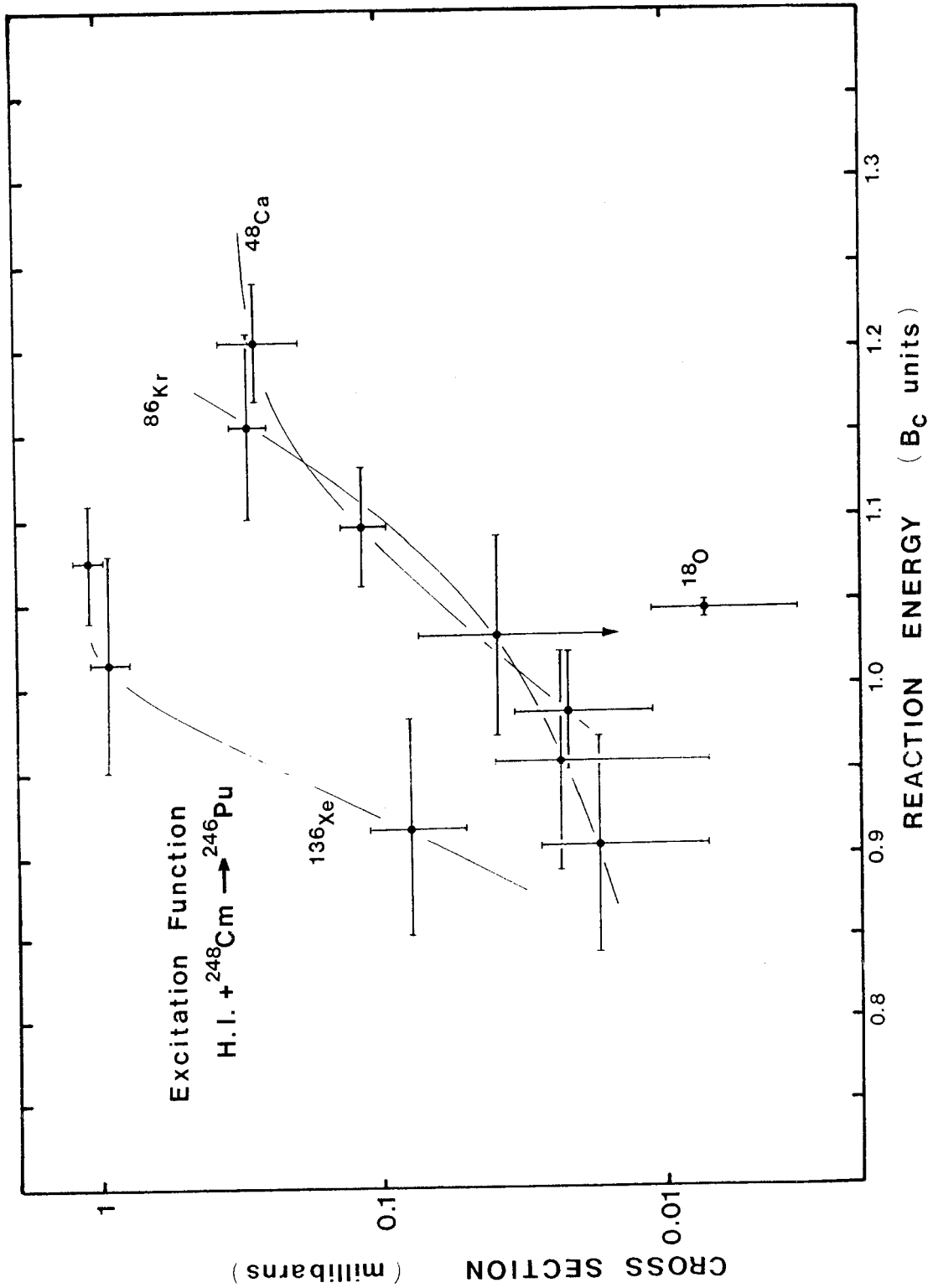


Figure 4t

XBL 836-10231

Section 5 - Determination of the Properties of ^{251}Bk Decay

One of the purposes of this work was to examine the possibility of making new neutron-rich nuclides in the near (Z,A) vicinity of the target ^{248}Cm with the heavy ions ^{18}O , ^{86}Kr and ^{136}Xe . It is very important to determine the production cross sections of as many of the most neutron-rich known nuclides as possible. A particularly troublesome nuclide is ^{251}Bk , the heaviest known berkelium isotope, which decays by beta-minus emission with a convenient half life followed by de-excitation by emission of gamma rays whose intensities are not known. Therefore, even though the ^{251}Bk gamma rays were observed in experiments ^{18}O -I and ^{18}O -II, no cross sections could be determined.

This section describes the determination of approximate absolute gamma ray intensities for ^{251}Bk decay.

5.1 Background

In the past, ^{251}Bk has only been produced indirectly as the daughter of activities formed by bombardment of heavy actinide targets with reactor neutrons. ^{251}Bk was first observed as the 8% alpha-decay daughter of 39.8-day ^{255}Es produced by multiple neutron capture in reactor targets of curium and californium [Dia67]. In these experiments, ^{251}Bk atoms recoiling from isotopically enriched samples of ^{255}Es following alpha decay were collected on thin foils and counted with gamma ray and beta particle detectors. The half life was measured to be (57.0 ± 1.7) minutes, which has proved to be a reliable value [Lou78]. The gamma ray energies obtained were not observed by others later, so their measurements of the beta particle endpoints of the decay ("... an E_{max} near 1/2 MeV; a less abundant component had an E_{max} near 1 MeV") are not too reliable. Later experiments with recoiling ^{251}Bk atoms [Hof70] established that two gamma rays are emitted in the decay at energies of 152.8 keV and 177.7 keV, in the ratio of 0.38 to 1. From the known levels in the ^{251}Cf daughter

[Ahm70], these gamma rays arise from the same $3/2^+$ state at 177.7 keV, and the $\log ft$ value for the decay is compatible with a ^{251}Bk ground state spin of $3/2^-$, consistent with that predicted from the Nilsson diagram for odd protons.

^{251}Bk has also been produced from the beta-minus decay of ^{251}Cm (16.8 minutes) which was produced by the neutron irradiation of ^{250}Cm [Lou78], a target nuclide only available by chemical isolation from the debris from a nuclear explosion [Hui57,Com68]. The beta endpoint of ^{251}Cm was determined, necessitating the deconvolution of its beta particles from those of its daughter, ^{251}Bk . The ^{251}Bk endpoint is given as "near 1 MeV," consistent with the upper, lower intensity value given in the discovery paper [Dia67]. The determination of the "absolute" intensities of the ^{251}Cm gamma rays suffers, in part, from determination of the daughter ^{251}Bk decay rate from its gross beta activity with an end window proportional counter.

In recent work [Lee82, Lee83], the yields of berkelium isotopes from transfer reactions of ^{16}O with ^{248}Cm were measured chemically. The distribution of Bk isotopes indicates that ^{251}Bk is made with a substantial cross section in these reactions; indeed, cross sections are given for ^{251}Bk , but these are based on a purely "calculational" branching ratio, derived from the assumption that only the 177.7 keV level in ^{251}Cf is populated by the beta decay, and that the total conversion coefficient for the 177.7 keV gamma ray is 8.0 [Lee83].

The work which follows in this section was aimed at determining the absolute intensities of the gamma rays arising from the decay of ^{251}Bk . The numbers which are determined are not model-independent, but are rooted as firmly in experiment as is possible at this level of treatment.

5.2 The Difficulties Inherent in a Direct ^{251}Bk Determination

The most direct way to determine the absolute intensities of the radiations

emitted in the decay of a particular nuclide is to relate the decay rate of this nuclide to a nuclide from which it decays or to a nuclide to which it decays. This requires that the intensities of the radiations and the half life of the parent or daughter nuclide and the fractional branch to or from the nuclide of interest are known, and that a good chemical separation can be performed to separate the known activity from the unknown activity. In this case the direct method could not be employed, for the reasons which follow. The decay data and neutron capture cross sections presented in the next two paragraphs, unless otherwise noted, are from reference [TOI78].

The ^{251}Bk daughter, ^{251}Cf , is a 100% alpha emitting nuclide. In principal, the gamma rays from ^{251}Bk decay could be normalized against the alpha decay rate of ^{251}Cf . Unfortunately this is not practical for two reasons: It is not possible to build up and separate enough ^{251}Bk (a 55.6 minute activity) to decay to an easily observable quantity of ^{251}Cf (a 900 year activity). Also, no matter whether the ^{251}Bk is obtained from heavy ion reactions or as the daughter of reactor-produced activities, the amount of ^{250}Bk (a 3.2 hour activity) present is going to be substantial compared with ^{251}Bk [Lee82,Dia67]; ^{250}Bk decays to ^{250}Cf (a 13 year activity) which, in terms of activity, will be present to roughly two orders of magnitude more than will ^{251}Cf , and whose alpha particles occur at the same energy (6.0 MeV) as the highest-energy alpha particle group of ^{251}Cf .

The alternate method, that of milking ^{251}Bk from ^{255}Es , is also possible, but again presents great practical difficulties. The only ways that ^{255}Es (a 40 day activity, 8% alpha branch to ^{251}Bk) can be isolated in sufficient amounts for the observation of ^{251}Bk gamma rays is through the irradiation of very heavy actinide targets in high flux reactors, followed by mass separation, or from bomb debris [Com66]; the latter is somewhat too ambitious for a thesis project. Though several milligrams of ^{253}Es (a 20.5 day activity) is produced every year

for reactor-irradiation programs [Kin81], its (n,γ) cross section to the ground state of ^{254}Es (a 270 day activity) is less than 3 barns, while that to the metastable state ^{254m}Es (a 39 hour activity, not decaying to the ground state, most of the decay ending in ^{250}Cf through the 3.2 hour alpha decay of ^{254}Fm) is 160 barns. The short half life and high fission cross section of ^{254m}Es makes it useless for ^{255}Es production. ^{254}Es has an (n,γ) cross section of less than 40 barns, but an $(n,\text{fission})$ cross section of 2800 barns. Equilibrium amounts of ^{255}Es are further lowered by its capture cross section of 65 barns. Plans are being made for production of ^{254}Es on the 10 microgram level [Kin81], but ^{255}Es will always be difficult to obtain.

This is a convincing argument for doing the less direct experiment described below.

5.3 Experimental Details

The target used in these experiments consists of $560 \mu\text{g}/\text{cm}^2$ of ^{248}Cm , present as the oxide, electrodeposited in a 7 mm diameter circle on a backing of $2.5 \text{ mg}/\text{cm}^2$ beryllium metal. The fabrication of the target is described in Section 2. The target system used in the irradiations is shown in figure 2c. Between 1 and 4 electrical microamperes of 111 MeV $^{18}\text{O}^{4+}$ produced by the Lawrence Berkeley Laboratory's 88-Inch Cyclotron was delivered to the target for approximately 45 minutes for each run. The energy of the beam after passing through the isolation foil, cooling gas and beryllium target backing, is calculated to be approximately 96 MeV [Nor70,Hub80], close to the energy used by Lee et.al. [Lee82]. Recoiling reaction products were collected on a $2 \text{ mg}/\text{cm}^2$ gold foil. After each irradiation, the gold foil was removed from the target chamber, transported to the chemistry laboratory and rapidly processed using the berkelium procedure outlined in section 2.4. The time interval between the end of the irradiation and the start of the first count of the berkelium activities

was usually between 35 and 45 minutes, less than the ^{251}Bk half life.

The berkelium chemical fraction was counted for both photons and electrons. The platinum backed samples were suspended between two pieces of 2 mg/cm^2 polyethylene in the narrow gap between an intrinsic germanium gamma ray detector and a beta detector, the side of the platinum with the activity on it facing the beta detector to minimize the degradation of the electrons. The detection of the gamma rays is discussed in Section 2. The detector efficiency as a function of photon energy was determined by counting the mixed radionuclide standard through each berkelium sample after the berkelium activities had decayed out. A typical gamma ray spectrum of a berkelium chemical fraction is shown in figure 5a.

The beta detector was one of two types, depending upon the nature of the data being taken. In experiments where the absolute amount of beta activity was determined, the detector was a gas-filled proportional counter with a 1 mg/cm^2 gold-plated mylar end window. The detector was operated in the "plateau" region at 2.0 kV, and events were summed at regular intervals in a scaler. The system has been described in greater detail elsewhere [Tho79]. The detector efficiency as a function of beta endpoint energy was determined with a set of five standard beta reference sources, each mounted on platinum foil facing the beta detector in the same fashion as the experimental berkelium fractions; this was to equalize contributions from back-scattered electrons. The 1 mg/cm^2 aluminized mylar housing the standards was assumed negligible in its effect on the detector efficiency; rather, it might be thought to help compensate for the self-absorption of the berkelium fractions, which were not always completely weightless. The calibration sources used were ^{14}C , with a beta particle endpoint of 0.155 MeV, ^{147}Pm , with a 0.225 MeV endpoint, ^{99}Tc , at 0.292 MeV, ^{38}Cl , at 0.709 MeV, and ^{90}Y (^{90}Sr), at 2.288 MeV (0.546 MeV) [TO178]. The

efficiency function is shown in figure 5b. Because the efficiency function determined from standards with low atomic numbers and no converted gamma transitions only roughly applies to nuclides like ^{251}Bk which has a high-Z beta spectral shape and intense internal conversion electrons, the "gross beta activity" determined for ^{251}Bk will be used only semi-quantitatively.

Scaler counts per unit time, as a function of time, and weighted proportionally to the square root of the scaler counts, were subjected to a four component decay curve analysis holding the half lives of ^{251}Bk (55.6 minutes), ^{250}Bk (3.22 hours), ^{248}Bk (23.5 hours) and the background (long) fixed. When the chemistry was as successful as that resulting in figure 5a, the fits to the data were excellent, as shown in figure 5c. The initial activity due to ^{251}Bk was corrected with the detector efficiency at its endpoint energy, resulting in the approximate gross beta activity at the end of bombardment for this nuclide.

In experiments where the beta energy spectrum of the berkelium fraction was measured, the beta detector was a plastic anthracene scintillator. The scintillator itself was a 2.5 cm thick, 3.8 cm diameter cylinder of plastic quenching material containing the anthracene; this rested directly on the flat face of a photomultiplier tube operated at a bias of +1100 V. The anthracene crystal was mirrored around the cylindrical surface and a 6 mg/cm² high purity aluminum foil covered the planar surface toward the sample. A thick aluminum collimator with a diameter of 3 cm was placed on the face of the detector. The entire assembly, except the detector face, was liberally covered with black tape to minimize light leaks. Light-producing events in the scintillator result in electron pulses from the photomultiplier tube which are picked up by a preamplifier and output as voltage signals to a linear amplifier. The amplifier output signals are fed into an ADC and then subjected to pulse height analysis to give a measure of the energies of the events. These energies are stored in a

4096 channel MCA and periodically stored on floppy disks for subsequent analysis.

The anthracene material, due to the low Z of its components, is relatively insensitive to gamma rays. Its efficiency for beta particle detection is roughly constant for electrons with energies of more than approximately 125 keV [Sch63] entering the anthracene, proportional to the solid angle subtended by a properly-collimated scintillator. The energy was calibrated using the same beta standard sources mentioned above, mounted in the same geometry. Energy resolution due to the detector response is linear and slowly changing for electron energies greater than 125 keV [Bir64] and applies as much to the calibration spectra as to the berkelium spectra, so to a first order no response function corrections are necessary. The response function for detectors of this size and type has a FWHM of less than 50 keV at electron energies of 1 MeV [Bir64]. Figure 5d shows a typical berkelium fraction electron spectrum with calibration endpoints also shown.

5.4 The Half Life of ^{251}Bk

The half life of ^{251}Bk was redetermined from the decay curve analysis of the 152.8 and 177.7 keV gamma ray lines in the gamma spectra. The description of this method is given in Section 3. Typical decay curves are shown in figure 5e.

The weighted average of seven separate determinations of the half life is (55.6 ± 1.1) minutes, in excellent agreement with the literature [Dia67,TOI78] and the value determined from decay curve analysis of the gross beta activity. Since it is difficult to prove that small amounts of contaminating activities are not present in the final chemical fractions, the gross beta half life was not used in computing the weighted average given above. In the work which follows, this half life was held constant.

5.5 The Decay Scheme of ^{251}Bk (^{251}Cf)

Figure 5f shows the known level scheme of ^{251}Cf , indicating those levels fed by the electron capture decay of ^{251}Es [Ahm70]. Since the same Nilsson level is occupied by the odd proton in both ^{251}Es and ^{251}Bk [TOI78], one could expect the population of similar levels in the beta-minus decay of ^{251}Bk , subject to differences in decay energy. Above the $3/2[622]$ rotational band, the next intrinsic level with $[\Delta J] \leq 1$ relative to the ^{251}Bk ground state is at 544 keV [TOI78], which corresponds to such a large decrease in the beta decay energy as to make it of negligible importance in the decay. Close examination of figure 5a discloses the existence of a previously unobserved gamma ray at 163.8 keV from ^{251}Bk decay to the $5/2+$ state in the $3/2[622]$ rotational band of ^{251}Cf . This gamma ray has been observed in the decay of both ^{251}Es and ^{255}Fm . A typical decay curve for this line is included in figure 5e.

Three component decay curve analysis (^{251}Bk , ^{250}Bk and ^{248}Bk with fixed half lives) was performed on the californium K X-rays, coming from vacancies in the K-shell electron orbitals due to internal conversion. The ^{251}Bk contribution to the X-ray intensity is by far the most significant of the three. The initial activities of the ^{251}Bk component of each of the four main K X-ray groups were determined individually.

Absolute intensities at the end of bombardment for each ^{251}Bk photon line were determined by correcting the initial activities from decay curve analysis for the detector efficiencies at the appropriate energies. Table 5-1 gives the intensities of these photons, relative to the 177.7 keV line, from the weighted average of several determinations. The relative gross beta activity measured with the gas proportional counter is also given.

Table 5-1 Relative intensities of the emitted radiations from ^{251}Bk decay, normalized to γ_{178} . The data are based on the weighted average of eight measurements.

Cf $K\alpha_2$ X-ray	2.02 ± 0.11
Cf $K\alpha_1$ X-ray	3.19 ± 0.14
Cf $K\beta_1$ X-ray	1.68 ± 0.09
Cf $K\beta_2$ X-ray	0.36 ± 0.05
152.8 keV γ -ray	0.385 ± 0.025
163.8 keV γ -ray	0.060 ± 0.012
177.7 keV γ -ray	1
gross β^- activity	≈ 33

The $\gamma_{153}/\gamma_{178}$ activity ratio of .385 is consistent with that from ^{251}Es decay, as expected, since both gamma rays arise from the same level in ^{251}Cf .

The beta endpoint of ^{251}Bk was determined by decay curve analysis on plastic scintillator spectra taken at regular intervals after the end of the chemistry. In principal, an electron spectrum in coincidence with the 177.7 keV gamma ray could have been used to discriminate against ^{250}Bk and ^{248}Bk decays, but it would have also eliminated any ^{251}Bk decays directly to the ground state of ^{251}Cf . Each electron spectrum was divided into energy windows, and the areas (intensities) of these windows were analyzed as a function of time with error bars equal to the square root of the area of the windows. The energy width of the windows was 10 keV, a compromise between the limitations due to resolution and statistics. Multiple component decay curve analysis was performed on each window as a function of time using fixed half lives for the berkelium activities. The activity in each window due to ^{251}Bk , extrapolated back to the end of the bombardment, yields an effective emitted electron

energy spectrum due to ^{251}Bk decay. Figure 5g shows a schematic of the procedure. Figure 5h shows the emitted electron energy spectra of both ^{250}Bk and ^{251}Bk resulting from this process. Non-zero activity beyond the apparent beta endpoints of the spectra is attributed to accidental small contributions to the fixed half life components by low level chemistry contaminants, summing, and the detector background. Error bars shown are based on the decay curve fit to the data of each window, not taking half life errors into account, and the data points are plotted at the energy central to the windows.

The endpoint regions of the standard sources were fit by the least-squares method to a Fermi-Kurie function [Mar69] to determine the energy calibration. To demonstrate the accuracy of the deconvolution technique described above, the two endpoints of ^{250}Bk were determined to be (705 ± 20) keV and (1820 ± 35) keV. The lower energy endpoint compares with (725 ± 15) keV measured previously [Van59] and 745 keV, predicted from the level scheme [TOI78]. The discrepancy is due, in part, to a deviation in the spectral shape due to conversion and Compton electrons from the intense ^{250}Bk gamma rays in the vicinity of the low energy beta endpoint. The upper energy endpoint is in reasonable agreement with the literature value of (1760 ± 50) keV [Van59] and the Q_β value of 1780 keV [TOI78].

Also plotted in figure 5h is a Fermi-Kurie plot of the ^{251}Bk electrons. The major beta-minus transition of ^{251}Bk has a measured endpoint of (915 ± 10) keV. A very weak component with an endpoint of (1130 ± 35) keV can also be seen. The Q_β predicted from systematics [Wap77] is 1120 keV. Most of the ^{251}Bk decay proceeds to the $3/2[622]$ rotational band, with no more than roughly 5% of the decays going directly to the ground state band.

The important gamma transitions in the ^{251}Cf daughter of ^{251}Bk decay are all $\Delta J = 0, 1$, with no parity change, and are therefore of M1 and E2 multipolar-

ity. The fraction of gamma transitions resulting in photons (as opposed to conversion electrons) is dependent upon the multipolarity of the transition.

The admixture of E2 and M1 radiations can be calculated from the single particle model. The Weisskopf estimate of electric multipole transition lifetimes [Wap59] is

$$\tau_E \approx \frac{0.645 \times 10^{-21}}{S} \left(\frac{140}{E_\gamma} \right)^{2L+1} A^{-2L/3} \text{ sec} \quad \text{V.1}$$

where E_γ is the transition energy in MeV, L is the multipolarity and the statistical factor S is given by

$$S = \frac{2 \left[1 + \left(\frac{1}{L} \right) \right]}{\left[(2L+1)!! \left(1 + \frac{L}{3} \right) \right]^2} \quad \text{V.2}$$

Therefore, the single particle rate of E2 transition from a state in ^{251}Cf is given by

$$R_{E2}(^{251}\text{Cf}) = 1.5 \times 10^{11} E_\gamma^5 \text{ sec}^{-1} \quad \text{V.3}$$

Moszkowski [Mos65] gives an estimate for magnetic multipolarity transition lifetimes of

$$\tau_M \approx \frac{29.3 \times 10^{-21}}{S} \left(\frac{140}{E_\gamma} \right)^{2L+1} A^{-2(L-1)/3} \left(1.4L - \frac{L}{L+1} \right)^{-2} \text{ sec} \quad \text{V.4}$$

where quantities are defined as before, except

$$S = \frac{2 \left[1 + \left(\frac{1}{L} \right) \right]}{\left[(2L+1)!! \frac{(2+L)}{3} \right]^2} \quad \text{V.5}$$

Single particle M1 transition rates for ^{251}Cf are therefore

$$R_{M1}(^{251}\text{Cf}) = 3.1 \times 10^{12} E_\gamma^3 \text{ sec}^{-1} \quad \text{V.6}$$

The admixture of E2 in ^{251}Cf transitions is given by

$$\frac{R_{E2}}{R_{M1}} = 4.8 \times 10^{-2} E_{\gamma}^2 \quad \text{V.7}$$

which is a very small fraction for gamma transitions of less than 0.2 MeV.

Most E2 rates are faster than those predicted from equation V.1 due to collective rotational and vibrational enhancement. Examination of other level schemes of odd-neutron actinides in the mass region of ^{251}Cf [TOI78] indicates that the E2 multipolarity rate is much slower than the M1 rate for gamma transitions between different rotational bands in spite of the enhancement. The ^{251}Cf level scheme (figure 5f) gives its own indications that E2 rates are relatively small. The gamma ray intensities of the transitions between these levels are known from ^{255}Fm alpha decay [Ahm71]. The Bohr-Mottelson gamma transition rates for gamma decays to the different members of a rotational band [Mar70] are related by

$$R(L) \propto E_{\gamma}^{2L+1} [\langle J_f K_f | J_i L K_i \Delta K \rangle]^2 \quad \text{V.8}$$

where J_f and K_f describe the total angular momentum of the final state and that of its band head, J_i and K_i describe the initial state and $\Delta K = K_f - K_i$. The Clebsch-Gordan coefficients are tabulated [Chi62]. Ignoring conversion of electrons for the moment, the E2 multipolarity intensity for the transition between the 5/2+ level at 211.6 keV and the 1/2+ ground state should be 26 times that arising from the transition between the same 5/2+ level and the 3/2+ rotational level at 24.8 keV. Though the latter photon is observed, the former is not, inconsistent with E2 multipolarity. In M1 transitions, the $\Delta J = 2$, 5/2+ to 1/2+ transition is forbidden. Similarly, the 3/2+ level at 177.7 keV decays to both the 1/2+ ground state and the 3/2+ level at 24.8 keV. If the photons arise from transitions of E2 multipolarity, the intensity of the 177.7 keV gamma ray should be roughly half as intense as the 152.8 keV gamma ray, rather than 3

times as intense, which is what is observed. The gamma transitions in ^{251}Cf following ^{251}Bk decay will be treated as being of pure M1 multipolarity in the calculations which follow.

Conversion coefficients as a function of transition energy and multipolarity and the nuclear charge are tabulated [Dra69,Hag68] and interpolation gives the data in Table 5-II.

Table 5-II Internal Conversion Coefficients for M1 gamma transitions from ^{251}Bk Decay.

Electron origin	Transitions depopulating the $\frac{3}{2}+$ state at 177.7 keV			Transitions depopulating the $\frac{5}{2}+$ state at 211.6 keV	
	177.7 keV	152.8 keV	129.9 keV	186.8 keV	163.8 keV
K shell	6.20	9.45	---	5.40	7.80
L shell	1.33	2.05	3.30	1.16	1.68
M shell	0.32	0.50	0.80	0.29	0.41
N shell	0.10	0.15	0.25	0.08	0.12
Total	7.95	12.15	4.35	6.93	10.01

The relatively small size of the total conversion coefficient for the 129.9 keV gamma transition (because of no contribution from K-shell fluorescence) indicates that the gamma ray intensity from this transition might be appreciable. Unfortunately, the K_{β_1} X-ray line (which contains the small K_{β_3} group) is at 130.8 keV [TOI78], so no individual resolution was possible. The relative intensities of the X-rays can be predicted to a 1% accuracy [Sal74] for ^{251}Cf :

$$K_{\alpha_2} / K_{\alpha_1} / K_{\beta_1} + K_{\beta_3} / K_{\beta_2} = 64.2 / 100 / 34.3 / 13.0$$

The experimental ratios (Table 5-1) are

$$K_{\alpha_2} / K_{\alpha_1} / K_{\beta_1} + K_{\beta_3} / K_{\beta_2} = (63.3 \pm 4.4) / 100 / (52.7 \pm 3.6) / (11.3 \pm 1.7)$$

Only the relative K_{β_1} (+ K_{β_3}) intensity derived from experiment disagrees with the calculated number. Subtraction of Table 5-I values yields a relative intensity of the 129.9 keV gamma ray of (0.59 ± 0.12) . The correction of observed gamma ray intensities for internal conversion to give gamma transition rates gives relative depopulation rates of the 177.7 keV state of

$$R(177.7 \text{ keV}) / R(152.8 \text{ keV}) / R(129.9 \text{ keV}) = 1 / (0.565 \pm 0.037) / (0.353 \pm 0.072)$$

The rates expected from M1 transitions, from equation V.8, are in the ratios

$$R(177.7 \text{ keV}) / R(152.8 \text{ keV}) / R(129.9 \text{ keV}) = 1 / 0.51 / 0.078$$

The experimental and calculated depopulation rates for the 177.7 keV and 152.8 keV gamma rays match very well, but the 129.9 keV gamma ray is about 4.5 times more intense than the calculated value. This is due to the properties of the 5/2+ receiving state at 47.8 keV.

The 163.8 keV gamma ray also terminates at the 47.8 keV state and is anomalously intense. Equation V.8 and the data in Table 5-II indicates that the ratio of the intensity of the 163.8 keV gamma ray to that of the 186.8 keV gamma ray should be 0.55. What is actually observed [Ahm71] is a ratio of about 19. Another anomaly involving the 5/2+ state at 47.8 keV is in the alpha hindrance factors from ^{255}Fm decay [TOI78]. Decay to each member of the $K = 1/2+$ rotational band from the $7/2+$ ^{255}Fm ground state must proceed by $l = 4$ alpha emission by the K selection rules and parity conservation [Seg77,Ras68]. It should be expected that the hindrance factor to each member of the rotational band should be roughly the same large number. The hindrance factors for alpha decay to the 1/2+, 3/2+ and 5/2+ levels in the ground state rotational band are 4800, 2900 and 540, respectively. Once again, decay to the 5/2+ state is too fast. Coriolis coupling of some state with $K > 1/2$ to this state is

effectively increasing its K, increasing the Clebsch-Gordan factor for gamma decays resulting in this state and decreasing the l -hindrance to alpha decay.

The intensity of the 163.8 keV gamma-ray relative to the 177.7 keV gamma ray is 0.060 ± 0.012 ; therefore, that of the 186.8 keV line is roughly 0.003. Correction of both gamma rays for internal conversion gives a transition rate for the depopulation of the 211.6 keV state of 0.68 ± 0.15 , relative to that depleting the 177.7 keV state of 17.2 ± 1.0 , from Table 5-I data. Remembering that approximately 5% of the ^{251}Bk decays populate the ground state band of ^{251}Cf , the population of the 211.6 keV level is approximately 4%, and that of the 177.7 keV level is 91%. The ratio of the population of the 211.6 keV state to that of the 177.7 keV state is slightly higher (about 4%) than that arising from ^{251}Es decay (about 3%), which is expected since the decay energy is higher. Error analysis is not possible in this determination, but the assignment of a value of $(90 \pm 5)\%$ for the fraction of ^{251}Bk decays populating the 177.7 keV state in ^{251}Cf seems to be conservative.

The absolute intensity of the 177.7 keV gamma ray can be determined by taking into account the population of the initial state, the fraction of the gamma transitions going to the final state (0.521 ± 0.027 from Table 5-I data), and the total conversion coefficient (7.95 from Table 5-II). This yields a value of

$$I_{\gamma_{178}} = (5.2 \pm 0.6) \% .$$

As a rough measure of the validity of this value, the production of electrons in the decay of ^{251}Bk detectable by an end-window proportional counter is roughly equal to one beta particle per decay and one conversion electron per decay not producing a gamma ray. This value, relative to the 177.7 keV photon, is calculated to be approximately 36, very near the experimental value of 33.

The number of K-shell vacancies produced per ^{251}Bk decay can be calcu-

lated from the fractional K-shell conversion coefficients, the level populations and transition probabilities to be roughly 0.53. The fluorescence yield of the K-shell of ^{251}Cf can be interpolated from tabulated data [Hag60] to be 0.97. The predicted value of the total K X-ray intensity relative to the 177.7 keV gamma ray is 10.0, compared with an experimental value of 6.7 ± 0.3 . The 30% discrepancy between these numbers can be attributed, in part, to the uncertainties in the K shell conversion coefficients and the total conversion coefficients, which both contribute to the ratio in the same direction. The implication is that the intensity of the 177.7 keV gamma ray predicted above may be slightly too low.

5.6 Summary

The half life of ^{251}Bk has been remeasured to be (55.6 ± 1.1) minutes, in agreement with the literature. Measurements of the relative intensities of the gamma rays, including previously unknown gamma rays at 129.9 and 163.8 keV, have been made. An estimate of the 177.7 keV gamma ray absolute intensity is given as $(5.2 \pm 0.6)\%$. A decay scheme is shown in figure 5i.

Figure Captions

Figure 5a - A typical gamma ray spectrum of the berkelium fraction from the reaction of 96 MeV ^{18}O with ^{248}Cm .

Figure 5b - The efficiency of the end window proportional counter for the detection of beta particles, as a function of end point energy.

Figure 5c - Decay curve analysis of the gross beta activity as a function of time, measured from a berkelium chemical fraction. Error bars are smaller than the data points.

Figure 5d - A typical electron spectrum of the berkelium fraction, from the reaction of 96 MeV ^{18}O with ^{248}Cm . Calibration sample end points are shown.

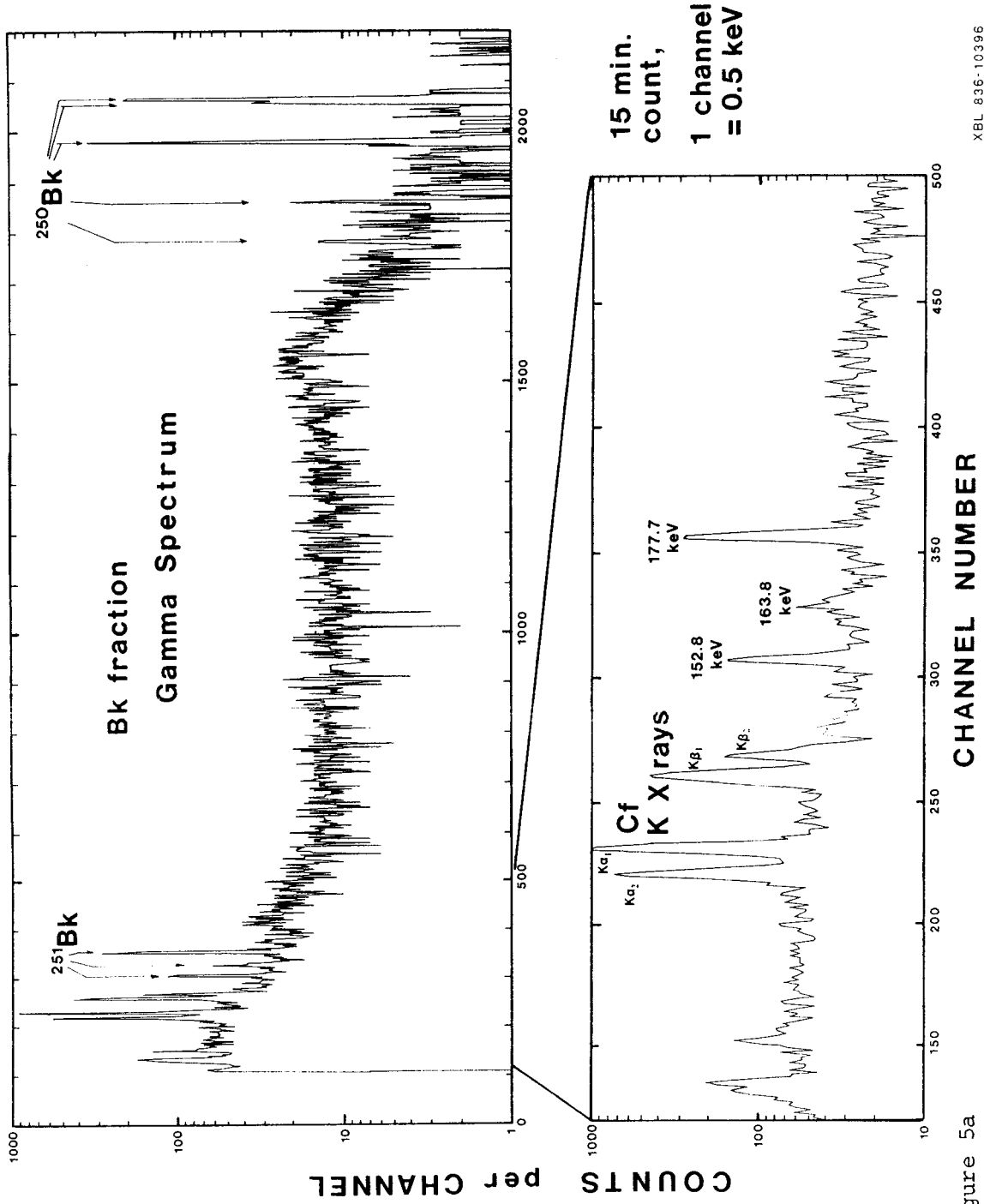
Figure 5e - A sample of the single component decay curve analysis of the gamma rays arising from ^{251}Bk decay. Also shown is the analysis of the weak 164 keV gamma ray.

Figure 5f - The known level scheme of ^{251}Cf [TOI78,Ahm70], indicating levels fed by ^{251}Es decay. ^{251}Bk and ^{251}Es both have an odd proton in the same Nilsson level in their ground states, so their decays can be expected to populate similar states in ^{251}Cf .

Figure 5g - The method of deconvolution of the spectral shape of beta particles from ^{251}Bk decay from the berkelium fraction beta particle energy spectra as a function of time after irradiation.

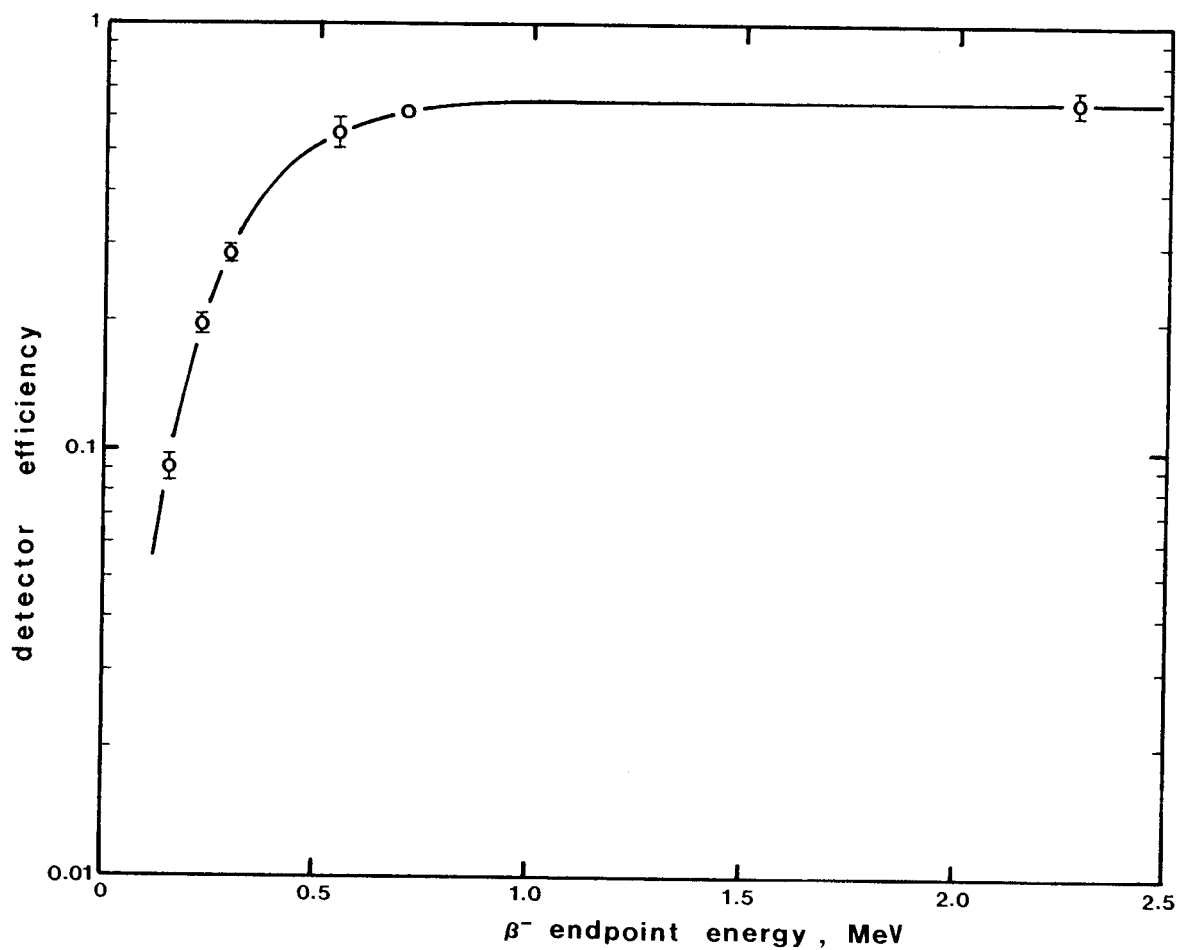
Figure 5h - The extracted beta particle spectral shapes of both ^{250}Bk and ^{251}Bk , with end points indicated, and a Fermi-Kurie plot of the endpoint region of ^{251}Bk .

Figure 5i - The decay scheme of ^{251}Bk . Gamma transitions are labelled with absolute photon intensities.



XBL 836-10396

Figure 5a



XBL 836-10297

Figure 5b

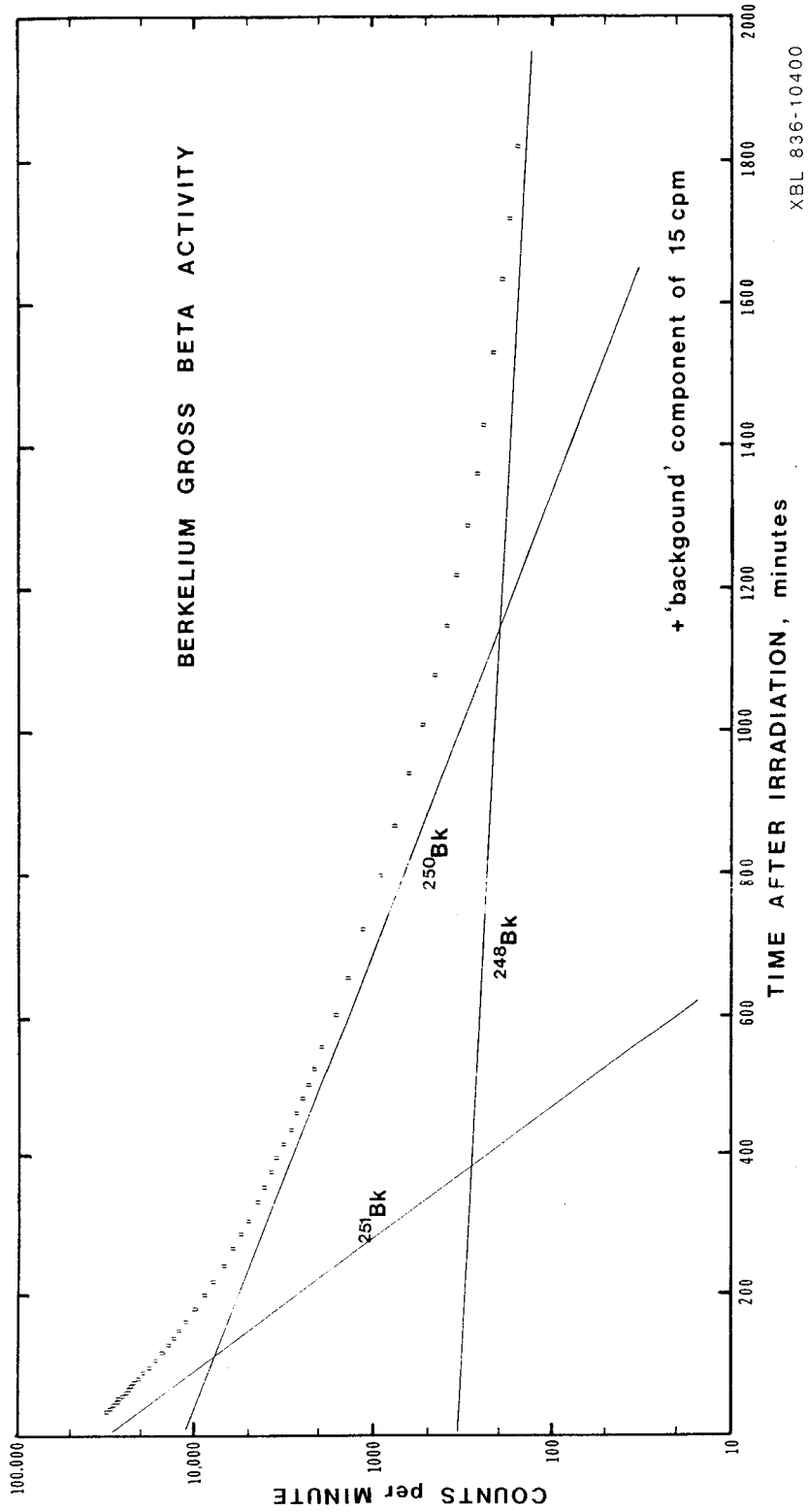


Figure 5c

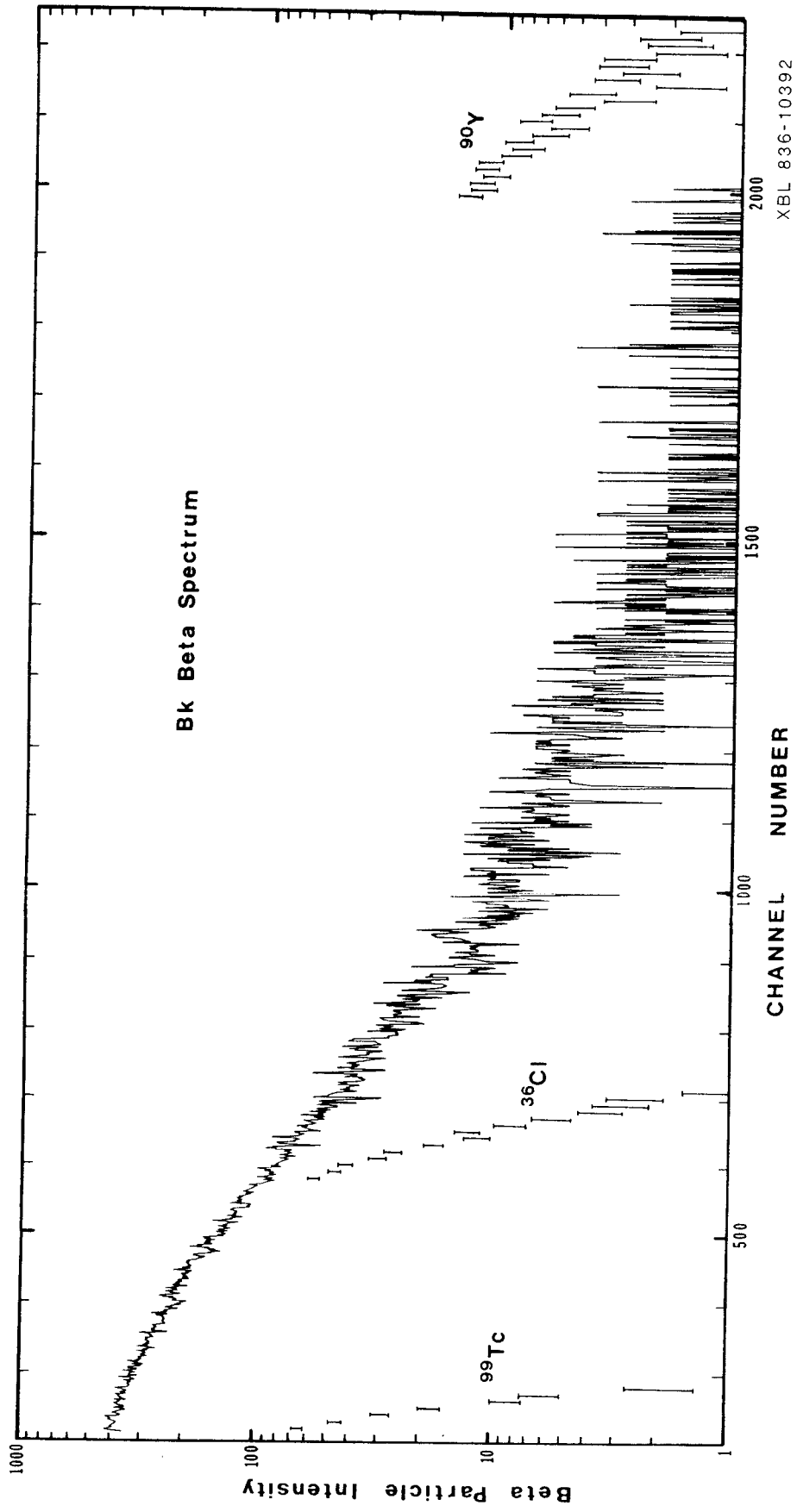
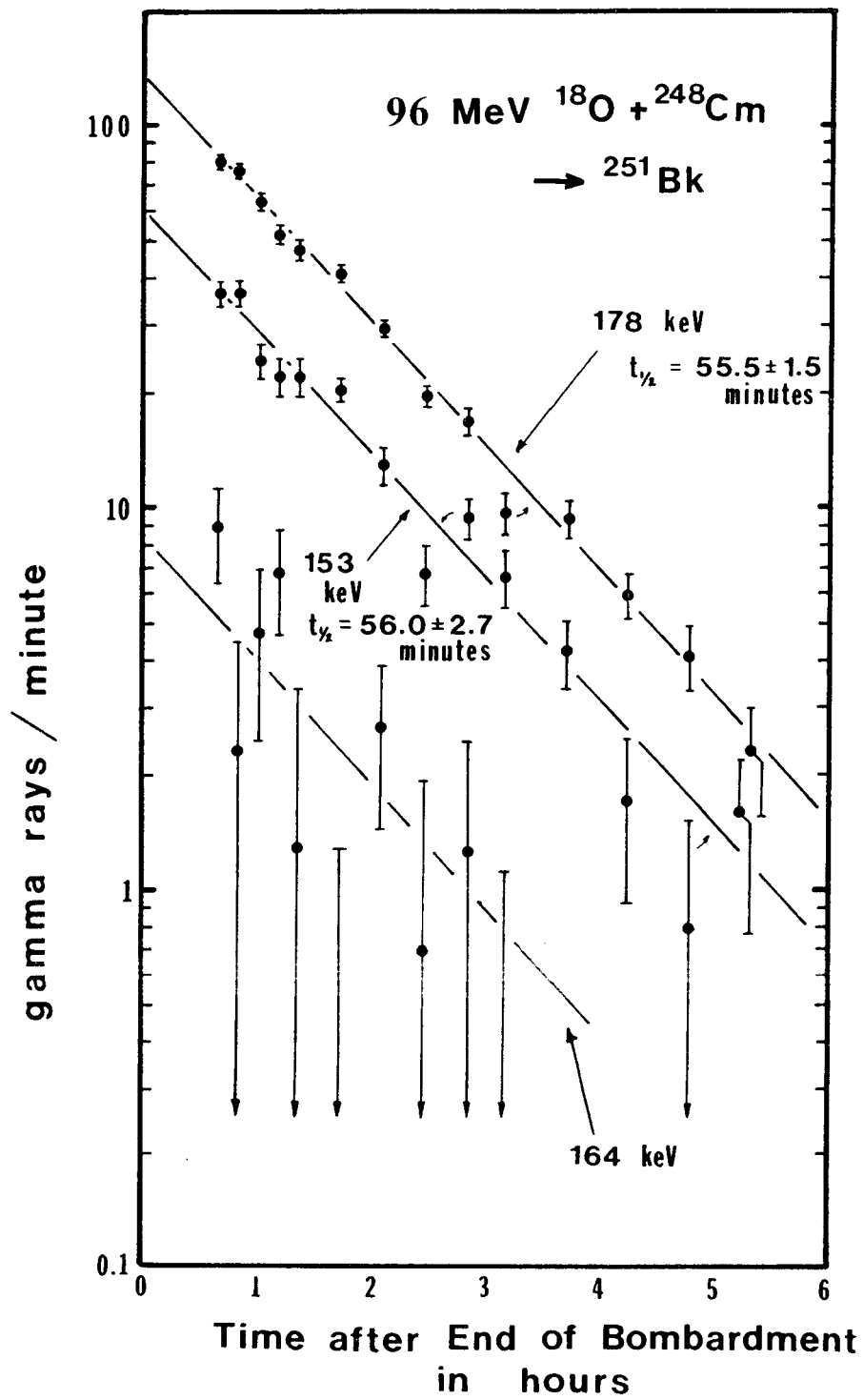
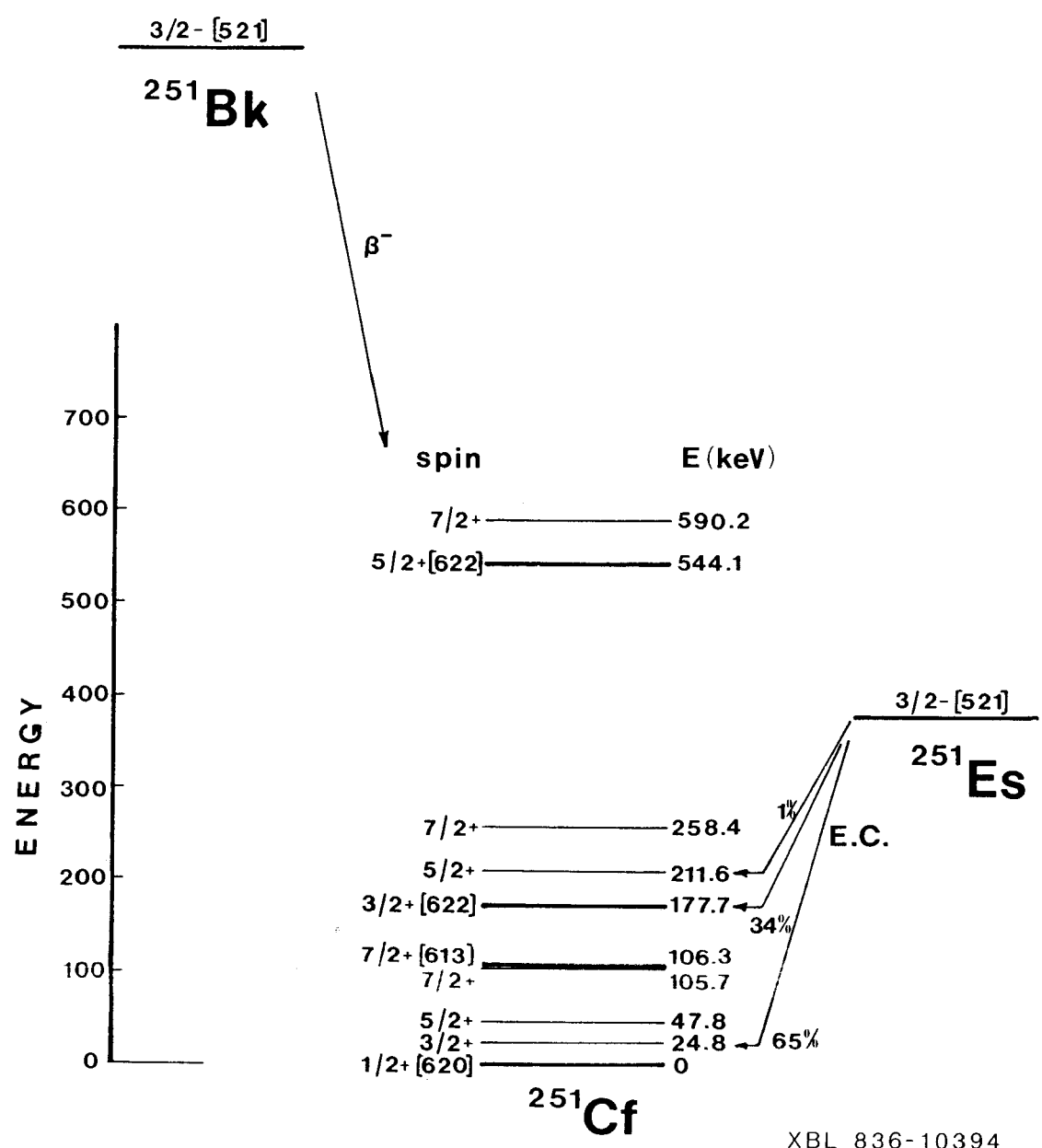


Figure 5d



XBL 836-10252

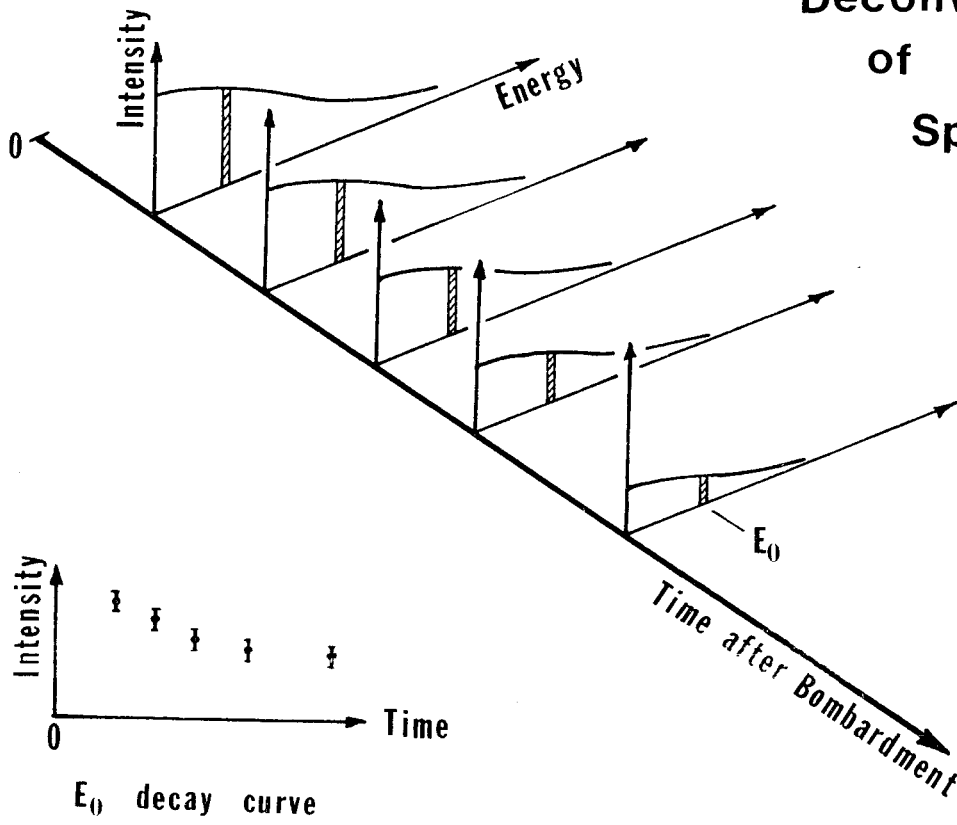
Figure 5e



XBL 836-10394

Figure 5f

Deconvolution of β^- Spectra



XBL 836-10254

Figure 5g

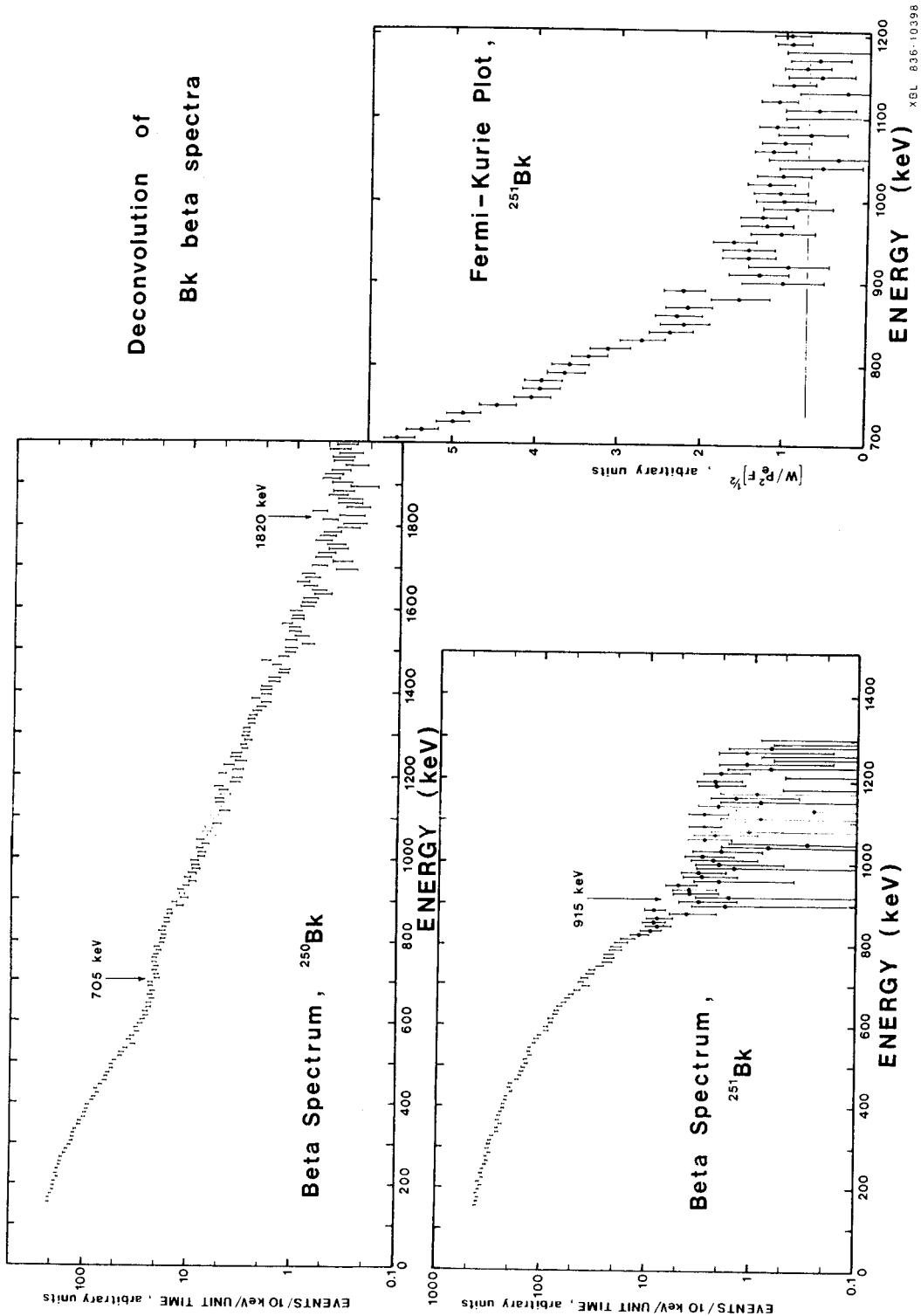
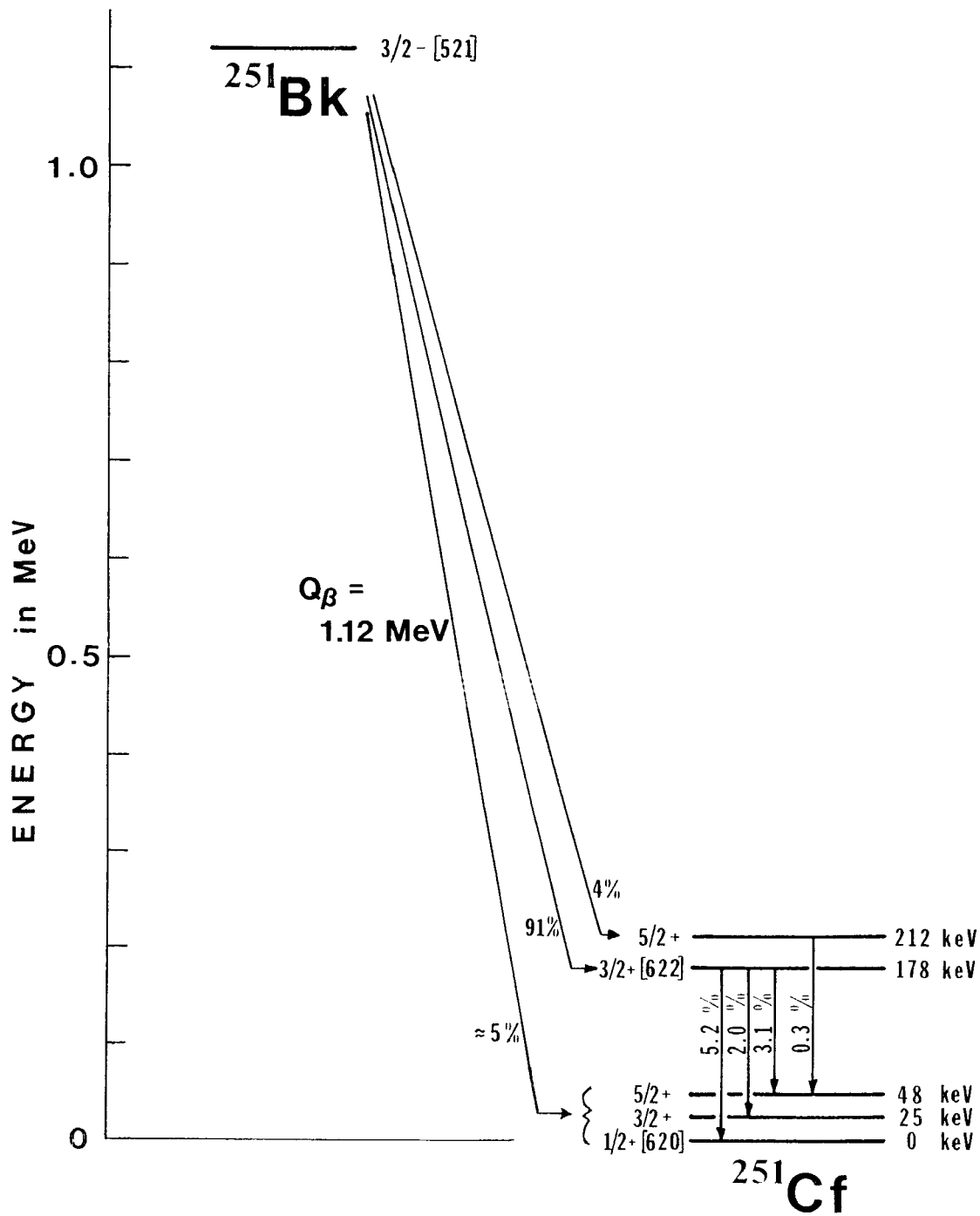


Figure 5h



XBL 836-10299

Figure 5i

Section 6 - The Search for ^{247}Pu

One of the conclusions drawn in Section 4 is that the reaction of very heavy, neutron-rich projectiles with neutron-rich actinide targets is a good way to produce new, neutron-rich actinide nuclides at a Z below that of the target. In an attempt to demonstrate this, 17 experiments were performed with ^{18}O , ^{86}Kr and ^{136}Xe ions to isolate ^{247}Pu from the reaction products from a ^{248}Cm target. Simple extrapolation of the plutonium yields in Section 4 indicates a production cross section for ^{247}Pu of as much as several hundred microbarns.

6.1 Predicted Properties of ^{247}Pu

The mass excess of ^{247}Pu has been calculated to be 69.28 MeV [Vio66], based on closed cycles of alpha- and beta-decays and on extrapolations of systematic behavior. Since 1966, a more comprehensive set of data has become available for extrapolation [Wap77]. Figure 6a shows the plot of experimental and extrapolated masses for mass numbers 243, 247 and 251, and those from two different theoretical mass predictions [Mye77,How80]. The mass calculations seem to accurately reproduce the shape and magnitude of the experimental distributions, but misplace the valley of beta stability by about one mass unit. Figure 6b shows the difference between the experimental and theoretical masses if the calculated mass parabolas [How80] are shifted one mass unit toward neutron excess. No justification is offered for doing this other than the accuracy of the resulting fits, depicted in figure 6b. Extrapolation of the behavior of the mass 247 curve along the lines of the 245 and 243 masses indicates a mass excess of approximately 69.1 MeV for ^{247}Pu . This yields a Q_β value of 2.0 MeV, which can also be obtained by extrapolating literature Q_β systematics [Bos77]. Figure 6c shows the experimental Q_α values for the plutonium isotopes, for the 247 mass chain, and for the 153 neutron isotone. Extrapolation of all three curves gives a Q_α of approximately 4.6 MeV for ^{247}Pu , as compared

with predicted 4.11 MeV [Vio66], 4.80 MeV [How80] and 4.63 MeV [Mye77] values in the literature. The extrapolation along the isotone is particularly valuable, because any effects coming from the weak 152 neutron shell will affect all the Q_α values similarly.

Alpha decay half lives can be estimated empirically from the relation of half life to alpha particle decay energy for the even-even nuclides of a particular element [Ras68]. With an alpha particle energy of 4.6 MeV for a ground state to ground state transition, an even-even plutonium isotope would have a partial alpha half life of approximately 10^8 years. The fact that ^{247}Pu is not even-even implies that the alpha decay need not most favorably proceed to the ground state, lowering the primary decay energy, and that the decay is hindered by a lower alpha particle preformation. Both effects lengthen the half life. It seems fairly safe to say, in the face of a Q_β value of 2.0 MeV, that ^{247}Pu does not have a significant alpha decay branch.

Spontaneous fission is a significant mode of decay in the actinides. The spontaneous fission half lives of the even-even nuclides as a function of the Z^2/A fissionability parameter [Str69] can be extrapolated to ^{247}Pu (fissionability parameter 35.8) to give a value near 10^7 to 10^8 years. Spontaneous fission half lives of odd mass nuclei are significantly longer than those for even-even nuclei. ^{247}Pu should not have a significant spontaneous fission decay branch.

The primary decay mode of ^{247}Pu is expected to be beta-minus decay to ^{247}Am . This is borne out by the presence of ^{247}Cm in nuclear debris [Com66]. The height of the fission barrier [How80] precludes the possibility of a significant beta-delayed fission branch [Thi83]. Prediction of beta decay half lives is more complicated than the prediction of alpha particle emission or spontaneous fission half lives. Not only must the ground state spin of the decaying species and the Q_β of the reaction be known, but the level structure of

the daughter nucleus **also** plays an important role. Usually the liquid drop model is used to give the Q_β value, the deformed Nilsson model is used to give the ground state spin of the parent [Gus67], and the beta strength is derived from the gross properties of the daughter averaged over final states. Usually only allowed and first-forbidden transitions are considered, since this is where the majority of the decay rate lies. Two different calculations using this approach give predictions for the ^{247}Pu half life of 11 minutes [Tak73] and 13 minutes [Kol75]. These half lives are long enough to be observable by normal chemical methods. Calculations performed after the start of this experimental project [See81,Kla80], using the wave functions of the states in the daughter nucleus from the deformed Nilsson potential to generate a "more realistic" beta strength function, resulted in a half life estimate of 2.2 minutes for ^{247}Pu . No matter which method is the more realistic, both depend on model calculations to which the nuclei do not necessarily conform.

Droplet model calculations predict a ground state deformation of about 0.18 for ^{247}Pu [Mye77]. From the Nilsson diagram for neutron energy levels [Gus67], this indicates a ground state J^π assignment of $7/2^+$ from a single 153^{rd} neutron occupying the $7/2[613]$ state. Examination of the level behavior of the odd-A, even-Z actinides, however, indicates that this assumption is not necessarily warranted; configuration mixing distorts the ideal behavior of the Nilsson levels. Figure 6d shows the "experimentally justified" Nilsson levels for the odd neutron of several odd-A actinides. This is similar to a previous treatment by Hoff [Hof76]. The data for this figure are compiled from the Nuclear Data Sheets [Sch77, Ell78, Sch77a, Ell78a, Ell81, Ell81a, Tul81] and some of the more recent literature [Bor79, Par81, Ahm82, Hof82]. Using the experimental band head assignments and referring to the theoretical Nilsson levels, the level structure of each nuclide is constructed by taking the energy difference

between the ground state and the level of interest and then deciding if the observed level is a particle or hole state. The vertical position of the diagram of a nuclide relative to those on either side of it is arbitrary. The level which is half-occupied in the ground state is marked with a hatch mark. The theoretical Nilsson levels are usually specified in terms of harmonic oscillator units, which are proportional to the inverse cube root of the nuclear mass [Des74], but $A^{1/3}$ is so slowly varying for nuclei in the region of mass 235 to 255 that the correction is neglected. Figure 6d is arranged in order of increasing neutron number, and a space is left for ^{247}Pu at one end of the 153 neutron isotone series. Band heads at both the lower and upper energy extremes of the figure are sometimes extrapolated from known excited members of the band using the level spacings of nearby nuclides where the same band is better defined. For N of less than 150, the level order is well behaved, though the relative energy spacing of the band heads is only poorly predictable. As the neutron number increases past 150, in the vicinity of the 152 neutron shell, many of the levels cross. If the behavior of the levels below $N = 150$ are simply extrapolated to higher neutron numbers, the prediction of a ground state configuration of $7/2+$ is obtained for ^{247}Pu , in agreement with the purely theoretical prediction. However, in the vicinity of $N = 152$, the $7/2+[613]$ and $1/2+[620]$ levels cross. Besides the data presented in the figure, the ground state spin of the $N = 155$ nuclide ^{251}Cm is $1/2+$ [Lou78], indicating a crossing between ^{251}Cm and ^{253}Cf . In the higher Z elements fermium and nobelium the $1/2+[620]$ state is permanently below the $7/2+[613]$ state [Tul81], but in the plutonium, curium and californium nuclides the cross over is still occurring and is not trivially predictable. Therefore, it cannot be said whether the ground state of ^{247}Pu is $7/2+$ or $1/2+$. The energy difference between the levels may be so small that the possibility of an isomeric state in ^{247}Pu exists, since transition between the two states would be of $M3 (E4)$

multipolarity. The only known odd-mass, even-Z isomer in the actinide region (excepting the shape isomers) is that in ^{235}U .

The ground state spin of ^{247}Am was determined from the levels of ^{247}Cm populated by the ^{247}Am beta decay and the $\log ft$ values to be $5/2$ [Ort67]. The parity of the ground state is not known. None of the excited states have been characterized. Figure 6e is similar to figure 6d, except that the odd-proton energy levels have been constructed. The same Nuclear Data Tables were used as before, as well as some supplementary data from the more recent literature [Gri78,Ahm79,Bem81,Ahm78]. As before, the nuclides are arranged in order of increasing neutron number; even though they are proton levels it is expected that the 152 neutron shell will disrupt their smooth behavior. A space is left for ^{247}Am at the lower end of the 152 neutron isotone. The order of the levels remains well behaved up until $N = 150$, at which point the levels begin to cross. Once again, not much of a definite nature can be said about the nuclide of interest. The ground state is probably $5/2+[642]$, but might be $5/2-[523]$; if it weren't for the determination by Orth that the spin is $5/2$, the $1/2+[400]$ level could not be eliminated as a possibility for the ground state. It seems fairly safe to say that at an energy of less than or equal to 200 keV are the $5/2+[642]$, $5/2-[523]$ and $1/2+[400]$ levels, and at an energy near 500 keV are the $3/2-[521]$, $7/2+[633]$ and, possibly, $1/2-[530]$ levels. Somewhere near an excitation energy of 1 MeV are the $1/2-[521]$ and $7/2-[514]$ states. From these postulates, the approximate level scheme of ^{247}Am depicted in figure 6f arises. Beta decay to the excited members of rotational bands built upon these Nilsson levels can also occur. It must be stressed that this level scheme is only for the purpose of half life estimation, and that there is no experimental data to verify it.

If the ground state rotational band of ^{247}Pu is based on the $1/2+[620]$ level, the possibility exists that the ground state of ^{247}Pu is $3/2+$ due to the decou-

pling factor for $K = 1/2$ bands. The nuclide ^{235}Pa is an example of this. Examination of all the nuclides in which the $1/2+[620]$ band is observed fails to locate even one example where the $3/2+$ state lies below the $1/2+$ state. The rotational spacing for a $K = 1/2$ band [Des74] is given by

$$E(I, K=1/2) = E(I=1/2) + \frac{\hbar^2}{2I} [I(I+1) + a (-1)^{I+\frac{1}{2}} (I+1/2)] \quad \text{VI.1}$$

where I is the spin of a level in the band, $E(I=1/2)$ is the energy of the band head, I is the moment of inertia of the nucleus and a is the decoupling parameter. Using equation VI.1 and the data in the literature for the level structures of nuclei isotonic with ^{247}Pu [TOI78], the decoupling parameters of ^{249}Cm ($a = 0.46$) and ^{251}Cf ($a = 0.28$) can be extracted. The decoupling parameter must be less than -1 for the $3/2$ state to lie below the $1/2$ state. If the ground state of ^{247}Pu is $K = 1/2$, the ground state spin is almost certainly $1/2+$. The beta decay of ^{247}Pu can be expected to occupy levels in the daughter based on the $1/2+[400]$ state (allowed transition, though the change in the n_z quantum number is 2, and therefore l -forbidden), the $1/2-[530]$ state (first forbidden transition), the $3/2-[521]$ state (first forbidden transition), the $1/2-[521]$ state (first forbidden transition) and the $5/2-[523]$ state (first forbidden, unique, transition). In ^{249}Cm and ^{251}Cm , the odd neutron occupies the $1/2+[620]$ level in the ground state, and the decay rates to the $1/2+[400]$, $1/2-[530]$, $1/2-[521]$ and $3/2-[521]$ states have been measured [TOI78]. Using tabulated $\log f$ values for allowed and first forbidden decays [Gov71], the $\log ft$ values are calculated in Table 6-I.

Table 6-I Calculation of $\log ft$ values for the beta-minus decay of two curium isotopes. Data from reference [T0178].

^{249}Cm , half life 65.3 minutes, ground state = $\frac{1}{2}^+ [620]$					
Daughter level	Decay Energy (MeV)	Partial half life (sec)	$\log f$ (allowed)	$\log f$ (1^{st} forbidden)	$\log ft$
$\frac{3}{2}^- [521]$	0.891	4.1×10^9		2.68	6.3
$\frac{1}{2}^+ [400]$	0.522	7.8×10^5	1.52		7.4
$\frac{1}{2}^- [530]$	0.331	3.9×10^5		0.63	6.2
$\frac{1}{2}^- [521]$	0.257	2.3×10^5		0.15	5.5
^{251}Cm , half life 16.8 minutes, ground state = $\frac{1}{2}^+ [620]$					
$\frac{3}{2}^- [521]$	1.42	1.4×10^8		3.76	6.9
$\frac{1}{2}^+ [400]$	1.11	1.4×10^5	2.61		7.8
$\frac{1}{2}^- [530]$	0.98	5.9×10^4		2.89	7.7
$\frac{1}{2}^- [521]$	0.88	6.3×10^3		2.65	6.4

For calculation of ^{247}Pu decay rates, the average $\log ft$ values for decay to the same levels from the two curium nuclides were assumed. A value of $\log ft = 8.5$ for the first forbidden, unique, decay to the $5/2^- [523]$ state is also assumed [Mar69]. "Reasonable" values of the decay energies to each state are taken from figure 6f, using the ground state to ground state Q_β of 2.0 MeV calculated above. Table 6-II outlines the calculation of the partial half lives for decay to the different rotational band heads in ^{247}Am from ^{247}Pu .

Table 6-II Calculation of the partial half lives of the beta decay of $1/2+[620]$ ^{247}Pu .

Daughter level	Approximate Decay Energy (MeV)	$\log ft$	$\log f$ (allowed)	$\log f$ (1^{st} forbidden)	Partial half life (sec)
$\frac{1}{2}+[400]$	1.9	7.6	3.41		1.5×10^4
$\frac{5}{2}-[523]$	1.9	≈ 8.5		4.40	1.3×10^4
$\frac{1}{2}-[530]$	1.7	7.0		4.14	7×10^2
$\frac{3}{2}-[521]$	1.6	6.6		3.99	4×10^2
$\frac{1}{2}-[521]$	1.0	6.0		2.91	2.5×10^3

In the first forbidden decays to the $1/2-[530]$ and $1/2-[521]$ rotational bands, decays to the $3/2-$ members are also permitted ($\Delta J = 1$). The relative population of different members of the same rotational band by beta decay is proportional to the squares of the Clebsch-Gordan coefficients for the transitions [Mar70]. However, the admixture of $L = 0$ and $L = 1$ multipolarities in first forbidden decays makes this calculation difficult to implement accurately. If it is assumed that the rotational energy spacings are negligible relative to the decay energies involved, the relative population of the different rotational levels of the same rotational band by beta decay from a particular Nilsson level should be roughly the same in any parent-daughter system in which the decays occur. The relative intensity data from the beta emitting curium isotopes [TOI78] average to give a partial half life to the $3/2-$ state of the $1/2-[530]$ band of 900 seconds and a partial half life to the $3/2-$ state of the $1/2-[521]$ band of 5400 seconds. This, with the Table 6-II data, gives an overall half life for $1/2+[620]$ ^{247}Pu of 2.7 minutes, in good agreement with the more recent literature [See81].

If the ground state of ^{247}Pu is $7/2+[613]$, the strength of the decay will be to levels in the bands based on the $5/2+[642]$ state (allowed transition, but with $\Delta n_z = 3$, strongly l -forbidden), the $5/2-[523]$ state (first forbidden transition), the $3/2-[521]$ state (first forbidden, unique, transition), the $7/2+[633]$ state (allowed transition, but with $\Delta n_z = 2$, l -forbidden), and the $7/2-[514]$ state (first forbidden transition). Excited states in the $K = 1/2$ bands are excluded by the K selection rule. Unfortunately, the extensive data which are available on the $1/2+[620]$ decay from the beta-emitting curiums are not available for the $7/2+[613]$ decay. The only known odd-A nuclide with an unpaired neutron in the $7/2+[613]$ level in the ground state is ^{253}Cf , which decays only to the $7/2+[633]$ state of ^{253}Es . Some more drastic approximations are necessary to come up with a set of $\log ft$ values.

The decay energy of ^{253}Cf is 0.287 MeV and the half life is 17.8 days [TOI78]. The $\log f_o$ is 0.73 [Gov71], giving a $\log ft$ of 6.9, consistent with an l -forbidden allowed decay. The nuclide ^{243}Pu has a ground state configuration of $7/2+[624]$ and a decay energy of 0.580 MeV to the ground state of ^{243}Am , which is $5/2-[523]$, one of the levels of interest in ^{247}Pu decay. This decay will be used to simulate the first forbidden decays of ^{247}Pu . The partial half life is 8.3 hours and the $\log f$ is 1.71 [Gov71], yielding a $\log ft$ of 6.2, similar to those for the first forbidden decays of the $1/2+[620]$ states in Table 6-1. The simulation of the allowed decay of a $7/2+$ state with $\Delta n_z = 3$ is not easy; the only nuclide which demonstrates this beta-minus transition is ^{165}Dy , which has a ground state configuration with an odd neutron in the $7/2+[633]$ level, partially decaying to an excited state in ^{165}Ho with a $7/2+[404]$ configuration [TOI78]. The partial half life of the decay is 170 days and the $\log f_o$ is 0.92, giving a $\log ft$ of 8.1. The first forbidden decay to the ground state of ^{165}Ho has a $\log ft$ of 6.9, comparable to the 6.2 value obtained from ^{243}Pu decay. Once again, the $\log ft$

of a first forbidden, unique, decay is assumed to be approximately 8.5. Table 6-III outlines the calculation of the partial half live for decay to the different rotational band heads in ^{247}Am from $7/2+[613]$ ^{247}Pu .

Table 6-III Calculation of the partial half lives of the beta decay of $7/2+[613]$ ^{247}Pu .

Daughter level	Approximate decay energy (MeV)	$\log ft$	$\log f$ (allowed)	$\log f$ (1 st forbidden)	Partial half life (sec)
$\frac{5}{2}+[642]$	2.0	8.1	3.50		4.0×10^4
$\frac{5}{2}-[523]$	1.9	6.2		4.40	60
$\frac{3}{2}-[521]$	1.6	8.5		3.99	3.2×10^4
$\frac{7}{2}+[633]$	1.6	6.9	3.14		5.8×10^3
$\frac{7}{2}-[514]$	1.0	6.2		2.91	1.9×10^3

In the first forbidden decays to the $5/2-[523]$ and $7/2-[514]$ rotational bands (the strongest transitions), decays to higher rotational members are also permitted, bounded by $\Delta J \leq 1$. The relative half lives of transitions to the $5/2-[523]$ band in ^{243}Pu decay are 1.0 for the $5/2-$ state, 6.7 for the $7/2-$ state and approximately 30 for the $9/2-$ state. The relative half lives of transitions to the $7/2-[523]$ band in ^{165}Dy decay are 1.0 for the $7/2-$ state and 5.5 for the $9/2-$ state. Once again, assuming that rotational energy effects are negligible with respect to the decay energy, direct application of these ratios to the data in Table 6-III gives partial half lives for ^{247}Pu decay to the $5/2[523]$ $7/2-$ state of 400 seconds, to the $5/2[523]$ $9/2-$ state of about 1800 seconds, and to the $7/2[514]$ $9/2-$ state of 1.0×10^4 seconds. The calculated half life of $7/2+[613]$ ^{247}Pu is 50 seconds.

It should be realized, of course, that an error of one unit in the $\log ft$ values assigned to the fastest transitions can change the calculated half life of ^{247}Pu by an order of magnitude. In the region of the 152 neutron shell, where configuration interactions in both the parent and the daughter are rapidly changing, this kind of error is quite possible. One conclusion which can be drawn concerns the observables from ^{247}Pu decay. If the ground state of ^{247}Pu is $7/2+$, most of the decay proceeds directly to the low-lying $5/2-[523]$ rotational band in ^{247}Am , so the high energy gamma rays which might arise from the population of higher states will be of very low intensity. On the other hand, if the ^{247}Pu ground state is $1/2+$, the decay is divided among the higher-lying $3/2-[521]$, $1/2-[530]$ and $1/2-[521]$ bands of the daughter, so gamma rays with energies on the order of 1 MeV might be expected to be fairly intense.

6.2 Experimental

No evidence for the presence of ^{247}Pu was observed.

The experiments aimed at detecting ^{247}Pu were performed with 1130 MeV ^{136}Xe ions (three irradiations), 730 MeV ^{86}Kr ions (six irradiations), 650 MeV ^{86}Kr ions (six irradiations), and 111 MeV ^{18}O ions (two irradiations). The chemistry was tested with several 146 MeV ^{22}Ne irradiations at low beam intensities. Irradiations were of thirty minutes duration. The target used in ^{86}Kr and ^{136}Xe bombardments was the 2.15 mg/cm^2 ^{248}Cm target used in the main work, the catcher foils were 45 mg/cm^2 nickel in the form of a truncated cone (Section 3), and the beam intensity was between 0.5 and 1.0 electrical microampere for each run. The target used in ^{18}O (and ^{22}Ne) runs was the same as that used in runs $^{18}\text{O-I}$ and $^{18}\text{O-II}$. Since the cross section extrapolated for the ^{247}Pu cross section from the reaction of 96 MeV (in the target) ^{18}O with ^{248}Cm is only on the order of microbarns, it is not surprising that no data resulted from the two ^{18}O irradiations, so these experiments will not be discussed further.

Samples were prepared for gamma ray detection using the chemical procedure outlined in Section 2. The start of the first accumulation of data with the Ge(Li) detector (Section 2) was within thirty minutes of the end of the irradiation and sometimes significantly sooner. The time of chemical separation of plutonium from its beta-minus decaying americium daughters was well defined by the end of the hydrochloric acid wash of the anion column, which took place approximately 3 to 5 minutes before the start of the first data acquisition. Ideally, the best way to first detect the presence of ^{247}Pu is to look for the growth and decay of the 285 keV, 23% abundant gamma ray of the 24 minute ^{247}Am daughter. The chemistry gives a good purification from 3+ actinides in the final plutonium fraction, which is necessary if the presence of ^{247}Am , formed directly in the reaction with a high cross section, is to be used as a criterion for ^{247}Pu decay.

Unfortunately, the chemistry gives a separation from cerium of only 10^2 to 10^3 . In experiments with ^{136}Xe ions, the plutonium fraction was loaded with the gamma rays of the cerium isotopes (and daughters) all the way from mass 129 to mass 146. Cerium of mass 131 has two isomeric states, one with a 5 minute half life and one with a 10 minute half life, both of which decay to ^{131}La , which has a half life of 59 minutes [Nor66]. One of the most intense gamma rays emitted in the decay of ^{131}La has an energy of 285 keV. Since the signature of ^{247}Pu is a growth and decay of this gamma line on the same time order as the growth and decay of ^{131}La , this is a serious interference. Figure 6g shows the first gamma ray spectra accumulated in two different ^{86}Kr experiments at 730 MeV out of the accelerator.

Simple extrapolation of the ^{86}Kr -I data in Section 4 indicates that the cross section for the formation of ^{247}Pu from the reaction of these ^{86}Kr ions with ^{248}Cm should be approximately $100 \mu\text{b}$. Taking an "average" bombardment 30

minutes long at 750 nanoamperes of $^{86}\text{Kr}^{22+}$ and a chemical yield of 50%, with a separation of plutonium from americium occurring 20 minutes after the end of bombardment, the number of atoms of ^{247}Pu present at the time of separation can be determined as a function of its half life. Solution of the decay equations for a growth and decay gives the number of atoms of daughter species N_d as a function of time after separation t from a given number of parent atoms N_p at time zero:

$$N_d = \frac{N_p \lambda_p}{\lambda_d - \lambda_p} \left(e^{-\lambda_p t} - e^{-\lambda_d t} \right) \quad \text{VI.2}$$

where λ_p and λ_d are the decay constants of the parent and daughter respectively. The time at which the number of daughter atoms (and hence daughter decays) is at a maximum, obtained by setting the derivative of VI.1 to zero, is

$$t_{\max} = \frac{\left[\ln (\lambda_p / \lambda_d) \right]}{\lambda_p - \lambda_d} \quad \text{VI.3}$$

Table 6-IV outlines the calculation of the maximum decay rate of ^{247}Am from ^{247}Pu decay as a function of ^{247}Pu half life.

Table 6-IV Maximum decay rate of ^{247}Am from ^{247}Pu decay for several values of the ^{247}Pu half life, for a 30 minute bombardment of $^{86}\text{Kr}^{22+}$ at 750 nA, assuming a chemical yield of 50%.

^{247}Pu half life (min)	Number of atoms present at end of bombardment	Number of atoms in the chemical fraction at separation	Time after chemistry when ^{247}Am is at maximum (minutes)	Maximum decay rate of ^{247}Am (minutes ⁻¹)
2	1.9×10^4	10	7.8	0.23
5	4.7×10^4	1.5×10^3	14.3	28
10	8.4×10^4	1.0×10^4	21.7	150
15	10.8×10^4	2.1×10^4	27.2	280
20	12.4×10^4	3.1×10^4	31.7	360

The 23% branching ratio of the gamma ray combined with the 5% detector efficiency at 285 keV makes only about 1% of the decays "detectable." Figure 6h shows "decay curves" for the 285 keV gamma line from two of the better chemistries from full energy ^{86}Kr runs. It can be seen that the contaminant level is on the order of one to three detected gamma rays per minute over much of the time region of interest. Nothing can be said about the growth and decay of ^{247}Am (maximum count rate less than or equal to 3 per minute) in the presence of this background. Even if the activity due to ^{131}La is subtracted, from calculations based on the activity of the other ^{131}La gamma rays, the error bars on the resulting data points almost encompass the possible ^{247}Am activity. No conclusions can be drawn about the half life of ^{247}Pu .

If ^{247}Pu decay results in gamma rays with nearly 100% abundance, a 10 minute half life would indicate an initial activity of 500 decays per minute, or an observable 1 to 5 decays per minute (depending on the detector efficiency) at the start of the first count. Examination of the first gamma ray spectra from each experiment where the plutonium yield was large and the cerium yield was relatively small turned up no gamma lines at this intensity which could not be attributed to cerium nuclides, daughter activities, or detector background. This means only that if the ^{247}Pu half life is observable, the gamma rays from its decay are on the order of 20% or less in intensity.

6.3 Summary

The half life of ^{247}Pu is predicted to be less than 3 minutes, in agreement with recent literature. The ^{247}Pu ground state is either $7/2+$ or $1/2+$, based on the Nilsson energy levels and the systematic behavior of the odd-A, even-Z actinides. An experimental search for the nuclide, assuming the half life to be longer than the estimate by a significant amount, was unsuccessful due to cerium contamination coming through the chemical procedure. This method of

observing ^{247}Pu is marginal, even in the absence of chemical contaminants.

Figure Captions

Figure 6a - Comparison of the extrapolated mass excess of Wapstra [Wap77] (circles) with the droplet predictions of Myers [Mye77] (upper curves) and Howard [How80] (lower curves) for masses 243,247 and 251.

Figure 6b - The difference between the extrapolated mass excesses of (A,Z) odd mass nuclei [Wap77] and the droplet predictions for the mass excess of (A,Z-1) nuclei [How80].

Figure 6c - Alpha decay energies derived from extrapolated mass excess data [Wap77], for the plutonium isotopes, for the N=153 isotone, and for the A=247 mass chain. The extrapolation to the ^{247}Pu Q_α is indicated.

Figure 6d - The systematic behavior of the experimentally determined odd-neutron Nilsson levels in the actinides. The vertical orientation of one level scheme relative to its neighbors is arbitrary.

Figure 6e - The systematic behavior of the experimentally determined odd-proton Nilsson levels in the actinides. The vertical orientation of one level scheme relative to its neighbors is arbitrary.

Figure 6f - A proposed approximate level scheme of ^{247}Am from the data in figure 6e, used in the half life determinations of ^{247}Pu described in the text. Only band heads are shown.

Figure 6g - The first gamma ray spectra of plutonium fractions arising from two irradiations of ^{248}Cm with ≈ 520 MeV ^{86}Kr . The top spectrum is a 10 minute accumulation started 25 minutes after E.O.B. The bottom spectrum is a 5 minute accumulation started 22 minutes after E.O.B.

Figure 6h - Typical "decay curves" of the 285 keV gamma ray activity from the plutonium fraction from the reaction of ^{86}Kr with ^{248}Cm .

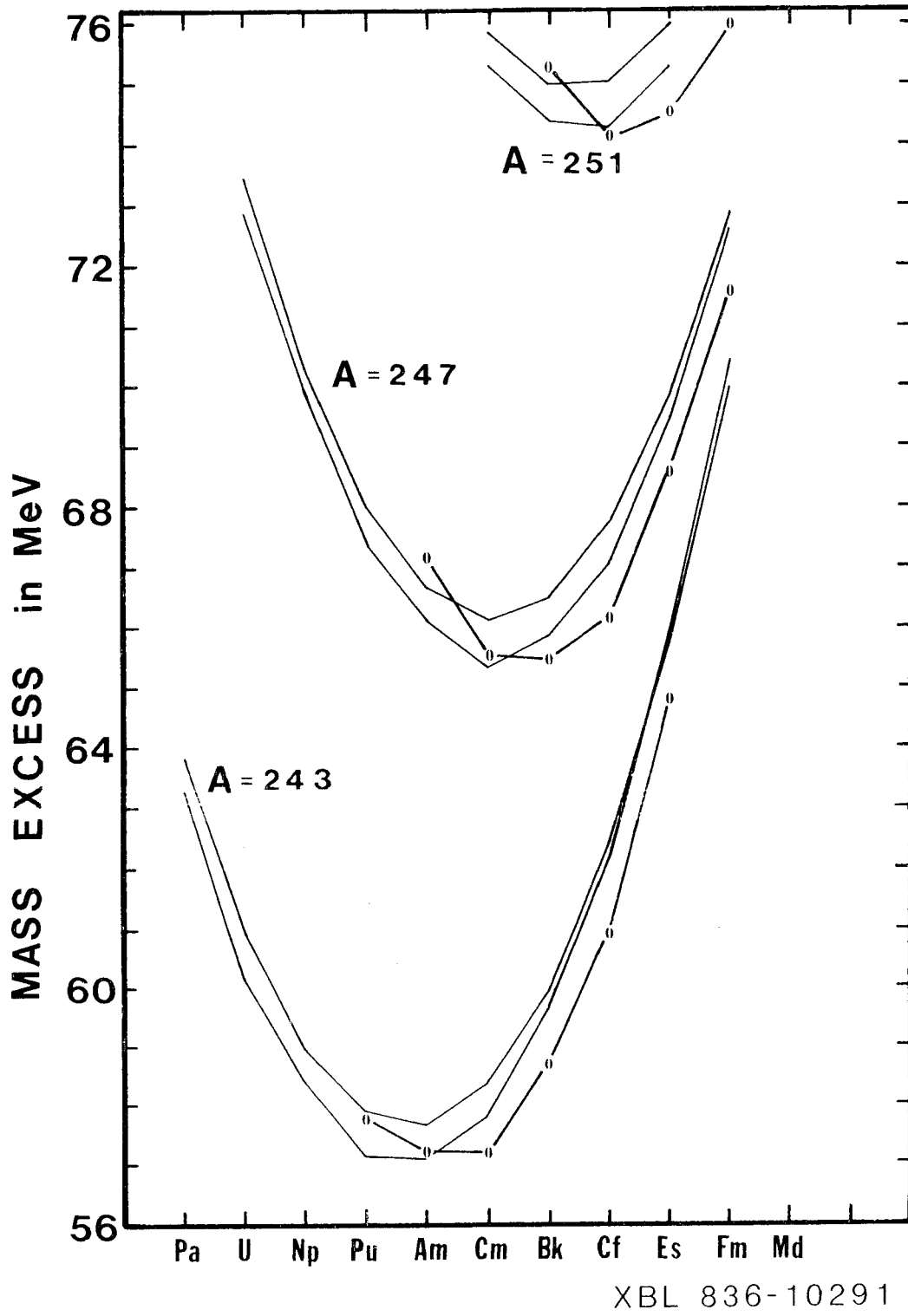
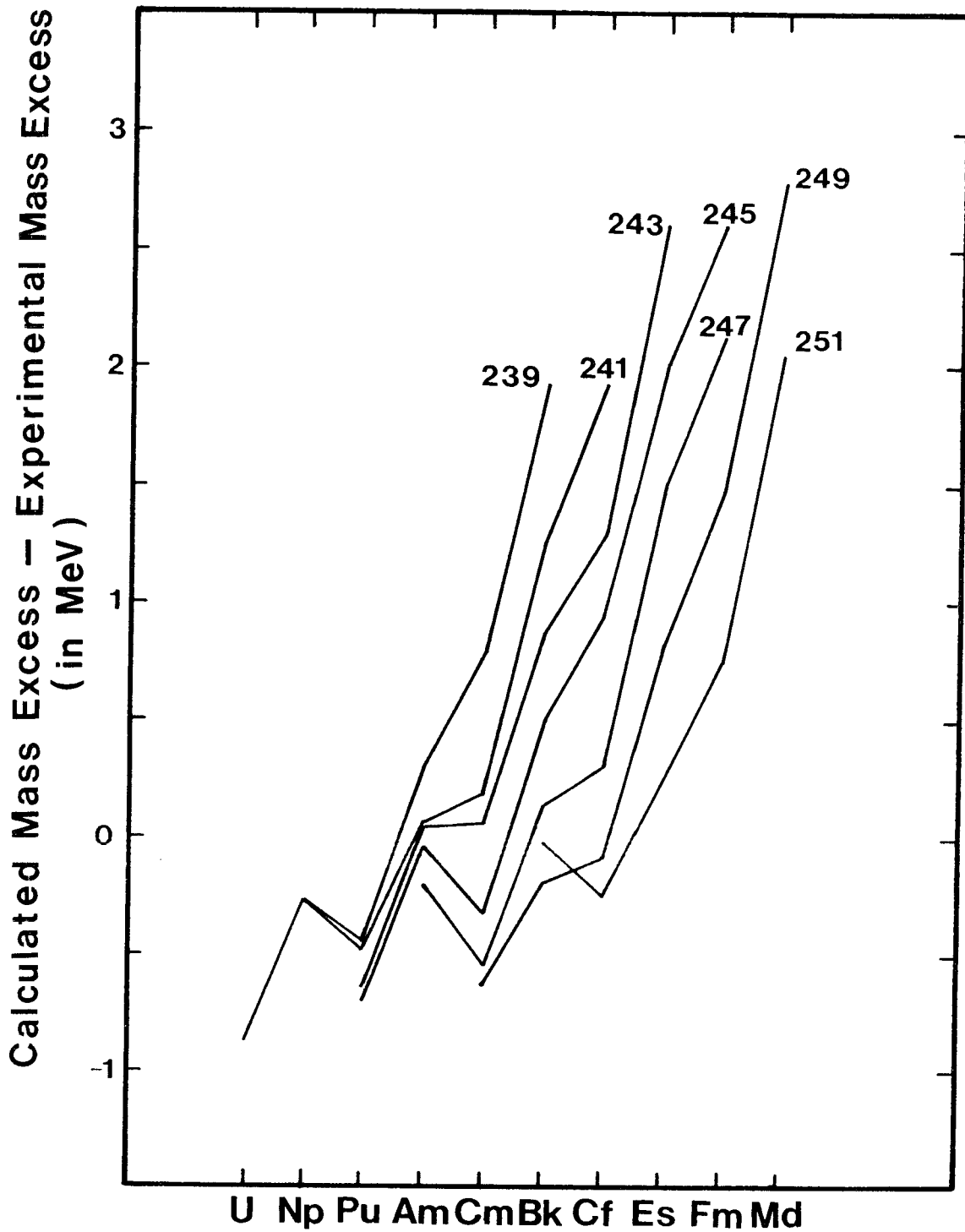


Figure 6a



XBL 836-10290

Figure 6b

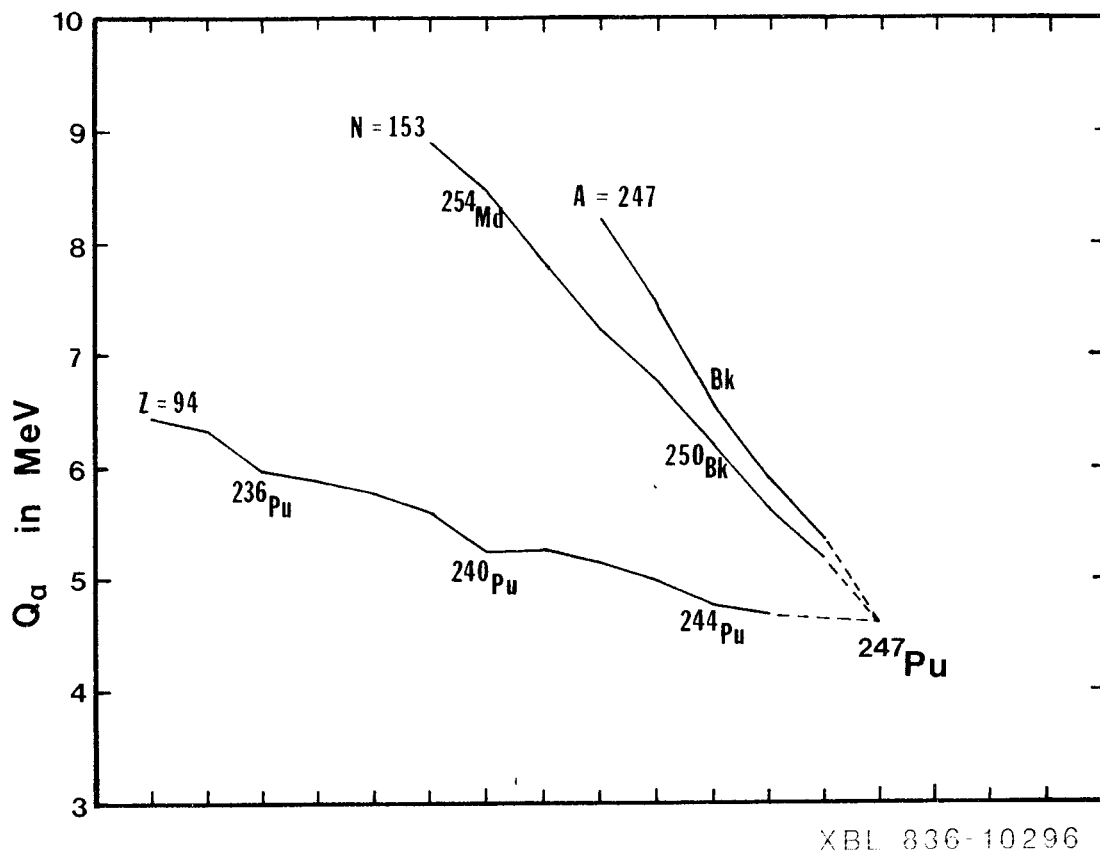


Figure 6c

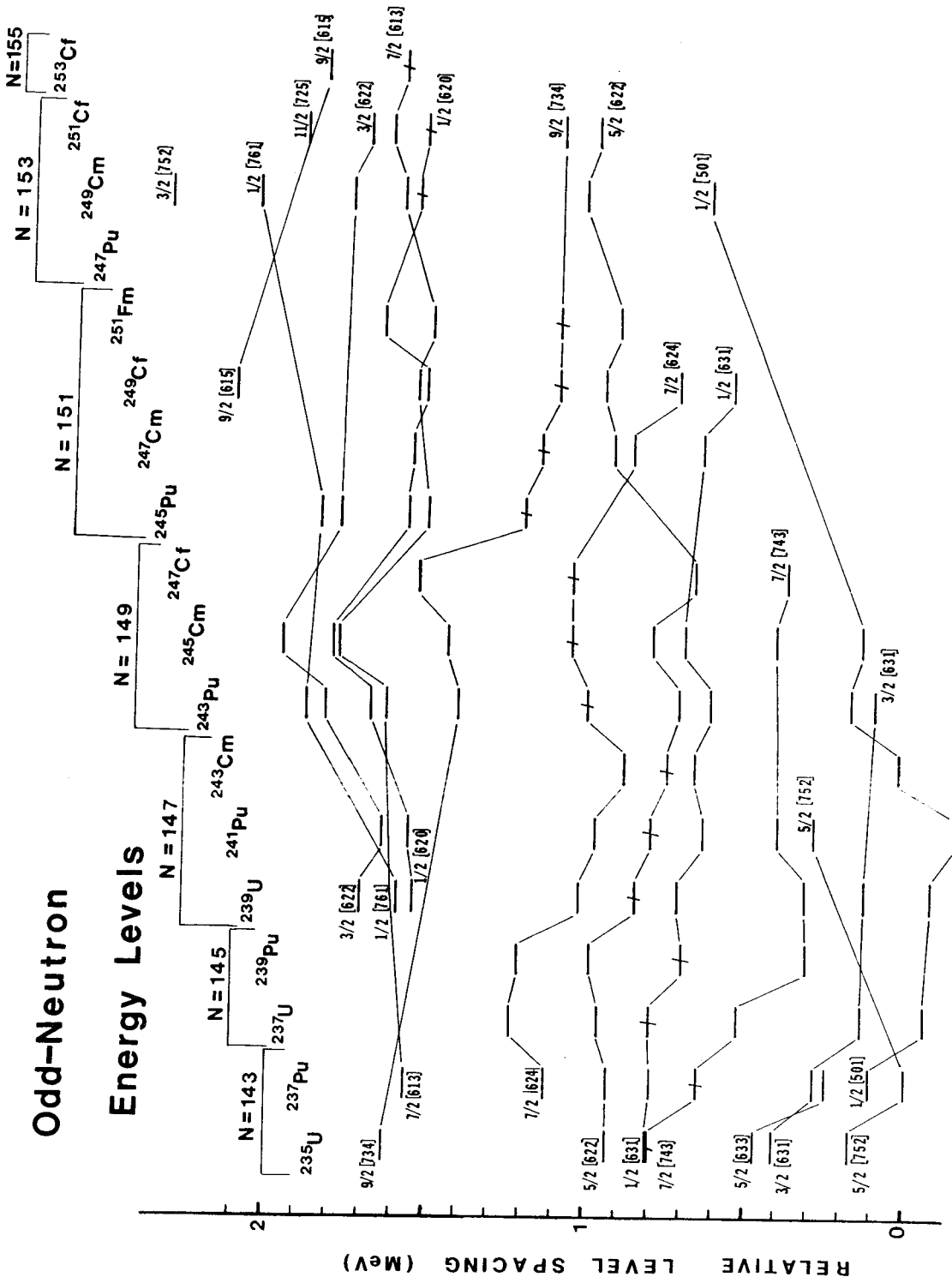
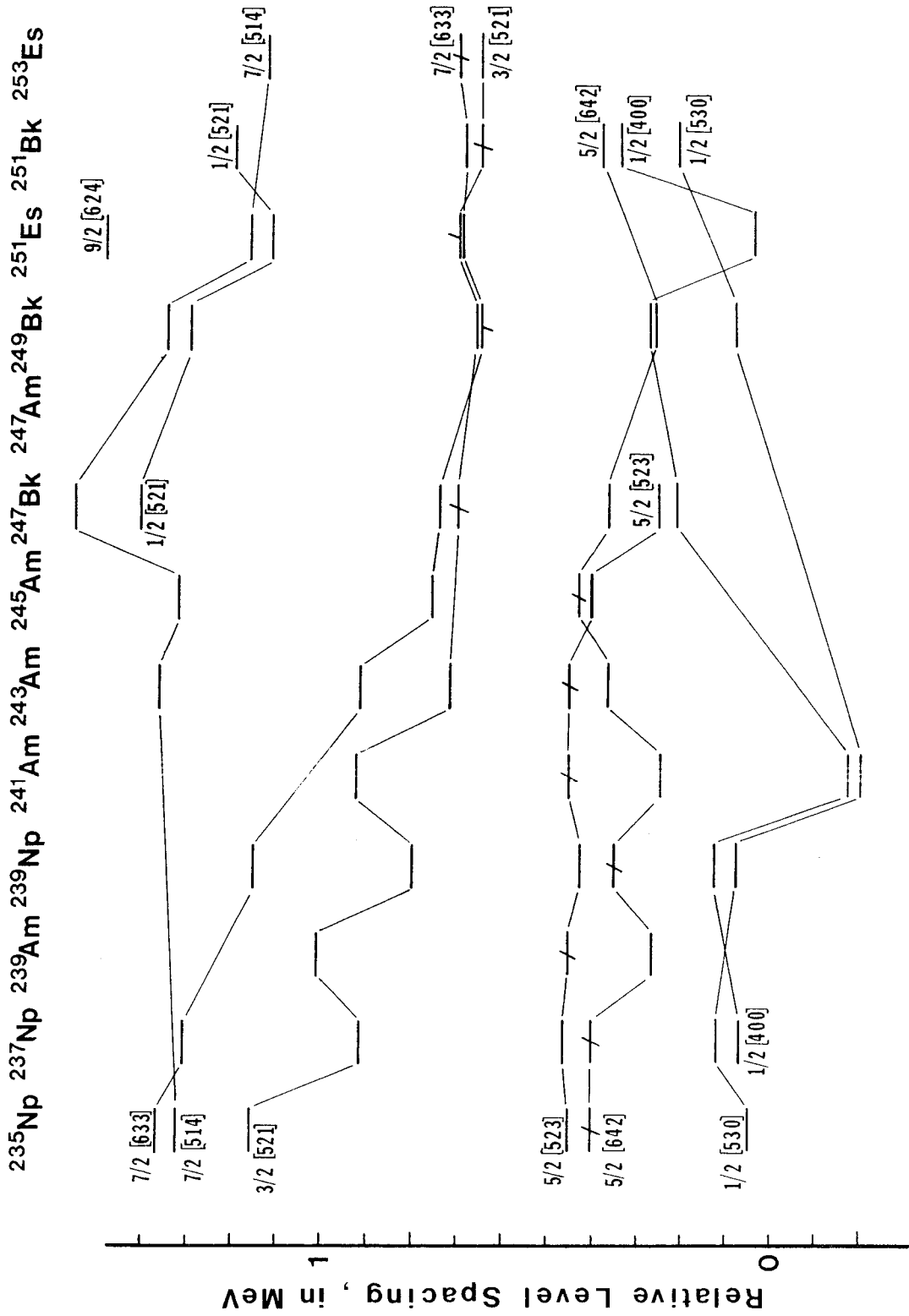


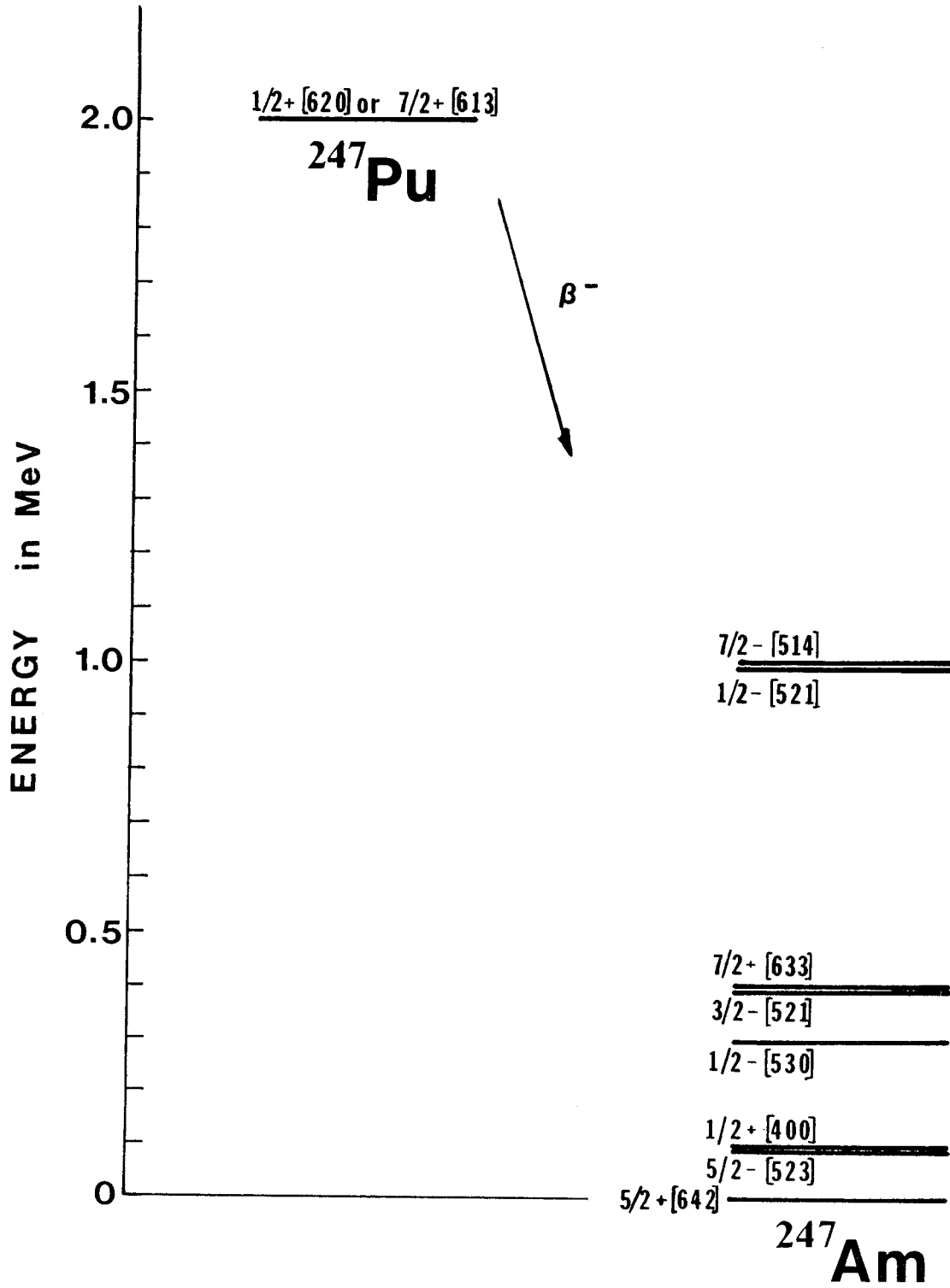
Figure 6d



ODD-PROTON ENERGY LEVELS

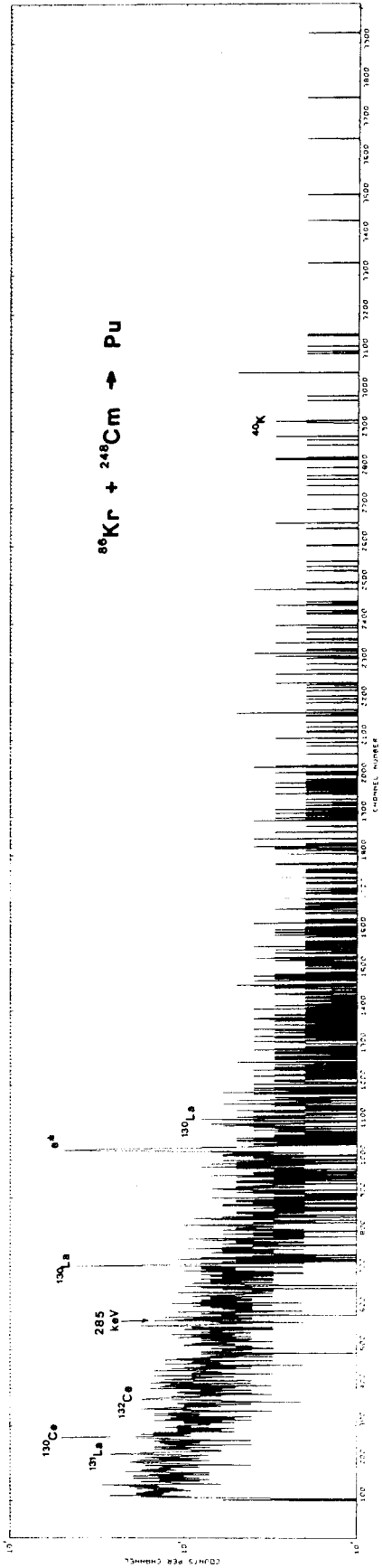
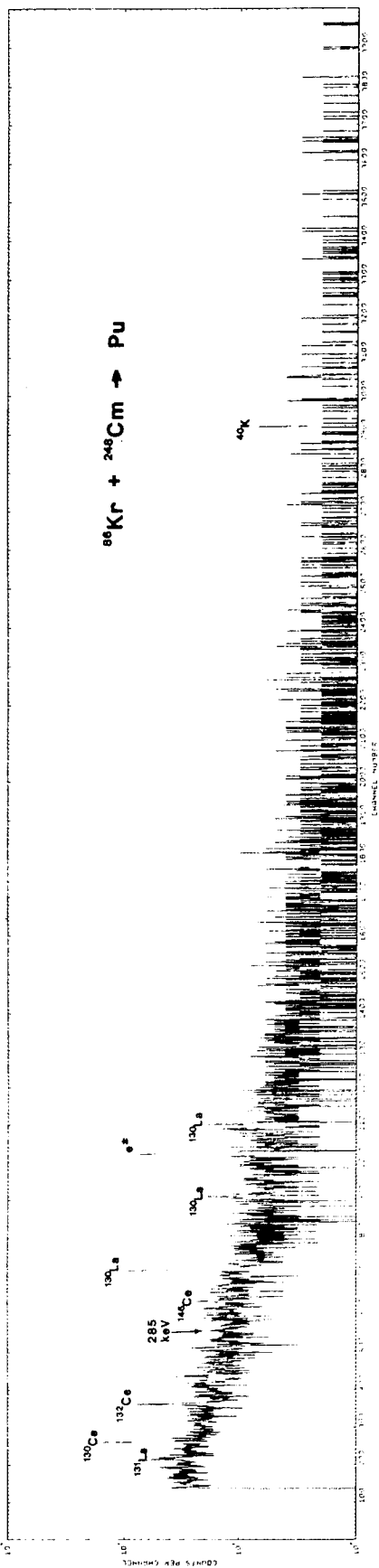
Figure 6e

XBL 836-10298



XBL 836-10294

Figure 6f



XBL 836-10397

Figure 69

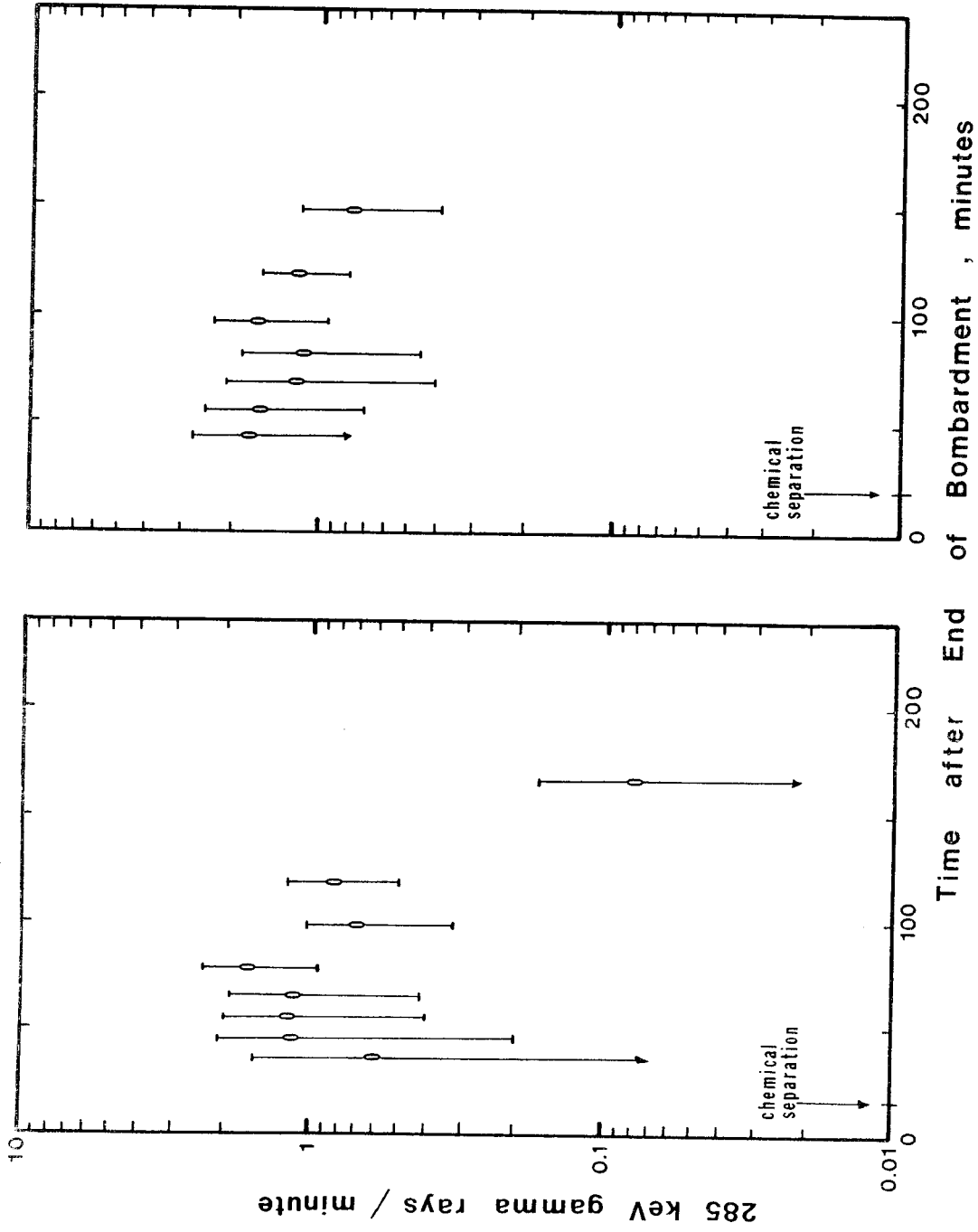


Figure 6h

XBL 836-10230

Section 7 - Conclusion

The reaction of heavy ions with neutron-rich actinide species is of very little use in producing new, neutron-rich nuclides at a higher Z than that of the target, though some hope exists in bombardments of ^{254}Es targets and ^{250}Cm targets, if they become available. Synthesis of new below-target nuclides, however, should occur with high yields. In reactions of ^{136}Xe or ^{238}U ions with ^{248}Cm , the production and isolation of new heavy americium and plutonium isotopes should be possible, though a preliminary search for ^{247}Pu described here failed, probably due to half life considerations. Other targets which should prove useful in new below-target actinide synthesis are ^{238}U , ^{244}Pu and ^{252}Cf , though handling the latter material is a problem due to its high specific activity.

References

- [Ahm70] Ahmad, I., R. Sjoblom, R. Barnes, E. Horwitz, P. Fields; Nucl.Phys. A140, 141 (1970).
- [Ahm71] Ahmad, I., F. Porter, M. Freedman, R. Barnes, R. Sjoblom, F. Wagner, J. Milsted, P. Fields; Phys.Rev. C3, 390 (1971).
- [Ahm78] Ahmad, I., R. Sjoblom, A. Friedman, S. Yates; Phys.Rev. C17, 2163 (1978).
- [Ahm79] Ahmad, I., S. Yates, R. Sjoblom, A. Friedman; Phys.Rev. C20, 290 (1979).
- [Ahm82] Ahmad, I., E. Horwitz; Nucl.Phys. A373, 434 (1982).
- [Ale75] Aleshin, V.; Sov.J.Nucl.Phys. 20, 267 (1975).
- [Art70] Artukh, A., V. Avdeichikov, L. Chelnokov, G. Gridnev, V. Mikheev, V. Vakatov, V. Volkov, J. Wilczynski; Phys.Lett. 32B, 43 (1970).
- [Art71] Artukh, A., V. Avdeichikov, J. Ero, G. Gridnev, V. Mikheev, V. Volkov, J. Wilczynski; Nucl.Phys. A160, 511 (1971).
- [Art71a] Artukh, A., V. Avdeichikov, G. Gridnev, V. Mikheev, V. Volkov, J. Wilczynski; Nucl.Phys. A176, 284 (1971).
- [Art72] Artukh, A., G. Gridnev, V. Mikheev, V. Volkov, J. Wilczynski; Nucl.Phys. A192, 170 (1972).
- [Art73] Artyukh, A., J. Wilczynski, V. Volkov, G. Gridnev, V. Mikheev; Sov.J.Nucl.Phys. 17, 586 (1973).
- [Art73a] Artukh, A., G. Gridnev, V. Mikheev, V. Volkov, J. Wilczynski; Nucl.Phys. A211, 299 (1973).
- [Art74] Artyukh, A., V. Volkov, G. Gridnev, A. Il'inov, V. Mikheev; Sov.J.Nucl.Phys. 19, 28 (1974).

- [Aum74] Aumann, D., G. Mullen; Nucl.Inst.Meth. 115, 75 (1974).
- [Ayi78] Ayik, S., G. Wolschin, W. Norenberg; Z.Phys. A286, 271 (1978).
- [Bar65] Barnett, G., J. Crosby, D. Ferrett; in Proceedings of the Seminar on the Preparation and Standardization of Isotope Targets and Foils, AERE-R 5097, paper 28 (1965).
- [Bec77] Beckerman, M., M. Blann; Phys.Lett. 68B, 31 (1977).
- [Bem81] Bemis, C., F. McGowan, J. Ford, W. Milner, R. Robinson, P. Stelson; Phys.Rev. C24, 2723 (1981).
- [Bev69] Bevington, P.; Data Reduction and Error Analysis for the Physical Sciences. New York: McGraw-Hill, 1969.
- [Bim72] Bimbot, R., H. Gauvin, Y. LeBeyec, M. Lefort, N. Porile, B. Tamain; Nucl.Phys. A189, 539 (1972).
- [Bim78] Bimbot, R., S. Della Negra, D. Gardes, H. Gauvin, A. Fleury, F. Hubert; Nucl.Inst.Meth. 153, 161 (1978).
- [Bim80] Bimbot, R., D. Gardes, H. Geissel, T. Kitahara, P. Armbruster, A. Fleury, F. Hubert; Nucl.Inst.Meth. 174, 231 (1980).
- [Bin77] Binder, I.; Lawrence Berkeley Laboratory Report LBL-6526 (Ph.D. thesis) (1977).
- [Bir64] Birks, J.; Theory and Practice of Scintillation Counting. Oxford: Pergammon Press, 1964.
- [Bjo82] Bjornholm, S., W. Swiatecki; Nucl.Phys. A391, 471 (1982).
- [Bla80] Blann, M.; Phys.Rev. C21, 1770 (1980).
- [Bor79] Borner, H., G. Barreau, W. Davidson, P. Jeuch, T. von Egidy, J. Almeida, D. White; Nucl.Inst.Meth. 166, 251 (1979).
- [Bos77] Bos, K., A. Wapstra; At.Nucl.Data Tables 19, 277 (1977).

- [Bru61] Bruninx, E., G. Rudstam; Nucl.Inst.Meth. 13, 131 (1961).
- [Bur74] Burney, G., R. Harbour; The Radiochemistry of Neptunium, Subcommittee on Radiochemistry, Nat'l.Acad.Sci.-Nat'l.Research Council, NAS-NS-3060 (1974).
- [But77] Butler, P., I. Lee, J. Newton, Y. El-Masri, M. Aleonard, P. Colombani, R. Diamond, F. Stephens, R. Lougheed, E. Hulet; Phys.Lett. 68B, 122 (1977).
- [Car57] Carswell, D., J. Milsted; J.Nucl.Energy I 4, 51 (1957).
- [Cha73] Chayawattanangkur, K., G. Herrmann, N. Trautmann; J.Inorg.Nucl.Chem. 35, 3061 (1973).
- [Chi62] Chi, B., A Table of Clebsch-Gordan Coefficients. Troy, New York: Rensselaer Polytechnic Institute, 1962.
- [Chi79] Chiang, T., D. Guerreau, P. Auger, J. Galin, B. Gatty, X. Tarrago, J. Girard; Phys.Rev. C20, 1408 (1979).
- [Coh74] Cohen, S., F. Plasil, W. Swiatecki; Ann.Phys. 82, 557 (1974).
- [Col65] Coleman, G., The Radiochemistry of Plutonium, Subcommittee on Radiochemistry, Nat'l.Acad.Sci.-Nat'l.Research Council, NAS-NS-3058 (1965).
- [Com66] Combined Radiochemistry Group; Phys.Rev. 148, 1192 (1966).
- [Cot80] Cotton, F., G. Wilkinson, Advanced Inorganic Chemistry, 4th ed. New York: John Wiley and Sons, 1980.
- [Dak65] Dakowski, M., H. Piekarz, M. Sowinski; Inst. of Nuclear Research, Report 595/IA/PL, Warsaw (1965).
- [Des74] deShalit, A., H. Feshbach, Theoretical Nuclear Physics, vol. 1. New York: John Wiley, 1974.
- [Des78] de Saint-Simon, M., R. Otto, G. Seaborg; Phys.Rev. C18, 1651 (1978).

- [Dia67] Diamond, H., R. Sjoblom, R. Barnes, J. Lerner, D. Henderson, P. Fields; *J.Inorg.Nucl.Chem.* 29, 601 (1967).
- [Dia68] Diamond, R., A. Poskanzer, F. Stephens, W. Swiatecki, D. Ward; *Phys.Rev.Lett.* 20, 802 (1968).
- [Dra69] Dragoun, O., H. Pauli, F. Schmutzler; *Nucl.Data Tables A6*, 235 (1969).
- [Duf80] Dufour, J., A. Fleury, R. Bimbot; Centre d'Etudes Nucleaires de Bordeaux-Gradignan Report CFNBG 8007 (1980).
- [Ede81] Edelstein, N.; Private Communication (1981).
- [Ell78] Ellis, Y.; *Nuclear Data Sheets* 23, 71 (1978).
- [Ell78a] Ellis, Y.; *Nuclear Data Sheets* 23, 123 (1978).
- [Ell81] Ellis-Akovali, Y.; *Nuclear Data Sheets* 33, 119 (1981).
- [Ell81a] Ellis-Akovali, Y.; *Nuclear Data Sheets* 33, 161 (1981).
- [Eme61] Emery, J., G. Leddicotte, The Radiochemistry of Gold, Subcommittee on Radiochemistry, Nat'l.Acad.Sci.-Nat'l.Research Council, NAS-NS-3036 (1961).
- [Eng55] Englekemeir, O., P. Fields, S. Fried, G. Pyle, C. Stevens, L. Asprey, C. Browne, H. Smith, R. Spence; *J.Inorg.Nucl.Chem.* 1, 345 (1955).
- [Esk71] Eskola, K., P. Eskola, M. Nurmi, A. Ghiorso; *Phys.Rev.* C4, 632 (1971).
- [Fie56] Fields, P., M. Studier, H. Diamond, J. Mech, M. Inghram, G. Pyle, C. Stevens, S. Fried, W. Manning, A. Ghiorso, S. Thompson, G. Higgins, G. Seaborg; *Phys.Rev.* 102, 180 (1956).
- [Fle73] Flerov, G., Yu. Oganessian; Joint Institute for Nuclear Research Report JINR E7-6838 (1973).

- [Fly79] Flynn, E., D. Hanson, R. Hardekopf; *Phys.Rev.* C19, 355 (1979).
- [Fre79] Freiesleben, H., K. Hildenbrand, F. Puhlhofer, W. Schneider, R. Bock, D. v.Harrach, H. Specht; *Z.Phys.* A292, 171 (1979).
- [Gag83] Gaggeler, H., W. Bruchle, M. Brugger, M. Schadel, K. Summerer, G. Wirth, A. Ghiorso, K. Gregorich, D. Lee, K. Moody, G. Seaborg, R. Welch, P. Wilmarth, G. Herrmann, J. Kratz, N. Trautmann, N. Hildebrand, U. Hickmann, C. Frink, N. Greulich, D. Hoffman, M. Fowler, H. von Gunten; *Gesellschaft fur Schwerionenforschung preprint GSI 83-9* (1983).
- [Gal76] Galin, J.; *J.Phys.(Paris) Colloque* C5, 83 (1976).
- [Gan67] Gangrskii, Yu., B. Gvozdev, B. Markov, S. Polikanov, H. Jungclaussen; *Sov.J.Nucl.Phys.* 5, 380 (1967).
- [Gat75] Gatty, B., D. Guerreau, M. Lefort, J. Pouthas, X. Tarrago, J. Galin, B. Cauvin, J. Girard, H. Nifenecker; *Z.Phys.* A273, 65 (1975).
- [Get65] Getoff, N., H. Bildstein; *Nucl.Inst.Meth.* 36, 173 (1965).
- [Get69] Getoff, N., H. Bildstein; *Nucl.Inst.Meth.* 70, 352 (1969).
- [Ghi70] Ghiorso, A., M. Nurmia, K. Eskola, P. Eskola; *Phys.Lett.* 32B, 95 (1970).
- [Ghi82] Ghiorso, A., et.al.; Experiments to search for superheavy elements with on-line gas-filled spectrometer SASSY, private communication (1982).
- [Gil71] Gilat, J., J. Grover; *Phys.Rev.* C3, 734 (1971).
- [Gla77] Glassel, P., R. Jared, L. Moretto; *Nucl.Inst.Meth.* 142, 569 (1977).
- [Glo65] Glover, K., P. Robinson; in *Proceedings of the Seminar on the Preparation and Standardization of Isotope Targets and Foils, AERE-R 5097*, paper 11 (1965).
- [Gou75] Goulding, F., B. Harvey; *Ann.Rev.Nucl.Sci.* 25, 167 (1975).

- [Gou76] Gough, R., R. Lam, C. Martinez, D. Morris; Lawrence Berkeley Laboratory Report 5046 (1976).
- [Gou79] Gough, R.; Private communication (1979).
- [Gov71] Gove, N., M. Martin; Nucl.Data Tables 10, 205 (1971).
- [Gri62] Grindler, J., The Radiochemistry of Uranium, Subcommittee on Radiochemistry, Nat'l.Acad.Sci.-Nat'l.Research Council, NAS-NS-3050 (1962).
- [Gri78] Griffioen, R., R. Thompson, J. Huizenga; Phys.Rev. C18, 671 (1978).
- [Gro67] Grover, J., J. Gilat; Phys.Rev. 157, 814 (1967).
- [Gro83] Groening, H., K. Moody, G. Seaborg; to be published in Nuclear Instruments and Methods (1983).
- [Gue80] Guerreau, D., J. Galin, B. Gatty, X. Tarrago, J. Girard, R. Lucas, C. Ngo; Z.Phys. A295, 105 (1980).
- [Gus67] Gustafson, C., I. Lamm, B. Nilsson, S. Nilsson; Ark.Fys. 36, 613 (1967).
- [Hag60] Hagedoorn, H., A. Wapstra; Nucl.Phys. 15, 146 (1960).
- [Hag68] Hager, R., E. Seltzer; Nucl.Data Tables A4, 1 (1968).
- [Hah74] Hahn, R., P. Dittner, K. Toth, O. Keller; Phys.Rev. C10, 1889 (1974).
- [Ham76] Hamilton Technology, Inc., 1976 Catalog.
- [Hau79] Haustein, P., H.-C. Hseuh, R. Klobuchar, E.-M. Franz, S. Katcoff, L. Peker; Phys.Rev. C19, 2332 (1979).
- [Her79] Herrmann, G.; Nature 280, 543 (1979).
- [Hig60] Higgins, G., The Radiochemistry of the Transcurium Elements, Subcommittee on Radiochemistry, Nat'l.Acad.Sci.-Nat'l.Research Council, NAS-NS-3031 (1960).
- [Hir75] Hirdes, D., E. Georg, H. Wollnik, R. Brandt; Nucl.Inst.Meth. 130, 15

(1975).

[Hof70] Hoff, R., R. Lougheed, P. Johnson; Lawrence Livermore Laboratory Report UCRL-72090 (1970).

[Hof76] Hoff, R.; in *Transplutonium 1975*, Ed. W. Muller, R. Lindner. Amsterdam: North-Holland, 1976.

[Hof76a] Hoffman, D., J. Weber, J. Wilhelmy, E. Hulet, R. Lougheed, J. Landrum, J. Wild; in *Transplutonium 1975*, Ed. W. Muller, R. Lindner. Amsterdam: North-Holland, 1976.

[Hof77] Hoffman, D., J. Wilhelmy, J. Weber, W. Daniels, E. Hulet, J. Landrum, R. Lougheed, J. Wild; Los Alamos Scientific Laboratory Report LA-UR-77-2901 (1977).

[Hof82] Hoff, R., W. Davidson, D. Warner, H. Borner, T. von Egidy; *Phys.Rev. C25*, 2232 (1982).

[Hof83] Hoffman, D., D. Lee; Private communication (1983).

[Hol64] Holcomb, H.; *Anal.Chem.* 36, 2329 (1964).

[How80] Howard, W., P. Moller; *At.Nucl.Data Tables* 25, 219 (1980).

[Hub80] Hubert, F., A. Fleury, R. Bimbot, D. Gardes; *Ann.Phys., Fr.* 5, 1 (1980).

[Hui57] Huizenga, J., H. Diamond; *Phys.Rev.* 107, 1087 (1957).

[Hui76] Huizenga, J., J. Birkelund, W. Schroder, K. Wolf, V. Viola; *Phys.Rev.Lett.* 37, 885 (1976).

[Hul77] Hulet, E., R. Lougheed, J. Wild, J. Landrum, P. Stevenson, A. Ghiorso, J. Nitschke, R. Otto, D. Morrissey, P. Baisden, B. Gavin, D. Lee, R. Silva, M. Fowler, G. Seaborg; *Phys.Rev.Lett.* 39, 385 (1977).

[Hul81] Hulet, E., R. Lougheed, J. Nitschke, R. Hahn, R. Ferguson, W. Bruchle, H. Gaggeler, J. Kratz, M. Schadel, G. Wirth, G. Herrmann, G. Tittel, N.

Trautmann; Pure Appl.Chem. 53, 965 (1981).

[Ign72] Ignatyuk, A., G. Smirenkin, A. Tishin; Sov.J.Nucl.Phys. 15, 622 (1972).

[Jac75] Jacmart, J., P. Colombani, H. Doubre, N. Frascaria, N. Poffe, M. Riou, J. Roynette, C. Stephan, A. Weidinger; Nucl.Phys. A242, 175 (1975).

[Jar74] Jarmie, N., L. Morrison, J. Martin; Nucl.Inst.Meth. 116, 451 (1974).

[Kal77] Kalpakchieva, R., Yu. Oganessian, Yu. Penionzhkevich, V. Polyanskii, H. Bruchertseifer, K. Gavrilov, C. Sek; Sov.J.Nucl.Phys. 26, 131 (1977).

[Kal77a] Kalpakchieva, R., Yu. Oganessian, Yu. Penionzhkevich, H. Sodan; Z.Phys. A283, 253 (1977).

[Kar69] Karamyan, S., Yu. Oganessian; Argonne National Laboratory Report ANL-trans-745 (1969).

[Kin81] King, L., J. Bigelow, E. Collins; Oak Ridge National Laboratory Report ORNL-5596 (1981).

[Kir82] Kirchner, R., O. Klepper, W. Kurcewicz, E. Roeckl, E. Zganjar, E. Runte, W.-D. Schmidt-Ott, P. Tidemand-Petersson, N. Kaffrell, P. Peuser, K. Rykaczewski; Nucl.Phys. A378, 549 (1982).

[Kla80] Klapdor, H., T. Oda; Astrophys.J. 242, L49 (1980).

[Kol75] Kolesnikov, N., A. Demin; Joint Institute for Nuclear Research Report JINR P6-9421.

[Kra73] Krappe, H., J. Nix; in Physics and Chemistry of Fission, 3rd Symposium. Vienna: IAEA, 1973.

[Kra74] Kratz, J., A. Norris, G. Seaborg; Phys.Rev.Lett. 33, 502 (1974).

[Kra76] Kratz, J., J. Liljenzin, A. Norris, G. Seaborg; Phys.Rev. C13, 2347 (1976).

- [Kra80] Kratz, J., W. Bruchle, H. Gaggeler, M. Schadel, K. Summerer, G. Wirth; Z.Phys. A296, 141 (1980).
- [Kra80a] Kratz, J.; Gesellschaft für Schwerionenforschung Report GSI 80-1 (1980).
- [Kra82] Kratz, J.; Gesellschaft für Schwerionenforschung Report GSI 82-7 (1982).
- [Kum63] Kumpf, H., E. Donets; Sov.Phys.JETP 17, 539 (1963).
- [Kuz67] Kuznetsov, V., N. Skobelev, G. Flerov; Sov.J.Nucl.Phys. 4, 70 (1967).
- [Lai82] Laichter, Y., H. Geissel, M. Schadel, P. Armbruster; Phys.Rev. A26, 1915 (1982).
- [Lan66] Lang, D.; Nucl.Phys. 77, 545 (1966).
- [Lee82] Lee, D., H. von Gunten, B. Jacak, M. Nurmi, Y.-F. Liu, C. Luo, G. Seaborg, D. Hoffman; Phys.Rev. C25, 286 (1982).
- [Lee82a] Lee, D.; Private communication (1983).
- [Lee83] Lee, D., K. Moody, M. Nurmi, G. Seaborg, H. von Gunten, D. Hoffman; Phys.Rev. C27, 2656 (1983).
- [Lef76] Lefort, M.; Rep.Prog.Phys. 39, 129 (1976).
- [Lef78] Lefort, M., C. Ngo; Ann.Phys.(Paris) 3, 5 (1978).
- [Lil73] Liljenzin, J.; Lawrence Berkeley Laboratory Report LBL-1912 (1973).
- [Liu83] Liu, Y.-F., C. Luo, K. Moody, D. Lee, G. Seaborg, H. von Gunten; J.Radioanalytical Chemistry 76, 119 (1983).
- [Lou78] Loughheed, R., J. Wild, E. Hulet, R. Hoff, J. Landrum; J.Inorg.Nucl.Chem. 40, 1865 (1978).
- [Lou79] Loughheed, R., E. Hulet; Nucl.Inst.Meth. 166, 329 (1979).
- [Lou82] Loughheed, R., E. Hulet, R. Landingham, J. Nitschke, H. Folger, J.

Kratz, W. Bruchle, H. Gaggeler; *Nucl.Inst.Meth.* 200, 71 (1982).

[Luc79] Lucas, R., J. Poitou, J. Kratz, G. Wirth; *Z.Phys.* A290, 327 (1979).

[Mal67] Malov, L., S. Polikanov, V. Solov'ev; *Sov.J.Nucl.Phys.* 4, 376 (1967).

[Mar69] Marmier, P., E. Sheldon, *Physics of Nuclei and Particles*, vol. 1.
New York: Academic Press, 1969.

[Mar70] Marmier, P., E. Sheldon, *Physics of Nuclei and Particles*, vol. 2.
New York: Academic Press, 1970.

[Mar80] Marinov, A., S. Eshhar, J. Weil, D. Kolb; "Production of Actinides and
Consequences Concerning the Possible Production of Superheavy Elements in
Tungsten Targets Irradiated with 24GeV Protons," unpublished (1980).

[Mat79] Mathews, G., L. Sobotka, G. Wozniak, R. Regimbart, R. Schmitt, G.
Rattazzi, L. Moretto; *Z.Phys.* A290, 407 (1979).

[McF82] McFarland, R.; Lawrence Berkeley Laboratory Report LBL-15027
(Ph.D. thesis) (1982).

[Mel76] Meldner, H., G. Cowan, J. Nix, R. Stoughton; *Phys.Rev.* C13, 182
(1976).

[Moo63] Moore, F.; *Anal.Chem.* 35, 715 (1963).

[Moo81] Moody, K., M. Nurmia, G. Seaborg; Lawrence Berkeley Laboratory
Annual Report 1979-1980, LBL-11588, 188 (1981).

[Moo82] Moody, K., D. Lee; Unpublished data (1982).

[Mor76] Moretto, L., R. Schmitt; *J.Phys.(Paris) Colloque C5*, 109 (1976).

[Mor79] Moretto, L.; Lawrence Berkeley Laboratory Report LBL-9130
(1979).

[Mor82] Moretto, L.; Lawrence Berkeley Laboratory Report LBL-14563
(1982).

- [Mos65] Moszkowski, S., Alpha- , Beta- , and Gamma-Ray Spectroscopy, ed. K. Siegbahn. Amsterdam: North-Holland, 1965.
- [Mou78] Moulton, J., E. Stephenson, R. Schmitt, G. Wozniak; Nucl.Inst.Meth. 157, 325 (1978).
- [Mul75] Mullen, G., D. Aumann; Nucl.Inst.Meth. 128, 425 (1975).
- [Mun81] Munzenberg, G., S. Hofmann, F. Hessberger, W. Reisdorf, K. Schmidt, J. Schneider, P. Armbruster, C. Sahm, B. Thuma; Z.Phys. A300, 107 (1981).
- [Mun82] Munzenberg, G., P. Armbruster, F. Hessberger, S. Hofmann, K. Poppenieker, W. Reisdorf, J. Schneider, W. Schneider; Z.Phys. A309, 89 (1982).
- [Mye77] Myers, W., Droplet Model of Atomic Nuclei. New York: IFI/Plenum, 1977.
- [Nil68] Nilsson, S.; Lawrence Berkeley Laboratory Report UCRL-18355 Rev. (1968).
- [Nit76] Nitschke, J.; Nucl.Inst.Meth. 138, 393 (1976).
- [Nit83] Nitschke, J.; Nucl.Inst.Meth. 206, 341 (1983).
- [Nor63] Northcliffe, L.; Ann.Rev.Nucl.Sci. 13, 67 (1963).
- [Nor66] Norris, A., G. Friedlander, E. Franz; Nucl.Phys. 86, 102 (1966).
- [Nor70] Northcliffe, L., R. Schilling; Nucl.Data Tables A7, 233 (1970).
- [Nor74] Norenberg, W.; Phys.Lett. 52B, 289 (1974).
- [Oga70] Oganessian, Yu., Yu. Lobanov, S. Tret'yakova, Yu. Lazarev, I. Koleskov, K. Gavrilov, V. Plotko, Yu. Poluboyarinov; Sov.At.Energy 28, 502 (1970).
- [Oga74] Oganessian, Yu., Yu. Penionzhkevich, N. Tac Ahn, A. Adamek, N. Quoc Bui, N. Mong Sinh; Sov.J.Nucl.Phys. 19, 119 (1974).
- [Oga74a] Oganessian, Yu., Yu. Penionzhkevich, N. Tac Ahn, D. Nadkarnee, K.

Gavrilov, K. De En, M. Yussonua; *Sov.J.Nucl.Phys.* 18, 377 (1974).

[Ort67] Orth, C., W. Daniels, B. Erkkila, F. Lawrence, D. Hoffman;
Phys.Rev.Lett. 19, 128 (1967).

[Ort73] Orth, C., W. Daniels, B. Dropesky; *Phys.Rev.* C8, 2364 (1973).

[Ott76] Otto, R., M. Fowler, D. Lee, G. Seaborg; *Phys.Rev.Lett.* 36, 135
(1976).

[Ott77] Otto, R., A. Ghiorso, D. Lee, R. Leber, S. Yashita, G. Seaborg;
Radiochimica Acta 24, 3 (1977).

[Ott78] Otto, R., D. Morrissey, G. Seaborg, W. Loveland; *Z.Phys.* A287, 97
(1978).

[Ott78a] Otto, R., G. Seaborg, M. Fowler; *Phys.Rev.* C17, 1071 (1978).

[Par60] Parker, W., M. de Croes, K. Sevier; *Nucl.Inst.Meth.* 7, 22 (1960).

[Par64] Parker, W., H. Bildstein, N. Getoff; *Nucl.Inst.Meth.* 26, 55 (1964).

[Par64a] Parker, W., H. Bildstein, N. Getoff, H. Fischer-Colbrie, H. Regal;
Nucl.Inst.Meth. 26, 61 (1964).

[Par81] Parekh, P., E.-M. Franz, S. Katcoff, L. Peker; *Phys.Rev.* C24, 2240
(1981).

[Pen60] Penneman, R., T. Keenan, *The Radiochemistry of Americium and Curium*, Subcommittee on Radiochemistry, Nat'l.Acad.Sci.-Nat'l.Research Council, NAS-NS-3006 (1960).

[Phi78] Phillips, G.; *Nucl.Inst.Meth.* 153, 449 (1978).

[Plo82] Ploszajczak, M., M. Faber; *Phys.Rev.* C25, 1538 (1982).

[Pol62] Polikanov, S., V. Druin, V. Karnaukhov, V. Mikheev, A. Plevé, N. Skobelev, V. Subbotin, G. Ter-Akop'yan, V. Fomichev; *Sov.Phys.JETP* 15, 1016 (1962).

[Ras68] Rasmussen, J.; in *Alpha-, Beta-, and Gamma-Ray Spectroscopy*,

- vol. 1, ed. K. Siegbahn. Amsterdam: North-Holland, 1968.
- [Rav79] Ravn, H.; Phys.Rep. 54, 201 (1979).
- [Rea65] Reames, D.; Phys.Rev. 137, B332 (1965).
- [Reu77] Reus, U., A. Habbestad-Watzig, R. Esterlund, P. Patzelt, I. Grant; Phys.Rev.Lett. 39, 171 (1977).
- [Rou69] Routti, J., S. Prussin; Nucl.Inst.Meth. 72, 125 (1969).
- [Ryk83] Rykaczewski, K., R. Kirchner, W. Kurcewicz, D. Schardt, N. Kaffrell, P. Peuser, E. Runte, W.-D. Schmidt-Ott, P. Tidemand-Petersson, K.-L. Gippert; Z.Phys. A309, 273 (1983).
- [Sal74] Salem, S., S. Panossian, R. Krause; At.Nucl.Data Tables 14, 91 (1974).
- [Sau65] Sautter, C.,E. Zimmerman; Phys.Rev. 140, A490 (1965).
- [Sch63] Schrain, E., R. Lambaert, Organic Scintillation Detectors. Amsterdam: Elsevier Publishing, 1963.
- [Sch77] Schmorak, M.; Nuclear Data Sheets 21, 117 (1977).
- [Sch77a] Schmorak, M.; Nuclear Data Sheets 21, 153 (1977).
- [Sch77b] Schroder, W., J. Huizenga; Ann.Rev.Nucl.Sci. 27, 465 (1977).
- [Sch78] Schadel, M., J. Kratz, H. Ahrens, W. Bruchle, G. Franz, H. Gaggeler, I. Warnecke, G. Wirth, G. Herrmann, N. Trautmann, M. Weis; Phys.Rev.Lett. 41, 469 (1978).
- [Sch79] Schadel, M.; Gesellschaft fur Schwerionenforschung Report GSI 79-8 (Ph.D. thesis) (1979).
- [Sch82] Schadel, M., W. Bruchle, H. Gaggeler, J. Kratz, K. Summerer, G. Wirth, G. Herrmann, R. Stakemann, G. Tittel, N. Trautmann, J. Nitschke, E. Hulet, R. Loughheed, R. Hahn, R. Ferguson; Phys.Rev.Lett. 48, 852 (1982).

[Sch82a] Schadel, M., R. Loughheed, J. Landrum, J. Wild, R. Dougan, A. Hoover, E. Hulet, G. Bethune, A. Ghiorso, M. Nurmi, L. Somerville, K. Moody, G. Seaborg; Lawrence Livermore Laboratory Nuclear Chemistry Division FY-82 Progress Report (1982).

[Sco77] Scott, D.; Lawrence Berkeley Laboratory Report LBL-7111 (1977).

[See81] Seelmann-Eggebert, W., G. Pfennig, H. Munzel, H. Klewer-Nebenius; Nuklidekarte, 5th ed. Lippe, West Germany: Druckhaus Haberbeck, 1981.

[Seg77] Segre, E., Nuclei and Particles, 2nd ed. London: Benjamin/Cummings, 1977.

[Sho74] Shoemaker, D., C. Garland, J. Steinfeld, Experiments in Physical Chemistry, 3rd ed. New York: McGraw-Hill, 1974.

[Sie71] Siemens, P., J. Bondorf, D. Gross, F. Dickmann; Phys.Lett. 36B, 24 (1971).

[Sik67] Sikkeland, T.; Ark.Fis. 36, 539 (1967).

[Sil73] Silva, R., P. Dittner, M. Mallory, O. Keller, K. Eskola, M. Nurmi, A. Ghiorso; Nucl.Phys. A216, 97 (1973).

[Sob79] Sobotka, L., G. Mathews, L. Moretto; Z.Phys. A292, 191 (1979).

[Som82] Somerville, L.; Lawrence Berkeley Laboratory Report LBL-14050 (Ph.D. thesis) (1982).

[Spe73] Sperber, D.; Phys.Lett. 47B, 209 (1973).

[Ste72] Steinberg, E., S. Kaufman, B. Wilkins, C. Gross, M. Fluss; Nucl.Inst.Meth. 99, 309 (1972).

[Str67] Strutinsky, V.; Nucl.Phys. A95, 420 (1967).

[Str68] Strutinsky, V.; Nucl.Phys. A122, 1 (1968).

[Str69] Strutinsky, V., H. Pauli; in Physics and Chemistry of Fission, 2nd

Symposium. Vienna: IAEA, 1969.

[Sup79] SuperHILAC User's Manual, Lawrence Berkeley Laboratory Publication Pub.102 (1979).

[Sve78] Sventek, J., L. Moretto; Phys.Rev.Lett. 40, 697 (1978).

[Swi82] Swiatecki, W.; Nucl.Phys. A376, 275 (1982).

[Tak60] Takahashi, K., H. Morinaga; Nucl.Phys. 21, 133 (1960).

[Tak73] Takahashi, K., M. Yamada, T. Kondoh; At.Nucl.Data Tables 12, 101 (1973).

[Thi83] Thielemann, F., J. Metzinger, H. Klapdor; Z.Phys. A309, 301 (1983).

[Tho74] Thompson, S., L. Moretto, R. Jared, R. Babinet, J. Galin, M. Fowler, R. Gatti, J. Hunter; Phys.Scripta 10A, 36 (1974).

[Tho79] Thomas, K.; Lawrence Berkeley Laboratory Report LBL-9886 (Ph.D. thesis) (1979).

[TOI78] Table of Isotopes, 7th ed. Ed. C. Lederer, V. Shirley. New York: Wiley, 1978.

[Tra69] Trautmann, N., R. Denig, G. Herrmann; Radiochimica Acta 11, 168 (1969).

[Tul81] Tuli, J.; Nuclear Data Sheets 34, 1 (1981).

[Uni72] Unik, J., E. Horwitz, K. Wolf, I. Ahmad, S. Fried, D. Cohen, P. Fields, C. Bloomquist, D. Henderson; Nucl.Phys. A191, 233 (1972).

[Van59] Vandenbosch, S., H. Diamond, R. Sjoblom, P. Fields; Phys.Rev. 115, 115 (1959).

[Van73] Vandenbosch, R., J. Huizenga, Nuclear Fission. New York: Academic Press, 1973.

[Var76] Varley, G., J. Willmott, F. Kearns; Nucl.Inst.Meth. 135, 167 (1976).

- [Vio66] Viola, V., G. Seaborg; *J.Inorg.Nucl.Chem.* 28, 697 (1966).
- [Vio80] Viola, V., A. Mignerey, H. Breuer, K. Wolf, B. Glagola, W. Wilke, W. Schroder, J. Huizenga, D. Hilscher, J. Birkelund; Report ORO-5172-15.
- [Vol78] Volkov, V.; *Phys.Rep.* 44, 93 (1978).
- [Wap59] Wapstra, A., G. Nijgh, R. van Lieshout; *Nuclear Spectroscopy Tables*. Amsterdam: North-Holland, 1959.
- [Wap77] Wapstra, A., K. Bos; *At.Nucl.Data Tables* 19, 177 (1977).
- [Wea82] Weast, R., M. Astle, *CRC Handbook of Chemistry and Physics*, 63rd ed. Boca Raton, Florida: CRC Press, 1982.
- [Wel80] Welch, R., K. Moody; computer code RANGY, private communication.
- [Wel82] Welch, R., Private communication.
- [Wel83] Welch, R., Private communication.
- [Wie76] Wiernik, M.; *Radiochimica Acta* 23, 46 (1976).
- [Wil71] Wilkins, B., M. Fluss, S. Kaufman, C. Gross, E. Steinberg; *Nucl.Inst.Meth.* 92, 381 (1971).
- [Wil78] Williams, K.; Lawrence Berkeley Laboratory Report LBL-7714 (Ph.D. thesis) (1978).
- [Wil79] Williams, K., G. Seaborg; *Phys.Rev.* C19, 1794 (1979).
- [Wil80] Wilcke, W., J. Birkelund, H. Wollersheim, A. Hoover, J. Huizenga, W. Schroder, L. Tubbs; *At.Nucl.Data Tables* 25, 389 (1980).
- [Yaf62] Yaffe, L.; *Ann.Rev.Nucl.Sci.* 12, 153 (1962).